UNIVERSITY OF CALIFORNIA

Santa Barbara

Ozone Variability and Deep Convection in the UTLS Over South America

A dissertation submitted in partial satisfaction of the

requirements for the degree Doctor of Philosophy in Geography

by

Brandi L. Gamelin

Committee in charge:

Professor Leila Carvalho, Chair

Professor Charles Jones

Professor Qinghua Ding

June 2020

The dissertation of Brandi L. Gamelin is approved.

_____

Charles Jones

_____

Qinghua Ding

_____

Leila Carvalho, Committee Chair

June 2020

Ozone Variability and Deep Convection in the UTLS Over South America

by

Brandi L. Gamelin

ACKNOWLEDGEMENTS

I would like to express my deepest gratitude to my advisor and committee chair, Professor Leila Carvalho, without whom this work would not be possible. Her help and unwavering guidance has allowed me to endure during difficult times and the strength to carry on. I am most grateful to her for my education, and extensive preparation for future endeavors.

I would like to thank my committee members, Professor Charles Jones and Professor Qinghua Ding, for their time and comments to improve this research. Their input is very much appreciated.

I would like to express my appreciation to the University of California, Santa Barbara's (UCSB) Graduate Division who provided me with two Fellowships to conduct this research. As well as UCSB's Department of Geography and the Earth Research Institute for their support throughout the years.

I would like to thank the members of the CLIVAC lab, past and present. I am profoundly grateful to my friends for their unending support during this research.

I am incredibly grateful for my family, especially the constant and unfailing support of my boys, and my mother, Karen Cihigoyenetche who has always supported my education and encouraged my need to learn more.

VITA OF BRANDI L. GAMELIN
June 2020

EDUCATION

Ph.D. Geography - University of California, Santa Barbara. (June 2020; expected)
M.A. Geography - California State University, Los Angeles. (June 1913)
B.S. Geography (cum laude) - California Polytechnic State University, Pomona. (June 2010)

RESEARCH AND FIELD EXPERIENCE

Advanced Study Institute: Field Studies of Convection in Argentina. RELAMPAGO (Remote Sensing of Electrification, Lightning, and Mesoscale/microscale Processes with Adaptive Ground Observations) field campaign in Cordoba, Argentina. (November 2018)

First Sundowner Wind Experiment (SWEX-I): Understanding Fire Weather Regimes in Santa Barbara, Santa Barbara, CA. *(*April-27-29, 2018)

Visiting Graduate Student Researcher. NASA Jet Propulsion Laboratory, Pasadena. Ocean Circulation and Air Sea Interaction group*: Los Angeles Urban Heat Island*. (summer 2013)

Graduate Student Researcher, NASA Jet Propulsion Laboratory, Pasadena. Atmospheric Infrared Sounder (AIRS) group. Master's Thesis: *Investigation of Arctic water vapor as a greenhouse gas, and variability related to northern hemisphere teleconnection patterns*. (2012 – 2013)

Graduate Research Assistant. California State University, Los Angeles. *Southern California coastal and desert precipitation responses to ENSO phases*. (2011)

Undergraduate Student Researcher Modeled snowpack elevation changes based on IPCC greenhouse gas scenarios and projected climate changes. California Polytechnic State University, Pomona. (2010)

TEACHING EXPERIENCE

Teaching Associate (Instructor):
University of California, Santa Barbara:
GEOG 148-Geography of California (spring 2020)
GEOG 5-People, Place and Environment (winter 2020)
GEOG 3B/4-Land Water and Life (summer 2016, fall 2016, summer 2018, summer 2019)
GEOG 110-Introduction to Meteorology (summer 2017)
GEOG 3A/3-Ocean and Atmosphere (summer 2015 and summer 2017)

California State University, Los Angeles:

URBA 180/1800-Urban World (spring 2014)

GEOG 160/1600-Physical Geography (fall 2012, fall 2013, winter 2014 and spring 2014)

GEOG 155/1550-Cultural Geography (fall 2013, winter 2014 and spring 2014)

Teaching Assistant:

University of California, Santa Barbara:

GEOG 131-Mountain Weather (fall 2019)

GEOG 3B/4-Land, Water and Life (spring 2016 and 2017)

GEOG 110-Intro to Meteorology (winter 2015, 2016, and 2017)

GEOG 133-Tropical Meteorology (fall 2015)

GEOG 3A/3-Ocean and Atmosphere (fall 2014)

California State University, Los Angeles:

GEOG 160/1600-Physical Geography (spring 2012)

PUBLICATIONS

Gamelin, B.L., L.M.V. Carvalho, and M. Kayano, 2019: *The Combined Influence of ENSO and PDO on the Spring UTLS Ozone Variability in South America.* (in review, Climate Dynamics)

Carvalho L. , G-J Duine, C. Jones, C. Clements, K. Zigner, **B. Gamelin**, H. Kane, C. Gore, G. Bell, D. Gomberg, T. Hall, M. Johnson, J. Dumas, E. Boldt, R. Hazard, and W. Enos, 2018: *The Sundowner Winds Experiment (SWEX) First Intensive Campaign: understanding downslope windstorms in the Santa Ynez Mountains, Santa Barbara, CA, Monthly Weather Review.*

Ye, H., E. Fetzer, A. Behrangi, S. Wong, B.H. Lambrigtsen, C.Y. Wang, J. Cohen, and **B.L. Gamelin**, 2016: *Increasing Daily Precipitation Intensity Associated with Warmer Air Temperatures over Northern Eurasia.* Journal of Climate, vol. 29, no. 2.

AWARDS

Excellence in Teaching Award (Geography Department, UCSB). (2020)

Graduate Research Mentorship Program Fellowship (UCSB). (2018 – 2019)

UCSB Geography Department Summer Fellowship. (2018)

Graduate Opportunity Fellowship (UCSB). (2017 – 2018)

American Geophysical Union's Outstanding Student Paper Award (OSPA), "Tropopause Ozone and Water Vapor Concentrations during the South American Monsoon System with AIRS Satellite Observations and MERRA-2 data." (December 2017)

Jack and Laure Dangermond Travel Award. (2016 – 2019)

Earth Research Institute Travel Award. (Annually 2016 – 2018)

Earth Research Institute Summer Fellowship. (2016 and 2017)
CSULA Etzel Pearcy Memorial Fellowship. (2012 – 2013)
CSULA Etzel Pearcy Memorial Fellowship. (2011 – 2012)

SERVICE

Campus Organizations and Honor Societies

Women in STEM Mentorship Program (Mentor), University of California, Santa Barbara. (2019 - Current)

Women in Geographical Sciences Committee, University of California, Santa Barbara. (2016 - Current)

Faculty Committee Graduate Student Reprehensive, University of California, Santa Barbara. (2016 – 2018)

Events Committee, University of California, Santa Barbara. (2014 – 2016)

Geography Club President, California Polytechnic State University, Pomona. (2009 – 2010)

Geography Club Member, California Polytechnic State University, Pomona. (2007 – 2010)

Pi Gamma Mu Honor Society Vice President, California Polytechnic State University, Pomona. (2009 – 2010)

Pi Gamma Mu Honor Society member, California Polytechnic State University, Pomona. (2008 – 2010)

COMMUNITY OUTREACH

Instituto Dante Alighieri School in Villa Carlos Paz, Argentina. Scientists and graduate students introduce the science goals and equipment for the field campaign to elementary to high school students in the region, November. (2018)

Bicentennial Civic Center in Córdoba, Argentina. Introduce the RELAMPAGO field campaign to Argentinian media sources and elementary school students, November. (2018)

Classroom assistant, Chino Unified School District, Chino Hills, CA. (2009 – 2013)

CONFERENCE PRESENTATIONS

Oral Presentations:

"ENSO Variability Influences Lower Stratosphere Ozone in South America," American Geophysical Union meeting (Invited). (2018)

"Identifying double tropopause events related to deep convection during RELAMPAGO," Advanced Study Institute, Field Studies of Convection in Argentina. (November 2018)

"South America ozone and temperature variability related to large-scale climate drivers with AIRS and MERRA-2," American Geophysical Union meeting. (April 2018)

"Arctic Water Vapor Variations and Influencing Teleconnection Patterns," Association of American Geographers meeting. (April 2013)

"Pacific Ocean Influences on Southern California Climate Changes," Satellite Educators Association (NOAA-CREST West sponsored researcher), California State University, Los Angeles. (August 2013)

"Southern California Precipitation: Coastal vs. Desert Reactions to Positive and Negative ENSO Phases," Association of American Geographers meeting. (February 2012)

"Global Circulation Models, Climate Change and California Hydrology," Comm University, Seattle, WA, February (Invited). (2012)

Poster Presentations:

"Extreme Fire Weather Conditions during a Summer 2018 Sundowner Event," American Geophysical Union meeting. (December 2019)

"Influences of a Mesoscale Convective Complex and Instability on Tropopause Thermodynamic Structure in the La Plata Basin," University of California, Santa Barbara (UCSB). (January 2019)

"Influences of a Mesoscale Convective Complex and Instability on Tropopause Thermodynamic Structure in the La Plata Basin," American Geophysical Union meeting. (December 2018)

"Tropopause Ozone and Water Vapor Concentrations during the South American Monsoon System with AIRS Satellite Observations and MERRA-2 data" American Geophysical Union. (December 2017) 2017 AGU Outstanding Student Paper Award

"Deep Convective Events Influence Ozone Variability in Southeast South America," American Geophysical Union meeting. (December 2016)

"Climate Change: Pacific Ocean and Land Use Changes Influence the Los Angeles Urban Heat Island," American Geophysical Union meeting. (December 2013)

"Modeling Snowpack in the Sierra Nevada Mountain Range Based on Projected Climate Change," Association of American Geographers meeting (April 2011)

ABSTRACT

Ozone Variability and Deep Convection in the UTLS Over South America

by

Brandi L. Gamelin

Stratospheric ozone protects Earth's surface from harmful ultraviolet radiation. Hence, understanding variability responsible for stratospheric ozone depletion is vital to protect human health and the environment. Despite low ozone concentration at 100 hPa in the upper troposphere-lower stratosphere (UTLS), ozone variability at this level plays an important role in regulating air temperatures, which in turn regulates troposphere to stratosphere exchanges and stratospheric chemistry. This work investigates the spatial and temporal ozone variability in the UTLS over South America, with an emphasis on the La Plata Basin (LPB). This variability is investigated to understand the influence of teleconnections originating in the Pacific Ocean, the El Niño-Southern Oscillation (ENSO) on interannual time scales, and the Pacific Decadal Oscillation (PDO) on interdecadal time scales. Variability in the UTLS and mechanisms driving stratospheric ozone variability over South America are not well understood. This work fills this knowledge gap with two overarching goals, 1) by identifying primary patterns of ozone variably related to large-scale processes (e.g. ENSO and PDO) with reanalysis (Chapters 1 and 2), and 2) by investigating local UTLS variability related to deep convection with an atmospheric numerical model, to

simulate deep convection in the LPB, and to quantify lower stratospheric hydration (Chapters 3 and 4). Results from the first goal shows that the primary patterns of UTLS ozone variability is strongly modulated by teleconnections with the tropical Pacific Ocean (e.g. El Niño) via Rossby wave trains interacting with South America. This teleconnection is further modulated by PDO phases. The strongest connections between the ENSO and UTLS ozone occur during the cool PDO phase and are dependent upon the location of sea-surface temperature anomalies in the tropical Pacific, especially the presence of Modoki-type El Niño events. Negative ozone anomalies are shown in South America during the wet season over the LPB and connected to El Niño during the cool PDO phase; and in the East and parts of the Southeast negative ozone anomalies are shown during the austral spring. For the second goal of this work, we investigated double tropopause events during three types of deep convection (discrete convective cells, mesoscale convective complex and squall line) to identity lower stratospheric hydration using the Weather Research and Forecasting model. Double tropopause events occurred during all convective types. The discrete convective cells did not produce stratospheric hydration due to the mixing of ice and water vapor in the tropopause, inhibiting net positive buoyancy and preventing the transport of material aloft. In contrast, the mesoscale convective complex and squall line both exhibit a dry layer in the tropopause, collocated with an ice layer, where net positive buoyancy contributed to stratospheric hydration as high as 20 km. Additional research is vital to understand how UTLS variability can affect surface processes, especially in a warming world.

TABLE OF CONTENTS

Introduction

Stratospheric ozone variability in South America is not well understood. The processes governing lower stratospheric ozone concentrations are dependent on upper tropospheric – lower stratosphere (UTLS) exchanges due to tropospheric weather and climate variability. South America is a continent dominated by an extensive network of (1) complex terrain - especially the Andes Mountain chain, (2) tropical climate systems - specifically the Amazon Rain Forest and wet season Monsoonal moisture, (3) midlatitude zonal wind patterns – general atmospheric variability related to the position of the upper level jet stream, (4) low level meridional wind patterns – also known as the South American low level jet, (5) surface pressure patterns – stable high pressure patterns located in the western Atlantic and eastern Pacific oceans, and (6) transient low pressure systems and wave trains originating in the Pacific Ocean. The result of such complex systems is a region susceptible to deep convective cloud processes capable of driving lower stratospheric ozone variability. The influence of this variability is investigated at multiple spatiotemporal scales to understand UTLS ozone patterns and thermodynamics in a region of South America known as the La Plata Basin.

The La Plata Basin

The La Plata river basin (LPB) is the fifth largest drainage basin in the world, the second largest in South America (after the Amazon River basin) and is located east of the Andes Mountains from 20 – 40˚ S (Fig. 1). This is a region of high soil fertility and its economic development is primarily based on agriculture and hydroelectric power (CIC 2016; Durkee et al. 2009). The La Plata Basin is one of the most important regions for agriculture

and livestock production and is known to play a central role in world's food production and food security (de Vasconcelos 2014).

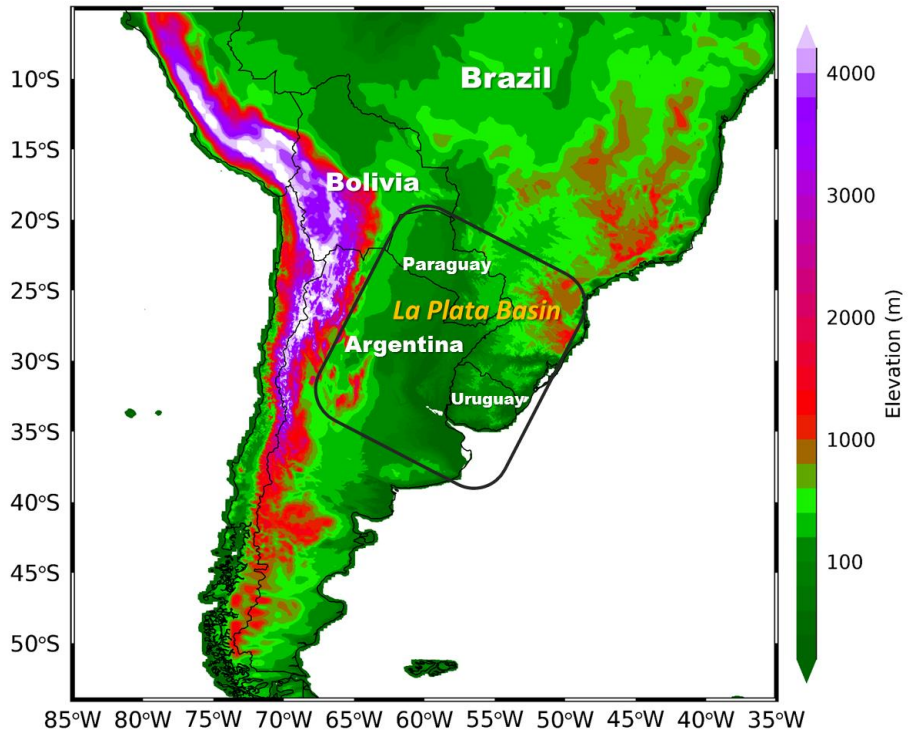

Fig. 1 South American topography generated with the weather research and forecasting model initiated with ERAi reanalysis data. The La Plata Basin region is shown (black box).

The LPB region is of particular interest because regional climate dynamics create an environment known to produce deep convective cloud processes capable of the detrainment of water vapor in the stratosphere. Water vapor in the stratosphere is notable because it can be chemically altered leading to ozone destruction (Bates and Nicolet, 1950). Additionally, the stratosphere is a known sink for harmful solar ultraviolet radiation (UV), and where ozone concentrations are decreasing, a larger amount of UV ration is capable of reaching Earth's surface which is harmful to vegetation and human health.

Stratospheric Ozone and Chemistry

On a global scale, the spatial distribution of ozone in the stratosphere is governed by the redistribution of ozone from the tropics to the poles. This stratospheric meridional circulation is known as the Brewer-Dobson Circulation (BDC; Brewer 1949; Dobson 1956; Butchart 2014; WMO, 2014). In the tropics, upwelling is related to convective cloud processes driving ozone concentrations to the upper-stratosphere. In the upper-stratosphere, ozone is then advected toward the poles, and settles in the lower stratosphere (Plumb 2002; Birner and Boenisch 2011). Figure 2 (left column) shows this pattern with October – March averaged Modern-Era Retrospective Analysis for Research and Applications version-2 (MERRA2) ozone data (Rienecker et al. 2011; Gelaro 2017). In the tropics, ozone concentrations at 100 hPa are lower where upwelling drives ozone to higher levels, and in the extra-tropics, ozone concentrations are higher. When comparing 100 to 10 hPa, the opposite pattern is shown at 10 hPa. In the mid-stratosphere, ozone concentrations are higher in the tropics, and lower in higher latitudes (Fig. 2).

The UTLS region is an important boundary between atmospheric layers and can govern stratospheric hydration and chemistry (Forster and Shine 2002). The location of the UTLS varies based on latitude, and in South America, the 100 hPa level may be considered part of the tropopause region throughout the tropics. This pressure level is generally associated with the lowermost stratosphere and the beginning of increasing ozone concentrations. Figure 2 is an area averaged profile of ozone concentrations ranging from low ozone concentrations in the tropopause (~150 – 100 hPa) to above 1 hPa, and showing the maximum at ~ 10 hPa. The tropopause behaves as a boundary regulated by temperature, and

temperature governs the transport of water vapor to the lower stratosphere. Once in the lower stratosphere, water vapor can influence stratospheric photochemistry (e.g. WMO 1995).

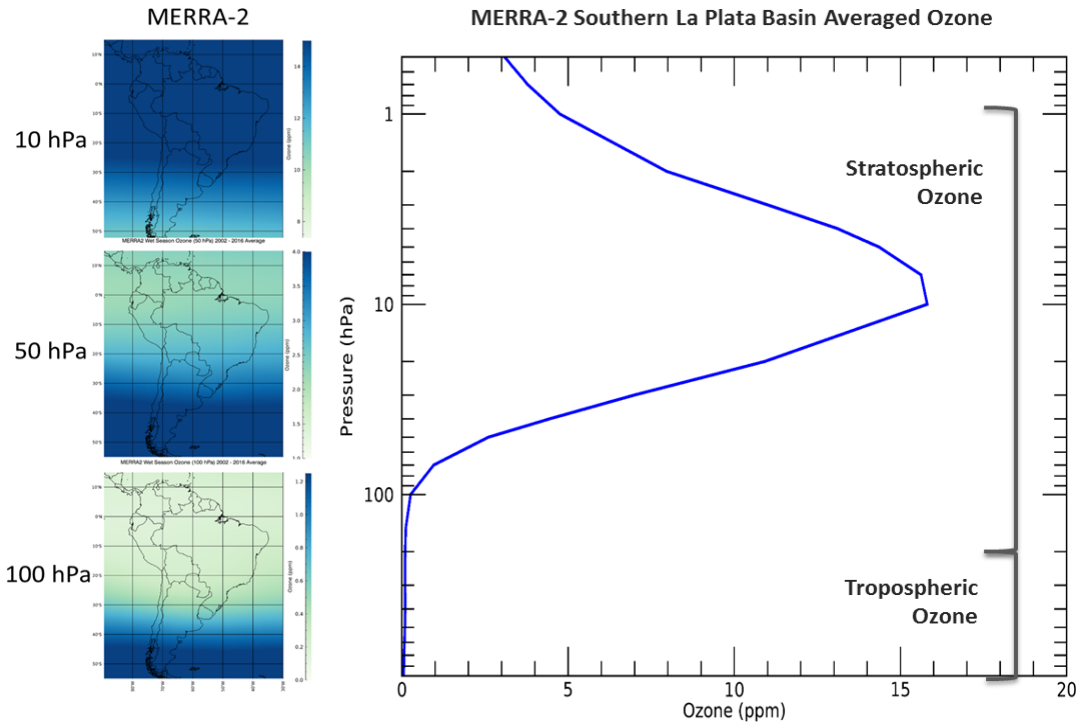

Fig. 2 October – March averaged Modern-Era Retrospective Analysis for Research and Applications version-2 (MERRA2) ozone data (Rienecker et al. 2011; Melod et al. 2015). Left: 100, 50 and 10 hPa. Right: area averaged ozone in the Southern La Plata Basin (see Fig. 3) from 900 – 1 hPa.

Water vapor in the stratosphere chemically reacts to become a catalyst for stratospheric ozone destruction (Bates and Nicolet 1950). Ozone (O_3) in the stratosphere chemically responds to UV to produce excited oxygen atoms ($O(^1D)$). Additionally, when $O(^1D)$ atoms interact with water vapor (H_2O), the response produces the hydroxyl free radical ($(O(1D) + H_2O \rightarrow 2OH)$ (e.g. Seinfeld and Pandis 1998). Furthermore, when OH interacts with O_3 it is converted to two oxygen molecules ($O_3 + OH \rightarrow 2O_2$). Ultimately, O_3 in the stratosphere absorbs harmful UV radiation and water vapor becomes a catalyst for OH production and O_3 destruction (Stenke and Grewe 2005). The result of decreased O_3 in the

stratosphere is an increase in UV radiation transferred to the troposphere (Forster and Shine 1999).

In the LPB, increasing shortwave radiation can lead to an array of adverse responses including oxidative stress and the need for long term metabolic acclimation in livestock production (Guidi 2011), a reduction of plant leaf size, limited photosynthesis, and a reduction of carbon dioxide uptake in agriculture and vegetation (Hall 2002). In addition, UV radiation has a deleterious effect on DNA integrity, increasing the risks of skin cancer in humans. Preliminary analysis of NASA's MERRA2 surface shortwave radiation flux data (Rienecker et al. 2011) in the LPB indicates that, despite large interannual variability, there is a statistically significant positive trend in January from 1981 – 2016 (Fig. 3). In this region, while multiple processes may be influencing the amount of incoming shortwave surface flux, according to Karoly, (1998) increasing shortwave radiation may also be responsible for the above-normal air temperature signals, which can impact precipitation by increasing evaporation. Ultimately, UTLS ozone variability may be directly connected to tropospheric weather and climate and requires further investigation.

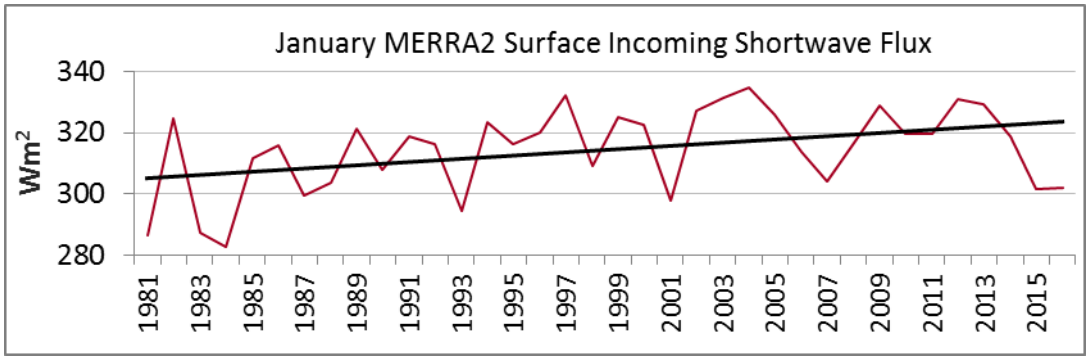

Fig. 3 1981 – 2016 January area averaged (southern LPB) MERRA2 surface incoming shortwave flux (W m^2). A statistically significant positive trend is detected where Mann-Kendall's $\tau = 0.3042$ and $p \leq 0.01$.

South American Climate Dynamics

In South America, some of the deepest and most intense convective storms in the world occur in the LPB (Zipser et al., 2006). These intense thunderstorms are often observed around 30˚S and are influenced by a combination of the moisture transport from the Amazon by the low-level jet from the north, and occasional disturbances moving across the Andes from the east creating frontal storm processes from the south. In recent decades, South America has exhibited rapid warming (Carvalho and Jones 2013) and there is observational evidence that extreme precipitation occurs from October – March and has increased over the southern LPB (Liebmann et al. 2001; Zilli et al. 2016) indicating possible changes to convective cloud processes and intensities.

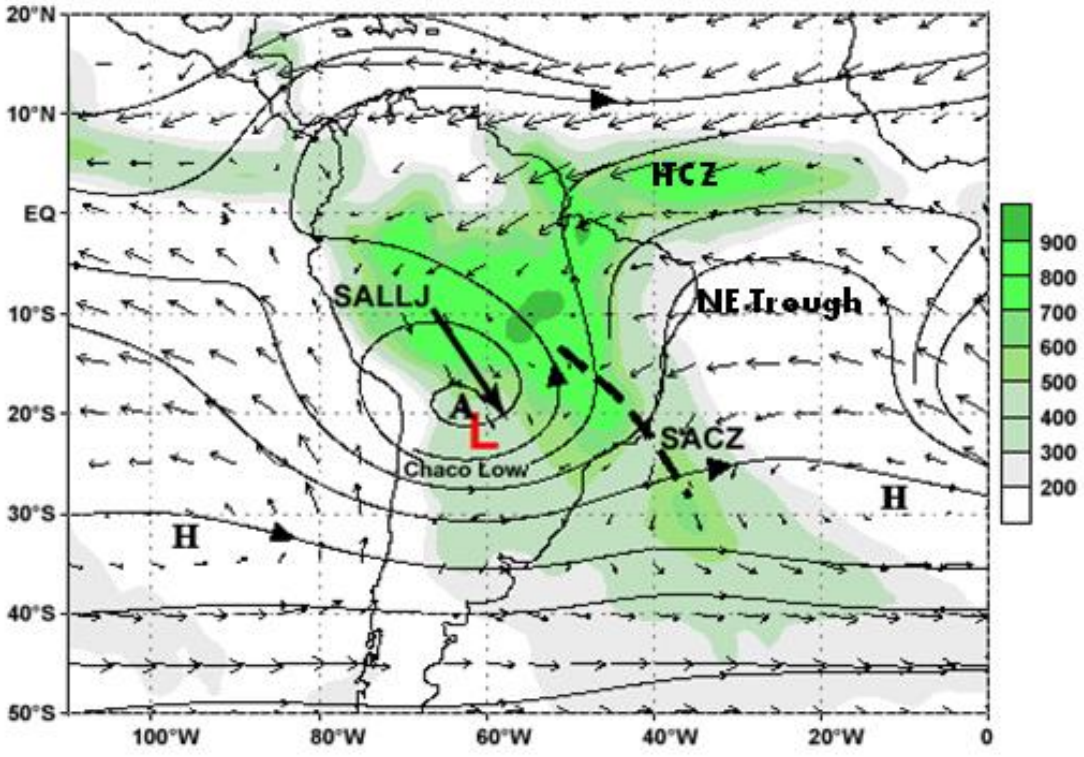

Fig. 3 December – March averaged South America climate dynamics 1979 - 1995. 925 hPa vector winds, 200 hPa streamlines, and precipitation is shaded (mm).
Modified from https://www.meted.ucar.edu/tropical/synoptic/tropic_extratropic/print.php.

In South America, the South American Low Level Jet (SALLJ) is the primary transport process along the eastern Andes Mountain chain from the equatorial Atlantic Ocean and Amazon Basin, to the LPB (Marengo et al. 2002; Nascimento et al. 2016; Oliveira et al. 2018; Vera et al. 2006). During an active SALLJ, intensified wind speeds occur approximately 1 – 2 km above the surface, with maximum wind speeds at approximately 850 hPa (Marengo et al. 2002; Salio et al. 2002). Furthermore, this transport of heat and moisture is known to drive deep convection and mesoscale convective processes in the LPB (e.g., Zipser et al., 2004: Salio et al., 2007; Repinaldo et al. 2015, Mullholand et al. 2018). The SALLJ can occur in all months. However, it is most frequent during the austral spring and summer months (Marengo et al. 2004). Moreover, large-scale climate processes like the El Niño-Southern Oscillation also influence the frequency of the SALLJ (Montini et al. 2019). The SALLJ was about twice as strong during austral summer 1998 El Niño, compared to the austral summer 1999 La Niña, which led to strong northerly moisture flux toward the LPB region (Ferreira et al. 2003).

Figure 3 illustrates several additional climate processes in South America influencing the LPB, including 925 hPa vector winds and 250 hPa streamlines from NCEP/NCAR reanalysis during the austral summer (1979 - 1995). The letter A is the approximate location of the Bolivian High: a semi-stationary upper level high, triggered by seasonal, high elevation diabatic surface heating in the Andes Mountains and maintained by latent heat release from the amazon (Lenters and Cook 1997). The Intertropical Convergence zone (ITCZ) is identified near the equator, precipitation is shaded, and the red L is the approximate location of the Gran-Chaco (thermal) Low. Surface cyclonic circulation around this low serves to enhance the SALLJ events.

The South American monsoon system (SAMS) is another important climate feature in South America and has been shown to influence the location of deep convection (Zhou and Lau 1998; Vera et al. 2006). Generally speaking, the SAMS has a pronounced wet season during the austral spring and summer (Zhou and Lau 1998; Vera et al. 2006; Silva and Carvalho 2007), and the onset of the wet season typically begins in October and ends by March (Liebmann et al. 2007). Furthermore, the wet season coincides with the locations of deep convection in the LPB between ~20˚S – ~35˚S (Zipser et al. 2006; Rasmussen et al. 2014; Rasmussen and Houze 2016; Rasmussen et al. 2016). The wet season is then followed by a pronounced dry season from approximately April to September. The dry season also coincides with a reduction in deep convection in the region. Figure 4 shows the primary locations of deep convection in South America and LPB region during the April – September averaged dry season (Fig. 4, left) and the October – March averaged wet season (Fig. 4, right). Shading represents the number of cloud tops between 100 – 70 hPa using Atmospheric Infrared Sounder (AIRS) Cloud Top Pressure satellite data. Cloud tops in the lower stratosphere may influence stratospheric ozone via the detrainment of water vapor and stratospheric chemistry. Climate dynamics and influences on climate dynamics in South America all work together to produce deep convective systems in the LPB capable of cross tropopause transport to the lower stratosphere.

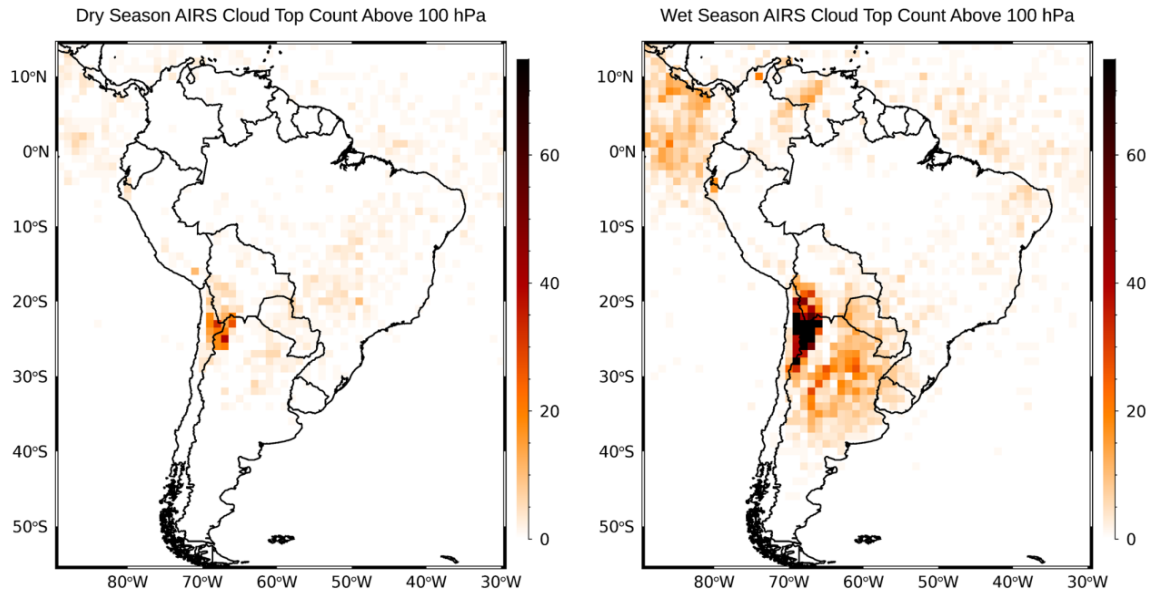

Fig. 4 Colors represent the number of cloud tops from 100 – 70 hPa using AIRS Cloud Top Pressure data. Left map: dry season (April – September). Right map: wet season (October – March).

On a local scale, Figure 5 illustrates the relationship we will investigate between water vapor and deep convection in the LPB with a profile of AIRS ozone (150-1 hPa, top) and AIRS water vapor (150-100 hPa, bottom) at 26˚S (52-66˚ W) on January 9, 2012. The increase of water vapor and decrease in ozone concentration in the same longitudes is noticeable (black boxes).

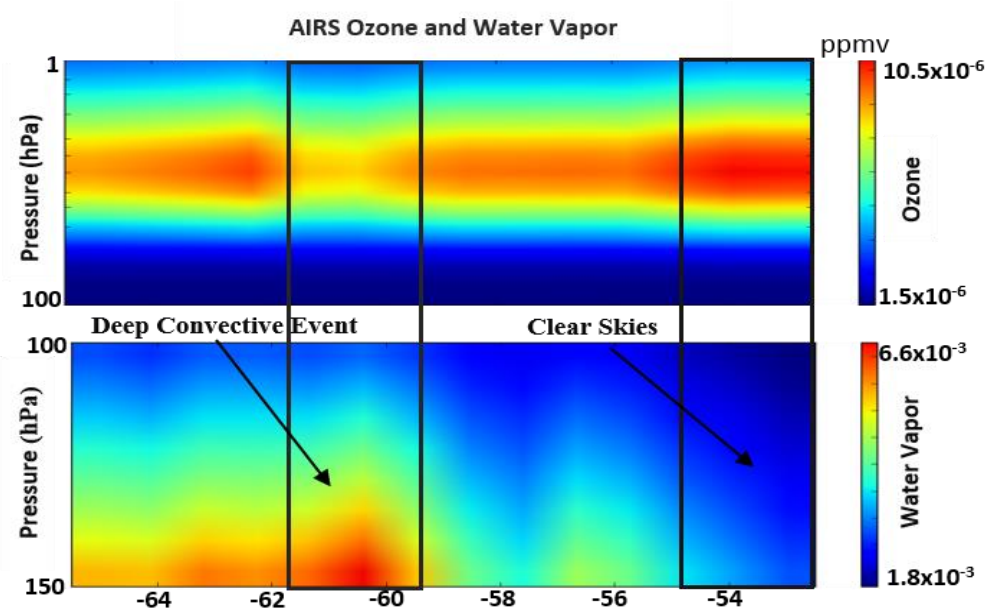

Fig. 5 January 9, 2012. Latitude: -26˚, Longitude: -52˚to -66˚. Top: Longitudinal cross section of AIRS ozone from 200 – 1 hPa. Bottom: Longitudinal cross section of AIRS water Vapor from 150 – 1 hPa.

Interannual (ENSO) and Interdecadal (PDO) Variability

The relationships between UTLS ozone, temperature and water vapor in South America may also be susceptible to interannual variably related to the El Niño – Southern Oscillation (ENSO). While the ENSO teleconnection originates in the tropics (e.g., Trenberth et al. 2002), it is considered the primary driver of interannual precipitation variability in the extratropical LPB (Berbery and Barros 2002; Tedeschi et al. 2013, 2015). During El Niño events equatorial Pacific Ocean warming is known to produce Rossby wave trains propagating to extratropical locations and contributing to the ENSO teleconnection (e.g. Karoly 1989; Seager et al. 2003).

Tropospheric weather variability in South America is generally attributed to El Niño induced Rossby wave trains originating near Australia (Ding et a. 2012), propagating across the South Pacific (e.g. Rodrigues and Woollings 2017) and modulated by the position of the

subtropical jet stream (Carvalho et al. 2005; Ding et al. 2012). In the Southern Hemisphere, as a Rossby wave train propagates across the extratropical Pacific Ocean (e.g. Karoly et al. 1989; McIntosh and Hendon 2018) it encounters South America and the Andes Mountains. On the lee side of the Andes, the interactions with complex terrain cause atmospheric stretching and the air mass to propagate towards the equator where it encounters tropical wind patterns. Furthermore, this change in wind sign creates a blocking mechanism and Rossby wave breaking (Hoskins and Karoly 1981).

Interannual variability in South America is strongly related to ENSO (e.g. Grimm 2003), however, the ENSO teleconnection can be modulated by decadal Pacific Ocean sea surface temperature variability known as the Pacific Decadal Oscillation (PDO) (e.g. McCabe and Dettinger 1999; Yu and Zweirs 2007; Andreoli and Kayano 2005; Newman et al 2016). PDO is characterized by persistent pattern of warm (cool) SST anomalies in the North Pacific along with cool (warm) SST anomalies in the equatorial Pacific Ocean (Mantua et al. 1997; Mantua and Hare 2002), and affects global climate (Newman et al. 2016).

In South America, the ENSO – PDO relationships have been examined to understand precipitation patterns and extreme rainfall events (Andreoli and Kayano 2005; Kayano and Andreoli 2007). The influence of PDO on the ENSO teleconnection produces a non-linear relationship which varies based on warm or cool PDO phase (Kayano and Andreoli 2007). The influence of the ENSO – PDO relationships on UTLS ozone over South America has not been explored.

UTLS Exchange and Double Tropopause Events

Local weather in the LPB is governed by global and regional dynamics. However, exchanges in the UTLS are governed by local atmospheric conditions. The tropopause acts as a boundary between the troposphere and stratosphere where the mechanisms driving vertical and horizontal transport of water vapor transport are determined by zonal and meridional wind processes, vertical temperature gradients, and available water vapor (Fueglistaler et al. 2009). In order to understand stratospheric chemical processes, it is important to understand tropopause boundary thermodynamics and transport of tropospheric materials, especially water vapor (Brewer 1949) to the stratosphere.

Within the troposphere, air temperature decreases with height as heating occurs from the surface upward due to terrestrial radiation and greenhouse gases (Fueglistaler et al. 2009). In the UTLS, the lowest temperatures represent the "cold point" in the lower atmosphere and can be considered the lower boundary for the stratosphere (Zhou et al. 2001). Temperature is the fundamental driver of most processes controlling tropopause boundary dynamics and is tied to motion (convection, advection, clouds, chemical reactions and water vapor transport) across the cold point (Fueglistaler et al., 2009), where local conditions (e.g. single or double tropopause) control exchange of gases at the boundary.

Homeyer et al. (2014) describes single and double tropopause events, where the single tropopause boundary demonstrates a single cold point, which can be observed in a stable atmosphere or unstable atmosphere. The double tropopause boundary tends to occur in mid-latitudes, and although it has been observed in the tropics and subtropics, it generally occurs in an unstable environment where stratospheric - tropospheric exchange demonstrates a layer of stratospheric air below or mixed among tropospheric air. Double tropopause events are also known as midlatitude "folds" and generally occur where the tropopause height decreases

rapidly between the subtropics and sub polar region. The steep gradient allows for the horizontal exchange of gases between the tropopause and stratosphere as well as convective transport in regions with strong thunderstorms.

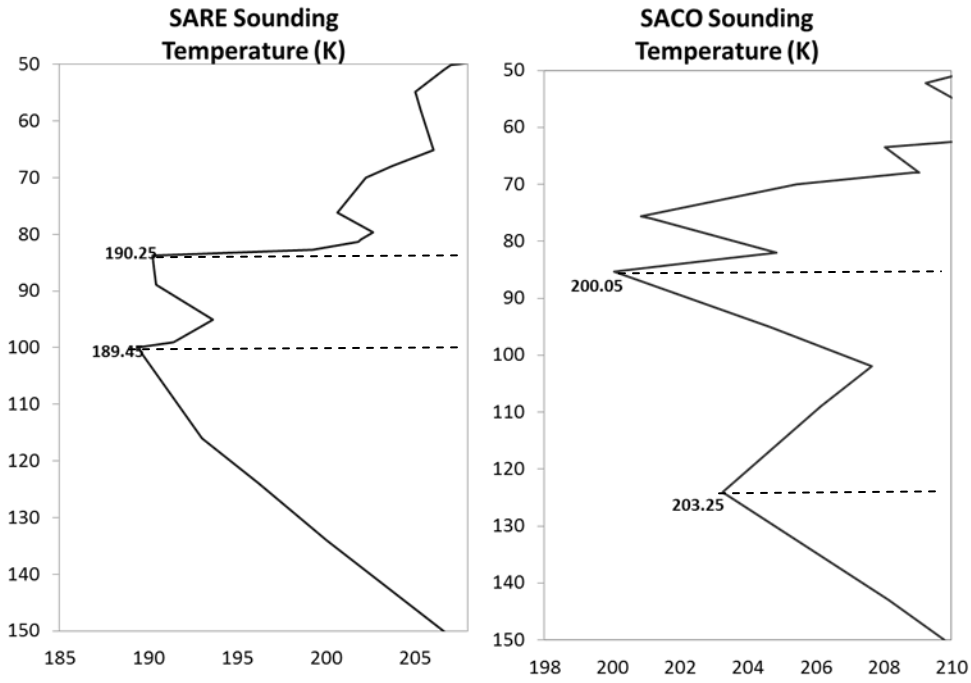

Fig. 6 Temperature (K) profiles from SARE 11/13/18 12 UTC (left) and SACO 11/03/18 12 UTC (right) radiosonde data. Cold point temperatures (K) for primary (189.45 K and 203.25 K) and secondary (190.25 K and 200.05 K) tropopause levels (dashed lines) are adjacent to the corresponding points.

South America has a high frequency of double tropopause events (Xue and Daren 2015). Figure 6 shows two temperature profiles from sounding data in the LPB. The profile from Cordoba Aero (SACO) is showing a double tropopause in Cordoba, Argentina. The SACO temperature profile is near a convective cell (not shown). The profile from Resistencia Aero (SARE) is showing a double tropopause event in Resistencia, Argentina with a higher tropopause boundary. The SARE profile is near a Mesoscale Convective Complex (not

shown) and showing the relationships between tropopause heights and deep convection, higher tropopause and colder temperatures. While this region is subject to deep convection and double tropopause events, this region has not been locally investigated to identify tropopause boundary dynamic and requires further study to understand the relationship between double tropopause events and the potential influence on lower stratospheric water vapor concentrations.

Dissertation Objectives

This research seeks to advance the scientific understanding of global and local influences on lower stratospheric ozone concentrations in the La Plata Basin. Ultimately to understand the influences of deep convection capable of perturbing tropopause thermodynamics leading to changes in stratospheric chemistry, decreasing ozone and increasing surface UV radiation. ***The objectives for this dissertation are:***

1) Compare satellite and reanalysis ozone data, and provide an overview of stratospheric ozone variability in South America, including trends and interactions between ENSO and PDO during the wet season (Chapter 1).
2) Establish relationships between UTLS ozone patterns to ENSO and PDO in South America during the austral spring, with an emphasis on local mechanisms driving UTLS ozone patterns, circulation, and temperature variability during El Niño events (Chapter 2).
3) Utilize the Weather Research and Forecasting (WRF) model to simulate MCSs and improve vertical model resolutions, and to reproduce observed double tropopause features in the UTLS for thermodynamic analysis during deep convective events (Chapter 3).
4) Investigate the influence of deep convection on UTLS double tropopause features and instability contributing to maximum water vapor height in the lower stratosphere (Chapter 4).

The first chapter of this dissertation focuses on spatial and temporal variability of wet season stratospheric ozone patterns in South America at 100, 50 and 10 hPa. Initially this work is conducted with AIRS satellite (2002 – 2016) and MERRA2 reanalysis data (1980 – 2016) to investigate ozone patterns and large-scale influences originating in the Pacific Ocean and driving ozone variability. Because of the limited AIRS data time frame, MERRA2 data is used for trend analysis to determine locations of decreasing ozone concentrations from 1980 – 2016, and to investigate the influence of ENSO and PDO on ozone patterns in the upper troposphere – lower stratosphere.

The second chapter continues to investigate ozone patterns in South America based on results from chapter one. The focus of this chapter is on the mechanism driving austral spring UTLS ozone variability related to El Niño and modulated by PDO phases. Here, the influence of El Niño driven Rossby wave trains on UTLS vertical and zonal circulations is investigated to understand their influences on UTLS temperature and ozone variability.

The third chapter of this dissertation focuses on mesoscale modeling of the UTLS with the Weather Research and Forecasting (WRF) numerical model (Skamarock 2008). For this chapter, sensitivity testing is conducted with two case studies during the austral spring to configure the model to simulate deep convection and mesoscale convective systems in the LPB, as well as determine the optimal model vertical resolution to simulate double tropopause features.

Chapter four of this dissertation utilizes the optimally configured WRF model output from chapter three to conduct case study analysis. The influence of deep convection on UTLS double tropopause events is investigated during discrete convective cells, a mesoscale convective complex and a squall line related to a frontal boundary to understand UTLS

temperature variability and quantify lower stratospheric hydration capable of influencing stratospheric chemistry.

References

Andreoli RV, Kayano MT (2005) ENSO-related rainfall anomalies in South America and associated circulation features during warm and cold Pacific decadal oscillation regimes. *Int. J. Climatol.* 25: 2017-2030. doi:10.1002/joc.1222.

Bates DR, Nicolet M (1950) The photochemistry of atmospheric water vapor, *J. Geophys. Res.,* 55, 301–327.

Berbery EH, VR Barros (2002) The Hydrologic Cycle of the La Plata Basin in South America. *J. Hydrometeor.,* **3**, 630–645, https://doi.org/10.1175/1525-7541(2002)003<0630:THCOTL>2.0.CO;2.

Birner T, Boenisch H (2011) Residual circulation trajectories and transit times into the extratropical lowermost stratosphere. *Atmos. Chem. Phys.* 11: 817–827, doi: 10.5194/acp-11-817-2011.

Brewer AW (1949) Evidence for a world circulation provided by the measurements of helium and water vapor distribution in the stratosphere, *Q. J. Roy., Meteor. Soc*., 75, 351–363.

Butchart N (2014) The Brewer-Dobson circulation, *Rev. Geophys.,* 52, 157–184, doi:10.1002/2013RG000448.

Carvalho LM, Jones C, Ambrizzi T (2005) Opposite Phases of the Antarctic Oscillation and Relationships with Intraseasonal to Interannual Activity in the Tropics during the Austral Summer, *J. Climate,* 18, 702–718, https://doi.org/10.1175/JCLI-3284.1.

Carvalho LMV, Cavalcanti IFA (2016) The South American Monsoon System (SAMS). In: de Carvalho L, Jones C (eds) The Monsoons and Climate Change, Springer Climate. Springer, Cham.

CIC., 2016: *Website: http://www.cicplata.org/.* The Intergovernmental Coordinating Committee of the Countries of La Plata Basin.

Ding Q, Steig EJ, Battisti DS, Wallace JM (2012) Influence of the Tropics on the Southern Annular Mode, *J. Climate,* 25, 6330–6348. https://doi.org/10.1175/JCLI-D-11-00523.1.

Dobson GMB (1956) Origin and distribution of polyatomic molecules in the atmosphere, *Proc. R. Soc.*, **A236**, 187–193.

Durkee JD, Mote TL, Shepherd JM (2009) The Contribution of Mesoscale Convective Complexes to Rainfall across Subtropical South America. *J. Climate,* **22**, 4590–4605, https://doi.org/10.1175/2009JCLI2858.1.

Ferreira RN, Rickenbach TM, Herdies DL, Carvalho LMV (2003) Variability of South American Convective Cloud Systems and Tropospheric Circulation during January–March 1998 and 1999. *Mon. Wea. Rev.*, 131, 961–973.

Forster PMF, Shine KP (1999) Stratospheric water vapour changes as a possible contributor to observed stratospheric cooling, *Geophysical Research Letters*, vol. 26, no. 21, 3309-3312.

Forster PMF, Shine KP (2002) Assessing the climate impact of trends in stratospheric water vapor. *Geophysical Research Letters,* 29, 6, 10. DOI: 10.1029/2001GL013909.

Fueglistaler S, Dessler AE, Dunkerton TJ, Folkins I, Fu Q, Mote PW (2009) Tropical tropopause layer, *Rev. Geophys*., 47, RG1004. doi:10.1029/2008RG000267.

Gelaro R, McCarty W, Suárez MJ, Todling R, Molod A, Takacs L, Randles CA, Darmenov A, Bosilovich MG, Reichle R, Wargan K, Coy L, Cullather R, Draper C, Akella S, Buchard V, Conaty A, da Silva AM, Gu W, Kim G, Koster R, Lucchesi R, Merkova D, Nielsen JE, Partyka G, Pawson S, Putman W, Rienecker M, Schubert SD, Sienkiewicz M , Zhao B (2017) The Modern-Era Retrospective Analysis for Research and Applications, Version 2 (MERRA-2). *J. Climate*, 30, 5419–5454. https://doi.org/10.1175/JCLI-D-16-0758.1.

Grimm AM (2003) The El Niño impact on the summer monsoon in Brazil: Regional processes versus remote Influences, *J. Climate*, 16, 263-280.

Guidi L, Degl'Innocenti E, Remorini D, Biricolti S, Fini A, Ferrini F, Nicese FP, Tattini M (2011) *Environ. Exp. Bot.*, 70, 88–95.

Hall R (2002) Effects of increased UV-B radiation on the lichen Cladonia arbuscula spp. mitis: UV absorbing pigments and DNA damage Department of Cell and Organism Biology, Lund University.

Homeyer CR, et al. (2014) Convective transport of water vapor into the lower stratosphere observed during double tropopause events, *J. Geophys. Res. Atmos.*, 119, 10 941–10 958, doi:10.1002/2014JD021485.

Hoskins BJ, Karoly DJ (1981) The Steady Linear Response of a Spherical Atmosphere to Thermal and Orographic Forcing. *J. Atmos. Sci.*, 38, 1179–1196, https://doi.org/10.1175/1520-0469(1981)038<1179:TSLROA>2.0.CO;2.

Karoly DJ (1989) Southern Hemisphere circulation features associated with El Niño–Southern Oscillation events. *J. Climate*, **2**, 1239–1252.

Karoly D, Vincent DG (1998) Meteorology of the Southern Hemisphere, *American Meterological Society,* Boston, MA, V. 27, N. 49, pp 319.

Kayano M, Andreoli R (2007) Relations of South American summer rainfall interannual variations with the Pacific Decadal Oscillation. *International Journal of Climatology*, 27. 10.1002/joc.1417.

Lenters JD, Cook KH (1997) On the Origin of the Bolivian High and Related Circulation Features of the South American Climate. *J. Atmos. Sci.*, 54, 656–678, https://doi.org/10.1175/1520-0469(1997)054<0656:OTOOTB>2.0.CO;2.

Liebmann B, Jones C, Carvalho LM de (2001) Interannual Variability of Daily Extreme Precipitation Events in the State of São Paulo, Brazil. *J. Climate*, 14, 208–218, https://doi.org/10.1175/1520-0442(2001)014<0208:IVODEP>2.0.CO;2.

Liebmann B, Camargo SJ, Seth A, Marengo JA, Carvalho LM, Allured D, Fu R, Vera CS (2007) Onset and End of the Rainy Season in South America in Observations and the ECHAM 4.5 Atmospheric General Circulation Model. *J. Climate,* **20**, 2037–2050, https://doi.org/10.1175/JCLI4122.1.

Mantua NJ, Hare SR (2002) The Pacific Decadal Oscillation, *Journal of Oceanography*, 58: 35. https://doi.org/10.1023/A:1015820616384.

Mantua NJ, Hare SR, Zhang Y, Wallace JM, Francis RC (1997) A Pacific interdecadal climate oscillation with impacts on salmon production. Bull. *Amer. Meteor. Soc.*, **78**, 1069–1079,doi:https://doi.org/10.1175/1520-0477(1997)078<1069:APICOW>2.0.CO;2.

Marengo JA, Douglas MW, Silva Dias PL (1999) The South American low-level jet east of the Andes during the, LBA-TRMM and LBA-WET AMC campaign, *J. Geophys. Res.*, 107(D20), 8079, doi:10.1029/2001JD001188, 2002.

Marengo JA, Soares W, Saulo W, Nicolini M (2004) Climatology of the LLJ east of the Andes as derived from the NCEP reanalyses. *Journal of Climate*, 17: 2261 – 2280.

Marengo JA, Douglas MW, Dias PLS (2002) The South American low‐level jet east of the Andes during the 1999 LBA‐TRMM and LBA‐WET AMC campaign. *Journal of Geophysical Research*, 107(D20), 8079. https://doi.org/10.1029/2001JD001188.

Marengo JA, Soares WR, Saulo C, Nicolini M (2004) Climatology of the low‐level jet east of the Andes as derived from the NCEPNCAR reanalyses: Characteristics and temporal variability. *Journal of Climate*, 17(12), 2261‐2280. https://doi.org/10.1175/1520 0442(2004)017<2261:COTLJE>2.0.CO;2.

Marengo JA, Liebmann B, Grimm AM,. Misra V, Silva Dias PL, Cavalcanti IFA, Carvalho LMV, Berbery EH, Ambrizzi T, Vera CS, Saulo AC, Nogues-Paegle J, Zipser E, Sethkand A, Alvese LM (2012) Recent developments on the South American monsoon system, *Int. J. Climatol.*32: 1 – 21, DOI: 10.1002/joc.2254.

Martius O, Rivière G (2016) Rossby wave breaking: Climatology, interaction with low-frequency climate variability, and links to extreme weather events. In J. Li, R. Swinbank, R. Grotjahn, & H. Volkert (eds.), Dynamics and Predictability of Large-Scale, High-Impact Weather and Climate Events (Special Publications of the International Union of Geodesy and Geophysics, pp. 69-78). *Cambridge: Cambridge University Press.* doi:10.1017/CBO9781107775541.006.

McCabe GJ, Dettinger MD, (1999) Decadal variations in the strength of ENSO Teleconnection with precipitation in the western United States, *Int. J. Climatol*. **19**: 1399 – 1410.

McIntosh PC, Hendon HH (2018) Understanding Rossby wave trains forced by the Indian Ocean Dipole, *Clim Dyn* 50: 2783. https://doi.org/10.1007/s00382-017-3771-1.

Montini TL, Jones C, & Carvalho LMV (2019) The South American low-level jet: A new climatology, variability, and changes, *Journal of Geophysical Research: Atmospheres*, 124, 1200–1218. https://doi.org/10.1029/2018JD029634.

Mulholland JP, Nesbitt SW, Trapp RJ, Rasmussen KL, Salio PV (2018) Convective Storm Life Cycle and Environments near the Sierras de Córdoba, Argentina. *Mon. Wea. Rev.*, **146**, 2541–2557, https://doi.org/10.1175/MWR-D-18-0081.1.

Nascimento MG, Herdies DL, Oliveira de Souza D (2016) The South American water balance: The influence of low‐level jets. *Journal of Climate*, 29(4), 1429‐1449. https://doi.org/10.1175/JCLI‐D‐15‐0065.1.

Newman M, Alexander MA, Ault TR, Cobb KM, Deser C, Di Lorenzo E, Mantua NJ, Miller AJ, Minobe S, Nakamura H, Schneider N (2016) The Pacific decadal oscillation, revisited. *Journal of Climate*, *29*(12), pp.4399-4427.

Oliveira MI, Nascimento EL, Kannenberg C (2018) A new look at the identification of low‐level jets in South America. *Monthly Weather Review*, 146(7), 2315‐2334. https://doi.org/10.1175/mwr‐d‐17‐0237.1.

Plumb RA (2002) Stratospheric transport. *J. Meteorol. Soc. Jpn*. 80: 793–809.

Rasmussen KL, Chaplin MM, Zuluaga MD, Houze RA (2016) Contribution of Extreme Convective Storms to Rainfall in South America. *J. Hydrometeor.*, **17**, 353–367, https://doi.org/10.1175/JHM-D-15-0067.1.

Rasmussen KL, Houze RA (2016) Convective Initiation near the Andes in Subtropical South America. *Mon. Wea. Rev.*, **144**, 2351–2374, https://doi.org/10.1175/MWR-D-15-0058.1.

Rasmussen, KL, Zuluaga MD, Houze Jr. RA (2014) Severe convection and lightning in subtropical South America, *Geophys. Res. Lett*., 41, 7359–7366, doi: 10.1002/2014GL061767.

Repinaldo HFB, Nicolini M, Skabar YG (2015) Characterizing the diurnal cycle of low-level circulation and convergence using CFSR data in southeastern South America. *J. Appl. Meteor. Climatol.*, 54, 671–690, https://doi.org/10.1175/JAMC-D-14-0114.1.

Rienecker MM, Suarez MJ, Gelaro R, Todling R, Bacmeister J, Liu E, Bosilovich MG, Schubert SD, Takacs L, Kim GK, Bloom S, (2011) MERRA: NASA's modern-era retrospective analysis for research and applications. *Journal of climate*, 24(14), pp.3624-3648.

Rodrigues RR, Woollings T (2017) Impact of Atmospheric Blocking on South America in Austral Summer. J. Climate, 30, 1821–1837, https://doi.org/10.1175/JCLI-D-16-0493.1.

Salio P, Nicolini M, Saulo A (2002) Chaco low‐level jet events characterization during the austral summer season. *Journal of Geophysical Research*, 107(D24), 4816. https://doi.org/10.1029/2001JD001315.

Salio P. Nicolini M, Zipser EJ (2007) Mesoscale convective systems over southeastern South America and their relationship with the South American low‐level jet. *Monthly Weather Review*, 135(4), 1290‐1309. https://doi.org/10.1175/MWR3305.1.

Seager R, Harnik N, Kushnir Y, Robinson W, Miller JA (2003) Mechanisms of hemispherically symmetric climate variability. *J. Climate*, **16**, 2960–2978.

Seinfeld JH, Pandis SN (1998) Atmospheric chemistry and physics: From air pollution to climate change, 1360 pp., John Wiley & Sons, Inc., New York, NY.

Silva AE, Carvalho LMV (2007) Large-scale index for South America monsoon (LISAM), *Atmos Sci Lett* 8:51–57.

Skamarock, WC, Klemp JB, Dudhia J, Gill DO, Barker DM, Duda MG, Huang X-Y, Wang W, Powers JG (2008) A Description of the Advanced Research WRF Version 3. NCAR Technical Note NCAR/TN-475+STR, doi:10.5065/D68S4MVH.

Stenke A, Grewe V (2005) Simulation of stratospheric water vapor trends: impact on stratospheric ozone chemistry, *Atmos. Chem. Phys.*, 5, 1257-1272, https://doi.org/10.5194/acp-5-1257-2005.

Tedeschi RG, Cavalcanti IFA, Grimm AM (2013) Influences of two types of ENSO on South American precipitation. *Int J Climatol* 33: 1382−1400.

Tedeschi RG, Grimm AM, Cavalcanti IFA (2015) Influence of Central and East ENSO on extreme events of precipitation in South America during austral spring and summer. *Int J Climatol* 35: 2045−2064.

Trenberth KE, Caron JM, Stepaniak DP, Worley S (2002) Evolution of El Niño–Southern Oscillation and global atmospheric surface temperatures, *J. Geophys. Res.*, 107(D8), doi:10.1029/2000JD000298.

de Vasconcelos ACF, Schlindwein SL, Lana MA (2014) Land use dynamics in Brazilian La Plata Basin and anthropogenic climate change, *Climatic Change* 127: 73. doi:10.1007/s10584-014-1081-8.

Vera C, et al. (2006) The South American Low-Level Jet Experiment. *Bull. Amer. Meteor. Soc*., **87**, 63–77.

WMO (1995) Scientific Assessment of Ozone Depletion, WMO 37, Geneva, Switzerland.

WMO (World Meteorological Organization; 2014) Scientific Assessment of Ozone Depletion: 2014: Global Ozone Research and Monitoring Project – Report No. 55, 416 pp., Geneva, Switzerland.

Xue W, Daren LÜ (2015) Ten-Year Climatological Features and Air Origin of Midlatitude Double Tropopauses. *Adv. Atmos. Sci.,* 32(12): 1592-1602.

Yu B, Zwiers FW (2007) The impact of combined ENSO and PDO on the PNA climate: a 1,000-year climate modeling study. *Climate Dynamics*, 29(7-8), pp.837-851.

Zhou XL, Geller MA, Zhang M (2001), Cooling trend of the tropical cold point tropopause temperatures and its implications, *J. Geophys. Res.,* 106(D2), 1511–1522.

Zhou J, Lau K-M (1998) Does a Monsoon Climate Exist over South America? *J. Climate*, 11, 1020–1040.

Zilli MT, Carvalho LMV, Liebmann B, Dias MAS (2016) A comprehensive analysis of trends in extreme precipitation of southeastern coast of Brazil, *Int. Journal of Climate,* 10.1002/joc.4840.

Zipser E, Salio P, Nicolini M (2004) Mesoscale convective systems activity during SALLJEX and the relationship with SALLJ events. *CLIVAR Exchanges*, 9(1), 14–18.

Zipser EJ, Cecil DJ, Liu C, Nesbitt SW, Yorty DP (2006) Where are the most intense thunderstorms on Earth. *Bull. Am. Meteorol. Soc*., 87, 1057–1071.

Chapter 1:

Stratospheric Ozone Variability during the South American Wet Season

1.1 Abstract

The influence of interannual and multi-annual El Niño-Southern Oscillation (ENSO) variability on stratospheric ozone over South America is investigated using October – March averaged AIRS and MERRA-2 ozone data at 10, 50 and 100 hPa (2002-2016). A principal component analysis (PCA) is applied to both data sets showing that the first PCA (PC1) is strongly correlated between both data sets at all levels. The temporal range in the PCA is then extended with MERRA-2 (1980 – 2016) and PC time-coefficients are correlated to Multivariate ENSO Index (MEI), Pacific Decadal Oscillation (PDO), and Antarctic Oscillation (AAO) climate indices and to the quasi-biennial oscillation (QBO). We show that PC1 at 10 hPa and 50 hPa is strongly correlated to QBO throughout both time periods, and patterns of variability in the principal components may be explained by the Brewer Dobson Circulation modulated by QBO. However, at 100 hPa we find that the main mode of ozone variability identified with PC1 is strongly correlated with ENSO and PDO from 2002 – 2016, which approximately coincides with the cool phase of the PDO, and not correlated from 1980 – 2016. The relationships between ENSO Rossby wave patterns and ozone variability during recent warm (1980 – 1997) and cool (1998 – 2016) PDO phases are investigated with 100 hPa ozone and 200 hPa geopotential height (h200). The strongest positive linear relationships between h200, PC1 and MEI are observed in the La Plata Basin region of Southeast South America during the cool PDO. In this region, when h200, MEI and PC1 are positive, 100 hPa October – March averaged ozone is decreasing. Trend analysis is then applied to Austral

spring and summer averaged MERRA2 100 hPa ozone data separately. At 100 hPa, spring trend patterns appear to be dominating the patterns in PC3 which are demonstrating a strong positive trend in the PC coefficients. This study indicates that during the warm PDO phase, inter-ENSO variability was larger, resulting in weaker correlations between PDO, ENSO and ozone variability. During the cool PDO phase, the PC1 pattern of ozone anomalies exhibits a more coherent relationship between Rossby wave trains extending from mid-latitudes to the tropics influencing stratospheric ozone in South America. Especially in the La Plata Basin where El Niño events enhance precipitation and stratospheric ozone is decreasing.

1.2 Introduction

Stratospheric ozone acts as an invisible shield that regulates the amount of ultraviolet radiation that reaches Earth's surface which influences human health as well as agriculture and vegetation (Garssen et al. 1998; Heisler and Grant 2000). Ozone is also the primary driver of globally averaged stratospheric temperature trends and has been connected to several tropospheric surface circulation processes (WMO Ozone Assessment 2010). Over time, human activities have led to several changes to concentrations of most greenhouse gases, including tropospheric and stratospheric ozone and ozone depleting substances (IPCC/TEAP 2005). Small changes in greenhouse gas concentrations alter the radiative balance of Earth's atmosphere by changing the balance between incoming solar radiation and outgoing infrared radiation.

Stratospheric ozone variability is related to three dynamical processes, (1) upwelling/downwelling associated with the Brewer Dobson Circulation (BDC) – the general stratospheric circulation pattern, (2) stratospheric zonal winds shift from easterlies to

westerlies, and vice versa, associated with the Quasi-Biennial Oscillation (QBO), and (3) the exchange of air masses through the tropopause layer associated with tropospheric convective processes (Fueglistaler et al. 2009). The first process, the BDC is driven by internal gravity waves in the atmosphere, which form when air flows over high mountain ranges and during tall thunderstorms. These types of vertically propagating gravity waves have been identified in South America (Hoffmann et al. 2013). The second process, the QBO is characterized by oscillating shifts in zonal wind pattern in the tropical lower stratosphere with an average period of 28 months (Baldwin et al 2001). The QBO can modulate the strength of the stratospheric polar jet that, in turn, affect tropospheric circulation (e.g., Holton and Tan 1980; Baldwin and Dunkerton 1998) and modulate the strength of the upwelling in the tropics related to BDC (Flury et al. 2013). Lastly, the third process relates to tropical and subtropical deep convective cloud processes, which are the primary vehicle for upper troposphere – lower stratosphere exchanges and the vertical transport of energy, moisture, momentum, and chemical constituents. In this regard, most changes to the lower stratosphere are generally attributed to the vertical transport of tropospheric gases via convective cloud processes at the tropopause boundary (Holton et al. 1995; Fueglistaler et al. 2009; Khaykin et al. 2009).

In South America, deep convective thunderstorms have been identified (Zipser et al. 2006) which may contribute to troposphere – stratosphere exchanges (STE) and ozone variability in the stratosphere. It has been shown that deep convective processes are responsible for water vapor and ice particle transport to the lower stratosphere (Brewer, 1949), and plays a significant role on stratospheric chemistry (e.g., WMO, 1995). Water vapor in the lower stratosphere chemically responds with ultraviolet radiation, and is a catalyst for stratospheric ozone destruction (Bates and Nicolet, 1950). Additionally, ozone

concentrations are directly related to stratospheric temperature variability and is the most important greenhouse gas controlling the temperatures in the upper troposphere-lower stratosphere (UTLS, Forster and Shine 2002). Moreover, in the tropics and subtropics the importance of investigating ozone variability during deep convection is vital to understand stratospheric chemistry and climate variability.

In South America, an important climate feature which modulates the location and frequency of deep convection is the South American monsoon system (SAMS) (Zhou and Lau 1998; Vera et al. 2006). The SAMS is characterized by a pronounced wet season during the austral spring and summer (Zhou and Lau 1998; Vera et al. 2006; Silva and Carvalho 2007). Furthermore, the onset of the wet season begins in October and generally subsides by March (Liebmann et al. 2007; Silva and Carvalho 2007). Additionally, the wet season coincides with the occurrence of deep convection in the La Plata Basin region between ~20˚S – ~35˚S (Zipser et al. 2006; Rasmussen et al. 2014; Rasmussen and Houze 2016; Rasmussen et al. 2016), which is followed by a pronounced dry season and a reduction in deep convection (Fig. 1). The SAMS exhibits variability on a broad range of scales (Carvalho and Cavalcanti 2016; Carvalho et al. 2011), and convection related to the SAMS is modulated by variability on intraseasonal (Nogues-Paegle et al. 2000; Jones and Carvalho 2002; Carvalho et al. 2002; 2011; Cunningham and Cavalcanti 2006; Muza et al. 2009), interannual (Zhou and Lau 2001; Grimm and Zilli 2009; Bombardi et al. 2014) and decadal timescales (Grimm and Saboia 2015; Apaéstegui et al. 2014).

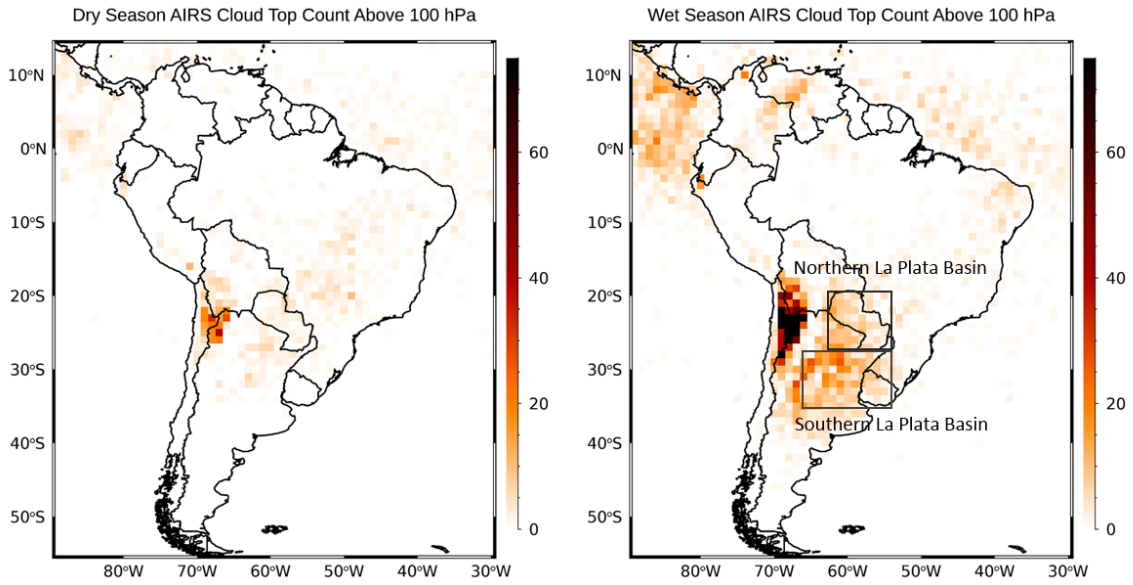

Fig. 1 South America and La Plata Basin region (boxes). Shading represent the number of cloud tops less than 100 hPa using Atmospheric Infrared Sounder Cloud Top Pressure satellite data. Left map: dry season (April – September). Right map: wet season (October – March).

A significant source of interannual variability on tropospheric circulation and precipitation in South America is the El Niño – Southern Oscillation (ENSO). ENSO originates in the tropics, and strong teleconnections are also observed in the extratropics associated with Rossby wave propagation (e.g., Trenberth et al. 2002). Previous studies have shown that during the warm phase of ENSO (El Niño), precipitation is suppressed in northern South America and enhanced in southeastern South America (Aceituno 1988; Marengo 1992; Ropelewski and Halpert 1987). ENSO is considered the primary driver of interannual precipitation variability in the La Plata basin (Berbery and Barros 2002; Tedeschi et al. 2013, 2015). The La Plata Basin is a region in southeastern South America between ~20˚S – 35˚S known for some of the deepest and most intense convective storms in the world (Zipser et al. 2006; Rasmussen et al. 2014; Rasmussen and Houze 2016; Rasmussen et al. 2016). During

the cold phase of ENSO (La Niña), precipitation anomalies are approximately opposite to those during El Niño (Grimm 2004).

In South America, the influence of ENSO varies throughout the austral spring and summer (Grimm 2003), and tropospheric circulation anomalies are often attributed to El Niño driven wave trains emerging from the South Pacific (e.g., Rodrigues and Woollings 2017). During an El Niño event, the anomalous rising motions over the eastern Pacific Ocean result in anomalous subsidence over the Amazon and anomalous Rossby wave activity propagating into South America via midlatitudes (Liebmann and Mechoso 2010). In the Southern Hemisphere (SH), a Rossby wave source is located in the upper troposphere, east of Australia along 30˚S. Rossby waves affecting South America are modulated by the strength and position of the subtropical jet (Carvalho et al. 2005; Ding et al. 2012).

The ENSO induced Rossby wave trains encounter the Andes Mountain's complex terrain and upon crossing they propagate towards the equator where they encounter northerly and easterly winds. This change of wind sign and blocking action can create a frontal boundary and cause the planetary "Rossby" waves to break. The influence of this frontal wave reaching the subtropics can induce anticyclonic Rossby wave breaking, destabilize the atmosphere and initiate convection with significant impacts on vertical motion within deep convective processes and on lower-stratospheric ozone (Martius, and Rivière 2016).

The intensity of Rossby wave motion is modulated by the strength and position of the subtropical jet. The position and intensity of the subtropical jet is controlled by the El Nino-southern oscillation on interannual time-scales (Berbery and Barros 2002; Tedeschi et al. 2013, 2015) and can be also related to the Southern Annular Mode (Carvalho et al. 2005; Ding et al. 2012). The Southern Annular Mode (e.g. Limpasuvan and Hartmann 2000;

Thompson and Wallace 2000; Lorenz and Hartmann 2001; Vallis et al. 2004; Rashid and Simmonds 2004), also known as the Antarctic Oscillation (AAO) (Gong and Wang 1999; Carvalho et al. 2005) is characterized by a dipole in the westerly wind strength with opposing centers at 40˚ and 65˚S, driving the atmospheric exchange of material between the mid and high latitudes (Kidson 1988; Thompson and Wallace 2000; Ding et al. 2012). During positive (negative) AAO events, the jet stream shifts poleward (equatorward) (Carvalho et al. 2005). The impacts of the AAO on the SH climate shows strong seasonality, and from December-February (DJF) is related to central and eastern Tropical Pacific SSTs influencing convection in the subtropics and midlatitudes (Ding et al. 2012), including ENSO events (Carvalho et al. 2005).

Rossby wave activity associated with ENSO indirectly influences tropical and extra-tropical lower-stratospheric ozone in South America by influencing tropospheric weather patterns and deep convective cloud processes (e.g. Randel et al. 2009; Calvo et al. 2010), and when the influences of ENSO and AAO are combined the sign of each process can enhance or suppress the effects of the teleconnection. Fogt et al. (2011) argue that the combination of negative (positive) ENSO and positive (negative) AAO reinforces the ENSO teleconnection. When the sign of both modes is the same, the combination suppresses the circulation in midlatitude, which may reduce the effects of ENSO teleconnection. According to the Fogt et al. study, the out of phase connections tend to occur more often from November - February. While ENSO and AAO are connected, the interactions between phases is likely nonlinear in nature and the interactions and responses differ from event to event (Carvalho et al. 2005). The interactions between ENSO and AAO may also be influenced by decadal-to-

multidecadal coupled modes of variability that may influence the magnitude of teleconnection effects.

Interdecadal and decadal variability originating from the tropical Pacific Ocean is primarily due to The Pacific Decadal Oscillation (PDO) (Zhang et al. 1997, Mantua et al. 1997; Gershunov and Barnett 1998), and is among the most relevant modes of ENSO-coupled variability influencing South America's climate (Andreoli and Kayano 2005). During the 20th century, positive PDO phases (warmer than average sea surface temperature anomalies in the Equatorial Pacific Ocean) occurred from 1922 – 1944 and again from 1978 – 1998, whereas negative PDO phases (colder than average sea surface temperature anomalies in the Equatorial Pacific Ocean) occurred from 1946 – 1977 (Salinger et al. 2001) and again from 1998 – 2012. The dates for the last negative phase are debatable as recent PDO values have become more positive. PDO phases have a less direct influence on localized weather patterns, but a strong influence on global teleconnection (e.g. ENSO and AAO) patterns. Andreoli and Kayano (2005) analyzed rainfall anomalies in South America related to ENSO during positive and negative PDO phases and found that ENSO related influences are driven by PDO.

The main objective of this study is to investigate large-scale interannual-to-multiannual stratospheric ozone variability at 100 hPa, 50 hPa and 10 hPa, with an emphasis on upper troposphere-lower stratosphere ozone patterns over South America and existing relationships with the Pacific Ocean, especially ENSO and PDO. This is accomplished by examining spatial and temporal patterns of stratospheric ozone based on remote sensing and reanalyses data during the austral spring and summer (October-March). Moreover, during spring and summer the ENSO teleconnections are well characterized in South America (e.g.

Grimm 2003; 2004). This study also examines the relationships between geopotential height anomalies at 200 hPa on lower-stratospheric ozone and planetary wave activity with EP Flux analysis (using reanalyses) to investigate possible relationships between ozone pattern and PDO. Finally, ozone trends at 100, 50 and 10 hPa with reanalysis data from 1980 – 2016 are investigated during the austral spring and summer to determine the spatial distribution of ozone changes over time.

This study is organized as follows. The data and methodologies are presented in section 1.3. Comparisons between ozone obtained from reanalyses and satellite data sets (based on the temporal range of the satellite data), and the spatial and temporal variability of ozone and relationships to large-scale ocean-atmosphere coupled modes (based on climate indices) are described in section 1.4. Ozone variability from 1980 – 2016 with reanalysis data is described in section 1.5. Interdecadal ozone variability and the relationships between Rossby wave trains, zonally averaged zonal winds, and planetary waves are described in section 1.6. Ozone trends from 1980 – 2016 are described in section 1.7. Conclusions are presented in section 1.8.

1.3 Data and Methods

Utilizing in-situ data to analyze stratospheric ozone on a climatological scale in South America is not possible. Data in this region is limited to locations with radiosonde/ozonesonde data collection sites, often only available below 100 hPa, and rarely with ozone data. Since the late 1990s and early 2000s, atmospheric data has been collected in this region by several polar orbiting satellites, and now reanalysis data have become available to extend the temporal range. This research utilizes a combination of satellite data:

Atmospheric Infrared Sounder (AIRS) (Chahine et al. 2006; Pittman et al. 2009) and Tropical Rainfall Mission Measurements (TRMM) (Huffman et al. 2007), and reanalysis data: Modern-Era Retrospective Analysis for Research and Applications Version 2 (MERRA2) (Rienecker et al. 2011; Gelaro 2017) and Global Climate Forecast System Reanalysis (CFSR) (Saha et al. 2010) to investigate spatial and temporal ozone variability in the upper troposphere and stratosphere.

1.3.1 Satellite Observations: AIRS and TRMM

The AIRS instrument is a cross-tracking scanning hyperspectral grating spectrometer on board NASA's EOS-Aqua satellite. AIRS measures infrared (IR) radiation in 2378 channels within the wavelength range of 3.7–15.4 μm (Chahine et al. 2006). This study analyzes AIRS+AMSU version 6 level 3 ozone daily data products. AIRS level 3 products have been binned into 1°x1° grid cells with a daily mean from the instrument's 15 daily orbits. AIRS ozone products are available in 24 pressure levels from September 2002 to December 2016 (Pittman et al. 2009; AIRS Science Team/Joao Texeira 2013), and this study utilizes the daily ascending orbit. The TRMM satellite and instrument provides 0.25˚x 0.25˚grid cells of 3 hourly precipitation estimates from 1998 – 2015 (Huffman et al. 2007).

1.3.2 Reanalyses: MERRA2 and CFSR

To extend the period of analyses, this study investigates stratospheric ozone variability using MERRA2 reanalysis (Gelaro et al. 2017). MERRA2 is produced with version 5.12.4 of the GEOS atmospheric data assimilation system and is available from 1980 – present with a spatial resolution of 0.5° latitude x 0.625° longitude) at 42 pressure levels from 1000 to 0.01 hPa.

The treatment of ozone data in MERRA2 represents advancements over the original MERRA data set and is a good representation of the variably of stratospheric ozone (Wargen et al. 2017). The MERRA2 assimilated ozone record has two distinct time periods, the Solar Backscatter Ultraviolet Radiometer (SBUV) period (January 1980–September 2004) and the NASA's EOS Aura satellite (Aura) period (from October 2004 to present). The SBUV instruments were onboard the NASA and NOAA satellites, and the Ozone Mixing Ratio (OMI) and Microwave Limb Sounder (MLS) instruments are currently on board the Aura satellite and described in detail in Wargen et al. (2017). Analyses requiring high vertical resolution, such as the study of interannual changes in midlatitude stratosphere–troposphere exchange are recommended for the MLS period only (Wargan et al. 2017). Therefore, this study utilizes MERRA2 ozone for long-term climatological changes over South America at individual pressure levels. Comparisons to AIRS are performed for the period from 2002 – 2016 to identify recent short-term temporal and spatial variability.

Additionally, we utilize the Global Climate Forecast System Reanalysis (CFSR) data available from the National Centers for Environmental Prediction (Saha et al. 2010), at 0.5˚ latitude x 0.5˚ longitude resolution and from 1980 – 2017. Daily CFSR geopotential height at 200 hPa is utilized in this study as an independent reanalyses to investigate dynamical patterns associated with ozone variability obtained with MERRA2.

1.3.3 Climate Indices

Several climate indices are examined to derive the influence of large-scale teleconnection patterns on ozone variability. These indices were particularly selected to elucidate the influences of atmospheric oscillations and ocean-atmospheric coupled modes known to modulate climate variability in South America on interannual-to-multiannual

timescales. The following indices are investigated here: The Pacific Decadal Oscillation (PDO) (Zhang et al. 1997; Mantua et al. 1997), the Multivariate ENSO Index (MEI) (Wolter and Timlin 1993), the Quasi-Biennial Oscillation (QBO), Tropical South Atlantic (TSA) (Enfield et al. 1999), and the Antarctic Oscillation (AAO) (downloaded from the NOAA Climate Prediction Center website (http://www.cpc.ncep.noaa.gov/data/indices/qbo.u30.index), (NOAA/Climate Prediction Center 2017).

1.3.4 Principal Component Analysis

One of the main goals of this study is to identify spatial and temporal patterns of variability of stratospheric ozone with focus on South America and identify relationships with ENSO on interannual-to-multiannual timescales. The main modes of stratospheric ozone variability are obtained by applying Empirical Orthogonal Function (EOF) analysis (Fukuoka 1951; Lorenz 1956), otherwise known as Principal Component Analysis (PCA). PCA is among the most widely and extensively used methods in atmospheric sciences (Hannachi et al. 2007) and was applied here to ozone anomalies to determine the main patterns of variability in AIRS and MERRA2. To ensure equal gridded areas for analysis, the square root of the cosine of latitude is applied (Ding et al. 2012). The North et al. (1982) rule was applied to determine independent eigenvalues by calculating a sampling interval for each eigenvalue. For the purposes of this work, an eigenvalue is considered independent when the confidence intervals do not overlap. Only independent modes are included in analyses. PCA is applied to the AIRS and MERRA2 ozone data at 10, 50 and 100 hPa from 2002 – 2016 as a means of comparing data sets. The Principal Component (PC) time-coefficients are correlated to the original data (mean seasonal ozone anomalies) at each pressure level to obtain the spatial

pattern for each mode. All other ozone analyses are investigated with MERRA2 ozone data. Long-term ozone patterns are analyzed by applying a PCA to MERRA2 ozone data from 1980 – 2016.

To investigate possible drivers for the lower-stratosphere ozone variability on interannual-to-multiannual time scales, Pearson's Product Moment correlation is applied to determine the magnitude of the linear relationship between each PC and each climate index listed in the data section (1.3.3). Spring and summer averaged (October – March) AAO, MEI and PDO indices are utilized for analyses.

Investigating dynamics and trends in the stratosphere is recognized as an essential component of ozone change assessments (e.g. World Meteorological Organization's (WMO) 2010). Ozone abundance is not only changed by photochemical destruction, but also via the influences on production, transport, and stratospheric climate (WMO 2010). This study analyzes changes to ozone during the austral spring and summer (October-March) and examines the potential influence of deep convective processes on stratospheric ozone in South America. The characteristics of ENSO depend on PDO phases. To further investigate how ENSO variations influenced the stratospheric ozone over South America we examined the positive and negative PDO phases from 1980 - 2016.

1.3.5 Mann-Kendal Trend Analysis

Trend analysis is used to determine whether gridded ozone concentrations are increasing or decreasing over time. Wet season averaged monthly MERRA-2 ozone data at 100, 50 and 10 hPa has been analyzed by applying the Mann-Kendall trend test (Mann 1945; Kendall 1962; Gocic and Trajkovic 2012) from 1980 – 2016. The Mann-Kendall test is a method for non-parametric trend detection which is less influenced by outliers (Lanzante

1996) in detecting change over time. Equations for the Mann-Kendall analysis are described in detail in Zilli et al. (2017). Trends are noted where they are statistically significant at the 5% significance level.

1.3.6 EP Flux

Eliassen-Palm (EP flux) vectors are utilized to examine planetary wave variability and cross tropopause exchange influencing stratospheric ozone (Randel et al. 2002). Monthly MERRA2 temperature, and zonal (u) and meridional (v) wind data are utilized for EP flux calculations to compare with South America ozone patterns at 100 hPa.

Here, EP-Flux is calculated based on Hartmann et al (1984) and described based on Li and Lau (2013):

$$F_{\phi} = -\rho_0 a cos\phi [v^* u^*] \quad (1)$$

$$F_p = f\rho_0 a cos\phi \frac{[v^*\theta^*]}{[\theta]_p} \quad (2)$$

$$\mathbf{F}=\{F_{\phi}, F_p\} \quad (3)$$

Where $u\ and\ v$ are zonal and meridional winds, respectively, $*$ denotes zonal mean, and brackets (e.g.$[v^*u^*]$) denotes the deviation from zonal means. Vertical instability is measured with $\rho_0(z) = \rho_s \exp\left\{-\frac{z}{H}\right\}$, where $\rho =$ air density, $z = -Hln(\frac{p}{p_s})$, $H = 7$ km (standard constant scale) and $\rho_s = 10^5\ Pa.$ The Coriolis parameter is $f = 2\Omega sin\phi$, where ϕ = latitude. Potential temperature (θ) and its partial derivative are denoted as θp = ∂θ/∂θp. To

visually represent the vector, each component is scaled by (Edmon et al. 1980; Taguchi and Hartmann 2006):

$$\mathbf{F}= \{F_{\phi}, F_{p}\}=cos\phi\{\ 1a*\ F_{\phi}\pi\ rad,\ F_{p}10E5\} \quad (4)$$

Planetary wave variability with EP flux is calculated with wet season averaged MERRA2 data. For all plots, EP Flux arrows have two components. Fy is the meridional component which in the Southern Hemisphere indicates the direction of the poleward (negative) and equatorward (positive) propagation of wave momentum. Fp is the vertical component which indicates the direction of the cross tropopause exchange, planetary momentum from troposphere to stratosphere (positive) and from the stratosphere to troposphere (negative). As a means of investigating all of South America, all EP Flux plots are from 90˚S to 15˚N. For this work we examine zonally averaged planetary wave variability by comparing EP flux vectors and zonally averaged zonal wind composites for each time frame (warm and cool PDO) and the differences.

For all statistical analysis, to determine significance a probability value (p-value) is calculated using a t-distribution test statistic with n - 2 degrees of freedom and considered statistically significant at 5% significance level.

1.4 AIRS and MERRA2 Spatial Patterns (2002 – 2016)

AIRS and MERRA2 ozone data are compared from September 2002 – September 2016. The goal of this comparison is to extend the AIRS temporal satellite range and determine the optimal pressure levels for further ozone analysis with MERRA2. Four levels

are initially utilized to compare the MERRA2 and AIRS data sets: 100, 50, 10 and 5 hPa. Because South America spans from the tropics to midlatitudes, ~15˚ N to ~55˚S, 100 hPa can be considered a part of the tropopause region throughout the tropics and subtropics, and in the lower stratosphere from the subtropics to midlatitudes. This pressure level is generally associated with the beginning of increasing ozone concentrations in the stratosphere, especially in the subtropics, where ozone concentrations transition from low tropopause ozone concentrations to the maximum concentrations generally located at ~ 10 hPa. Because a steep gradient in ozone concentration is observed between 100 hPa and 10 hPa, the 50 hPa level represents a transition in concentration between the two levels and is also utilized. Furthermore, the two data sets are also compared in the upper region of the stratosphere at 5 hPa.

.

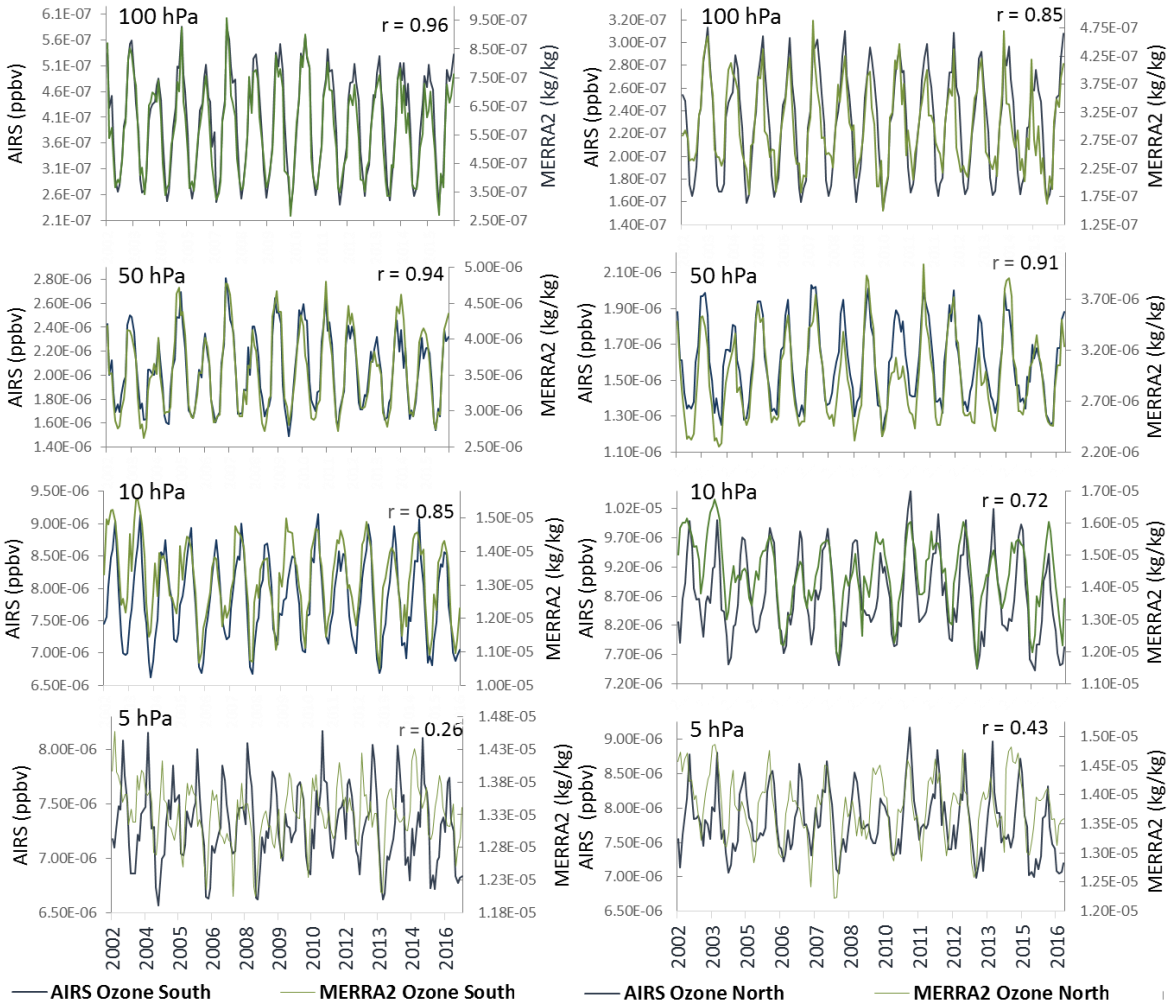

Fig. 2 Correlations between area averaged AIRS (green line) and MERRA2 (blue line) for the Southern La Plata Basin (left column) and Northern La Plata Basin (right column).

Given the known locations of deep convection in the La Plata basin, area averaged, monthly AIRS and MERRA2 ozone data in the Northern La Plata Basin (NLPB, Fig 1) and in the Southern La Plata Basin (SLPB, Fig. 1) are compared from September 2002 – 2016 including all months (Fig. 2). Seasonal variability is observed in both data sets at 100, 50 and 10 hPa. In the lower stratosphere, seasonal ozone variability is generally related to tropospheric processes and photochemistry. At 100 hPa, higher ozone concentrations are occurring during the dry season (austral winter), with a seasonal maximum generally

occurring in September. At 100 hPa lower ozone concentrations are occurring during the wet season (austral summer), with a seasonal minimum generally occurring in January. Conversely, at 10 hPa ozone concentrations are more dependent on photochemistry and less related to tropospheric processes, and at this level maximum concentrations occur during the warm season with more direct incoming solar radiation (Perliski et al. 1989). Pearson's correlation analysis is applied to both data sets. It should be noted that the strong seasonal cycle demonstrated by ozone at each level is influencing the correlation coefficients, but is shown without the annual cycle to investigate the seasonal variability in the MERRA2 and AIRS data. The strongest correlations between both data sets are observed in the lower stratosphere, at 100 hPa r = 0.96 (0.85) in the SLPB (NLPB), and at 50 hPa r = 0.94 (0.91). Weaker correlations are observed in the mid to upper stratosphere, at 10 hPa r = 0.85 (0.72) in the SLPB (NLPB). The weakest correlations are occurring at 5 hPa r = 0.26 (0.43) when the seasonal cycles are out-of-phase. Due to the weak agreement between data sets at 5 hPa, this level is removed from further analysis.

To spatially compare all of South America with data sets of different spatial resolutions, the MERRA2 data (0.5° x 0.625°) is re-gridded to the AIRS spatial resolution (1° x 1°). Figure 3 shows wet season averaged ozone concentrations obtained from AIRS and MERRA2 data sets. Notice that the range in concentration is not the same at each level. We observe that MERRA2 ozone concentrations are higher than AIRS for all levels. The positive bias in MERRA2 reanalysis can be partially explained by the fact that only the ascending orbit of AIRS (1:30 pm) is considered in the total average. Regardless of biases, monthly averaged MERRA2 and AIRS show consistent latitudinal patterns of ozone and ozone

gradients at all levels, with the largest differences observed in low latitudes and caused by satellite swaths.

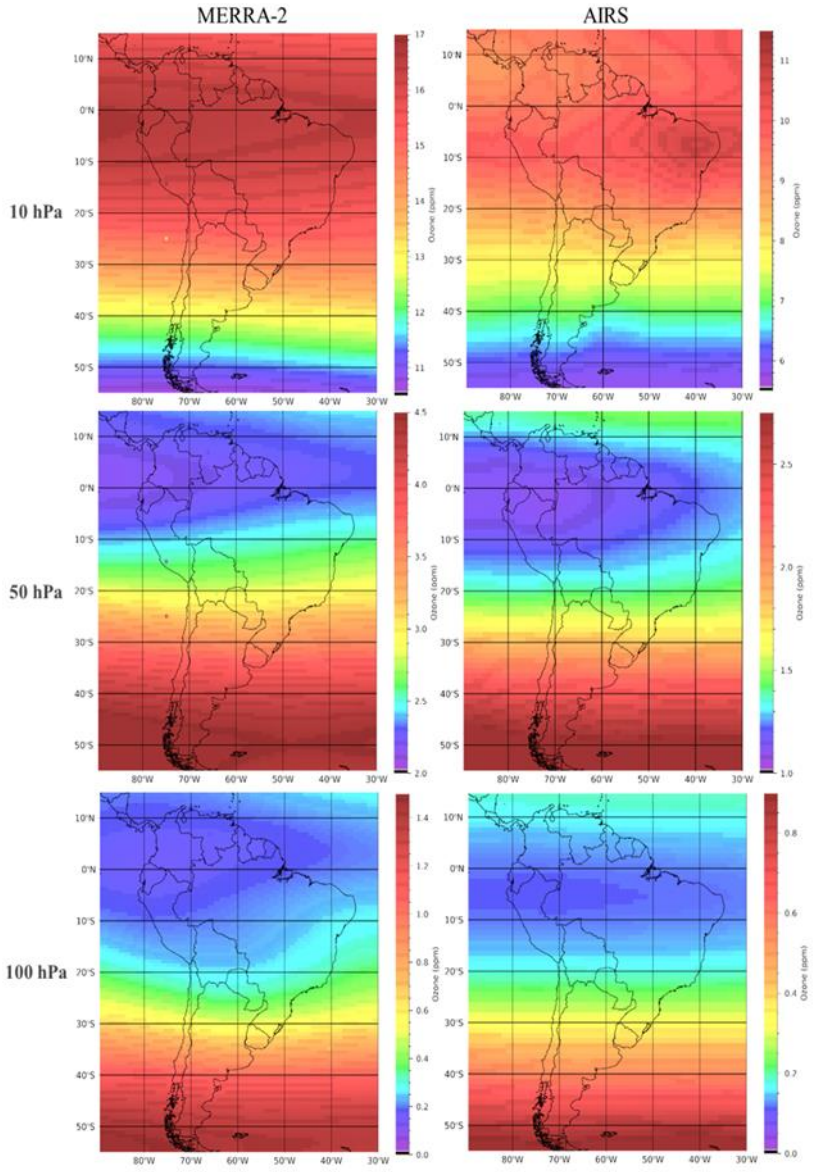

Fig. 3 MERRA2 and AIRS (PPM) wet season averaged ozone from 2002 – 2016. The left column is MERRA2 averaged ozone (ppmv) and right column is AIRS averaged ozone. Top row: 10 hPa. Middle row: 50 hPa. Bottom row: 100 hPa. Note that ozone concentrations in colorbars are different between data sets and at each level.

To account for problems with satellite sampling, and considering the overall similarity in the spatial patterns of ozone, PCA was applied to both data sets at 10, 50 and 100 hPa to characterize and compare their main patterns of variability during the period when AIRS data is available (2002 - 2016). The explained variances for the first mode, which are independent according to the North et al. (1982) rule, are shown in Table 1. The spatial patterns of the first mode (PC1) obtained for each data set and time coefficients are shown in Fig. 4. The spatial patterns were obtained by correlating each PC time coefficient (shown with bars in Fig. 4) with the respective ozone wet season ozone anomalies at each pressure level.

	2002 - 2016	
	MERRA2	**AIRS**
	10 hPa	
PC 1	78.15%	47.63%
	50 hPa	
PC 1	75.36%	39.36%
	100 hPa	
PC 1	38.05%	41.30%

Table 1. The percentage of variance explained for 2002 – 2016 MERRA2 and AIRS PCs at 100, 50 and 10 hPa.

At 10 hPa, PC1 explains about 78% of the total variance for MERRA2 and 48% for AIRS. However, the spatial patterns show good spatial agreement between the two data sets in terms of the magnitude of the coefficient in the tropics and the location of the sign change. At this level positive correlation patterns are especially consistent north of 10˚S (Fig. 4). Conversely, negative correlations are primarily poleward of 10˚S, and in AIRS limited regions are significant (e.g. Central Andes, Atlantic Ocean between 35 – 40˚S), as compared

to MERRA2, whereas all areas poleward of 15˚S in the domain exhibit statistical significance. The correlation coefficient between the PC1 MERRA2 and AIRS time-coefficients (~0.80) is statistically significant on a 99% confidence interval.

At 50 hPa, PC1 spatial patterns are similar, although the magnitude of the correlation between ozone anomalies and the PC1 varies spatially. Like at 10 hPa, the percentage of explained variance between the MERRA2 and AIRS at 50 hPa are not reasonably similar (~75.36% for MERRA2 and ~39.36% for AIRS), and a weaker correlation exists between the time-coefficients (r~0.56) compared to 10 hPa. At this level, the AIRS data set has two small regions with weak positive correlations between PC1 and ozone anomalies in Northern Brazil compared to strong positive correlations between 10˚N and 10˚S in MERRA2 (Fig.4). A notable characteristic observed in both data sets is the statically significant negative correlations over Southeast South America (Fig.4).

We show that the spatial patterns of PC1 at 10 and 50 hPa are very similar and significantly correlated. The spatial distribution of ozone concentrations at these two levels are primarily regulated by the Brewer Dobson Circulation (BDC) and the Quasi-Biennial Oscillation (QBO). The tropical vs. extra-tropical ozone patterns in PC1 indicates the influence of the BDC - where tropical upwelling is forced by Rossby Wave Pumping (Plumb, 2002), and the vertical velocity which is modulated by QBO (Flury et al., 2013). QBO is an oscillating zonal wind pattern in the tropical lower stratosphere which shifts on average every 28 months (Baldwin et al 2001) and can modulate the strength of the stratospheric polar jet and in turn affect tropospheric circulation (e.g., Holton and Tan 1980; Baldwin and Dunkerton 1998). In the tropics, vertical velocity related to BDC is anticorrelated with QBO, and when QBO is negative (positive), easterlies (westerlies) are prevalent in the tropical

stratosphere and vertical velocity is enhanced (suppressed) (Minschwaner et al., 2016). Some modeling studies have shown that as vertical velocity at 70 hPa decreases, the ozone concentrations at 50 hPa increases (Butchart, 2014). PC1 patterns at 10 and 50 hPa demonstrate this idea with both the spatial patterns and time coefficients.

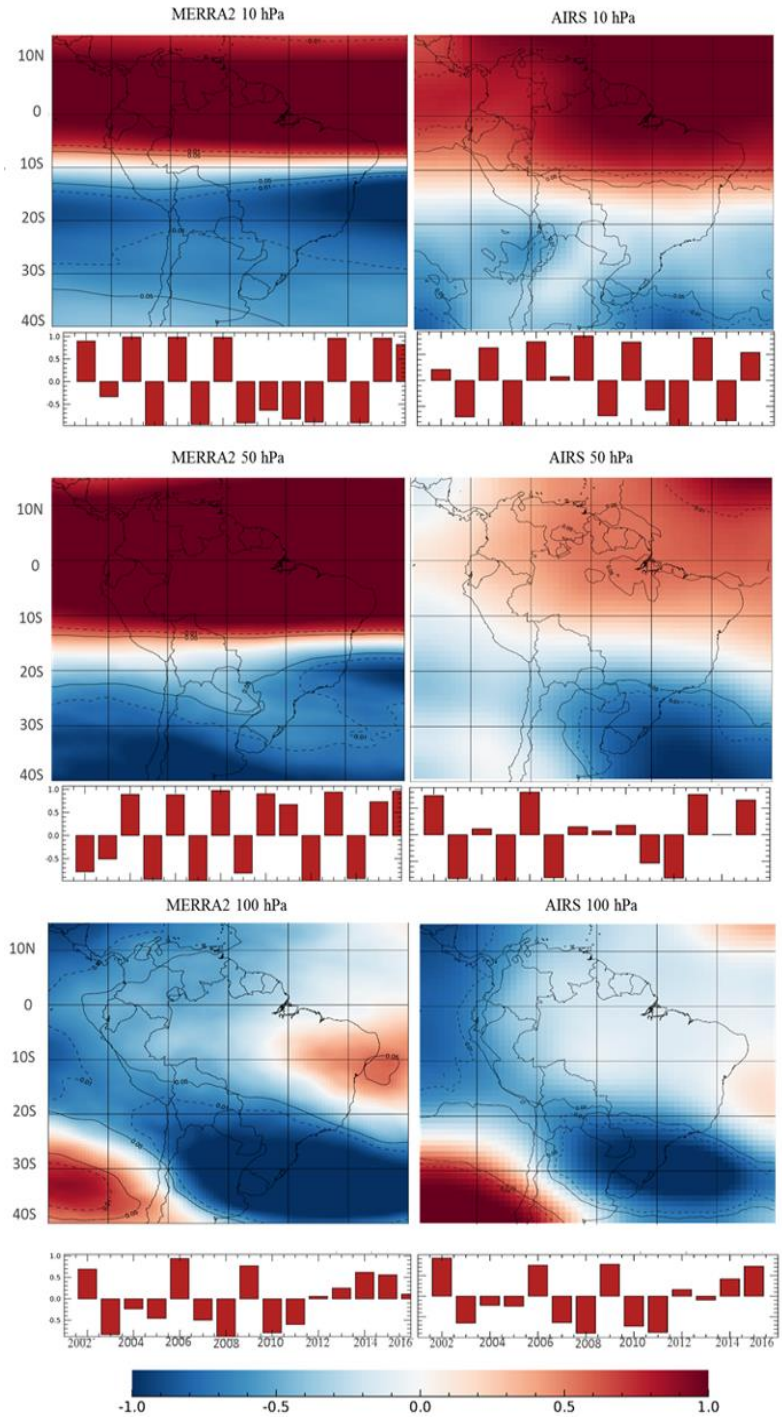

Fig. 4 October – March averaged MERRA2 (left column) and AIRS (right column) 2002 -2016 Principal Component (PC) 1. Correlations are obtained between each PC time coefficient (indicated with the bar plots at the bottom of each frame) and the wet season ozone anomalies. Colors indicate the magnitude of the correlation between the principal component and the ozone anomalies. Solid lines are statically significant on a 5% significance level, dashed lines on a 1% significance level. Time series of wet season PC1 time coefficients are illustrated in the bar graph.

At 10 and 50 hPa the correlation coefficients between PC1 and QBO are strongly positive, and when PC1 is positive (Fig. 2), the pattern along the equator shows a positive correlation between PC1 and ozone concentrations; in other words, the stronger the positive time coefficient (westerly stratospheric winds) the weaker the vertical velocity (suppressed BDC) and the higher the ozone concentrations. This may explain the interannual variability in the time coefficients and tropical ozone patterns. The strong positive correlation coefficient values along the equator (Fig. 2) are consistent with previously demonstrated relationships to BDC and QBO. It should be noted however, that the QBO oscillating signal in the time coefficients (bar graphs) is more pronounced with the MERRA2 data when compared to AIRS, and more pronounced at 50 hPa when compared to 10 hPa. Similarly, a PCA was applied to 100 hPa ozone, and while the patterns with MERRA2 and AIRS are very similar and the time coefficients are significantly correlated (r ~0.96), no connection is evident to QBO.

At 100 hPa, very good agreement exists between MERRA2 and AIRS. The PC1 time-coefficients are strongly correlated (r ~ 0.96), and the spatial patterns are generally similar, except over a small area in Northeast South America where positive correlations with PC1 are stronger for MERRA2 compared to AIRS. Unlike at 10 and 50 hPa, the amount of explained variance between MERRA2 and AIRS at 100 hPa are reasonably similar (~38.05% for MERRA2 and ~41.30% for AIRS). At this level, poleward of 30˚S a zonal dipole of positive and negative anomalies are similar in both patterns (Fig. 4). However, the magnitude of negative correlations in Southeast South America are greater in MERRA2 than AIRS, whereas the magnitude of positive correlations in the Pacific Ocean (~35˚S) is greater in

AIRS compared to MERRA2. In both patterns, most of northern South America shows no statistical correlations between PC1 and wet season averaged ozone anomalies.

1.5 MERRA2 Stratospheric Ozone: Spatial and Temporal Patterns (1980 – 2016)

Patterns of stratospheric ozone variability over South America obtained with AIRS and MERRA2 from 2002 – 2016, characterized by PC1, may only be representative of this particular period of common data. To verify this hypothesis, a new PCA was performed with wet season mean averaged MERRA2 ozone anomalies from 1980 – 2016 at 100, 50 and 10 hPa. At 10 and 50 hPa, PC1 ozone patterns are quite similar between the 2002 – 2016 patterns and the extended 1980 – 20216 time frame (not shown). Interestingly, at 100 hPa, the pattern of ozone variability during the wet season obtained from 1980 – 2016 (Fig. 5, left column) exhibits remarkable differences over subtropical and tropical latitudes in South America depending on the time frame considered. For instance, areas with a negative correlation between the PC time coefficients and ozone greatly decreased during the expanded time frame as compared to 2002 – 2016 (Fig.4). Additionally, the positive correlations in the Southeast Pacific Ocean and Northeast Brazil are inconsistent. During the extended time frame, the positive correlations in Northeast Brazil are stronger, stretching to the Amazon, and areas in the Pacific Ocean near equatorial latitudes exhibit weak correlation without significance. To further understand these differences, we examined how these PCs are related to the various climate indices investigated in this study: MEI, AAO, QBO, and PDO.

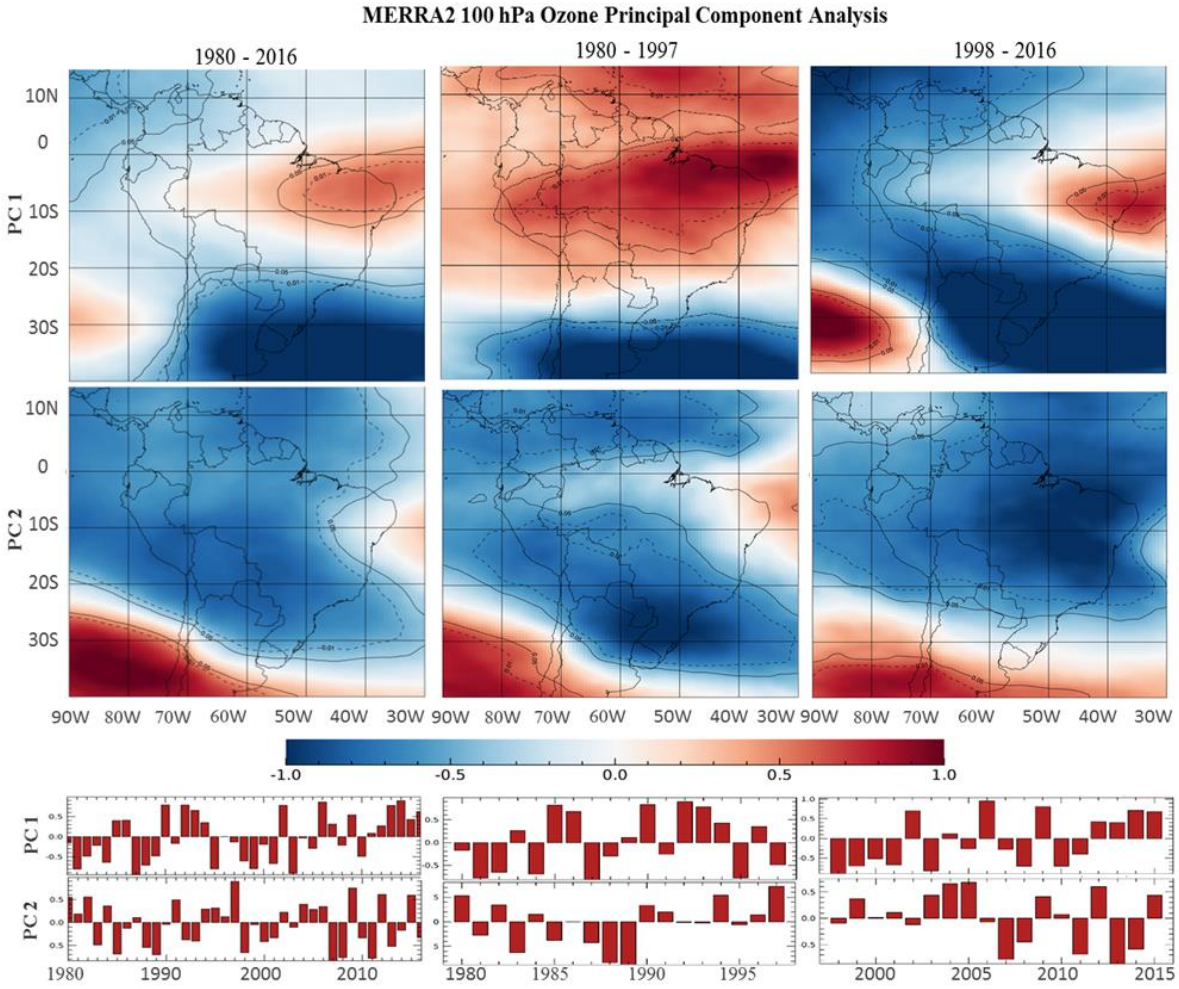

Fig. 5 Principal components and corresponding time-coefficients of MERRA2 ozone at 100 hPa from 1980 – 2016, 1980 – 1997, and 1998 – 2016. First row: PC1. Second row: PC2. Each PC time coefficient is correlated to wet season ozone anomalies. Time coefficients for each PC are displayed in the bar plots. Colors indicate the magnitude of the correlation between the principal component and ozone anomalies. Solid lines indicate statically significant correlations on a 5% significance level, dashed lines on a 1% significance level.

Table 2 shows the percentage of variance explained (PV) and the Pearson correlation coefficient (r) for each mode and at each pressure level analyzed (1980 – 2016). At 10 hPa, the first mode (PC1) explains 52.98% of the variance and exhibits a strong correlation with QBO (r~0.71). The second mode (PC2) explains 18.4% of the variance, it is statistically independent of PC1, and exhibits a weak negative correlation to QBO (r~-0.32). At 50 hPa, PC1 explains 52.21% of the variance and is positively correlated to QBO (r~0.52). PC2

explains ~15.27% of the variance and has no significant correlations to any climate indices discussed here. These results indicate that the primary influence on seasonal ozone concentrations at 50 hPa are the changes in zonal wind pattern associated with phases of the QBO.

MERRA2 Wet Season Ozone (1980 - 2016)						
	PV	MEI	AAO	QBO	PDO	TSA
			10 hPa			
Mode 1	52.98%	0.199	0.038	***0.716***	0.179	0.224
Mode 2	18.40%	0.024	-0.034	**-0.315**	0.158	-0.254
Mode 3	13.17%	-0.071	0.163	-0.074	-0.144	**0.308**
			50 hPa			
Mode 1	52.21%	-0.058	0.203	***0.522***	**-0.296**	0.038
Mode 2	15.27%	0.164	**-0.288**	0.208	0.181	-0.172
Mode 3	11.61%	0.150	**-0.280**	**-0.328**	0.161	0.223
			100 hPa			
Mode 1	33.19%	0.288	-0.138	0.068	0.214	-0.061
Mode 2	23.48%	***0.641***	***-0.432***	0.018	**0.353**	0.139
Mode 3	12.39%	-0.091	0.115	0.026	-0.126	***0.405***

Table 2. 1980 - 2016 MERRA2 correlation coefficients between the first two Principal Component modes (PC) and each climate index. PV is the percentage of explained variance. Bold values are statistically significant on a 5% significance level, and bold and italicized on a 1% significance level.

At 100 hPa, PC1 explains 33.19% of the ozone variability; surprisingly, this mode does not exhibit any significant correlations to any of the climate indices investigated here. Conversely, the second mode (PC2), which explains 23.48% of the variance, is significantly correlated to MEI (r~0.64), AAO (r~-0.43) and PDO (r~0.35). At 100 hPa, PC1s obtained for AIRS and MERRA2 from the 2002 – 2016 period show distinct relationships to climate indices (Table 3), which is not observed at 10 and 50 hPa (not shown). At 100 hPa (2002 – 2016), AIRS PC1 explains ~41.30% of the variance (Table 1), and exhibits strong correlation

with MEI (r~0.82; Table 3) and PDO (r~0.74; Table 3). Similarly, MERRA2 PC1 explains ~38.0% of the variance (Table 1) and has strong correlation with MEI (r~0.75; Table 3) and PDO (r~0.66; Table 3).

AIRS 100 hPa Ozone (2002 - 2016)				
	MEI	**AAO**	**QBO**	**PDO**
PC 1	***0.824***	-0.395	-0.032	***0.739***
PC 2	0.187	0.122	0.328	0.205
MERRA2 100 hPa Ozone (2002 - 2016)				
PC 1	***0.745***	-0.282	-0.015	***0.663***
PC 2	0.394	-0.243	-0.127	0.091

Table 3. 2002 – 2016 AIRS (top) and MERRA2 (bottom) correlation coefficients between the first 2 ozone PCs and each climate index at 100 hPa. Bold values are statistically significant on a 5% significance level, and bold and italicized on a 1% significance level.

However, this is not the case when considering MERRA2 from 1980 – 2016. At 100 hPa, PC1 exhibits no statistically significant correlation with any other climate indices. Because results indicate strong relationships between PC1, ENSO and PDO during the 2002 – 2016 period, a reasonable hypothesis is that the ENSO's influence as a teleconnection on lower-stratosphere ozone is not consistent over time; rather, it may depend on the phase of the PDO. To test this hypothesis, we investigate possible interactions between ozone patterns and ENSO according to the recent warm and cool phases of the PDO. Given that the most relevant teleconnections with ENSO are observed in the lower-stratosphere, the focus of the remainder of the PCA analyses will be on ozone variability at 100 hPa.

1.5.1 Influence of PDO Phases on MERRA2 100 hPa Ozone Patterns

The austral spring and summer averaged (wet season) MERRA2 ozone patterns at 100 hPa are investigated during recent positive (warm) and negative (cool) PDO phases between 1980 and 2016. To be consistent with previous analyses, a PCA is applied to wet season averaged ozone during 1980 – 1997 (warm phase) and to 1998 – 2016 (cool phase). In fact, during the cool phase the seasonally averaged PDO index oscillates from cool early in the period to warm late in the decade (Fig. 6). Figure 5 shows the patterns and time coefficients obtained for the first two (statistically independent) PC modes from 1980 – 2016 and separated according to PDO phases. Differences between PDO phases are evident in the spatial patterns, as well as in the correlations between each mode and climate indices.

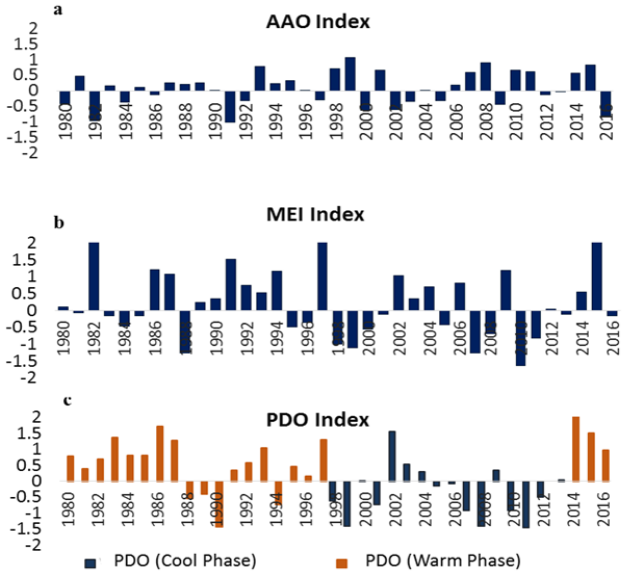

Fig. 6 October – March averaged climate indices. (a) Antarctic Oscillation (AAO), (b) Multivariate ENSO Index (MEI), (c) Pacific Decadal Index (PDO). PDO from 1980 – 1997 is generally warm and considered a warm phase. PDO from 1998 – 2013 is generally cool and considered a cool phase.

The results show that during the warm (cool) PDO phase from 1980 – 1997 (1998 – 2016), PC1 explains approximately the same percentage of seasonal ozone variance 38.04%

(40.97%), but the spatial ozone patterns differ considerably between the two time frames (Table 4). During the warm phase, the tropical-subtropical dipole is evident from the positive correlations between PC1 and the MERRA2 ozone anomalies equatorward of 20˚S and negative correlations poleward of 30˚S. Therefore, when PC1 is positive, ozone concentration increases throughout most of northern and central Brazil and parts of Bolivia and Peru, and decreases poleward of 30˚ S over South America.

MERRA2 Wet Season Ozone 100 hPa					
	PV	**MEI**	**AAO**	**QBO**	**PDO**
1980 - 2016					
PC 1	33.19%	0.288	-0.138	0.068	0.214
PC 2	23.48%	***0.641***	***-0.432***	0.018	**0.353**
1980 - 1997 (Warm PDO)					
PC 1	38.04%	0.071	-0.196	-0.121	0.170
PC 2	20.34%	***-0.558***	**0.473**	-0.342	-0.020
1998 - 2016 (Cool PDO)					
PC 1	40.97%	***0.766***	-0.336	-0.085	***0.660***
PC 2	24.35%	-0.324	0.285	-0.006	-0.126

Table 4 MERRA2 correlation results between the first 2 MERRA2 ozone PCs and each climate index in three time frames: 1980 – 2016, 1980 – 1997, and 1998 – 2016. PV is the percentage of explained variance. Bold values are statistically significant on a 5% significance level, and bold and italicized on a 1% significance level.

However, this pattern changes dramatically during the cool PDO phase. The large area with a positive correlation previously observed in Brazil has been reduced to a small area over northeast Brazil. The pattern of negative correlations between PC1 and the original ozone anomalies has expanded to include large areas from southeast to northwest South America, the subtropical Atlantic Ocean and tropical Pacific Ocean (Fig. 5). These patterns of correlation suggest a possible association with Rossby wave activity as the wave train

propagates north resulting in positive precipitation anomalies in southeast South America (Grimm 2003; Liebmann and Mechoso 2010). These relationships will be demonstrated in section 1.6.

Correlations between PC1 and each climate index differ between the warm and cool phases (Table 4). Like the results from 1980 – 2016, during the warm phase, the first mode is not correlated to any of the climate indices. Conversely, during the cool phase the first mode indicates a very strong correlation with MEI (r~0.77) and PDO (r~0.66), but not with AAO or QBO. The results for the full data set (1980 – 2016) appear to include processes from both time frames but are far more related to the warm phase. Ozone variability during the cool PDO phase shows stronger relationships to ENSO.

1.6 Global Geopotential Height at 200 hPa and Southern Hemisphere Planetary Waves

The PCAs at 100 hPa indicate strong modulation of ozone variability from the tropics to the extratropics over South America and correlations with climate indices suggest that these relationships may be explained by ENSO variability. Daily CFSR geopotential height at 200 hPa is utilized in this study as an independent reanalyses to investigate dynamical patterns associated with ozone variability obtained with MERRA2. While global geopotential height anomalies related to ENSO and PDO are well documented, here we use geopotential height anomalies to investigate the relationships between wet season MERRA2 ozone PCs and Rossby wave activities influencing South America.

1.6.1 Geopotential Height Anomalies and PCs: 1980 – 1997 (warm PDO phase)

Global wet season averaged CFSR geopotential height anomalies at 200 hPa (h200) from 1980 – 1997 (warm PDO) are correlated to PC1 time coefficients, and then compared to h200 anomalies correlated to MEI and AAO (Fig. 7 left column). For this time frame, the results indicate a weak correlation between PC1 and h200 anomalies, and regions statistically significant are primarily located in the southern hemisphere midlatitudes, poleward of 30˚S. While there are areas outside South America with a negative relationship between PC1 and h200 anomalies, no ENSO related Rossby wave train is evident. The relationships between MEI and h200 anomalies indicate Rossby wave initiation over Eastern Australia and the Western Indian Ocean with a dipole of anomalies centered at 30˚S. Additionally, during this time frame AAO is showing weak positive correlations to h200 anomalies in the southern region of South America. While ENSO is showing strong linear relationships to h200 anomalies, there is no apparent influence on PC1 during the warm PDO.

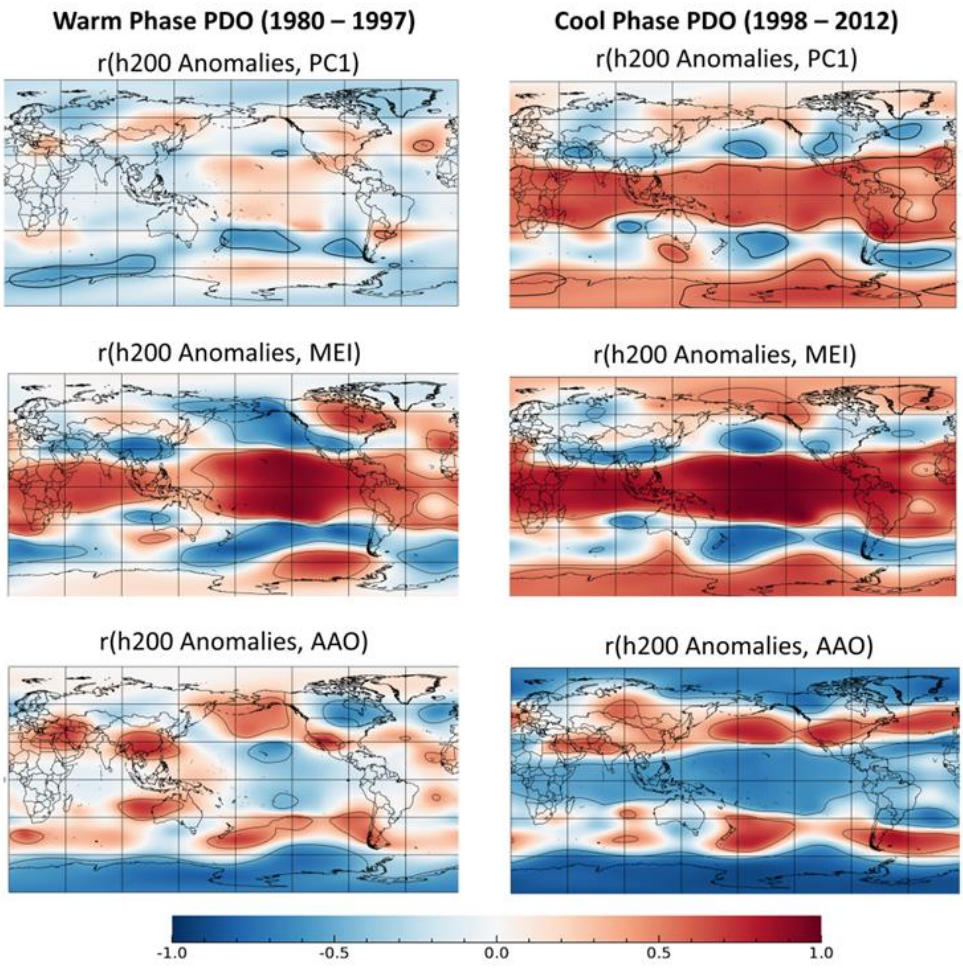

Fig. 7 Left Panel: 1980 – 1997 (warm PDO phase) CFSR geopotential height anomalies at 200 hPa correlated to PC1, MEI and AAO. Right Panel: same as left, except 1998 – 2012 (cool PDO phase). Solid lines are statistically significant on a 5% significance level.

1.6.2 Geopotential Height Anomalies and PCs: 1998 – 2012 (cool PDO phase)

The relationships between PC1, CFSR h200 anomalies and the climate indices are much stronger from 1998 – 2012 (cool PDO) (Fig. 7 right column) compared to 1980 – 1997 (warm PDO) (Fig. 7 left column). Unlike the warm phase, PC1 has a stronger relationship to MEI and PDO during the cool phase. This is also evident with respect to the correlations between h200 anomalies and MEI (Fig. 7 right panel).

PC1 and h200 anomalies in South America are strongly correlated throughout the tropics and subtropics during this time frame (Fig. 7 right column). The strongest positive correlations are observed in the La Plata Basin region of Southeast South America. As previously described, when PC1 is positive ozone is decreasing in the La Plata Basin. Consequently, correlation results between PC1 and h200 anomalies show that when geopotential heights are increasing in this region, ozone is decreasing. On the other hand, in southern South America there are no significant correlations between PC1 and h200 anomalies.

During the cool PDO phase, when h200 anomalies are correlated to MEI strong relationships are observed throughout South America (Fig. 7 right column). In the La Plata Basin Results, show that when MEI is increasing, h200 anomalies are increasing. This may indicate that during El Niño events h200 anomalies are higher. Higher geopotential heights in upper levels generally correspond to lower surface pressure, and this may be contributing to known convective processes in this region which are capable of cross tropopause exchanges and influencing ozone.

1.6.3 EP flux: Positive and Negative PC1 and PDO phases

To better understand the influence of large-scale planetary waves on cross tropopause energy transport and momentum between the equator and poles, Eliassen-Palm flux (EP flux) vectors have been utilized to investigate the influence of tropospheric and stratospheric circulations (Edmon et al. 1980, Hartmann et al. 1984, Randel 1992, Randel et al. 2002, Li and Lau 2013) on 100 hPa ozone patterns. EP flux vectors have two components: a vertical and a meridional component. In Figure 8 (left and center columns), the vertical component of

the EP flux vector (Fp) is driven by the meridional eddy heat flux, and when the vector is directed upward it shows planetary wave energy propagating into the stratosphere from the troposphere. Furthermore, the meridional component (Fy) is driven by momentum flux, and illustrates the zonal momentum between the equator and poles. Because F values in the stratosphere are small compared to the troposphere, points above 100 hPa are multiplied by ten and arrows are plot with proportional heads as a means of visualizing the magnitude and direction of the flow. Zonally averaged zonal [u] winds are also utilized to better understand the acceleration or weakening of the southern hemisphere tropospheric and stratospheric westerly wind patterns. Composites of warm and cool PDO [u] winds show a core of stronger westerly winds at 50˚S between 200 – 250 hPa during the cool PDO (Fig. 8).

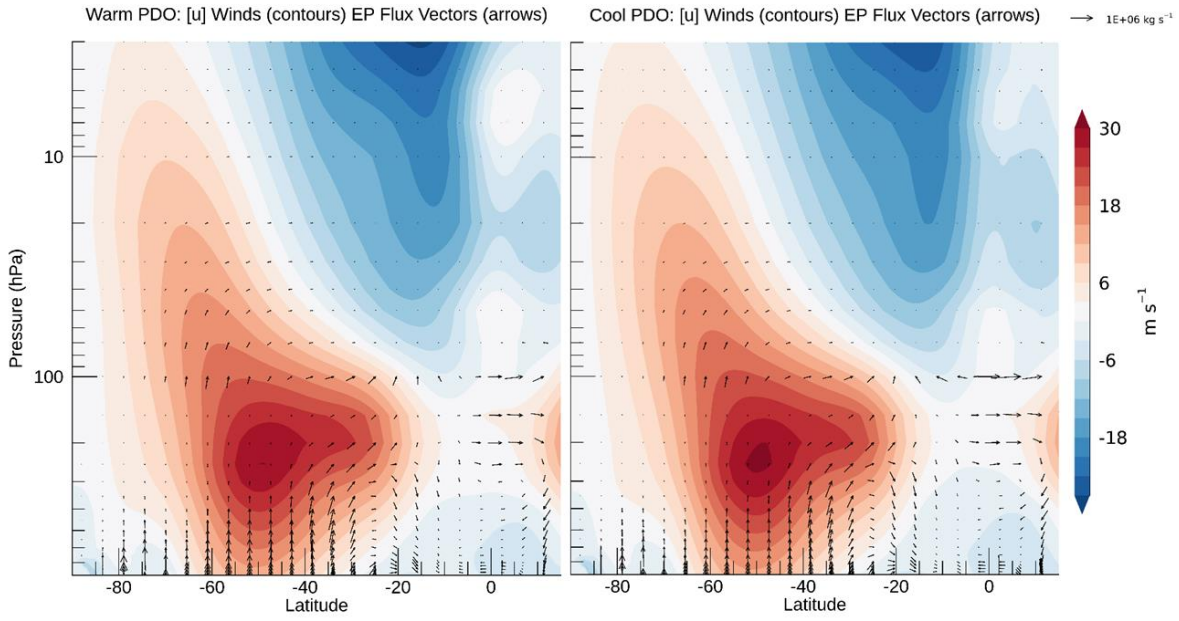

Fig. 8 Composites of EP flux vectors (arrows) and zonally averaged zonal [u] winds (shading) from 800 hPa to 3 hPa. Right: 1980 – 1997 averaged (warm PDO). Left: 1998 – 2012 averaged (cool PDO).

To better understand the wave energy in both patterns during each PDO phase, composites of EP-Flux vectors during positive and negative PC1 years are compared during

warm PDO and cool PDO. During the warm PDO (Fig. 9, top row) the difference plot (right column) shows nearly no significant differences at 100 hPa between positive and negative PC1s. The only notable differences between the two patterns are occurring in mid-latitudes where tropospheric vertical wave propagation at 40˚S is weaker during the positive pattern, and at 60˚S is stronger during the positive pattern. Garfinkel and Hartmann (2008) have suggested that when analyzing composites of El Niño and La Niña EP Flux vectors, the lack of statistical differences may be attributed to QBO or other dynamical mechanism. This may be the case during the warm phase.

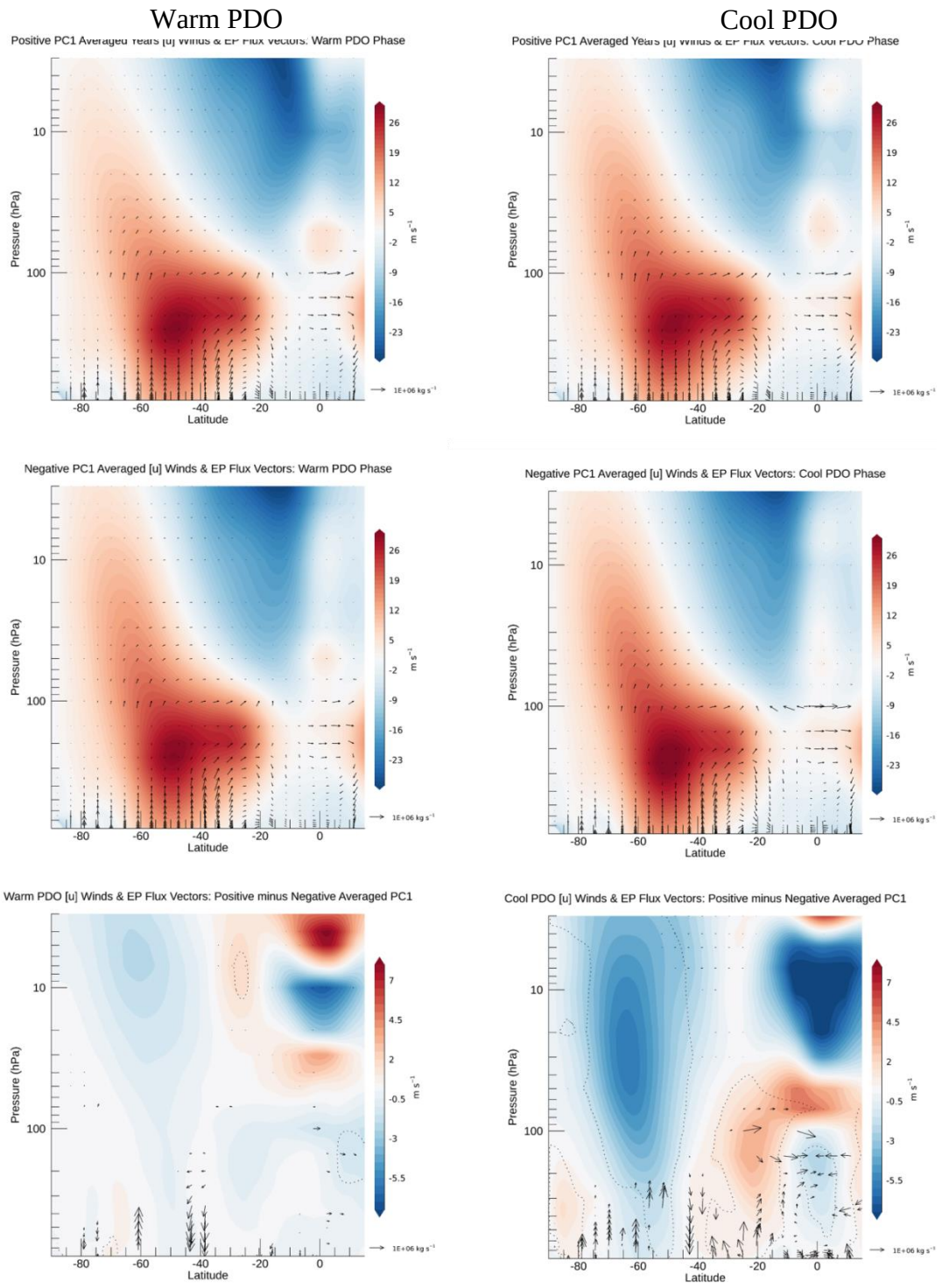

Fig. 9 Positive and negative PC1 averaged EP flux vectors (arrows) and zonally averaged zonal [u] winds (shading) from 800 hPa to 3 hPa. Left column: 1980 – 1997 averaged (warm PDO). Right column: 1998 – 2012 averaged (cool PDO). Top row: Positive PC1. Middle row: Negative PC1. Bottom row: Difference plots (positive minus negative). For the difference plots, only statistically

significant vectors between the two time frames are shown and dashed lines are statistically significant [u] winds, both are on a 5% significance level.

When comparing positive and negative PC1 composites during the cool PDO phase, several statistically significant differences are occurring in the troposphere and stratosphere (Fig. 9, bottom row), which may be influencing troposphere to stratosphere exchanges and 100 hPa ozone patterns. During the positive PC1 years, the tropical UTLS is showing stronger, equatorward wave energy compared to the negative PC1, which is showing poleward momentum from ~5 - 20˚S. From ~20 – 35˚S weak meridional (Fy) momentum and stronger upward propagation in the vertical momentum (Fp) in the troposphere during positive PC1. Between 40 – 45˚S, Fp is reduced compared to the negative PC1, indicating the meridional eddy heat flux is reduced. From ~50 – 70˚S, the meridional eddy heat flux is enhanced during positive PC1 compared to negative PC1. Additionally, during ENSO events it has been shown that wave energy from the upper troposphere to the lower stratosphere is enhanced (Weare 2010), and while this method may be demonstrating this during the positive PC1 composites in the tropics and high latitudes. In the midlatitudes between 37– 45˚S, weaker Fp is observed.

Furthermore, during the cool PDO, upward vertical momentum from 15 – 37˚S coincides with stronger westerly [u] winds during the positive PC1 years (Fig. 9). Conversely, strong differences in [u] stratospheric winds are occurring in high latitudes, where winds are weaker during positive PC1 years. In the tropical stratosphere, as mentioned previously, QBO dominates the tropical stratosphere and is likely influencing tropical differences.

1.7 Temporal Ozone Variability in South America 1980 – 2016

1.7.1 Wet Season Ozone Trends at 100, 50 and 10 hPa

Investigating dynamics and trends in the stratosphere has been recognized as an essential component of ozone change assessments (e.g., WMO 1995, 2011, 2014). Ozone changes over time can have a direct impact on stratospheric temperatures (WMO 2014), and where stratospheric ozone is decreasing, UVB radiation in the troposphere is increasing which influences photochemistry (e.g. Tang et al. 1998) and harming living organisms (WMO 2014). Here we investigate ozone trends with MERRA2 data (Schoeberl et al., 2012) by applying a Mann-Kendall trend analysis (Wilks 2011) at 10, 50 and 100 hPa to wet season averaged (October – March) data from 1980 – 2016 (Fig. 10). Dots indicate statistically significant trend on a 5% significance level.

Tropical mid-stratospheric ozone is primarily regulated by photolysis of molecular oxygen. As a reminder, stratospheric photochemistry and water vapor chemistry is described in detail in the introduction of this dissertation. At 10 hPa, negative ozone trends are found over most of subtropical South America, and the largest magnitude are occurring in southeast South America and throughout Argentina (Fig. 10, top). It is important to note that while mid-stratosphere ozone is primarily influenced by photochemistry, it can also be influenced by tropospheric dynamics, most notably locations susceptible to deep convective overshooting and stratospheric hydration. Furthermore, the presence of water vapor in the stratosphere can become a catalyst for ozone destruction (Bates and Nicolet 1950). At 10 hPa, the location of the negative trends across central and northwest South America are collocated to the locations cloud tops in the lower stratosphere (Fig.1), especially over the

Andes Mountains, and southeast South America where large mesoscale convective systems are known to produce deep convection (Gettelman et al. 2002; Zipser et al., 2006; Salio et al., 2007; Mulholland et al., 2018; Bruick et el. 2019) capable of stratospheric hydration. The presence of stratospheric water vapor in this region will be investigated in Chapter 4. However, the direct influence of water vapor on ozone concentrations in this region is outside the scope of this work.

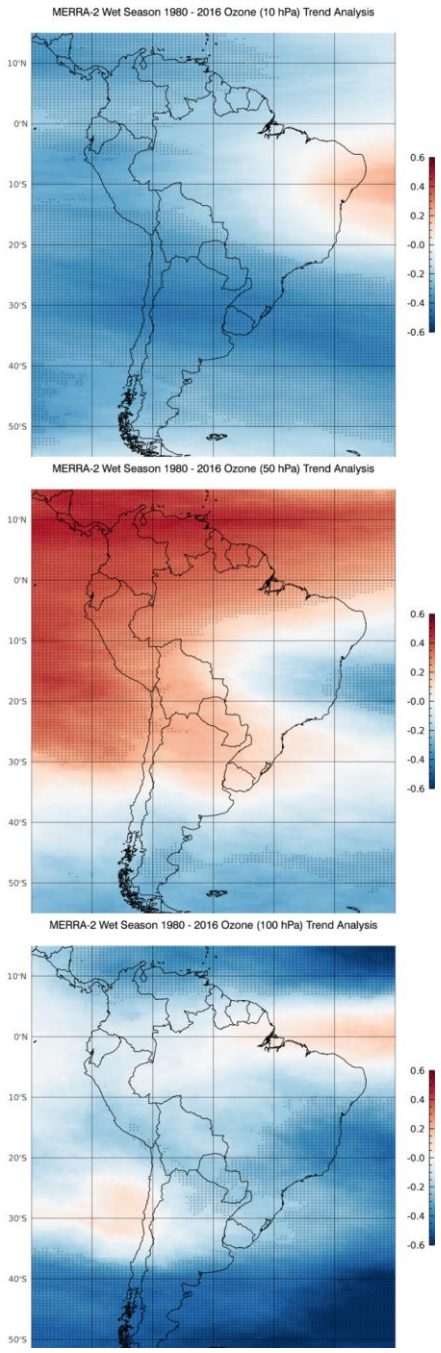

Fig. 10 Mann-Kendall trend analysis applied to MERRA2 October – March averaged (wet season) ozone at 100, 50, and 10 hPa. Grid spaces with dots indicate a statistically significant trend on a 5% significance level. Blue shading indicates a negative trend, red shading indicates a positive trend from 1980 – 2016.

At 50 hPa, ozone concentrations are generally driven by BDC in the tropics and modulated by QBO (Flury et al., 2013). In section 1.5.1, we have shown a linear relationship between the primary mode of variably (PC1) and QBO during this time frame (Table 2). In South America the trends at this level are localized to the tropics during the wet season. Along the equator ozone concentrations are increasing and outside the equatorial region few significant trends are found.

In the lower stratosphere, the influences on ozone flux are generally related to exchanges between the troposphere and stratosphere due to the position of the upper level jet (Newell 1963), folding of the tropopause (Danielsen 1968), BDC (Brewer 1949) and extratropical deep convection (Poulida et al. 1996; Fischer et al. 2003; Gray 2003; Hegglin et al. 2004). At 100 hPa, weak statistically significant negative trends are observed in eastern South America, eastern Paraguay and Northern Argentina. At this level, strong negative trends are also found at all locations poleward of 40^{o}.

Here we also investigate two areas in South America with deep convection during the wet season (boxes Fig. 1). For this we calculate the annual averages of 100 hPa ozone in the Southern La Plata Basin (SLPB) and in the Northern La Plata Basin (NLPB). We then applied a Mann-Kendall trend analysis (Wilks 2011) to each area averaged time series (Fig. 11). Ozone concentrations in both areas are significantly decreasing on a 5% significance level. Determining changes to ozone concentrations during the wet season is likely highly localized. A trend is detected in the area averaged data (Fig. 11), yet not in the gridded MERRA2 data (Fig. 10). The SLPB is also showing large interannual variability as compared to the NLPB, and is collocated to known areas of deep convection (Gettelman et al. 2002; Zipser et al., 2006; Salio et al., 2007; Mulholland et al., 2018; Bruick et el. 2019). This may

also be related to a steep gradient in tropopause height between the tropics and polar region. The SLPB represents a region not only influenced by the upper level jet, but it also represents a transition between the influences of the SAMS during the wet season and drier regions in southern South America (Gonzalez et al. 2013).

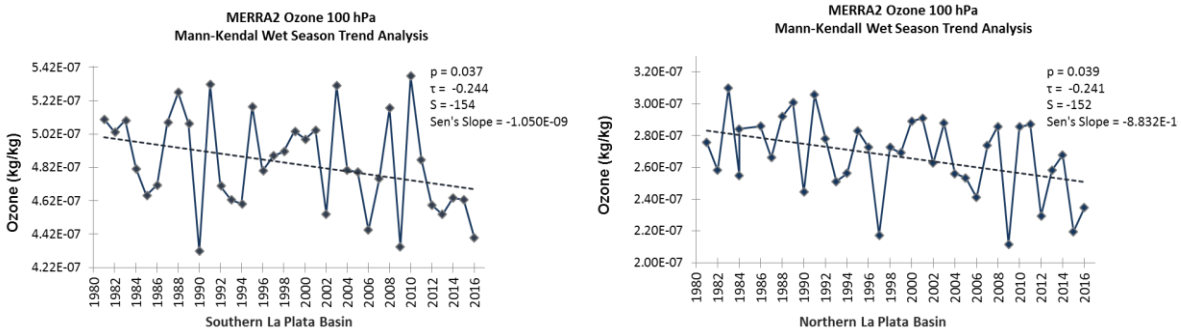

Fig. 11 Mann-Kendall trend analysis applied to wet season averaged MERRA2 ozone data from 1980 – 2016. The SLPB (left) and NLPB (right) trends (dashed lines) are statistically significant on a 5% significance level

1.7.2 Austral Spring and Summer Ozone Trends

Overall, the analysis for this work has focused on wet season averaged ozone data as a means of understanding ozone variability during the seasons with deep convective processes (October – March). However, previous research has shown significant differences in the spatial and temporal distribution of deep convection and extreme precipitation in South America during the austral spring and summer, especially related to ENSO (e.g. Grimm 2003, Berbery and Barros 2002; Tedeschi et al. 2013, 2015). As a result, in this section we separate the wet season into two seasons: October – December (Vera et al. 2004) and January – March (Fig. 12, left and center columns, respectively). We also extend our investigation to include trends detected in the wet season PCA analysis at 10, 50 and 100 hPa from 1980 -

2016 (Fig. 12, right column). The MERRA2 data used for this analysis was not detrended; as a result the PCA may detect modes with PCs changing over time. Trends in the PC coefficients are observed at each level. at 10 hPa PC3, at 50 hPa PC2 and at 100 hPa PC3, all observed trends in the PCs are positive trends over time. Results are used to compare both the spring and summer trend patterns to the wet season PCA patterns showing significant trends. The goal is to identify whether one season is exhibiting a stronger influence on the wet season PCA patterns over another.

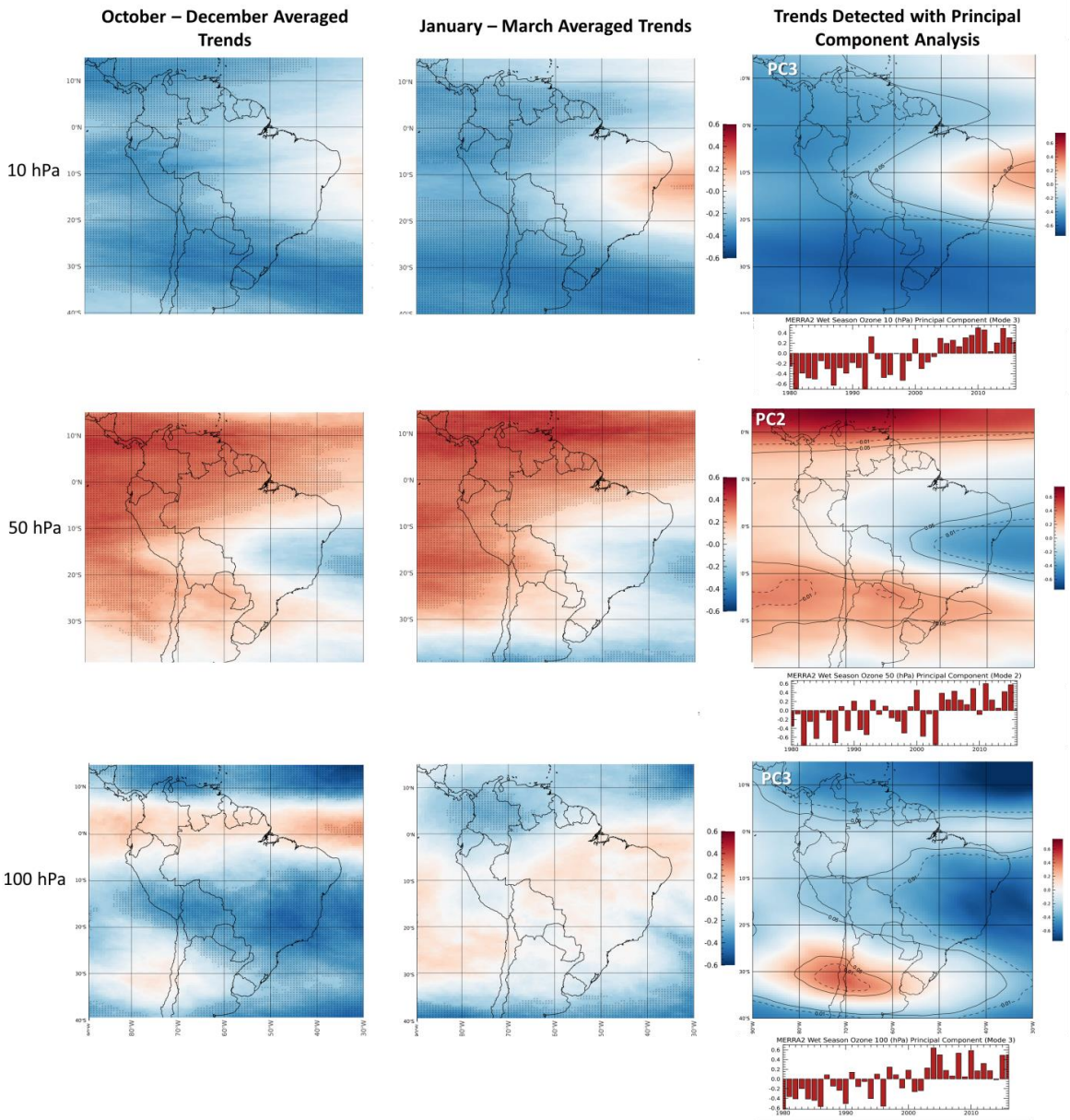

Fig. 12 Mann-Kendall trend analysis applied to MERRA2 ozone data from 1980 – 2016 and compared to trends detected in the principal component analysis. October – December averaged (left column), January – March averaged (center column) and detected trends in the principal component (PC) analysis (right column). Dots in the grid cells of the spring and summer analysis indicates a statistically significant change at 5%. Solid lines in the PC analysis (right column) indicate a statistically significant correlation between the PC coefficient and ozone anomalies at a 5% level. Dashed lines in the PC analysis (right column) indicate a statistically significant correlation between the PC coefficient and ozone anomalies at a 1% level.

At 10 hPa, the third mode of the wet season PCA (PC3) explains 13.1% of the variance, and time coefficients are showing a strong positive linear trend (Fig. 12 top row, right column).When comparing spring and summer ozone trends to the wet season patterns in the PC3, we observe large similarities between the both trend patterns between 20 - 40˚S where ozone is decreasing over time. During the spring and summer, wide spread negative trends are significant on a 5% level and occurring throughout the Andes mountain range. During the summer, the negative trends are extending into the western Amazon. For this level, similar spring and summer ozone trend patterns are likely driving the ozone trends in the wet season analysis.

At 50 hPa, the second mode of the wet season PCA (PC2) explains 15.2% of the variance and time coefficients are also showing a clear positive linear trend (Fig. 12 middle row, right column). Like the 10 hPa ozone trends, when comparing the trend patterns between spring and summer the observed patterns are very similar. When comparing the spring and summer trend patterns to PC2, the patterns are similar poleward of 10˚S. While the positive ozone trends along the equator in the spring and summer analysis and over the northern Amazon and Andes Mountains are not observed in the PCA analysis, overall the patterns of trends at this level are quite similar to PC2. Like the 10 hPa analysis, similar spring and summer ozone trend patterns are likely driving the ozone patterns in the PC2 patterns at 50 hPa.

At 100 hPa, the third mode of the wet season PCA (PC3) explains 12.4% of the variance. Like at 50 and 10 hPa, 100 hPa is showing a clear linear trend in the PC3 time coefficients which is strengthening the patterns in this mode over time (Fig. 12 bottom row, right column). When comparing the spring and summer ozone trends at 100 hPa the patterns

are dissimilar. The observed patterns in spring are showing a pattern of statistically significant negative ozone trends across southeast South America, Paraguay, Bolivia, and southern Peru. Conversely, throughout most of South America few trends are detected in summer, and these trends are primarily located in Colombia and southern Argentina. At this level, spring ozone trend patterns are likely driving the ozone patterns in the wet season analysis.

1.7.3 100 hPa Ozone Anomalies, ENSO and PDO

Lastly, we finish our analysis of long-term variability by showing patterns related to ENSO and PDO in the UTLS. For this we analyzed wet season averaged ENSO (MEI), 100 hPa PC1, and 100 hPa ozone trends during the recent warm and cool PDO phases. Results for three distinct time frames are shown in Figure 13 (1980 – 2016, warm PDO and cool PDO). MEI is correlated to ozone anomalies and shown in the top row (Fig. 13a, b, c), PC1s from Figure 5 are shown in the middle row (Fig. 13d, e, f), and ozone trend analysis is shown in the bottom row (Fig. 13g, h, i). The relationships between ozone anomalies at 100 hPa and ENSO are evident during the cool PDO phase (1998-2016). During the cool PDO, the negative trend patterns in the southern La Plata Basin (SLPB) are collocated to locations known for deep convection (Fig. 1), and show strong linear relationships to ENSO and PC1 (Fig. 13). This indicates that during this time frame, the El Niño teleconnection is decreasing UTLS ozone in the southern LPB.

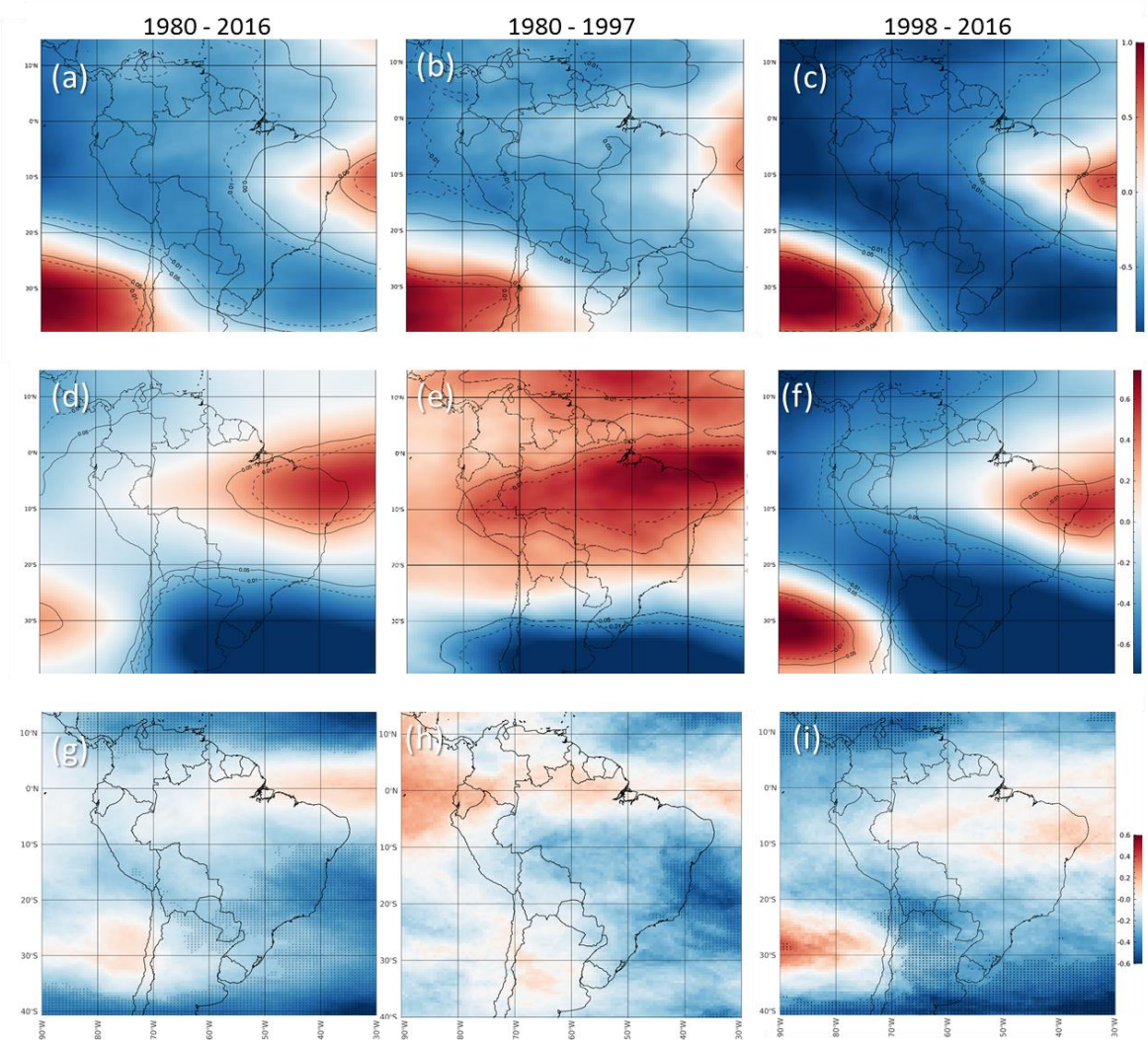

Fig. 13 Wet season averaged MERRA2 100 hPa ozone correlated to ENSO (MEI) from 1980 – 2016 (a), warm PDO (b), cool PDO (c). Wet season PC1 from 1980 – 2016 (d), warm PDO (e), cool PDO (f). Colors indicate the magnitude of the correlation. Solid lines indicate statically significant correlations on a 5% significance level, dashed lines on a 1% significance level. Wet season Mann-Kendall trend analysis from 1980 – 2016 (g), warm PDO (h), cool PDO (i). Dots in grid spaces indicate statistically significant trends on a 5% significance level.

To further test the ENSO-ozone relationship during the cool PDO phase, we calculated correlations between wet season averaged TRMM total daily precipitation and PC1 during the 1998 – 2012 TRMM satellite data time frame (Fig. 14). Patterns of correlation are consistent with the expected ENSO teleconnections with precipitation; that is,

El Niño (La Niña) events are related to enhanced (decreased) precipitation over the La Plata Basin (north-northeast Brazil) in a region known for Mesoscale Convective Systems (Fig. 14, right).

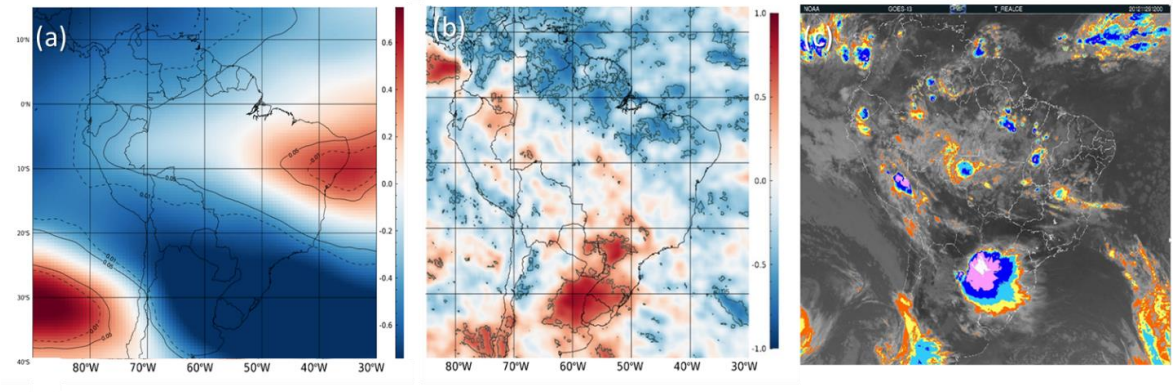

Fig. 14 October – March averaged (wet season) PC1 (a), and wet season daily TRMM total Precipitation (1998 – 2012) correlated to MERRA2 PC1 (1998 – 2012; b). GOES 13 color enhanced satellite infrared imagery on 11/29/2012 12 UTC of a Mesoscale Convective System (MCS) with deep convection (white colors) in the La Plata Basin (c). Solid grey lines are statically significant areas on a 5% significance level.

1.8 Discussion and Conclusions

The purpose of this study is to understand the spatial and temporal variability of stratosphere ozone with an emphasis on UTLS ozone variability related to El Niño – Southern Oscillation (ENSO), and investigate whether these relationships may depend on PDO phase. We applied a PCA to October – March (wet season) ozone to compare two distinct datasets: AIRS and MERRA2 from 2002 – 2016 at three pressure levels: 10, 50 and 100 hPa.

At 10 and 50 hPa, we show that the MERRA2 and AIRS data sets are very similar, and the PC1 coefficients for both data sets are positively related to QBO. Furthermore, when

PC1 is positive, QBO is positive (westerly stratospheric winds over the tropics), and vertical velocity related to BDC is suppressed. This mechanism results in reduced ozone transport aloft and higher ozone concentrations at 50 and 10 hPa, as observed in the PC1 patterns in the tropics at both levels. Interannual variability in the time coefficients is demonstrating this relationship to the oscillating QBO signal, which is more pronounced with MERRA2 compared to AIRS. The signal is also more pronounced at 50 hPa compared to 10 hPa. In the lower stratosphere, a PCA was applied to 100 hPa ozone anomalies. At this level, the MERRA2 and AIRS patterns are very similar, and the time coefficients are significantly correlated. However, no connection to QBO is evident.

Next, we investigated the influence of teleconnections and large-scale circulation on stratospheric ozone with wet season averaged climate indices: AAO, MEI, and PDO. Each index was correlated to the MERRA2 and AIRS PCs (2002 – 2016). At 10 and 50 hPa, no significant results are shown with AAO, MEI or PDO. However, at 100 hPa, the tropospheric influence is evident in the interannual ozone variability, and results show statistically significant relationships to teleconnection originating in the tropics, especially between PC1 and MEI, and PC1 and PDO.

To extend the investigation in the UTLS, a PCA was applied to MERRA2 100 hPa ozone anomalies from 1980 – 2016. The spatial patterns with the extended temporal range are dissimilar to the 2002 – 2016 spatial patterns. In fact, PC1 from 1980 – 2016 shows no significant relationships with any climate indices investigated in this study. Instead, the second mode, PC2 patterns are significantly correlated to MEI, AAO and PDO during the extended time frame. Overall, from 2002 – 2016, the dominant pattern of ozone variability

characterized by PC1 shows significant relationships to ENSO and PDO, whereas PC1 from the 1980 – 2016 analysis does not.

To investigate these differences, we applied a PCA to 100 hPa ozone anomalies during separate PDO phases. PC1 during the 1980 – 1997 (warm PDO) phase exhibits a well-defined pattern of anomalies with opposite sign between tropics and subtropics. Conversely, during the 1998 – 2012 period (cool PDO), PC1 pattern of ozone anomalies clearly show a tripole of anomalies which indicates a possible relationship with Rossby-wave trains extending from mid-latitudes to the tropics in South America. This may explain the stronger correlations between PC1 and MEI during the cool PDO phase. However, strong correlations between PC2 and MEI during the warm PDO phase suggest that ENSO played a secondary (although relevant) role in ozone variability during this phase, but was not the dominant factor explaining ozone anomalies in the tropics and subtropics of South America.

Rossby wave activity influences patterns of rainfall and circulation in the upper troposphere over the tropics and subtropics of South America that can, in turn, influence the exchange of ozone at the UTLS interface. Our results show that negative ozone anomalies at 100 hPa are generally related to positive 200 hPa h200 anomalies. ENSO-related patterns and intensity of h200 anomalies varied during the two phases of the PDO, elucidating the relative importance of ENSO explained by PC1 in each phase.

To further investigate Rossby wave activity in South America we applied the Eliassen-Palm flux (EP flux) analysis to composites of positive and negative PC1 time coefficients separately to understand planetary wave variability during the warm and cool PDO. Zonally average zonal winds [u] were also calculated to identify tropospheric and stratospheric wind variably driving planetary wave variability. During the warm PDO phase

the only notable differences between the positive and negative EP Flux composites are found between 40 - 45°S. While it is demonstrating enhancement of the lower and mid tropospheric wave momentum, it is not showing an influence in the upper troposphere – lower stratosphere (UTLS) wave variability.

Conversely, during the cool PDO phase, the EP Flux analysis shows several statistically significant differences in both the troposphere and stratosphere. During the positive PC1 years, we found that the tropical UTLS is showing weak vertical momentum and a stronger meridional component driving wave energy toward the equator. In the mid and high latitudes, the meridional eddy heat flux (Fp) dominates with stronger vertical planetary wave momentum throughout the troposphere and stratosphere. Interestingly, the positive PC1 composites of [u] winds show weak stratospheric and polar jets during the cool PDO phase, which may explain Rossby wave variability during this time frame. This explanation would require further investigation outside the scope of this work.

To identify ozone changes from 1980 – 2016 over South America, we applied a Mann-Kendall trend test to wet season averaged MERRA2 ozone at 10, 50 and 100 hPa. At 10 hPa, decreasing trends are generally located between 20 – 40°S. At 50 hPa, increasing trends are located along the equator and may indicate a weakening of the BDC as previously mentioned. At 100 hPa, ozone is decreasing throughout the midlatitudes, including eastern Brazil and Paraguay. Because 100 hPa is influenced by tropospheric processes and seasonal variability, this result is investigated further to understand if wet season averaged changes over time are dominated by spring or summer ozone trends.

Furthermore, a Mann-Kendall trend analysis was applied separately to spring and summer averaged MERRA2 ozone data from 1980 – 2016. The results were compared to

PCA modes exhibiting trends in the PC time coefficients. At 10 hPa, a strong positive linear trend is detected in the PC3 time coefficients, and the patterns of trends are similar to both spring and summer trend patterns. At 10 hPa, neither season is demonstrating a dominating influence on the wet season PC3 patterns. Similarly, at 50 hPa, a positive trend is observed in the PC2 the time coefficients, and the spring trends and summer trend patterns are quite similar to wet season PC2 patterns. Conversely, at 100 hPa, while a strong trend is detected in the PC3 time coefficients, the spring and summer trend patterns are dissimilar when compared to PC3 at this level. At 100 hPa, the patterns in PC3 are more related to the spring trend patterns especially over southern Brazil. However, in the summer, very weak changes in ozone are occurring between 1980 and 2016. At 100 hPa, the spring trend patterns are showing a dominating influence in the wet season PC3 patterns.

Overall, this study demonstrates the interannual variability in the UTLS ozone and influence of ENSO teleconnections on stratospheric ozone. These results may have additional implications for a potential feedback in the La Plata Basin. A recent study by Wu and Polvani (2017), using the Community Earth System Model Large Ensemble experiments (1955 – 2005), shows that decreasing stratospheric ozone may influence extreme precipitation in Southeast South America. We have shown that ENSO variability is modulated by PDO (e.g. Andreoli and Kayano 2005), and that during El Niño events, particularly in recent decades, ozone decreases over the La Plata Basin. This has implications for a possible positive feedback, as extreme precipitation and deep convective transport of cloud material in the lower stratosphere is enhanced, it may further contribute to the decrease in ozone, which in turn may enhance extreme precipitation. Further investigation is required to properly

understand patterns of ozone depletion, especially variability during the spring and summer seasons affecting populated areas of South America.

1.9. Acknowledgements

This research was supported by the University of California, Santa Barbara Graduate Opportunity Fellowship. The remotely sensed AIRS data used in this research was developed by the AIRS Science Team/Joao Texeira; the TRMM data was developed by the TRMM Science Team, processed by the TRMM Science Data and Information System (TSDIS) team and the TRMM office, and archived and distributed by the Goddard Distributed Active Archive Center. The MERRA-2 reanalysis data used in this study/project has been provided by the Global Modeling and Assimilation Office (GMAO) at NASA Goddard Space Flight Center. The CFSR reanalysis data used in this research were developed by NCEP and provided by NCAR. We thank Dr. Charles Jones for the computational support for this research.

1.10 References

AIRS Science Team/Joao Texeira (2013) AIRS/Aqua L3 Daily Standard Physical Retrieval (AIRS+AMSU) 1 degree x 1 degree V006, Greenbelt, MD, USA, Goddard Earth Sciences Data and Information Services Center (GES DISC), Accessed July 2016. 10.5067/AQUA/AIRS/DATA301

https://disc.gsfc.nasa.gov/datasets/AIRX3STD_006/summary.

Andreoli RV, Kayano MT (2005) ENSO-related rainfall anomalies in South America and associated circulation features during warm and cold Pacific decadal oscillation regimes. *Int. J. Climatol.*, 25: 2017-2030. doi:10.1002/joc.1222.

Apaéstegui J, Cruz FW, Sifeddine A, Vuille M, Espinoza JC, Guyot JL, Khofri M, et al. (2014) Hydroclimate variability of the northwestern Amazon Basin near the Andean foothills of Peru related to the South American Monsoon System during the last 1600 years. *Climate of the Past* **10**: 1967–1981.

Baldwin M, Dunkerton T (1998) Quasi-biennial modulation of the Southern Hemisphere stratospheric polar vortex. *Geophysical Research Letters* - GEOPHYS RES LETT. 25. 3343-3346. 10.1029/98GL02445.

Baldwin MP et al. (2001) The quasi-biennial oscillation, *Rev. Geophys.,* 39 179–229.

Bates, D. R. and Nicolet, M. (1950) The photochemistry of atmospheric water vapor, *J. Geophys. Res.,* 55, 301–327.

Berbery EH, VR Barros (2002) The Hydrologic Cycle of the La Plata Basin in South America. *J. Hydrometeor.,* **3**, 630–645, https://doi.org/10.1175/1525-7541(2002)003<0630:THCOTL>2.0.CO;2.

Bombardi RJ, Carvalho LM, Jones C, Reboita MS. (2014) Precipitation over eastern South America and the South Atlantic Sea surface temperature during neutral ENSO periods, *Clim. Dyn.* 42:1553-68.

Brewer AW (1949) Evidence for a world circulation provided by the measurements of helium and water vapor distribution in the stratosphere, Q. J. Roy., *Meteor. Soc.,* 75, 351–363.

Bruick ZS, Rasmussen KL, Rowe AK, McMurdie LA (2019) Characteristics of Intense Convection in Subtropical South America as Influenced by El Niño-Southern Oscillation. *Mon. Wea. Rev.*, https://doi.org/10.1175/MWR-D-18-0342.1.

Butchart N (2014) The Brewer-Dobson circulation, *Rev. Geophys.*, 52, 157–184, doi:10.1002/2013RG000448.

Calvo N, RR Garcia, Randel WJ, Marsh DR (2010) Dynamical Mechanism for the Increase in Tropical Upwelling in the Lowermost Tropical Stratosphere during Warm ENSO Events. *J. Atmos. Sci.*, **67**, 2331–2340. https://doi.org/10.1175/2010JAS3433.1.

Carvalho LM, Silva Dias MAF (2002) Intraseasonal largescale circulations and mesoscale convective activity in tropical South America during the TRMM-LBA campaign. *J. Geophys. Res.*, 107, 8042, doi:10.1029/2001JD000745.

Carvalho LM, Jones C, Ambrizzi T (2005) Opposite Phases of the Antarctic Oscillation and Relationships with Intraseasonal to Interannual Activity in the Tropics during the Austral Summer. *J. Climate,* 18, 702–718, https://doi.org/10.1175/JCLI-3284.1.

Carvalho LMV, Silva AE, Jones C et al. (2011) Moisture transport and intraseasonal variability in the South America monsoon system. *Clim Dyn,* 36: 1865. https://doi.org/10.1007/s00382-010-0806-2.

Carvalho LMV, Cavalcanti IFA (2016) The South American Monsoon System (SAMS). In: de Carvalho L, Jones C (eds) The Monsoons and Climate Change. *Springer Climate*.

Chahine M, Pagano TS, HH Aumann, Atlas R, Barnet C, Blaisdel J, Chen L,Divakarla M, Fetzer EJ, Golberg M, Gautier C, Granger S, Hannon S, Irion FW, Kakar R, Kalnay E, Lambrigtsen BH, Lee SY, Le Marshall J, McMillan WW, McMillin L, Olsen ET, Revercomb H, Rosenkranz P, Smith WL, Staelin D, LL Strow LL, Susskind J, Tobin

D, Wolf W, Zhou L (2007), AIRS improving weather forecasting and providing new data on greenhouse gases. *Bull. Am. Meteorol. Soc.,* 87 (7), pp. 911-926, 10.1175/ BAMS-87-7-911T.S http://journals.ametsoc.org/doi/abs/10.1175/BAMS-87-7-911.

Cunningham CAC, Cavalcanti IFD (2006) Intraseasonal modes of variability affecting the South Atlantic convergence zone. *Int. J. Climatol.*, 26, 1165–1180.

Danielsen EF (1968) Stratospheric-tropospheric exchange based on radioactivity, ozone and potential vorticity, *J. Atmos. Sci.*, **25**, 502–518.

Ding Q, Steig EJ, Battisti DS, Wallace JM (2012) Influence of the Tropics on the Southern Annular Mode. *J. Climate,* 25, 6330–6348, https://doi.org/10.1175/JCLI-D-11-00523.1

Edmon HJ, Hoskins BJ, McIntyre ME (1980) Eliassen-Palm cross sections for the troposphere. J. Atmos. Sci. 37:2600–2616.

Enfield DB, Mestas AM, Mayer DA, Cid-Serrano L (1999) How ubiquitous is the dipole relationship in tropical Atlantic sea surface temperatures? *JGR-O*, 104, 7841-7848.

Fischer H., et al. (2003) Deep convective injection of boundary layer air into the lowermost stratosphere at midlatitudes, *Atmos. Chem. Phys.*, **3**(3), 739–745, doi:10.5194/acp-3-739-2003.

Flury T, Wu DL, Read WG (2013) Variability in the speed of the Brewer–Dobson circulation as observed by Aura/MLS, Atmos. *Chem. Phys.*, 13, 4563-4575, https://doi.org/10.5194/acp-13-4563-2013.

Fogt RL, Bromwich DH, Hines KM (2011) Understanding the SAM influence on the South Pacific ENSO teleconnection, *Clim Dyn*, 36: 1555. https://doi.org/10.1007/s00382-010-0905-0.

Forster PM deF, Shine KP (2002) Assessing the climate impact of trends in stratospheric water vapor, *Geophys. Res. Lett.*, 29(6), doi:10.1029/2001GL013909.

Fueglistaler S, Dessler AE, Dunkerton TJ, Folkins I, Fu Q, Mote PW (2009) Tropical tropopause layer, *Rev. Geophys*., 47, RG1004. doi:10.1029/2008RG000267.

Fukuoka A (1951) A Study of 10-day Forecast (A Synthetic Report), Vol. XXII, The Geophysical Magazine: Tokyo; 177–218.

Garssen J, Norval M, El-Ghorr A, Gibbs N K, Jones CD, Cerimele D, De Simone C, Caffieri S, Dall`Acqua F, De Gruijl FR, Sontag Y, Van Loveren H (1998) Estimation of the effect of increasing UVB exposure on the human immune system and related resistance to infectious diseases and tumours. *J. Photochem. Photobiol.* B. 42, 167 ± 179.

Gelaro R, McCarty W, Suárez MJ, Todling R, Molod A, Takacs L, Randles CA, Darmenov A, Bosilovich MG, Reichle R, Wargan K, Coy L, Cullather R, Draper C, Akella S, Buchard V, Conaty A, da Silva AM, Gu W, Kim G, Koster R, Lucchesi R, Merkova D, Nielsen JE, Partyka G, Pawson S, Putman W, Rienecker M, Schubert SD, Sienkiewicz M , Zhao B (2017) The Modern-Era Retrospective Analysis for Research and Applications, Version 2 (MERRA-2). *J. Climate*, 30, 5419–5454. https://doi.org/10.1175/JCLI-D-16-0758.1.

Garfinkel CI, Hartmann DL (2008) Different ENSO teleconnections and their effects on the stratospheric vortex, *J. Geophys. Res.*, 113, D18114, doi:10.1029/2008JD009920.

Gershunov A, Barnett TP (1998) Interdecadal Modulation of ENSO Teleconnections. Bull. Amer. Meteor. Soc., **79**, 2715–2726, https://doi.org/10.1175/1520-0477(1998)079<2715:IMOET>2.0.CO;2.

Gettelman A, Salby ML, Sassi, F (2002) Distribution and influence of convection in the tropical tropopause region, *J. Geophys. Res.*, 107(D10), doi:10.1029/2001JD001048.

Gocic M, Trajkovic S (2013) Analysis of changes in meteorological variables using Mann-Kendall and Sen's slope estimator statistical tests in Serbia, *Global Planet Change*, 100: 172-182.

Gong D, Wang S (1999) Definition of Antarctic oscillation index. GRL, 26(4), pp.459-462.

Gonzalez PLM, Polvani LM, Seager R (2014) Stratospheric ozone depletion: a key driver of recent precipitation trends in South Eastern South America. *Clim Dyn* **42,** 1775–1792 https://doi.org/10.1007/s00382-013-1777-x.

Gray SL (2003) A case study of stratosphere to troposphere transport: The role of convective transport and the sensitivity to model resolution, *J. Geophys. Res.*, **108**(D18), 4590, doi:10.1029/2002JD003317.

Grimm AM (2003) The El Niño impact on the summer monsoon in Brazil: Regional processes versus remote Influences. *J. Climate,* 16, 263-280.

Grimm AM (2004) How do La Niña events disturb the summer monsoon system in Brazil? Climate Dynamics **22**(2–3): 123–138.

Grimm AM, Tedeschi RG (2009) ENSO and Extreme Rainfall Events in South America. *J. Climate*, 22, 1589–1609. https://doi.org/10.1175/2008JCLI2429.1.

Grimm AM, Zilli MT (2009) Interannual Variability and Seasonal Evolution of Summer Monsoon Rainfall in South America. *J. Climate,* 22, 2257–2275. https://doi.org/10.1175/2008JCLI2345.1.

Grimm AM, Saboia JP (2015) Interdecadal Variability of the South American Precipitation in the Monsoon Season. *J. Climate*, **28**, 755–775. https://doi.org/10.1175/JCLI-D-14-00046.1.

Hannachi A, Jolliffe IT, Stephenson DB (2007) Empirical orthogonal functions and related techniques in atmospheric science: A review. *Int. J. Climatol.*, 27: 1119–1152. doi:10.1002/joc.1499.

Hartmann DL, Mechoso CR, Yamazaki K (1984) Observations of Wave-Mean Flow Interaction in the Southern Hemisphere. *J. Atmos. Sci.*, **41**, 351–362, https://doi.org/10.1175/1520-0469(1984)041<0351:OOWMFI>2.0.CO;2.

Hegglin MI et al. (2004) Tracing troposphere-to-stratosphere transport above a mid-latitude deep convective system, *Atmos. Chem. Phys.*, **4**(3), 741–756, doi:10.5194/acp-4-741-2004.

Heisler GM, Grant RH, (2000) Ultraviolet radiation in urban ecosystems with consideration of effects on human health, *Urban Ecosystems*, 4: 193. https://doi.org/10.1023/A:1012210710900.

Hoffmann L, Xue X, Alexander MJ (2013) A global view of stratospheric gravity wave hotspots located with Atmospheric Infrared Sounder observations, *J. Geophys. Res. Atmos.*, 118, 416–434, doi:10.1029/2012JD018658.

Holton J, Tan H (1980) The influence of the equatorial quasibiennial oscillation on the global circulation at 50 mb. *J. Atmos. Sci.*, 37, 2200–2208.

Holton JR, Haynes PH, McIntyre ME, Douglass AR, Rood RB, Pfister L (1995) Stratosphere-troposphere exchange, *Rev. Geophys.*, 33(4), 403–439. doi:10.1029/95RG02097.

Huffman GJ, Adler RF, Bolvin DT, Gu G, Nelkin EJ, Bowman KP, Hong Y, Stocker EF, Wolff DB (2007) The TRMM Multisatellite Precipitation Analysis (TMPA): quasi-global, multiyear, combined-sensor precipitation estimates at fine scales. *J. of Hydrometeorology* 8(1): 38–55.

Ipcc/teap (2005) Special Report on Safeguarding the Ozone Layer and the Global Climate System: Issues Related to Hydrofluorocarbons and Perfluorocarbons. *Cambridge: Published for the Intergovernmental Panel on Climate Change, Cambridge University Press.*

Jones C, Carvalho LMV (2002) Active and break phases in the South American monsoon system. *J. Climate*, 15, 905– 914.

Karoly DJ (1989) Southern Hemisphere circulation features associated with El Niño Southern–Oscillation events. *J. Climate*, 2, 1239–1252.

Kendall MG (1962) Rank correlation methods (third ed.), *Hafner Publishing Company*, New York.

Khaykin S, Pommereau J-P, Korshunov L, Yushkov V, Nielsen J, Larsen N, Christensen T, Garnier A, Lukyanov A, Williams E (2009) Hydration of the lower stratosphere by ice crystal geysers over land convective systems, *Atmos. Chem. Phys.*, 9, 2275–2287, https://doi.org/10.5194/acp-9-2275-2009.

Kidson JW (1988) Indices of the Southern Hemisphere zonal wind. *J. Climate*, 1, 183–194.

Lanzante JR (1996) Resistant, robust and non-parametric techniques for the analysis of climate data: theory and examples including applications to historical radiosonde station data, *International Journal of Climatology*, 16, pp. 1197-1226.

Li Y, Lau N, (2013) Influences of ENSO on Stratospheric Variability, and the Descent of Stratospheric Perturbations into the Lower Troposphere. *J. Climate,* **26**, 4725–4748, https://doi.org/10.1175/JCLI-D-12-00581.1.

Liebmann B, Camargo SJ, Seth A, Marengo JA, Carvalho LM, Allured D, Fu R, Vera CS (2007) Onset and End of the Rainy Season in South America in Observations and the ECHAM 4.5 Atmospheric General Circulation Model. *J. Climate,* **20**, 2037–2050, https://doi.org/10.1175/JCLI4122.1.

Liebmann B, Mechoso CR (2010) The South American Monsoon System. In: The Global Monsoon System: Research and Forecast, 2nd Edition. C. P Chang et al., (eds.) World Scientific Publishing: Singapore. 550pp.

Limpasuvan V, Hartmann DL (2000) Wave-maintained annular modes of climate variability. *J. Climate,* 13, 4414– 4429.

Lorenz DJ, Hartmann DL (2001) Eddy–zonal flow feedback in the Southern Hemisphere. *J. Atmos. Sci.,* 58, 3312–3327.

Lorenz EN (1956) Empirical Orthogonal Functions and Statistical Weather Prediction. Technical report, Statistical Forecast Project Report 1, Dep of Meteor, MIT: 49.

Mann HB (1945) Non-parametric tests again trend, *Econometrica*, 13, pp. 245-259.

Mantua NJ, Hare SR, Zhang Y, Wallace JM, Francis RC (1997) A Pacific interdecadal climate oscillation with impacts on salmon production. *Bull. Amer. Meteor.* Soc., **78**, 1069–1079,doi:https://doi.org/10.1175/1520-0477(1997)078<1069:APICOW>2.0.CO;2.

Martius O, Rivière G (2016) Rossby wave breaking: Climatology, interaction with low-frequency climate variability, and links to extreme weather events. In J. Li, R.

Swinbank, R. Grotjahn, & H. Volkert (eds.), Dynamics and Predictability of Large-Scale, High-Impact Weather and Climate Events (Special Publications of the International Union of Geodesy and Geophysics, pp. 69-78). Cambridge: Cambridge University Press. doi:10.1017/CBO9781107775541.006.

McIntosh PC, Hendon HH (2018) Understanding Rossby wave trains forced by the Indian Ocean Dipole. *Clim Dyn*, 50: 2783. https://doi.org/10.1007/s00382-017-3771-1.

Minschwaner K, Su H, Jiang JH (2016) The upward branch of the Brewer-Dobson circulation quantified by tropical stratospheric water vapor and carbon monoxide measurements from the Aura Microwave Limb Sounder, *J. Geophys. Res. Atmos.*, 121, 2790–2804, doi:10.1002/ 2015JD023961.

Mo KC, Paegle J N (2001) The Pacific–South American modes and their downstream effects. *Int. J. Climatol.*, 21: 1211-1229. doi:10.1002/joc.685.

Mulholland JP, SW Nesbitt, RJ Trapp, KL Rasmussen, Salio PV (2018) Convective Storm Life Cycle and Environments near the Sierras de Córdoba, Argentina. *Mon. Wea. Rev.*, **146**, 2541–2557, https://doi.org/10.1175/MWR-D-18-0081.1.

Muza MN, Carvalho LMV, Jones C, Liebmann B. (2009) Intraseasonal and interannual variability of extreme dry and wet events over southeastern South America and subtropical Atlantic during the austral summer. *J. Climate*, 22, 1682– 1699.

Newell RE (1963) Transfer through the tropopause and within the stratosphere, *Q. J. R. Meteorol. Soc.*, **89**(380), 167–204.

NOAA Climate Prediction Center (2017) AAO, MEI, QBO, solar flux, TSA. https://www.esrl.noaa.gov/psd/data/climateindices/list/

North GR, Bell TL, Cahalan RF, Moeng FJ (1982) Sampling Errors in the Estimation of Empirical Orthogonal Functions. *Mon. Wea. Rev.*, 110, 699–706, https://doi.org/10.1175/1520-0493(1982)110<0699:SEITEO>2.0.CO;2.

Nogues-Paegle J, Byerle LA, Mo KC (2000) Intraseasonal modulation of South American summer precipitation. *Mon. Wea. Rev.*, 128, 837–850.

Perliski LM, Solomon S, London J (1989) On the interpretation of seasonal variations of stratospheric ozone, *Planetary and Space Science*, Volume 37, Issue 12, pp. 1527-1538.

Pittman JV, Pan LL, Wei JC, Irion FW, Liu X, Maddy ES, Barnet CD, Chance K, Gao RS (2009) Evaluation of AIRS, IASI, and OMI ozone profile retrievals in the extratropical tropopause region using in situ aircraft measurements. *J. Geophys. Res.*, 114, D24109, doi:10.1029/2009JD012493.

Plumb RA (2002) Stratospheric transport. *J. Meteorol. Soc.* Jpn., 80, 793–809. doi:10.2151/jmsj.80.793.

Poulida O, Dickerson RR, Heymsfield A (1996), Stratosphere-troposphere exchange in a midlatitude mesoscale convective complex, *J. Geophys. Res.*, **101**(D3), 6823–6836.

Randel WJ, (1992) Global atmospheric circulation statistics, 1000-1 mb, *NCAR Tech. Note, NCAR/TN-366+STR*, 256 pp. Natl. Cent. for Atmos. Res., Boulder, Colo.

Randel WJ, Garcia RR, Calvo N, Marsh D (2009) ENSO influence on zonal mean temperature and ozone in the tropical lower stratosphere. *Geophys. Res. Lett.*, 36, L15822, doi:10.1029/2009GL039343.

Randel W, Wu F, Stolarski R (2002) Changes in Column Ozone Correlated with the Stratospheric EP Flux. *Journal of the Meteorological Society of Japan.* 80. 849-862. 10.2151/jmsj.80.849.

Rashid HA, Simmonds I (2004) Eddy–zonal flow interactions associated with the Southern Hemisphere annular mode: Results from NCEP–DOE reanalysis and a quasi-linear model. *J. Atmos. Sci.,* 61, 873–888.

Rasmussen KL, Chaplin MM, Zuluaga MD, Houze RA (2016) Contribution of Extreme Convective Storms to Rainfall in South America. *J. Hydrometeor.*, **17**, 353–367, https://doi.org/10.1175/JHM-D-15-0067.1.

Rasmussen KL, Houze RA (2016) Convective Initiation near the Andes in Subtropical South America. *Mon. Wea. Rev.*, **144**, 2351–2374, https://doi.org/10.1175/MWR-D-15-0058.1.

Rasmussen, KL, Zuluaga MD, Houze Jr. RA (2014) Severe convection and lightning in subtropical South America, Geophys. Res. Lett., 41, 7359–7366, doi: 10.1002/2014GL061767.

Rienecker MM, Suarez MJ, Gelaro R, Todling R, Bacmeister J, Liu E, Bosilovich MG, Schubert SD, Takacs L, Kim GK, Bloom S, (2011) MERRA: NASA's modern-era retrospective analysis for research and applications. *J. of climate*, 24(14), pp.3624-3648.

Rodrigues RR, Woollings T (2017) Impact of Atmospheric Blocking on South America in Austral Summer. *J. Climate,* 30, 1821–1837, https://doi.org/10.1175/JCLI-D-16-0493.1

Salinger MJ, Renwick JA, Mullan AB (2001) Interdecadal Pacific Oscillation and South Pacific climate. *Int. J. Climatol.,* 21: 1705–1721. doi:10.1002/joc.691.

Salio P, Nicolini M, Zipser, EJ (2007) Mesoscale convective systems over southeastern South America and their relationship with the South American low-level jet. *Monthly Weather Review*, 135(4), 1290–1309. https://doi.org/10.1175/MWR3305.1.

Schoeberl MR, et al. (2008) QBO and annual cycle variations in tropical lower stratosphere trace gases from HALOE and Aura MLS observations. *J. Geophys. Res.*, 113, D05301, doi:10.1029/2007JD008678.

Schoeberl MR, Dessler A, Wang T (2012) Simulation of stratospheric water vapor and trends using three reanalyses, Atmos. Chem. Phys., 12, 6475-6487, doi:10.5194/acp-12-6475-2012.

Silva AE, Carvalho LMV (2007) Large-scale index for South America monsoon (LISAM), Atmos Sci Lett 8:51–57.

Solomon S. (1988), The mystery of the Antarctic Ozone "Hole", *Rev. Geophys.*, 26(1), 131–148, doi:10.1029/RG026i001p00131.

Taguchi M, Hartmann DL (2006) Increased Occurrence of Stratospheric Sudden Warmings during El Niño as Simulated by WACCM., 19, 324–3.

Tang, X, Madronich S, Wallington T, Calamari D (1998) Changes in tropospheric composition and air quality, J. Photochem. Photobiol. B, 46, 83-95.

Tang Q, Prather MJ, Hsu J (2011) Stratosphere-troposphere exchange ozone flux related to deep convection, *Geophys. Res. Lett.*, 38, L03806, doi:10.1029/2010GL046039.

Tedeschi RG, Cavalcanti IFA, Grimm AM (2013) Influences of two types of ENSO on South American precipitation. *Int. J. Climatol* 33: 1382−1400.

Tedeschi RG, Grimm AM, Cavalcanti IFA (2015) Influence of Central and East ENSO on extreme events of precipitation in South America during austral spring and summer. *Int. J. Climatol* 35: 2045−2064.

Thompson DWJ, Wallace JM (2000) Annual modes in the extratropical circulation, Part I: month-to-month variability. *J. Clim.,* 13, 1000–1016.

Trenberth KE, Caron JM, Stepaniak DP, Worley S (2002) Evolution of El Niño–Southern Oscillation and global atmospheric surface temperatures. *J. Geophys. Res.,* 107(D8), doi:10.1029/2000JD000298.

Vallis GK, Gerber EP, Kushner PJ, Cash BA (2004) A mechanism and simple dynamical model of the North Atlantic Oscillation and annular modes. J. Atmos. Sci., 61, 264–280.

Vera C, Silvestri G, Barros V Carril A (2004) Differences in El Niño response over the southern hemisphere. *Journal of climate*, *17*(9), pp.1741-1753.

Vera C, et al. (2006) Toward a unified view of the American monsoon systems. *J. Clim* 19:4977–5000.

Wargan K, Labow GJ, Frith SM, Pawson S, Livesey NJ, Partyka GS, (2017) Evaluation of the Ozone Fields in NASA's MERRA-2 Reanalysis. *J. Clim*, 30, 2961–2988. DOI:10.1175/JCLI-D-16-0699.1.

Weare, BC (2010) "Tropospheric-stratospheric wave propagation during El Niño-Southern Oscillation." *Journal of Geophysical Research: Atmospheres* 115.D18 (2010).

Wilks DS (2011) Statistical methods in the atmospheric sciences. Vol. 100. Academic Press: San Diego, CA

WMO, Scientific Assessment of Ozone Depletion (1995), WMO 37, Geneva, Switzerland

WMO (2011) Scientific Assessment of Ozone Depletion: 2010 Global Ozone Research and Monitoring Project-Report No. 52, 516 pp., Geneva, Switzerland.

WMO (2014) Scientific Assessment of Ozone Depletion: 2014 Global Ozone Research and Monitoring Project Report, World Meteorological Organization, p. 416, Geneva, Switzerland, 2014.

Wolter K, Timlin MS, (1993) Monitoring ENSO in COADS with a seasonally adjusted principal component index. Proc. of the 17th Climate Diagnostics Workshop, Norman, OK, NOAA/NMC/CAC, NSSL, Oklahoma Clim. Survey, CIMMS and the School of Meteor., Univ. of Oklahoma, 52-57.

Wu Y, Polvani LM (2017) Recent Trends in Extreme Precipitation and Temperature over Southeastern South America: The Dominant Role of Stratospheric Ozone Depletion, *J. Climate*, 30, 6433-6441.

Zhang Y, Wallace JM, Battisti DS (1997) ENSO-like interdecadal variability: 1900–93. *J. Climate*, **10**, 1004–1020, doi:https://doi.org/10.1175/1520-0442(1997)010<1004:ELIV>2.0.CO;2.

Zhou JY, Lau KM (1998) Does a monsoon climate exist over South America? *J. Climate*, 11:1020–1040.

Zhou J, Lau KM (2001) Principal modes of interannual and decadal variability of summer rainfall over South America. *Int. J. Climatol.*, 21(13), 1623-1644.

Zilli MT, Carvalho LMV, Liebmann B, Silva Dias MA (2017) Comprehensive analysis of trends in extreme precipitation over southeasten coast of Brazil, *Int. J. Climatol.* **37**: 2269–2279.

Zipser EJ, Cecil DJ, Liu C, Nesbitt SW, Yorty DP (2006) Where are the most intense thunderstorms on Earth. Bull. *Am. Meteorol. Soc.*, 87, 1057–1071.

Chapter 2:

The Combined Influence of ENSO and PDO on the Spring Upper Troposphere -Lower Stratosphere Ozone Variability in South America

Brandi L. Gamelin[1], Leila M. V. Carvalho[1,2], and Mary Kayano[3]

[1]Department of Geography, University of California, Santa Barbara

[2]Earth Research Institute, University of California, Santa Barbara

[3]Instituto Nacional de Pesquisas Espaciais, Centro de Previsão de Tempo e Estudos Climáticos, São José dos Campos, Brazil

2.1 Abstract

Ozone in the upper troposphere-lower stratosphere (UTLS) is primarily regulated by tropospheric dynamics. Understanding mechanisms driving ozone variability at the UTLS is crucial to evaluate the transport of mass to and from the lower stratosphere. The El Niño-Southern Oscillation (ENSO) is the primary coupled mode acting on interannual timescales modulating tropospheric circulation worldwide. The effects of the ENSO teleconnection depend on the phases of the Pacific Decadal Oscillation (PDO) and on the characteristics of the warming over central and eastern tropical Pacific. This study investigates the role of ENSO in the UTLS ozone variability with focus on South America (SA) and examines patterns of teleconnections in the two recent warm (1980-1997) and cool (1998-2012) PDO phases. The dominant mode of ozone variability is identified by applying a principal component analysis (PCA) to Modern-Era Retrospective analysis for Research and Applications, Version 2 (MERRA-2) ozone data from September-November (SON). SON is

the season with the largest UTLS ozone variance over SA. The first mode resembles a Rossby wave train across SA with spatial patterns that depend on phases of the PDO. We show that the ENSO teleconnection and respective influences on SON UTLS ozone are stronger during the cool PDO when ENSO and PDO are mostly in phase. Additionally, the strength of the ENSO teleconnection appears to depend on patterns of SST anomalies over tropical Pacific. The decadal variability in the ENSO-PDO relationships and teleconnections with the Southern Hemisphere resulted in a shift in upper tropospheric circulation in tropical and subtropical regions of SA.

2.2 Introduction

Ozone in the lower stratosphere is primarily regulated by cross tropopause exchanges associated with tropospheric circulation processes. In the stratosphere, ozone regulates the amount of ultraviolet radiation that reaches Earth's surface and is the primary driver of globally averaged stratospheric temperature trends (Steinbrecht et al. 2003; WMO Ozone Assessment 2010). Stratospheric ozone variability is related to three dynamical processes, (1) upwelling/downwelling associated with the Brewer Dobson Circulation (BDC) – the general stratospheric circulation pattern, (2) stratospheric zonal winds shift from easterlies to westerlies, and vice versa, associated with the Quasi-Biennial Oscillation (QBO), and (3) the exchange of air masses through the tropopause layer associated with tropospheric convective processes (Fueglistaler et al. 2009). The first process, the BDC a global circulation pattern driven by upwelling of air from the troposphere to the stratosphere in the tropics, and downwelling in the polar region (Brewer 1949; Butchart 2014).The second process, the QBO is characterized by oscillating shifts in zonal wind pattern in the tropical lower stratosphere

with an average period of 28 months (Baldwin et al 2001). The QBO can modulate the strength of the stratospheric polar jet that, in turn, affect tropospheric circulation (e.g., Holton and Tan 1980; Baldwin and Dunkerton 1998) and modulate the strength of the upwelling in the tropics related to BDC (Flury et al. 2013). Lastly, the third process relates to tropical and subtropical deep convective cloud processes, which are the primary vehicle for upper troposphere – lower stratosphere exchanges and the vertical transport of energy, moisture, momentum, and chemical constituents.

Exchanges of mass between the troposphere and stratosphere are reliant on local tropopause dynamics related to deep convection and extra-tropical tropopause folding (Brewer, 1949; Danielsen 1968; Holton et al. 1995). In the tropics, shallow moist convection is common, especially over the tropical oceans. However, vertical transport of gases from the troposphere to the stratosphere via deep convection is greater over land, especially in the subtropics where localized areas of precipitating deep convection can have a large impact on stratospheric ozone (Liu and Zipser 2005). During the austral spring and summer deep convective clouds associated with mesoscale convective systems (MCSs) in South America are capable of reaching the tropopause (Gettelman et al. 2002). These MCSs are strongly modulated by atmospheric variations on synoptic-to-interannual time scales (Ferreira et al. 2003; Zipser et al. 2006; Salio et al. 2007; Mulholland et al. 2018; Bruick et el. 2019).

A significant source of interannual variability on tropospheric circulation and precipitation in South America is the El Niño – Southern Oscillation (ENSO). ENSO originates in the tropics and strong teleconnections are also observed in the extratropics associated with Rossby wave propagation (e.g., Trenberth et al. 2002). Previous studies have shown that during the warm phase of ENSO (El Niño), precipitation is suppressed in northern

South America and enhanced in southeastern South America (Aceituno 1988; Marengo 1992; Ropelewski and Halpert 1987). ENSO is considered the primary driver of interannual precipitation variability in the La Plata basin (Berbery and Barros 2002; Tedeschi et al. 2013, 2015), a region in southeastern South America between ~20˚S – 35˚S known for some of the deepest and most intense convective storms in the world (Zipser et al. 2006; Rasmussen et al. 2014; Rasmussen and Houze 2016; Rasmussen et al. 2016). During the cold phase of ENSO (La Niña), precipitation anomalies are approximately opposite to those during El Niño (Grimm 2004).

In South America, the influence of ENSO varies throughout the austral spring and summer (Grimm 2003), and tropospheric circulation anomalies are often attributed to El Niño driven wave trains emerging from the South Pacific (e.g., Rodrigues and Woollings 2017). During an El Niño event, the anomalous rising motions over the eastern Pacific Ocean result in anomalous subsidence over the Amazon and anomalous Rossby wave activity propagating into South America via midlatitudes (Liebmann and Mechoso 2010). In the Southern Hemisphere (SH), a Rossby wave source is located in the upper troposphere, east of Australia along 30˚S. Rossby waves affecting South America are modulated by the strength and position of the subtropical jet (Carvalho et al. 2005; Ding et al. 2012).

While the Southern Hemisphere source of Rossby wave initiation related to El Niño is in the Pacific and Indian Oceans, Rossby wave breaking can occur in South America. Extra-tropical anticyclonic Rossby wave breaking (RWB) events are associated with cold fronts connected to strong surface low pressure areas as well as weak warm fronts (Martius and Rivière 2016). As planetary waves propagate across the Pacific Ocean (e.g., Karoly 1989; McIntosh and Hendon 2018), they encounter the Andes Mountains. Crossing the mountain

barrier, the wave trains are compressed on the windward slope and stretched on the leeward side of the mountain (Hoskins and Karoly 1981). The effect produces high pressure over the Andes and a pronounced trough on the lee side (Boffi 1949). On the lee side, as air moves towards the equator, it encounters northerly or easterly winds, and this change of wind sign and blocking action may cause the planetary "Rossby" waves to break. Frontal wave process reaching the South American subtropics and anticyclonic RBW can destabilize the atmosphere and initiate convection with significant impacts on vertical motion within deep convective processes and, consequently, on lower-stratospheric ozone (Martius and Rivière 2016).

Decadal variability of the Pacific Ocean sea surface temperature (SST) anomalies has been related to global teleconnections that influence climate worldwide (Trenberth and Hurrell, 1994; Mantua et al. 1997; Zhang et al. 1997). The Pacific Decadal Oscillation (PDO), defined by the leading mode of empirical orthogonal function (EOF) of the North Pacific sea surface temperature anomalies, is characterized by persistent pattern of warm (cool) SST anomalies in the North Pacific along with cool (warm) SST anomalies in the equatorial Pacific Ocean (Mantua et al. 1997; Mantua and Hare 2002). The PDO is considered a combination of physical and dynamical processes operating on distinct time scales that direct and indirectly affect global climate (Newman et al. 2016). The PDO during the 1980s and 1990s was described as an extended El Niño pattern, and while similarities exist between ENSO and PDO, their timescales are markedly different (Mantua and Hare 2002). Although the causes of PDO variability are not well understood, the effects of PDO are observed throughout the tropics and extratropics (Zhang and Delworth, 2015), and have

been found to modulate the influence of ENSO teleconnections (e.g, McCabe and Dettinger 1999; Yu and Zweirs 2007; Andreoli and Kayano 2005; Newman et al 2016).

The PDO has been associated with variations in ENSO teleconnections influencing South America's climate. For instance, Andreoli and Kayano (2005) analyzed El Niño related rainfall anomalies in South America during positive and negative PDO phases and found that rainfall anomalies are driven by PDO phases, with enhanced precipitation in November - December over southern Southeast South America during the positive (warm) PDO phase compared to the negative (cool) PDO phase. Furthermore, Kayano and Andreoli (2007) found a non-linear relationship between ENSO and rainfall extremes based on warm or cool PDO phases. Their results show a strong relationship between ENSO and rainfall when PDO and ENSO are in phase, and a weak relationship when out of phase.

Motivated by the importance of ENSO and PDO phases in modulating precipitation and circulation over tropical and subtropical South America, this study examines two main questions: does ENSO modulate the upper troposphere – lower stratosphere (UTLS) ozone patterns in South America? Do these relationships depend on the phase of the PDO? More specifically, this study investigates the influence of the PDO and ENSO variability on South America circulation and UTLS (i.e, 100 hPa) ozone patterns on interannual-to-multiannual timescales. Despite low ozone concentration at 100 hPa in the UTLS, ozone variability at this level plays an important role in regulating air temperatures which in turn regulates troposphere to stratosphere exchanges and stratospheric chemistry (Forster and Shine 2002). This variability is investigated to understand the influence of teleconnections originating in the Pacific Ocean. This is accomplished by examining spatial and temporal patterns of UTLS ozone using Modern-Era Retrospective analysis for Research and Applications, Version 2

(MERRA2) reanalysis data (Gelaro et al. 2017) during the austral spring (September – November, SON). Mechanisms explaining patterns of UTLS ozone SON anomalies and relationships between ENSO and PDO are further examined with focus on regions where ENSO teleconnections are strongest (Ropelewski and Halpert 1987; Grimm 2003; 2004; Gonzalez et al 2017; Bruick et al. 2019).

This chapter is organized as follows. The data and methods are presented in section 2.3 Austral Spring Ozone Patterns (1980 – 2012) are presented in 2.4. South America UTLS ozone variability and El Niño are examined in section 2.5. ENSO Driven Circulation Patterns over the Amazon and Southern La Plata Basins are presented in section 2.6. Conclusions are presented in section 2.7.

2.3 Data and Methods

Conducting long-term analysis of stratospheric ozone in South America with in-situ data is not possible. Data for the Upper Troposphere-Lower Stratosphere (UTLS) region is limited to locations with radiosonde/ozonesonde data collection sites, often only available one or two times per day and below 100 hPa, and rarely available with ozone data. For this work, reanalysis data is useful in extending the spatial and temporal range for analysis. The 100 hPa pressure level is generally associated with the tropical lowermost stratosphere and is utilized to investigate UTLS ozone and temperature variability related to tropospheric processes. Changes to ozone and temperature in the UTLS have implications for BDC circulation and upwelling (Randel et al. 2006).

This study investigates stratospheric ozone variability using MERRA-2 reanalysis data (Gelaro et al. 2017). MERRA-2 is produced with version 5.12.4 of the GEOS

atmospheric data assimilation system, and is available from 1980 – present with a spatial resolution of 0.5° latitude x 0.625° longitude at 42 pressure levels from 1000 to 0.01 hPa. To examine tropospheric mechanisms driving UTLS ozone patterns, monthly MERRA2 zonal winds, vertical pressure velocity (ω; hereafter also known as vertical velocity), potential temperature, and geopotential height from 1980 – 2012 are utilized. The 1980 – 2012 time frame represents the recent warm PDO (1980 – 1997) and cool PDO (1998- 2012).

The treatment of ozone data in MERRA2 represents advancements over the original MERRA data set, providing a good representation of the variably of stratospheric ozone (Wargan et al. 2017). The MERRA-2 assimilated ozone record has two distinct time periods: the Solar Backscatter Ultraviolet Radiometer (SBUV) period (January 1980–September 2004) and the NASA's EOS Aura satellite (Aura) period (from October 2004 to present). The SBUV instruments were onboard the NASA and NOAA satellites, and the Ozone Mixing Ratio (OMI) and Microwave Limb Sounder (MLS) instruments are currently on board the Aura satellite. According to Wargan et al (2017), MERRA-2 reproduces the interannual to weekly variability of the UTLS ozone as well as the sharp gradient of ozone concentrations across the tropopause. However, discontinuities can be present and may result in artificial trends. Therefore, to minimize this problem, this study utilizes MERRA2 ozone for long-term climatological studies at individual pressure levels after removing long-term trends.

The main modes of stratospheric ozone variability are obtained by applying Empirical Orthogonal Function (EOF) analysis (Fukuoka 1951; Lorenz 1956), otherwise known as Principal Component Analysis (PCA). The PCA is applied to detrended spring averaged ozone anomalies at 100 hPa to determine the main patterns of ozone variability. To ensure equal gridded areas for analysis, the square root of the cosine of latitude is applied (Ding et

al. 2012). The North et al. (1982) rule is applied to determine independent PCs by calculating a sampling interval for each eigenvalue. For the purposes of this work, an eigenvalue is considered independent when the confidence intervals associated with each eigenvalue do not overlap. Only independent modes are included in the analyses. The Principal Component (PC) time-coefficients are correlated to detrended ozone data (mean seasonal ozone anomalies) to obtain the spatial pattern for each mode.

The focus of this study is on the Austral spring (September-November, SON) because this season is associated with the largest UTLS ozone variance over South America (Fig 1). When comparing seasonally averaged standard deviation during seasons with the strongest convectively driven processes (spring, summer and fall), the largest variability occurs during spring in the tropical and extra-tropical regions between 20 – 40˚ S, especially over southeast South America (Fig. 1). To avoid the influence of springtime Antarctic ozone variability, the PCA is applied from 15˚N to 40˚S and from 90˚W to 30˚W.

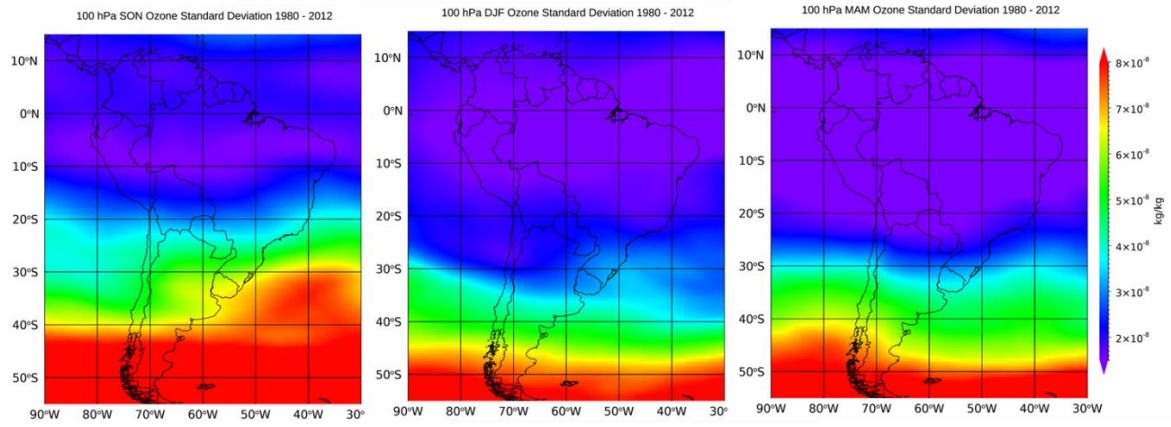

Fig. 1 1980 – 2012 standard deviation of 100 hPa MERRA2 ozone mixing ratio. September – November (left), December – February (center), and March – May (right).

To evaluate the combined influence of ENSO and PDO on the interannual to multiannual variability of UTLS ozone, this study uses the multivariate ENSO index (MEI) (Wolter and Timlin, 1993) and PDO index (Zhang et al. 1997; Mantua et al. 1997) averaged during SON. Only the last two PDO phases 1980 – 1997 (warm PDO) and 1998 – 2012 (cool PDO) that coincide with available MERRA-2 data are investigated in this study.

2.4 Austral Spring Ozone Patterns in South America (1980 – 2012)

Figure 2 shows the results of the PCA applied to MERRA2 100 hPa ozone data from 1980 – 2012 with a domain centered over South America. The first mode (PC1) explains 27.66% of the total variance and is statistically independent based on the North et al. (1982) rule (Fig. 2). The second mode explains 18.34% of the variance and is also statistically independent according to North et al. (1982). However, the second mode is not significantly correlated to PDO or MEI and for this reason, will not be discussed in this study.

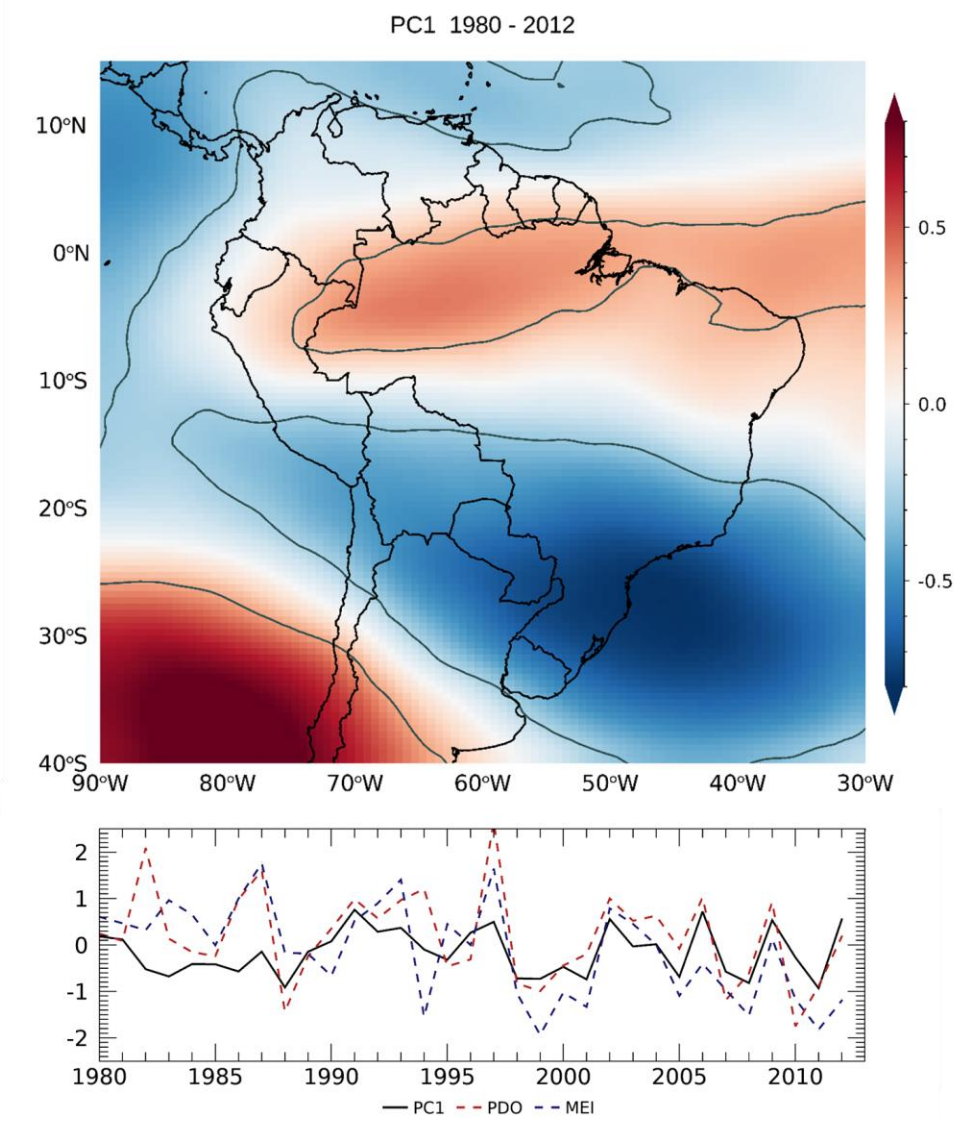

Fig. 2 PC-1 of spring (SON) averaged detrended MERRA2 ozone anomalies at 100 hPa from 1980 – 2012. PC1 time coefficients are correlated to SON averaged ozone anomalies. Colors indicate the magnitude of the correlation between the principal component and ozone anomalies. Solid grey lines indicate statistically significant correlations on a 5% significance level. Time series of SON averaged MEI index and PDO index (graph left side y-axis), and PC1 time coefficients (graph right side y-axis) are illustrated on the line graph.

PC1 exhibits a clear tri-pole feature in ozone anomalies, suggesting relationships with Rossby wave trains (Fig. 2). Spatial patterns generally associated with a Rossby wave trains often exhibit a sequence of alternating anomalies which correspond to alternating surface ridges and troughs (Hoskins and Karoly 1981). This alternating pattern is shown in the tripole

feature of ozone anomalies. When the PC1 time coefficients are positive (negative), ozone at 100 hPa decreases (increases) in central and southeast South America. This region has known relationships between precipitation extremes and ENSO (Ropelewski and Halpert 1987; Trenberth et al. 1998; Marengo 1992; Aceituno 1988; Grimm et al 2000). In contrast, over Northern Amazon region, when PC1 is positive (negative), ozone increases (decreases). This region also exhibits strong teleconnections with ENSO (Trenberth et al 1998). Ozone also increases (decreases) over southern Argentina and Southeastern Pacific Ocean when PC1 is positive (negative).

Although PDO is a decadal coupled mode of variability, the oscillation also exhibits interannual variability within each phase (Fig. 2). Correlations between SON averaged PDO and SON averaged MEI indicate that during the warm PDO the linear relationship between the two modes is weak and not statistically significant (r=0.386); however, during the cool PDO the linear correlation increases and is statistically significant on a 1% level (r=0.764), indicating that both modes were mostly in phase on interannual time scales. Additionally, linear correlations (r) between PC1 and MEI (r = 0.58), and PC1 and PDO (r = 0.45) from 1980 – 2012 are positive and statistically significant (5% significance level).

Interestingly, correlations between PC1, MEI and PDO appear to vary depending on PDO phase. During the warm PDO phase (1980-1997) the correlation between PC1 and PDO (MEI) is 0.18 (0.40) and not statistically significant, while during the cool PDO phase (1998-2012) the correlation between PC1 and PDO (MEI) increases to 0.72 (0.77) and is significant at 1% level. The relationships between PC1 and MEI during both PDO phases are illustrated with scatterplots (Fig. 3), and show a strong (weak) positive correlation between MEI and

PC1 is during the cool (warm) PDO. To further understand these differences, global upper tropospheric circulation is investigated during both PDO phases separately.

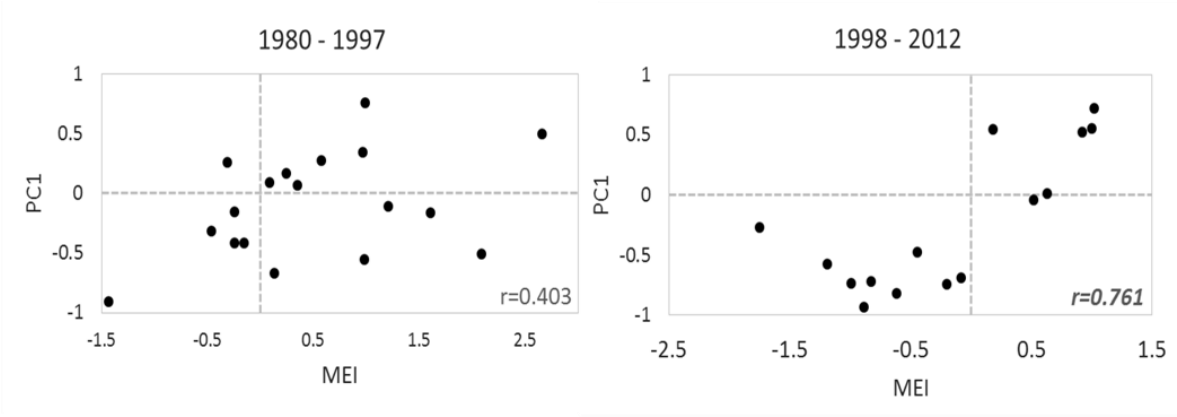

Fig. 3 MEI index correlated to PC1 from 1980 – 1997 (warm PDO phase, left) and from 1998 – 2012 (cool PDO phase, right). Correlation (r) values are in the lower right corner, bold and italicized are statistically significant correlations on 1% significance level.

2.4.1 PC1, PDO and Global UTLS

In the Southern Hemisphere, Rossby wave variability is regulated by the strength and position of the tropospheric jet stream (Carvalho et al. 2005; Ding et al. 2012). Jet stream position has been shown to have a direct influence on midlatitude cyclogenesis (Holton, 2004) which in turn can also influence UTLS thermodynamics. Temperature variability in the UTLS, specifically cold point temperature and cold point potential temperature, has also been shown to decrease during convective events related to heating in the lower troposphere and higher geopotential heights aloft (Sherwood et al. 2003). To understand these processes related to UTLS ozone patterns in South America we begin our investigation by globally assessing the linear relationships between PC1 and relevant upper troposphere variables: 200 hPa geopotential height anomalies (h200), 100 hPa potential temperature anomalies (θ100),

and 100 hPa ozone anomalies ($O_3$100). PC1 is correlated to each variable separately during both the warm and cool PDO phases (Fig. 4).

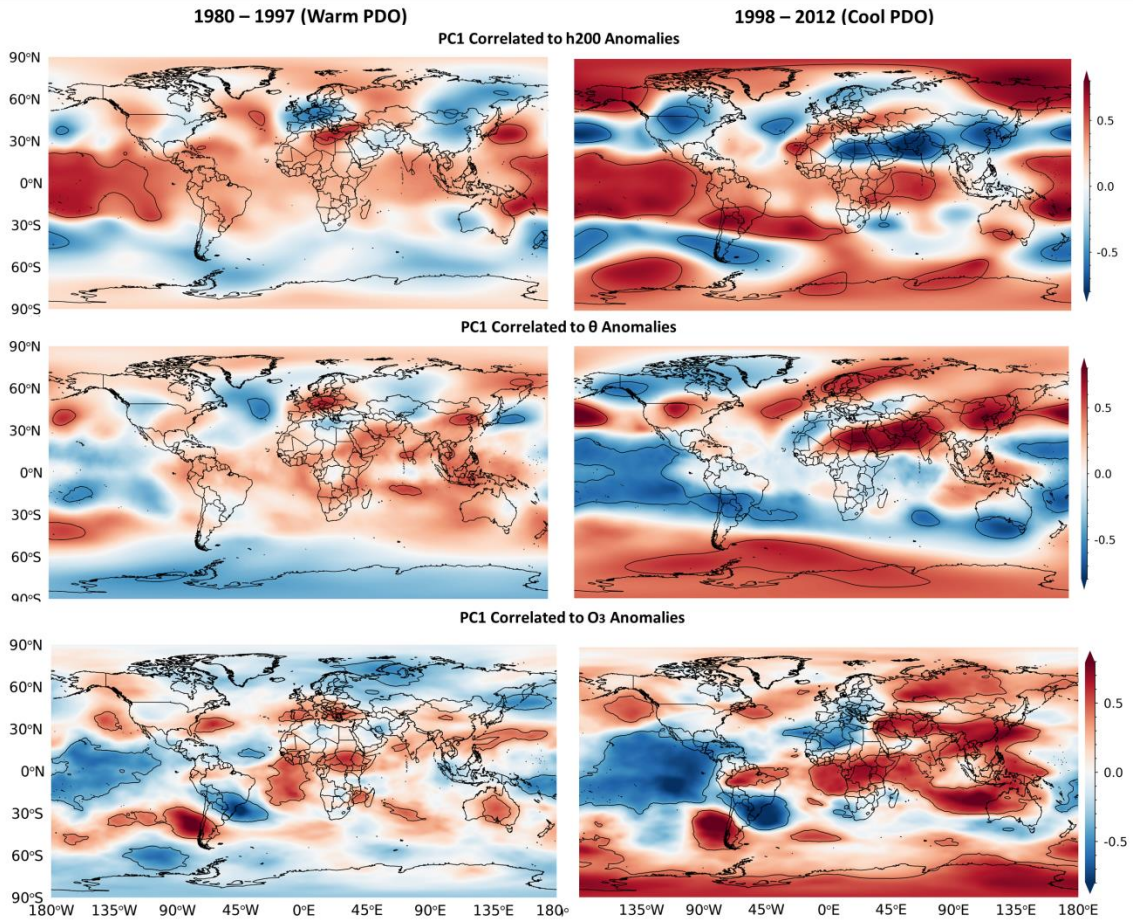

Fig. 4 Linear correlation (Pearson coefficient) between PC1 and: (top row) 200 hPa geopotential height anomalies; (middle row) 100 hPa potential temperature anomalies; (bottom row) 100 hPa detrended ozone anomalies. The warm PDO phase (1980 – 1997) is in the left column and the cool PDO phase (1998 – 2012) is in the right column. Solid lines in the bottom row indicate statistically significant correlations on a 5% level.

Patterns of correlations indicate that the influence of Rossby wave activity related to PC1 is more prominent during the cool PDO phase compared to the warm phase (Fig. 4). During the warm PDO, the correlations between PC1 and h200 anomalies are relatively weak in both hemispheres, with few statistically significant regions with positive correlations over

tropical Pacific Ocean (Fig. 4, top). On the other hand, during the cool PDO we observe much stronger linear correlations between PC1 and h200 anomalies. In the tropics and in the cool PDO phase, correlations with geopotential height anomalies are strong and suggest a Rossby wave train pattern in the Southern Hemisphere originating in the equatorial Pacific Ocean that resembles the Pacific South America teleconnection Pattern (PSA) (Mo and Paegle 2001; Irving and Simmonds 2016) . Typically during SON, an El Niño induced Rossby wave train will propagate poleward toward the West Antarctic coast and Amundsen Sea, and then be reflected equatorward toward South America (Ding et al. 2012). This pattern strongly resembles PC1 during the cool PDO, which is notably absent during the warm PDO. Moreover, patterns of correlation in subtropical and extratropical latitudes of the Northern Hemisphere during the cool PDO phase resemble the Pacific North American Pattern (PNA) (Straus and Shukla, 2002).

To investigate the global relationship between PC1 and UTLS temperatures, we correlated PC1 to θ100 anomalies (Fig. 4, middle). Again, during the warm phase the PDO teleconnection is weak and the few statistically significant correlations are found primarily in the extra-tropical oceans. However, during the cool phase, a strong equatorial Pacific Ocean signal is present indicating that when PC1 increases, potential temperature anomalies at 100 hPa throughout the tropical Pacific Ocean decreases. The pattern of decreasing potential temperature extends through subtropical South America and western South Atlantic Ocean. Another region showing significant linear relationships between PC1 and θ100 is observed at high latitudes of the Southern Pacific and Atlantic Oceans. The strong and statistically significant correlations between PC1 and θ100 during the cool PDO phase clearly contrast with the weak correlations during the warm phase (Fig. 4 middle).

To evaluate the relationships between PC1 and global ozone at 100 hPa we correlated PC1 to global $O_3$100 anomalies during warm and cool PDO (Fig. 4, bottom). The patterns in South America are similar to patterns shown in Figure 3. During the warm PDO most statistically significant linear relationships between PC1 and ozone at 100 hPa are observed over the Equatorial Pacific, Equatorial Atlantic, Europe and western Antarctica near the Antarctic Peninsula. Different pattern of correlations emerge during the cool PDO phase. Strong negative correlations are observed over the equatorial and tropical Pacific, extending towards subtropical South America, while positive correlations are observed throughout the Eastern Hemisphere around Antarctica. Additionally, the dipole observed in Figure 3 is more pronounced. During the cool PDO, PC1 ozone patterns at this level appear directly related to θ100 patterns of anomaly, especially in the tropics and midlatitudes.

A plausible explanation for the enhanced ENSO teleconnection and stronger association with the PSA during the cool PDO is the fact that ENSO and PDO appear typically in phase (positively correlated) during SON during this phase. These results are consistent with Yu and Zweirs (2007) who showed observational and numerical evidence that the ENSO-PNA pattern and respective teleconnections with precipitation and circulation in the Northern Hemisphere are much stronger when PDO and ENSO are in phase. They also showed indication that similar teleconnection mechanisms are enhanced in the Southern Hemisphere. Our results indicate that these teleconnection mechanisms are observed during the Austral spring and are likely stronger during the cool PDO phase. More importantly, these teleconnections appear crucial in modulating UTLS interannual ozone variability during SON.

During the cool PDO phase, subtropical South America is an area of specific interest. This area coincides with statistically significant linear relationships between PC1 and h200, θ100 and $O_3$100 anomalies. In this region, when PC1 is positive, h200 anomalies increase, while θ100 anomalies and $O_3$100 anomalies decrease. In other words, PC1 indicates that high geopotential heights aloft are associated with lower 100 hPa potential temperatures and lower 100 hPa ozone concentrations. These relationships are examined further to understand the influence of ENSO on these interactions and the dependence on PDO phases.

2.4.2 PC1, ENSO and PDO

In South America the ENSO teleconnection has been shown to strengthen and shift the subtropical jet poleward during El Niño events (e.g. Grimm 2003). In addition, ENSO influences the strength and exit of the South America low level jet east of the Andes (e.g. Ferreira et al. 2003; Montini et al. 2019), modifying the transport of heat and moisture from the tropics to the subtropics of South America (Fernandes and Rodrigues 2018; Montini et al. 2019). These changes in circulation alter the strength and location of deep convection (Bruick et al. 2019) and precipitation anomalies over the Amazon, subtropical and southeast South America (e.g., Ropelewski and Halpert 1987). Thus, ENSO teleconnections strongly impact atmospheric dynamics over South America and these teleconnections may be influenced by PDO phases (Andreoli and Kayano, 2005; Kayano and Andreoli, 2007; Fernandes and Rodrigues, 2018).

El Niño and La Niña 1980 - 2012						
ENSO	Warm PDO Phase			Cool PDO Phase		
El Niño	1982	1986	1987	2002	2004	2006
	1991	1994	1997	2009		
La Niña	1985	1988		1998	1999	2007
				2008	2010	2011

Table 1. El Niño and La Niña years utilized for composites and analyses.

To investigate mechanisms explaining these relationships we examine composites of 200 hPa zonal wind (u200) anomalies and h200 anomalies during El Niño years when SON averaged MEI is greater than or equal to 0.5 (Table 1), and positive PC1 years, where the PC1 time coefficient (Fig. 2) is greater than or equal to 0.10 (Table 2).

PCA 1980 – 2012						
PC1	Warm PDO Phase			Cool PDO Phase		
Positive	1980	1992	1991	2002	2006	2009
	1991	1993	1996	2012		
	1997					
Negative	1982	1983	1984	1998	1999	2000
	1985	1986	1987	2001	2005	2007
	1988	1989	1994	2008	2010	2011
	1995					

Table 2. Positive and negative PC1 years utilized for composites and analyses.

a) Global upper tropospheric circulation and ENSO

The objective of this section is to examine the mean characteristics of 200 hPa zonal wind anomalies during ENSO events and how they compare to PC1 years for warm and cool PDO phases. With composites (Fig. 5), we investigate 10 El Niño events (SON averaged

MEI ≥ 0.5) and 7 La Niña events (SON averaged MEI ≤ -0.5). The PC1 composites include 10 positive PC1 (PC1 time coefficient ≥ 0.10) and 18 negative PC1 cases (PC1 ≤ –0.10). Each PDO phase is investigated separately for ENSO years and PC1 years. Table 1 shows El Niño and La Niña years and Table 2 shows positive and negative PC1 years during each PDO phase that were used in these composites.

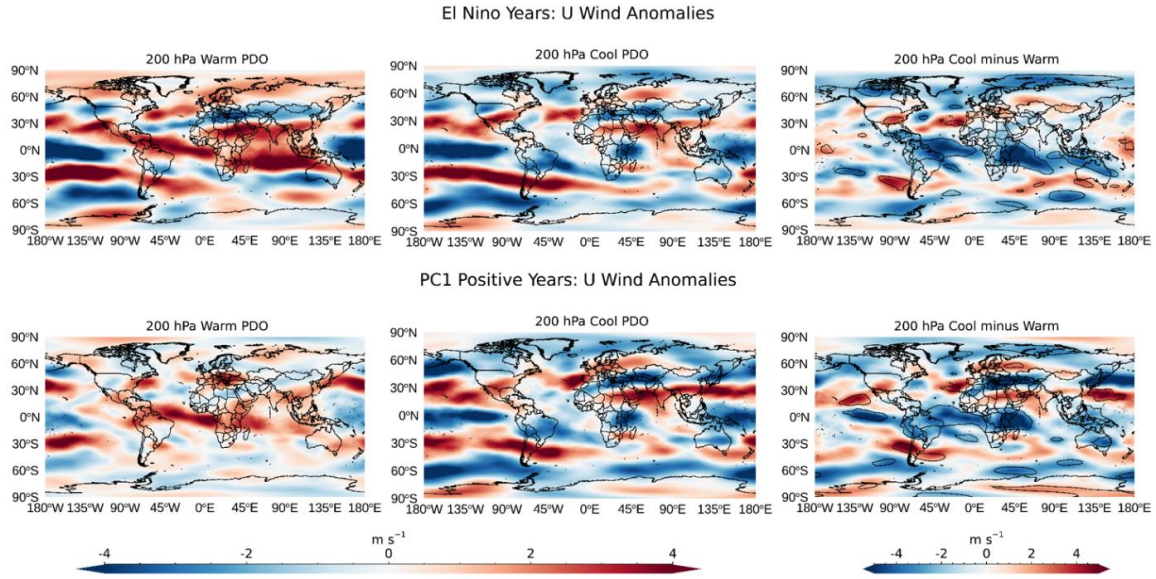

Fig. 5 200 hPa zonal (u) wind anomaly composites for El Niño years (top row) and positive PC1 (bottom row). Left column is for the warm PDO phase (1980 – 1997), the middle column is for the cool PDO phase (1998 – 2012), and the right column is the difference between PDO phases (cool minus warm). Solid lines in the difference maps indicates statistical significance of the difference between PDO phases on a 5% significance level. It should be noted that the color bar for the difference maps are not the same as the composites.

An enhanced subtropical jet is expected in South America during El Niño events (Grimm et al., 2000). Thus, when comparing El Niño composites of u200 anomalies during the warm and cool PDO phase in South America, enhanced westerly winds in the subtropics are observed in both PDO phases. When comparing separate warm and cool PDO phases, stronger positive wind anomalies occur during the cool PDO over the Pacific Ocean, approaching the Andes Mountain range between 30˚ – 40˚ (Fig. 5, top row). However,

during the warm PDO, the largest differences are characterized by strong positive anomalies in northern South America. At this level, zonal winds in northern South America are generally weak. Over most of the Amazon, SON averaged u200 winds are westerlies, and at the same latitude on the western flank of the Andes Mountain range, SON averaged u200 winds are easterlies (not shown). Throughout most of the Amazon and Northeast Brazil the winds in the El Niño composites are stronger during the warm PDO phase.

The positive PC1 u200 composites in Figure 5 (bottom row) illustrate larger differences between the warm and cool PDO phases compared to the El Niño composites. During the warm PDO, weak anomalies are observed across South America, and the only similarity between the warm PDO El Niño and PC1 patterns is observed in the equatorial Atlantic Ocean and northern South America. During the cool PDO, the patterns of anomalies are very similar to the El Niño composites, with a stronger subtropical jet crossing the Andes at 30˚S in Northern Argentina.

b) Upper level circulation: El Niño vs. La Niña

Previous studies have shown that anomalies related to the ENSO teleconnection are generally opposite when comparing El Niño and La Niña events (e.g. Grimm 2004; Grimm and Tedeschi 2009). For this work, as expected, the La Niña composites of anomalies generally show opposite patterns as compared to the El Niño patterns, which is consistent with the Negative PC1 composites as compared to the Positive PC1 composites. Figure 6 illustrates this with composites of u200 anomalies during La Niña and Negative PC1. In South America during the warm PDO phase, the wind anomalies are weaker in the La Niña and Negative PC1 composites than in the El Niño and Positive PC1 composites. Locations of

note are over equatorial South America, Atlantic ITCZ and equatorial Africa where the anomalies are not opposite between El Niño/Positive PC1 and La Niña/Negative PC1, although weaker during La Nina. These areas show the largest differences between warm and cold PDO composites, with anomalous westerlies during the warm PDO and easterlies during the cold PDO (Figs 5 and 6). In South America, during the Cool PDO phase, the subtropical jet is weaker and shifted equatorward during La Niña and Negative PC1. When comparing the position and strength of the u200 anomalies between PDO phases, westerlies are stronger from 20˚N – 25˚S during cool PDO, and weaker from 35˚ - 45˚S during the warm PDO (Fig. 6).

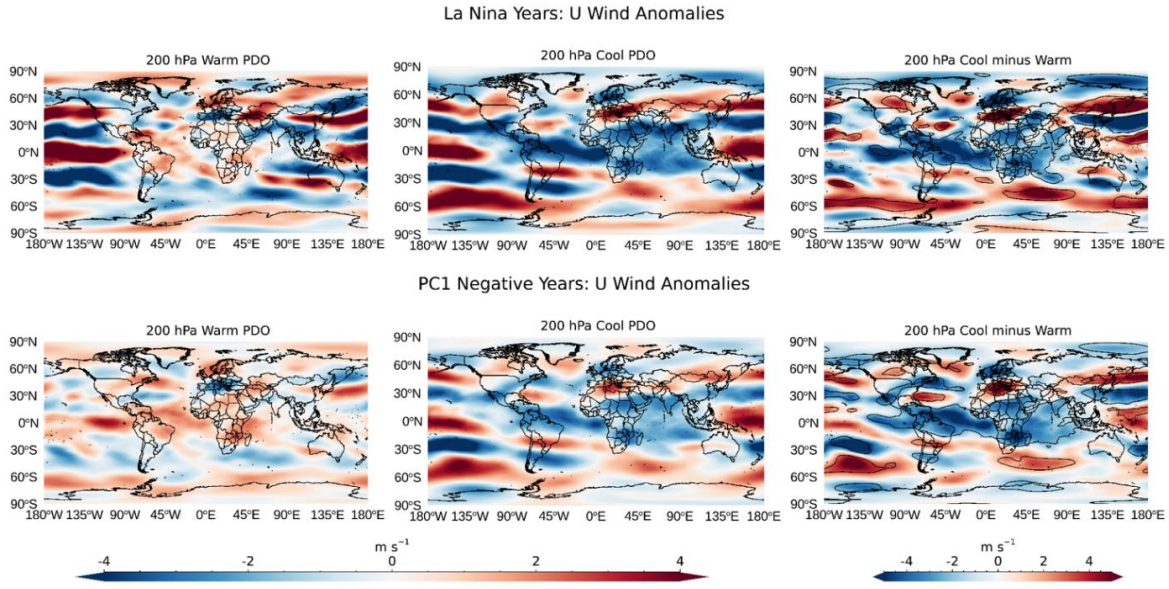

Fig. 6 Same as Fig. 5 except for La Niña years (top row) and negative PC1 years (bottom row).

Zonally averaged composites of upper level winds in South America further explain the inverse patterns related to ENSO, PC1 and jet stream variability between PDO phases. Composites of El Niño/La Niña and positive/negative PC1 and zonally averaged u200 wind anomalies (62˚W – 54˚W) from 5˚N – 40˚S illustrate the shift in the subtropical jet during

PDO phases (Fig. 7). Outside of the equatorial region, El Niño composites have few differences between the warm and cool PDO phases, and the differences are also similar for the La Niña anomalies (Fig. 7, top two panels). The statistically significant differences between warm and cool PDO phases are found in the equatorial upper level winds. It should be noted that tropical stratospheric zonal wind variability is strongly tied to QBO, where zonal wind patterns shift every ~ 28 months and maximizes at approximately 40 hPa (Baldwin and Dunkerton 1998; Baldwin et al. 2001). We also find that during SON El Niño events the subtropical jet over South America is shifted poleward (consistent with Grimm et al. 2003) with stronger winds during the cool PDO phase compared to the warm phase.

During the cool PDO phase, the Positive PC1 composites are similar to the El Niño composites, except where the core of the westerly anomalies in the subtropical jet is enhanced and shifted upward from ~ 250 hPa to ~ 200 hPa (Fig. 7). During this time frame the surface easterlies between $0^{\circ} - 6^{\circ}S$ are enhanced (not shown). The enhanced low level flow east of the Andes during the cool PDO phase over the tropics coincides with SON heat and moisture transport to the subtropics via the South American Low Level Jet during El Niño events (Montini et al. 2019). The negative PC1 composites show the opposite pattern during the cool PDO phase. Similar to the La Niña patterns, the subtropical jet is shifted equatorward (Grimm 2003), and located in the transition between the tropics and subtropics (Fig. 7, lower panel). Upper level winds in the equatorial region are quite consistent when comparing the composites between warm and cool PDO phases. The warm PDO phase illustrates positive upper troposphere wind anomalies, which are stronger in the El Niño/Positive PC1 composites compared to the La Niña/Negative PC1 composites, and negative anomalies during the cool PDO phase.

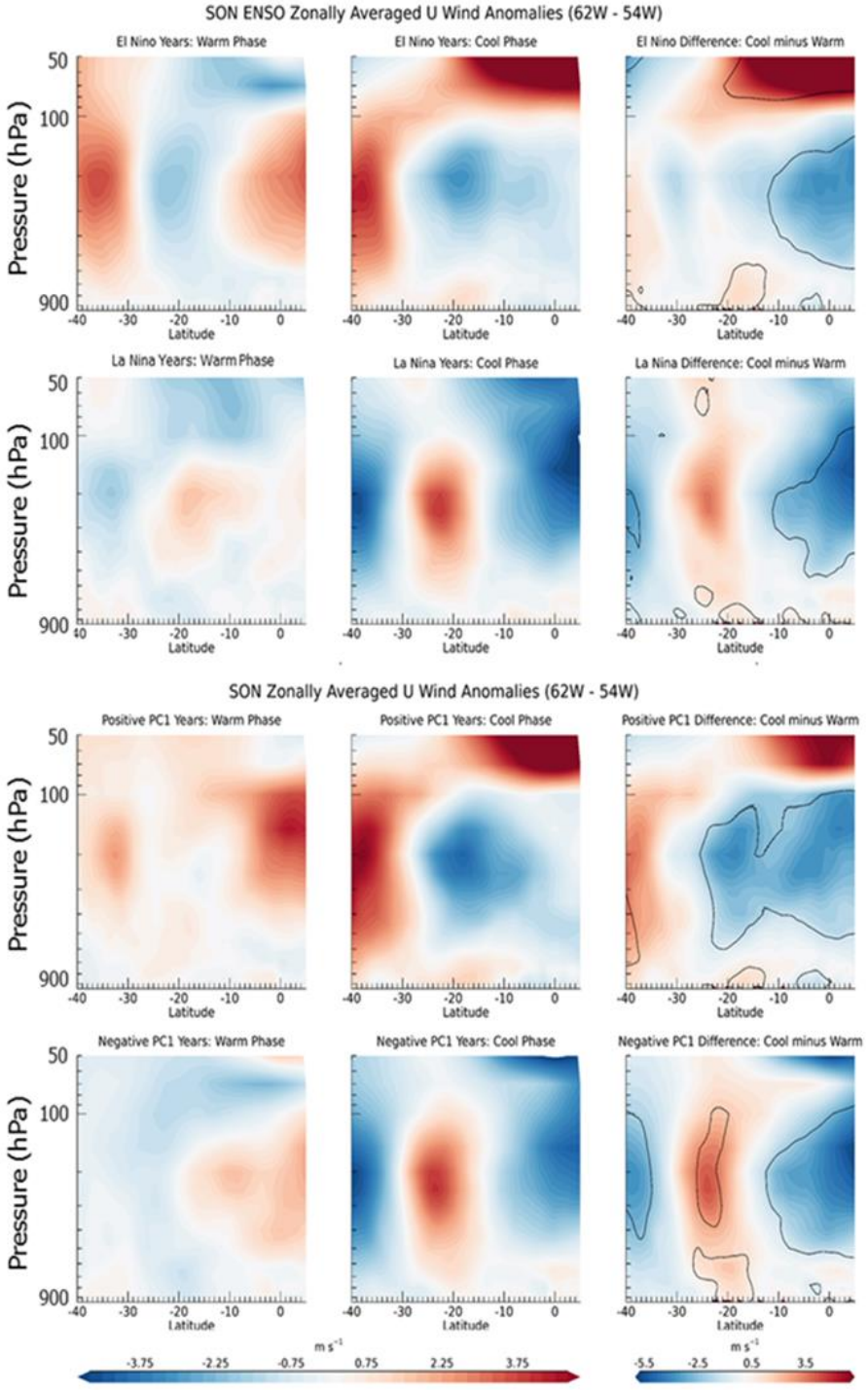

Fig. 7 Latitude-pressure composites of zonally averaged (62W – 54W) zonal wind anomalies for El Niño and La Niña (top 2 rows) and for positive and negative PC1 (bottom 2 rows). The left column is for the warm PDO phase (1980 – 1997), the middle column is for the cool PDO phase (1998 – 2012), and the right column is the difference between PDO phases (cool minus warm). Solid black lines on the difference composites indicates statistical significance on a 5% confidence interval.

2.4.3 Linear and Non-linear 200 hPa Geopotential Height Responses to ENSO

Upper level zonal winds and geopotential heights are strongly influenced by ENSO. However, El Niño and La Niña teleconnections over South America do not always mirror one another (Kayano and Andreoli 2007), and the linear and non-linear h200 response to ENSO is discussed here. ENSO exhibits a strong linear component in the response to SST anomalies where the sign changes is equal and opposite between El Niño (warmer eastern Pacific Ocean SSTs) and La Niña (cooler eastern Pacific Ocean SSTs) events (Hoerling et al., 1997). Locations where the linear components of El Niño and La Niña SST anomalies are not equal in magnitude may contribute to the non-linear component of the ENSO teleconnection. This problem is illustrated with composites of global SON h200 anomalies during El Niño and La Niña (Fig. 8). The differences between the two patterns show the linear components (Fig. 8c and 8g) while the sum of El Niño and La Niña captures the non-linear features (Fig. 8d and 8h).

Comparing the SON h200 anomalies linear response to ENSO between the warm and cool PDO phases shows a Rossby wave train pattern present during both PDO phases exhibiting opposite signs between El Niño and La Niña composites (Fig. 8). The El Niño and La Niña composites indicate significant differences in h200 anomalies between phases of the PDO in both hemispheres and remarkable differences in the Rossby wave train and respective influence over South America (Fig. 8a,b,c,d). Notably, during the warm PDO the pattern is weak in southeast South America possibly indicating that the wave pattern may not be reflected equatorward upon crossing the Andes Mountains and breaking over southeast South America; instead, the wave train may be propagating into the Southern Atlantic Ocean. The non-linear component of ENSO is showing a stronger wave train pattern across the Southern

Atlantic Ocean during the warm PDO (Fig. 8d) compared to the cool PDO phase (Fig. 8h). In this region the non-linearity between ENSO phases is more relevant, rather than RWB occurring in South America, wave trains are extending in midlatitudes, from Antarctica, across the Atlantic Ocean and into the Indian Ocean.

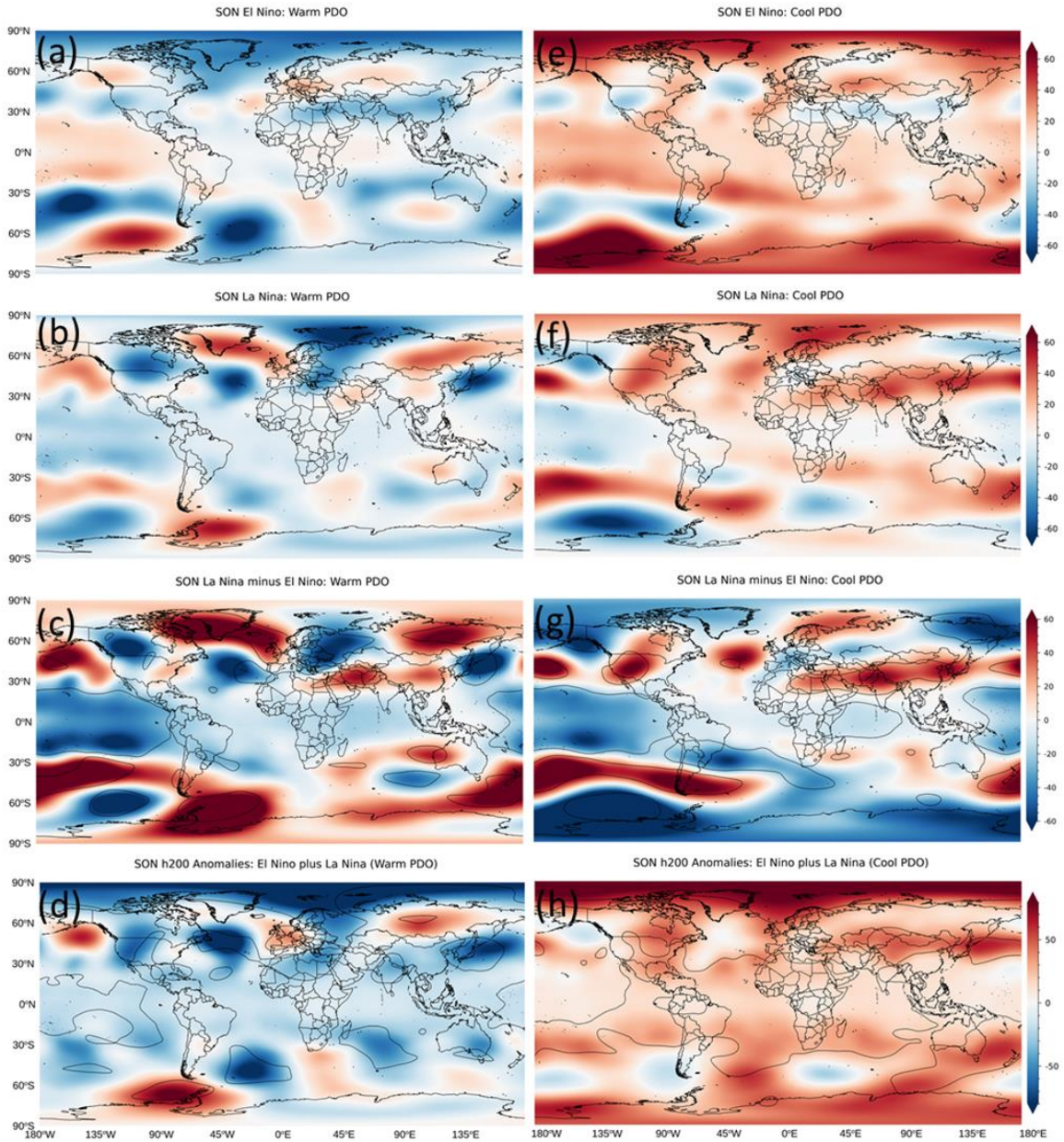

Fig. 8 Composites of September – November (SON) averaged 200 hPa geopotential height (h200) anomalies. The left column is during the warm PDO phase for: (a) El Nino years, (b) La Nina years, (c) La Nina minus El Nino (linear component), and (d) La Nina plus El Nino (non-linear component). The right column is during the cool PDO phase for: (e) El Nino years, (f) La Nina years, (g) La Nina minus El Nino (linear component), and (h) La Nina plus El Nino (non-linear component). Solid black isolines in the linear (c and g) and non-linear (d and h) plots are significant on a 5% significance level.

Here we compare the linear and non-linear response of SON h200 anomalies with respect to positive and negative PC1 composites during warm and cool PDO phases (Fig. 9). During the warm PDO, the positive PC1 and negative PC1 h200 composites show very weak patterns of anomalies and no statistically significant linear relationships in the southern hemisphere outside of the western Pacific Ocean (Fig 9c). During the cool PDO, the patterns are very similar to the ENSO patterns and the Rossby wave trains shown earlier (Fig. 9g). When comparing the PC1 and ENSO patterns, the magnitude of the upper level h200 anomalies are generally similar in the southern hemisphere in both patterns. However, the anomalies in eastern Antarctic in the positive PC1 composite are stronger than in the El Nino composites (Fig. 8e and 9e). These results indicate that during the warm PDO variations in UTLS ozone anomalies characterized by PC1 were forced possibly by multiple mechanisms, resulting in large case-to-case variability in patterns of h200. This is also reflected in the low correlation between PC1 and ENSO. Conversely, the UTLS ozone variability was, to a large extent, influenced by ENSO and exhibited contrasts between positive and negative PC1 that are approximately linear during the cool PDO phase. The influences of upper level circulation and El Niño on UTLS ozone patterns in South America are examined in the next section.

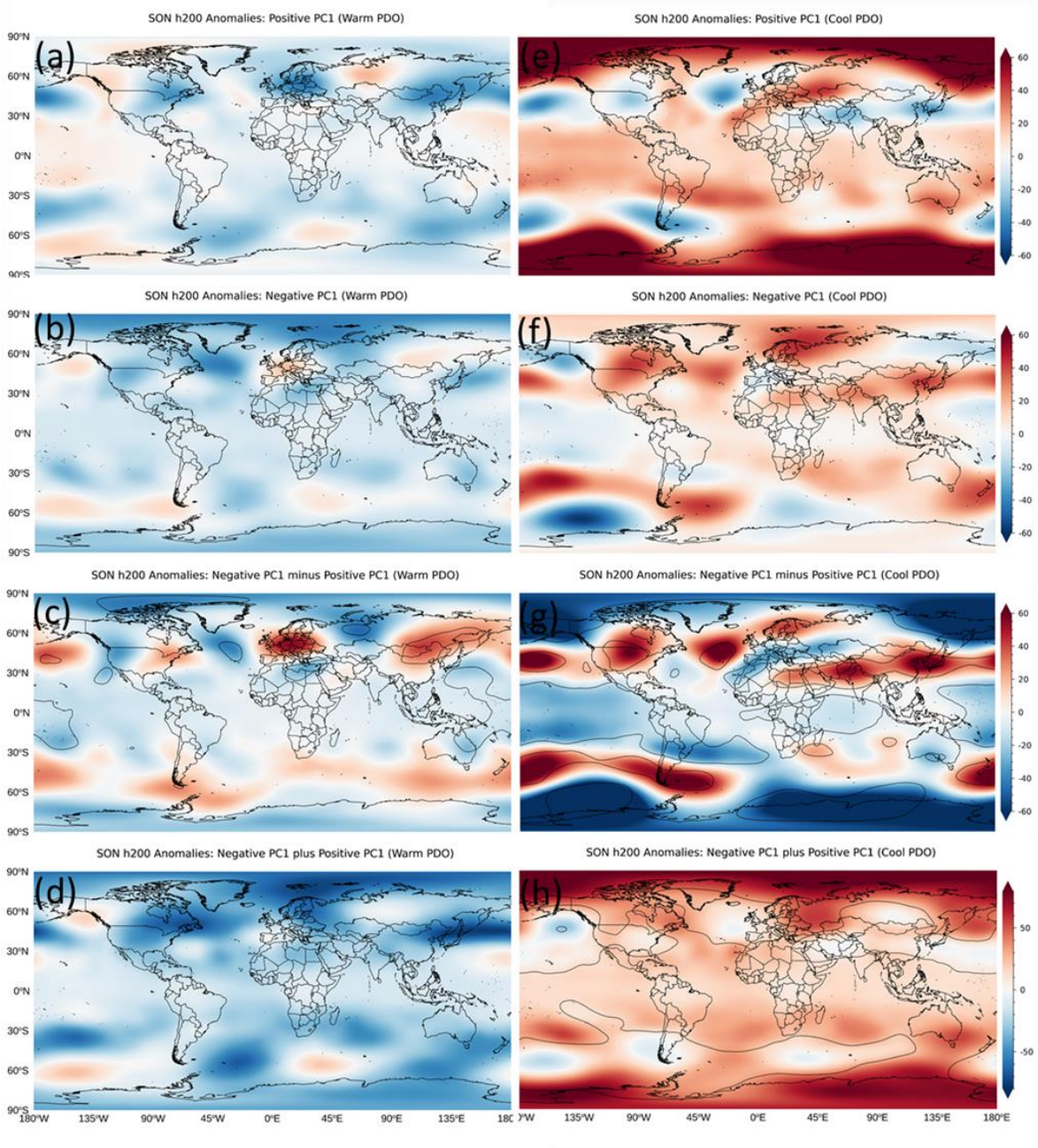

Fig. 9 Same as Fig. 8 except for positive and negative PC1

2.5 South America UTLS Ozone Variability and El Niño

Upper level divergence related to El Niño in the equatorial Pacific Ocean is a known Rossby Wave source (Revell et al. 2001; Terray and Dominiak, 2005), and the subsequent

wave train influences South America. Composites of h200 anomalies during El Niño and positive PC1 show a strong dipole in South America during the cool PDO phase (Fig. 8). The location of the shift in the sign coincides with the shift in subtropical jet location (Fig. 7), and in Southeast South America, positive h200 anomalies indicate higher than average upper level geopotential heights, similar to the results in Aceituno (1989). This is observed where upper level positive geopotential heights may correspond to low sea level pressure along with enhanced precipitation anomalies, consistent with previous studies (e.g. Grimm et al. 2003). However, during the warm PDO phase, relatively weak anomalies occur during positive PC1 years, as compared to El Niño years. The El Niño composites during the warm PDO phase also show areas of strong upper level negative anomalies in both the Pacific and Atlantic Oceans. In these areas, upper level negative geopotential heights may indicate weakening of surface high pressure, likely related to the South Pacific high variability.

Generally speaking, tropopause height variability is strongly related to temperatures and stability of the atmosphere directly below (Seidel et al., 2001). Previous work in subtropical South America has shown that during El Niño events, deep convection can be 1 – 2 km taller compared to a La Niña (Bruick et al. 2019) and regions with enhanced convection are subject to colder tropopause temperatures (Fueglistaler et al. 2009). Here, we analyze upper troposphere – lower stratosphere potential temperatures during El Niño and Positive PC1 years in both PDO phases. Composites of 100 hPa potential temperature (θ100) anomalies (Fig. 10) show that positive PC1 patterns are similar to El Niño patterns during both PDO phases. However, when comparing PDO phases separately, large differences emerge for PC1 and for El Niño, especially in subtropical South America. Statistically significant differences occur between 20˚S and 32˚S, which are collocated and inverse to

h200 anomalies during the cool PDO phase (Fig.8). In the El Niño composites, the patterns of differences between the warm and cool PDO phases in the subtropics are similar between h200 anomalies and θ100 anomalies. During both time frames anomalies are weak with no statistically significant differences throughout South America. For the PC1 composites, weak anomalies occur in the tropics, and negative anomalies in the subtropics centered in Northern Argentina during the cool PDO phase.

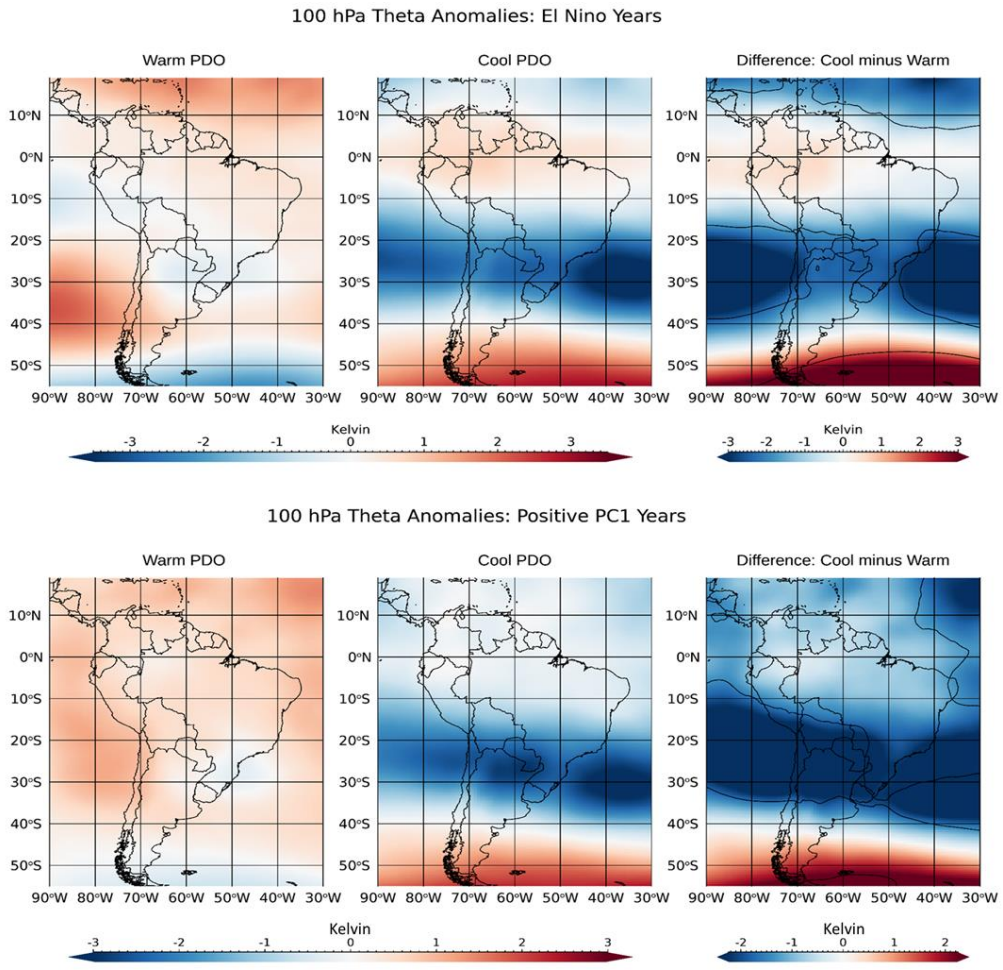

Fig. 10 Composites of 200 hPa potential temperature anomalies during warm and cool PDO phases during (top row) El Niño events and (bottom row) positive PC1 years. Differences between PDO phases are demonstrated in the right column. Solid black isolines are statistically significant on a 5% significance level.

UTLS potential temperatures are further evaluated with a longitude-height difference plot (cool PDO minus warm PDO) of zonally averaged (62˚W – 54˚W) θ100 during positive PC1 years (Fig. 11). The box in Figure 11 is the area used for the zonal averages, as well as the u200 wind analysis in Figure 7. This zonally averaged cross-section indicates a strong relationship to the positive PC1 ozone patterns (Fig 11, left). During the cool PDO, lower stratospheric cooling from ~ 10˚S to 35˚S and from ~ 10˚N to 15˚N coincides with decreasing ozone during positive PC1. This upper level cooling also coincides with lower and mid tropospheric warming during the cool PDO phase as compared to warm PDO. Areas within the La Plata Basin (northern Argentina, Paraguay, southern Brazil and Uruguay) correspond to known areas of enhanced precipitation (e.g., Ropelewski and Halpert 1987) and deep convection related to El Niño (Bruick et al. 2019). Our results show that during austral spring the tropopause is expanded to higher heights.

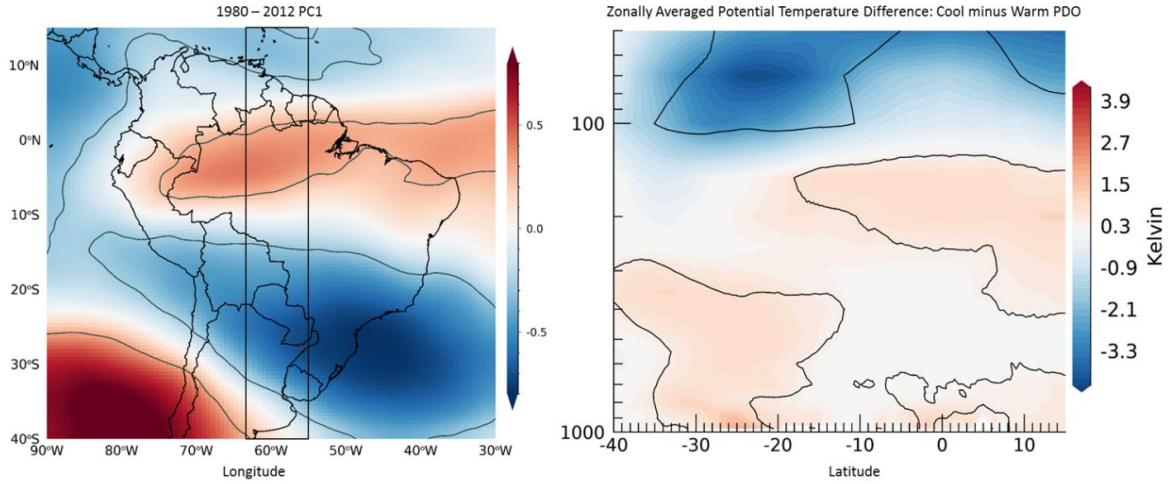

Fig. 11 PC1 calculated from1980 - 2012 (left). Difference between cool and warm PDO phase of 100 hPa zonally averaged potential temperature (θ) from 1000 hPa to 50 hPa (right). Solid black isolines are statistically significant on a 5% significance level. The box on the PC1 map demonstrates the area for zonally averaged calculations (left).

2.6 ENSO Driven Circulation Patterns over the Amazon and Southern La Plata Basins

Correlations between ozone anomalies and PC1 indicated remarkable differences between warm and cool PDO phases that were also evident for h200 and θ100 (Fig. 4). To better understand how the primary modes of ozone variability varied between the recent warm and cool PDO phases separately, a PCA is repeated and applied to 100 hPa MERRA2 detrended ozone anomalies in South America for two time frames, 1980 – 1997 (warm PDO) and 1998 – 2012 (cool PDO). Based on the North et al. (1982) rule the first mode (PC1) of each analysis is independent and describes ~ 27% and ~ 40% of the variability, respectively (Fig. 12). Notice that the variance explained by PC1 during the warm PDO is about the same as for the PC1 calculated to the entire period, whereas the respective PC1 variance during the cool PDO is much higher.

Although similarities exist between the two periods, one remarkable difference that emerges is a tripole feature in the ozone anomalies during the cool PDO phase. During the warm PDO phase, a dipole in ozone anomalies is observed between midlatitudes of South America (south of 30°S) and over subtropical South America (approximately between 10 - 25°S). This dipole is not associated with statistically significant anomalies north of 10°S. Conversely, during the cool PDO phase, the tripole feature is associated with a poleward shift in the patterns of negative and positive anomalies observed during the warm PDO phase. Additionally, a center of positive anomalies appears approximately east of the Andes, north of 10^{o}S over the Amazon, extending equatorward (Fig. 12 top right).

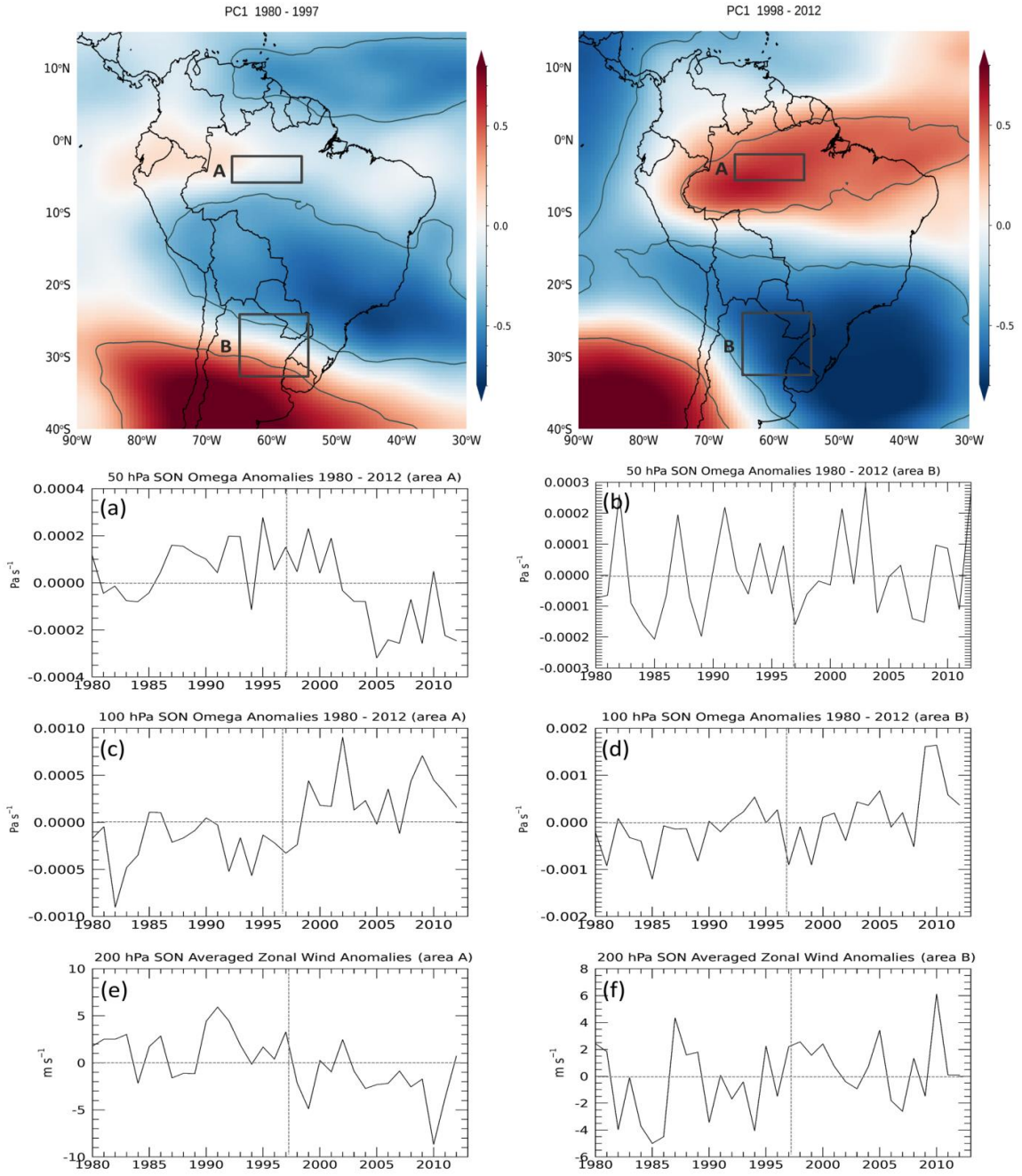

Fig. 12 PCA mode 1 of September to November averaged detrended MERRA2 100 hPa ozone anomalies 1980 – 1997 (left) and 1998 – 2012 (right). Principal Component (PC) time coefficients are correlated to spring averaged detrended ozone anomalies. Colors indicate the magnitude of the correlation between the principal component and ozone anomalies. Solid lines indicate statically significant correlations on a 5% significance level. Area averaged time series for two locations, area A (Amazon) and area B (southern La Plata Basin). (a) and (b) are ω50 hPa vertical velocity anomalies for area A and area B, respectively. (c) and (d) are ω100 hPa for area A and B,

respectively; (e) and (f) are 200 hPa zonal wind anomalies for area A and area B, respectively. The vertical dashed lines separate warm and cool PDO phases.

To evaluate possible mechanisms explaining the transition in ozone patterns at the UTLS between the two phases we investigate the variability of 100 hPa and 50hPa vertical velocity anomalies (ω100 and ω50, respectively) and 200 hPa zonal wind anomalies (u200) in two sub-regions over South America (A and B, Fig. 12). Both sub-regions are within the domain investigated in the cross-section analysis in sections 3 and 4 and are collocated where we observe significant shifts in patterns of ozone anomalies between the two PDO phases. Region A is located near the equator over the Amazon Basin, and region B is located in the subtropics over the Southern La Plata Basin (SLPB, primarily northern Argentina and Uruguay). The time series of SON ω50 anomalies, ω100 anomalies and u200 anomalies are shown in Fig. 12 for area A (12a, 12c, and 12e) and area B (12b, 12d, and 12f).

a) The Amazon Basin (Area A)

At 50 hPa, location A shows a remarkable shift in ω50 mean anomalies from predominantly positive between 1985 - 2001 to predominantly negative between 2002 - 2012 (Fig 12a). General opposite behavior is observed at 100 hPa, with a phase shift in SON ω100 anomalies from predominantly negative coinciding with the warm PDO to predominantly positive coinciding with the cool PDO phase (Fig. 12c). Notice that the negative (positive) ω100 anomalies coincide with a transition between predominantly positive (negative) u200 anomalies in the warm (cool) PDO (Fig. 12e). These changes in anomalies appear remarkably abrupt around the time of the transition of PDO phases (Fig. 12, dashed lines), suggesting a phase shift in circulation rather than a linear trend.

Studies have shown that tropical upwelling due to the BDC is driven by gravity waves propagating from the troposphere into the stratosphere which is generally enhanced during El Niño events (Garfinkel et al. 2018; Hardiman et al. 2007), influencing tropical ozone and temperatures (Randel et al. 2009). Calvo et al. (2010) also noted that during 'extreme' El Niño events, tropical regions are subject to anomalous downwelling below 16 km. While the tropics are generally driven by upward motion related to the Hadley cell and BDC, the tropical UTLS is strongly influenced by the atmosphere directly below. During enhanced convective processes, the tropopause is driven to higher altitudes and overshooting produces downwelling where cloud detrained material is cooler than the lower stratosphere's ozone rich warmer environment (Sherwood et al. 2003; Salby and Callaghan 2004). Above regions with enhanced deep convection and overshooting, gravity waves propagate upward and enhanced upwelling occurs aloft. Randel et al., 2006 used radiosonde stations and satellite data throughout the tropics to show cooler tropopause temperatures corresponding to decreased ozone and may be the result of increased upwelling. Conversely, Randel et al. (2006) also showed one location in South America (Natal, Brazil) with weak increasing ozone from 1998-2004, coinciding with the beginning of the cool PDO phase.

Here we investigate these concepts to better understand circulation over area A and relationships with ENSO events during each PDO phase. For this purpose, we examined the mean SON ω100 and ω50 calculated for each area along with PC1 (Fig. 13). The bar graphs in Figure 13 illustrate the PC1 time coefficients from the recalculated PCA analyses, 1980 – 1997 (Fig. 13 a and c) and 1998 – 2012 (Fig. 13 b and d), and the bars are color coded based on ENSO phase (red: El Nino, blue: La Nina, white: neutral), and line graphs are area averaged mean vertical velocity at 100 hPa and at 50 hPa.

During the warm PDO phase no coherent patterns of variability are observed between positive PC1, El Niño, area averaged ω50 and area averaged ω100. That is, PC1 interannual variability appears independent of ENSO, with positive values observed during El Nino and La Nina years (Fig. 13a). Additionally, no coherent pattern accompanies upwelling and downwelling at 100 hPa and 50 hPa relative to El Niño events. In the Amazon Basin vertical velocity at 50 hPa is expected to be related to upwelling related to the BDC (Garfinkel et al. 2018; Hardiman et al. 2007; Randel et al., 2009). However, during the warm PDO phase the average ω50hPa is positive (downwelling) for most of the period. ENSO seems to be uncorrelated to mean ω100 variability at this location (Fig. 13a).

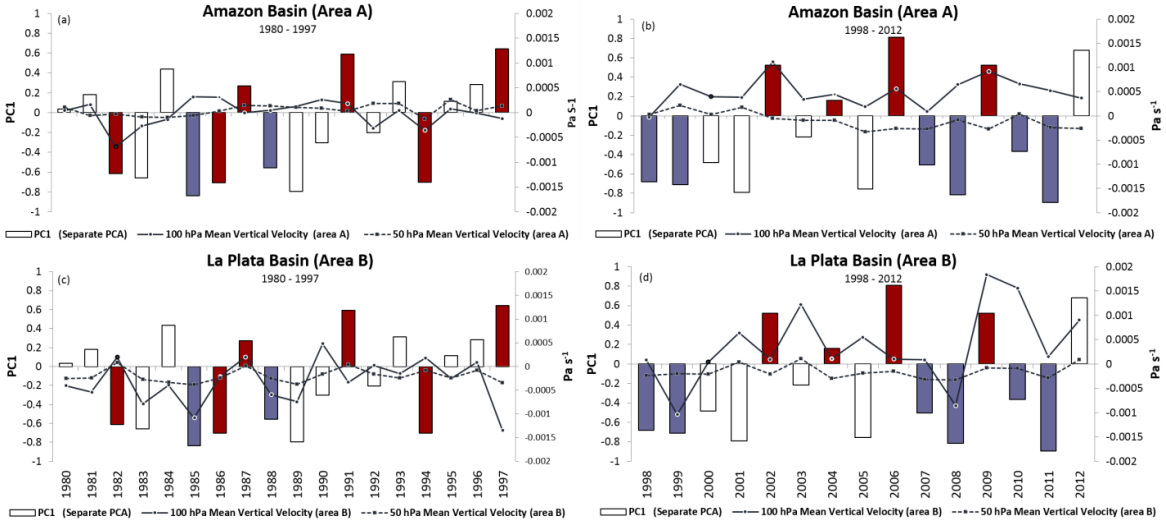

Fig. 13 PC1 time coefficients from separate PCAs (1980 – 1997 (a) and (c), 1998 – 2012 (b) and (d)) are represented with bars indicating ENSO phase (red: El Niño, blue: La Niña, and white: neutral). Solid lines are 100 hPa SON averaged vertical velocity and dashed lines are 50 hPa SON averaged vertical velocity. The top time series (a) and (b) are for area A (Amazon) and the bottom time series (c) and (d) are for area B (Southern La Plata Basin).

Unlike the warm PDO phase, during the cool PDO, positive (negative) PC1 is observed more frequently during El Niño (La Nina) events. On average, the SON mean basic

state is predominantly characterized by downwelling at 100 hPa and upwelling at 50 hPa. This basic state is consistent with more ozone at 100 hPa. A close inspection of the mean ω100 and ω50 in area A (Fig. 13b) reveals that during the cool PDO, El Niño events (and thus positive PC1) were associated with an increase in downwelling (upwelling) at 100 hPa (50 hPa), the opposite is observed for La Nina events. This increase in downwelling at 100 hPa during El Niño events explain the increase of UTLS ozone in the Amazon Basin associated with positive PC1. Enhanced downwelling can cause ozone rich air to be transported to lower levels at 100 hPa. While this is suggested as possible mechanisms for positive ozone anomalies over the Amazon during the cool PDO, it would require further examination outside the scope of this work.

b) The Southern La Plata Basin (Area B)

Location B is within a region where the subtropical jet stream interacts with the Andes Mountain range. At 50 hPa, there is no remarkable changes in ω50 (Fig. 12b) as observed in area A. However, an apparent increase in positive ω100 anomalies is observed after 2000 (Fig. 12 d) as observed in area A. Additionally, SON anomalies of u200 are generally positive during the cool PDO phase (Fig. 12f). However, during the 2002, 2006 and 2009 SON El Niño events, u200 anomalies are negative (Fig. 12f).

However, when observing the SON mean state in area B we notice a phase shift in area averaged ω100 between the warm and cool PDO phases in (Fig. 13c, d). Area B is situated in the subtropics and is subject to tropopause height gradient as heights decrease rapidly between the tropics and midlatitudes. This location is subject to large vertical velocity variability related the shallow branch of the BDC. At 100 hPa, we observe that the mean

vertical velocity vary from upwelling during the warm PDO to downwelling during the cool PDO (Fig. 13c, d).

When observing the fluctuations in the mean state, we notice that during the cool PDO, with the exception of the 2009 El Nino, a coherent relationship between the decrease downwelling at 100 hPa and El Nino years emerges. This is opposite to what was observed in area A and consistent with ENSO teleconnections in South America (Ropelewski and Halpert, 1987). That is, the decrease in downwelling at 100 hPa in area B is consistent with the influence of local deep convection driven by Rossby waves during El Niño events. This relative decrease in downwelling at 100 hPa result in the decrease in the transport of ozone to the UTLS, which may explain the pattern of negative ozone anomalies that appears in region B when PC1is positive during the cool phase of the PDO.

Another possible mechanism for negative ozone anomalies may be related to deep convection. In South America, especially in the La Plata Basin region, RWB events are associated with cold fronts connected to strong surface low pressure areas as well as weak warm fronts (Martius and Rivière 2016). One explanation for decreasing ozone at 100 hPa may be directly related to deep convection due to RWB events. In the extratropics deep convective overshooting may hydrate the lower stratosphere and decrease ozone via stratospheric chemistry. Furthermore, tropopause temperatures are generally warmer in the extratropics compared to the tropical tropopause (Dessler et al. 1995). Warmer cold point temperatures are generally capable of larger troposphere-stratosphere exchanges and may lead to higher water vapor mixing ratios in the lower stratosphere (Dessler et al., 2004; Dessler et al. 2013). While we suggest mechanisms for negative ozone anomalies in the southern La Plata Basin, demonstrating this concept is outside the scope of this study.

2.6.1 Relationships between PC1, PDO, ENSO, QBO and AAO

We have shown that the variability of the UTLS ozone appears to depend on PDO phases. To further this discussion, we investigate the influence of the Antarctic Oscillation (AAO) (Gong and Wang 1999; Carvalho et al. 2005) and QBO on the behavior of the UTLS ozone variability. Additionally, we examined the relative impacts of tropical Pacific warming during ENSO events. This was done by performing correlations between PC1 patterns and the following climate indices for each time-frame: MEI, PDO, QBO, Antarctic Oscillation (AAO), Tropical South Atlantic (TSA), Nino 3.4, and Nino 1 + 2. These results are shown in Table 3. For all three time frames, correlations between PC1 and QBO and PC1 and Tropical South Atlantic (TSA) indices are not statistically significant. The AAO is characterized by a dipole in the westerly wind strength with opposing centers at 40˚ and 65˚S, driving the atmospheric exchange of mass between the mid and high latitudes (Kidson 1988; Thompson and Wallace 2000; Ding et al. 2012). During positive (negative) AAO events, the jet stream shifts poleward (equatorward) (Carvalho et al. 2005). The correlations between PC1 and AAO are negative and statistically significant 1980 – 2012, however, for separate PDO phases correlations are weak and not statistically significant. We recall that the AAO and ENSO are not independent and both modes are anti-correlated (Carvalho et al. 2005).

Previous studies have shown that the effects of El Niño teleconnection can differ based on the location of the Tropical Pacific warming (Ashok et al. 2007). Typically, the warm pool associated with El Niño events is located in the tropical eastern Pacific Ocean. However, during Modoki El Niño events, stronger SST anomalies are located in the central Pacific with very weak warming, or weak cooling in the western and eastern Pacific Ocean (Ashok et al., 2007; Kao and Yu, 2009). To investigate the linear relationships between PC1

and the location of the warm pool, we use sea surface temperatures (SST) associated with the Niño 3.4 (N3.4) index for the central Pacific Ocean region (5°N–5°S, 170°W–120°W) and the Niño 1 + 2 (N1+2) index for the eastern Pacific Ocean region (5°N–5°S, 150°W–90°W). Correlations are obtained after removing the SON average (relative to the 1980 – 2017 period) for each index. Results are shown in Table 3.

PV	MEI	PDO	AAO	QBO	TSA	Niño 3.4	Niño 1+2
			1980 - 2012				
27.66%	***0.575***	**0.446**	**-0.384**	0.101	-0.109	***0.595***	**0.392**
			1980 - 1997 (Warm PDO)				
27.41%	0.245	**0.509**	-0.305	-0.061	0.320	0.234	0.287
			1998 - 2012 (Cool PDO)				
39.84%	***0.746***	***0.665***	-0.440	0.141	-0.110	***0.758***	**0.638**

Table 3. Correlation between PC1 and each SON averaged climate index: Multivariate ENSO index (MEI), Pacific Decadal Oscillation (PDO), Antarctic Oscillation (AAO), Quasi-biennial Oscillation (QBO), and Tropical South Atlantic (TSA), and SON averaged Pacific Ocean SST anomalies (Nino 3.4 and Nino 1+2) in three time frames: 1980 – 2016, 1980 – 1997 (warm PDO), and 1998 – 2012 (cool PDO). PV is the percentage of explained variance. Bold values are statistically significant on a 5% significance level, and bold and italicized on a 1% significance level.

When PC1 is correlated to SON SST anomalies during the 1980 – 2012 time frame, N3.4 and N1+2 are both positively correlated to PC1 (r=0.595 and r=0.392, respectively). During the warm PDO phase (1980 – 1997), neither N3.4 nor N1+2 are significantly correlated to PC1. During the cool PDO phase (1998 – 2012), both N3.4 and N1+2 are significantly positively correlated. The correlation between N3.4 and PC1 is r=0.758 and is significant at 1%; for N1+2 and PC1, r=0.638 and is significant at a 5%. While both are statistically significant, the central Pacific Ocean SST anomalies, which are in the region of the Modoki El Niño events, have a stronger linear relationship to PC1. Figure 14 shows the

SON averaged N3.4 and N1+2 SST anomalies. The shaded areas indicate N3.4 is greater than 0.5 and classified as an El Niño event, and while concurrent N1+2 anomalies in the eastern Pacific are not showing cooler than average SSTs (Ashok et al. 2007), when compared to N3.4 anomalies, they are cooler than the central Pacific anomalies, reinforcing the Modoki El Niño classification. During the cool PDO phase, three of the four El Niño events are classified as Modoki events (Yu et al. 2012), and during the warm PDO phase, five of seven El Niños are eastern/canonical El Niños. The location of the warm pool in the Pacific may have influenced the effects of the El Niño teleconnection on South America.

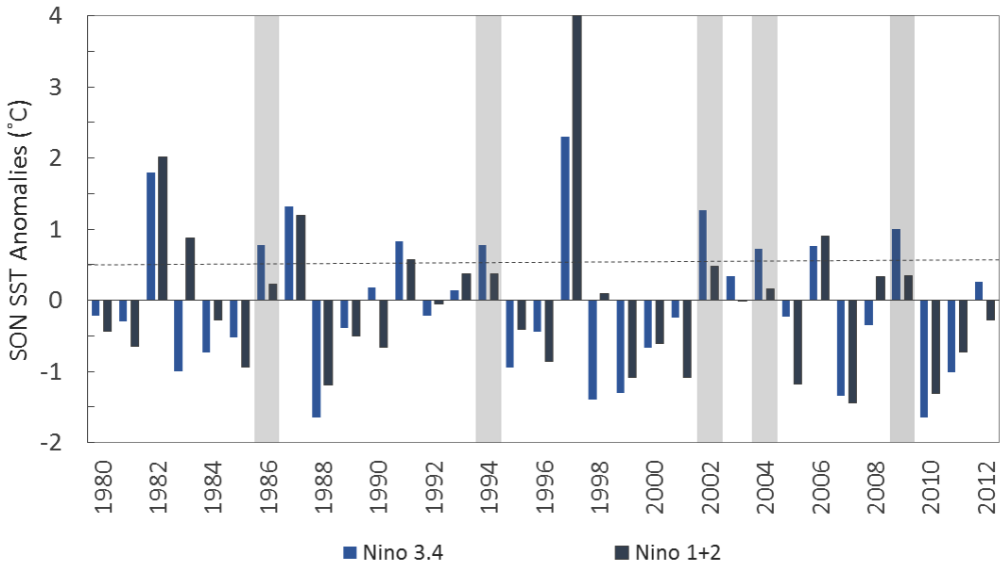

Fig. 14 SON averaged sea surface temperature anomalies. Blue bars: Nino 3.4 (central Pacific Ocean) region. Grey bars: Nino 1 + 2 (eastern Pacific Ocean) region. Anomalies are created by removing the SON averaged time mean (relative to 1980 – 2018) from the SON area averaged SST. Shaded regions show where El Nino is classified in the Nino 3.4 region and not 1 + 2 region.

2.7 Conclusions

This article investigates the interannual-to-multiannual variability of austral spring UTLS ozone with focus on South America (SA). Understanding mechanisms driving ozone variability at the UTLS is important because of troposphere – stratosphere exchanges and the associated transport of ozone to the lower troposphere (Davies and Schuepbach, 1994), and the transport of water vapor and other gases to the lower stratosphere. Since ENSO is the primary mode of interannual variability affecting SA climate, this research examines two aspects: 1) the role of ENSO in modulating UTLS SON ozone variability over South America and 2) the dependence of the ENSO teleconnection, and respective influences on UTLS ozone variability, on PDO phases. To address these issues we investigate the last two PDO phases: 1980 – 1997 (warm PDO) and 1998 – 2012 (cool PDO).

The primary mode of SON UTLS ozone variability over SA is identified by performing Principal Component Analysis considering the period extending from 1980-2012. The first mode (PC1) of UTLS ozone variability (1980 – 2012) characterizes a tripole of ozone anomalies over SA. When PC1 is positive, negative ozone anomalies are observed over subtropical SA while positive anomalies are observed along the equator and in Southwest SA.

Our results show that during SON there are significant differences in the relationships between the ENSO teleconnections on UTLS ozone variability, and these differences depend on PDO phases. PDO exhibits variations on interannual time scales and a key finding of this study is that SON PDO and ENSO (MEI) indices exhibited distinct linear correlations in the two phases of the PDO investigated here. During the cool PDO both indices were in phase, showing a strong positive linear relationship during SON for most ENSO events, while

during the warm PDO these two modes exhibited a much more uncorrelated behavior. Previous studies (e.g, Yu and Zwiers 2007) have shown compelling observational and modeling evidence that when PDO and ENSO are in phase, ENSO teleconnections in the Northern Hemisphere are enhanced. The present study indicates that ENSO teleconnections with the Southern Hemisphere via PSA are also dependent on the combined phases of PDO and ENSO with impacts to the UTLS ozone variability.

Changes in ENSO teleconnections in the Southern Hemisphere in distinct PDO phases and implication to ozone variability in the UTLS are demonstrated in many ways. During the warm PDO, outside of the tropical Pacific Ocean, no statistically significant relationships exist between PC1 and h200 during the warm PDO phase in the Southern Hemisphere; conversely, during the cool PDO a Rossby wave train pattern is clearly identified, possibly associated with the PSA. Correlations between PC1 and global 100 hPa potential temperature anomalies indicate that potential temperatures in SA do not have a linear relationship to PC1 during the warm PDO, and yet during cool PDO, results show a negative statistically significant correlation in central SA. We also evaluated UTLS global ozone anomalies and PC1. Again, no relationships are found during the warm PDO, while during the cool PDO statistically significant negative correlations exist in central SA. These results show that during the cool PDO phase, h200 anomalies and potential temperature anomalies in central SA explain well the patterns of global ozone anomalies characterized by PC1. In central SA, when PC1 is positive, h200 anomalies are also positive, 100 hPa potential temperatures anomalies are negative, and 100 hPa ozone anomalies negative. These patterns are not well characterized during warm PDO phase.

Additionally, composites of u200 suggest a poleward shift of the subtropical jet during the cool PDO phase (Fig. 5) coinciding with anomalous higher h200 equatorward of the subtropical jet, and anomalous lower 100 hPa potential temperature during El Niño and positive PC1 years. This result is also supported in latitude-height cross section of zonally averaged potential temperatures over South America (Fig. 11). From 10 – 40°S a cooler lower stratosphere and warmer troposphere occur during the cool PDO compared to the warm PDO. This cooling in the lower stratosphere corresponds to decreasing ozone during the positive PC1 years.

We evaluated the linear and non-linear h200 response to ENSO in the two PDO phases and showed that both responses (linear and non-linear) exhibit distinct spatial characteristics that depend on PDO. During the cool PDO phase the linear response shows a Rossby wave train propagating into southeast South America where known RWB occurs (Martius and Rivière 2016), and a weak non-linear response throughout the tropics. During the warm PDO phase, the linear response characterizes a wave train propagating poleward. The non-linear response exhibits the structure of a wave train propagating across the Southern Atlantic and Indian Oceans. The strong non-linear response in the extratropics during the warm PDO may have contributed to non-linear ENSO-PSA teleconnections that resulted in large interannual variability in the patterns of SON UTLS ozone and consequent low correlation between PC1 and ENSO.

In addition to the linear and non-linear response, we evaluated the effects of El Niño teleconnection based on the location of positive SST anomalies in the Pacific Ocean. We found stronger linear correlations between ozone patterns (PC1) and central Pacific Ocean SST anomalies (Nino 3.4) or Modoki El Niños, as compared to eastern Pacific Ocean SST

anomalies (Nino 1 + 2) that characterize the canonical El Niños. Thus, during cool PDO, PC1 has a stronger correlation to Niño 3.4 than Niño 1 +2. During the cool PDO, Modoki El Niños have a stronger influence on 100 hPa ozone patterns than canonical El Niños.

To evaluate differences in the spatiotemporal patterns of ozone anomalies between the warm and cool PDO phases, the PCA was recalculated separately in each phase. PC1 in the warm PDO shows a di-pole of ozone anomalies, with negative anomalies centered between 10 – 20° S, and positive anomalies in southern Argentina and Chile. During the cool PDO, a tri-pole of ozone anomalies is shown with the center of negative anomalies shifted poleward and a large region of positive anomalies along the equator east of the Andes. Differences in SON mean and anomalies of upper level zonal winds (u200) and omega at 50 hPa and 100 hPa (ω50 and ω100, respectively) are examined between PDO phases in two primary areas where we observe the greatest transitions between phases: the Amazon Basin and the Southern La Plata Basin (SLPB). Both are also important regions with well-known teleconnections with ENSO. The results show evidence of shift in ω50 and ω100 mean and anomalies between PDO phases over the Amazon, from predominantly negative anomalies (upwelling) during the warm PDO phase to predominantly positive (downwelling) anomalies during the cool PDO phase. During the cool phase, the positive relationship between ozone anomalies and PC1 is likely due to downwelling. Ozone in the tropics is typically upwelled to higher altitudes, decreased upwelling, or in this case downwelling, would reduce ozone transport and increase ozone concentrations at this level. This is observed in the positive ozone anomalies.

In the La Plata Basin domain the mean basic state also changes at 100 hPa from predominantly upwelling during the warm PDO to predominantly downwelling during the

cool PDO. No shifts in the mean ω50 are noticeable over this domain. Decreasing ozone at 100 hPa may be directly related to deep convection due to RWB events. Warmer tropopause and cold point temperatures, relative to the tropics are generally capable of larger STE and may lead to higher water vapor mixing ratios in the lower stratosphere (Dessler et al., 2004; Dessler et al. 2013), and become a catalyst for stratospheric ozone destruction (Bates and Nicolet, 1950). This may be responsible for lower ozone anomalies observed in the La Plata Basin.

Although an increase in downwelling is observed in both regions (Amazon Basin and La Plata Basin), during the cool PDO anomalies in ω50 and ω100 are strongly related to ENSO and are generally of opposite sign between the two regions, reinforcing the enhanced ENSO teleconnections patterns during the cool PDO and ENSO modulation of ozone anomalies in the UTLS.

Because the focus of this investigation is on the relationships between El Niño and ozone patterns during the recent PDO phases based on reanalyses, only two phases of the PDO have been investigated during a period of relatively rapid global warming. Shifts in the subtropical jet and subsequent upper level geopotential height variability influence UTLS ozone and temperatures, and these results warrant further investigation in a warming world.

2.8 Acknowledgements

This research was supported by the University of California, Santa Barbara Graduate Research Mentorship Program Fellowship. The Modern-Era Retrospective analysis for Research and Applications, Version 2 (MERRA-2) reanalysis data used in this study/project

has been provided by the Global Modeling and Assimilation Office (GMAO) at NASA Goddard Space Flight Center.

2.9 References

Aceituno P (1988) On the functioning of the Southern Oscillation in the South American sector. Part I: Surface climate. *Mon. Wea. Rev*, **116,** 505–524.

Aceituno P (1989) On the Functioning of the Southern Oscillation in the South American Sector. Part II. Upper-Air Circulation. *J. Climate*, **2**, 341–355, https://doi.org/10.1175/1520-0442(1989)002<0341:OTFOTS>2.0.CO;2.

Andreoli RV, Kayano MT (2005) ENSO-related rainfall anomalies in South America and associated circulation features during warm and cold Pacific decadal oscillation regimes. *Int. J. Climatol.* 25: 2017-2030. doi:10.1002/joc.1222.

Ashok K, Behera SK, Rao SA, Weng H, Yamagata T (2007) El Niño Modoki and its possible teleconnection. *J. Geophys. Res.* **112**: C11007.

Baldwin M, Dunkerton T (1998) Quasi-biennial modulation of the Southern Hemisphere stratospheric polar vortex. *Geophysical Research Letters*, 25. 3343-3346. 10.1029/98GL02445.

Baldwin MP, Gray LJ, Dunkerton TJ, Hamilton K, Haynes PH, Randel WJ, Holton JR, Alexander MJ, Hirota I, Horinouchi T, Jones DBA, Kinnersley JS, Marquardt C, Sato K, Takahashi M(2001) The quasi-biennial oscillation, *Rev. Geophys.*, 39 179–229.

Berbery EH, VR Barros (2002) The Hydrologic Cycle of the La Plata Basin in South America. *J. Hydrometeor.,* **3**, 630–645, https://doi.org/10.1175/1525-7541(2002)003<0630:THCOTL>2.0.CO;2

Boffi JA (1949) Effect of the Andes Mountains on the General Circulation Over the Southern Part of South America. *Bull. Amer. Meteor. Soc.,* 30, 242–247, https://doi.org/10.1175/1520-0477-30.7.242.

Brewer AW (1949) Evidence for a world circulation provided by the measurements of helium and water vapor distribution in the stratosphere, Q. J. Roy., *Meteor. Soc.,* 75, 351–363.

Bruick ZS, Rasmussen KL, Rowe AK, McMurdie LA (2019) Characteristics of Intense Convection in Subtropical South America as Influenced by El Niño-Southern Oscillation. *Mon. Wea. Rev.*. https://doi.org/10.1175/MWR-D-18-0342.1.

Calvo N, RR Garcia, Randel WJ, Marsh DR (2010) Dynamical Mechanism for the Increase in Tropical Upwelling in the Lowermost Tropical Stratosphere during Warm ENSO Events. *J. Atmos. Sci.,* **67**, 2331–2340. https://doi.org/10.1175/2010JAS3433.1.

Carvalho LM, Jones C, Ambrizzi T (2005) Opposite Phases of the Antarctic Oscillation and Relationships with Intraseasonal to Interannual Activity in the Tropics during the Austral Summer. *J. Climate,* 18, 702–718, https://doi.org/10.1175/JCLI-3284.1.

Danielsen, EF (1968) Stratospheric-tropospheric exchange based on radioactivity, ozone and potential vorticity, *Journal of the Atmospheric Sciences*, 25, 502–518, 1968.

Davies TD, Schuepbach E (1994) Episodes of high ozone concentrations at the earth's surface resulting from transport down from the upper troposphere/lower stratosphere: a review and case studies. *Atmospheric Environment*, *28*(1), pp.53-68.

Dessler AE, Hintsa EJ, Weinstock EM , Anderson JG, Chan KR (1995) Mechanisms controlling water vapor in the lower stratosphere: “A tale of two stratospheres”, *J. Geophys. Res.*, 100(D11), 23,167–23,172.

Dessler AE, Sherwood SC (2004) Effect of convection on the summertime extratropical lower stratosphere, *J. Geophys. Res.*, *109*, D23301, doi:10.1029/2004JD005209.

Dessler AE, Schoeberl MR, Wang T, Davis SM, Rosenlof KH (2013) Stratospheric water vapor feedback. *Proceedings of the National Academy of Sciences of the United States of America*, *110*(45), 18087–18091. doi:10.1073/pnas.1310344110.

Ding Q, Steig EJ, Battisti DS, Wallace JM (2012) Influence of the Tropics on the Southern Annular Mode. *J. Climate*, 25, 6330–6348. https://doi.org/10.1175/JCLI-D-11-00523.1.

Fernandes LG, Rodrigues RR (2018) Changes in the patterns of extreme rainfall events in southern Brazil. *Int. J. Climatol*, 38: 1337-1352. doi:10.1002/joc.5248.

Ferreira R N, Rickenbach TM, Herdies D L, Carvalho L M (2003) Variability of South American convective cloud systems and tropospheric circulation during January–March 1998 and 1999. *Monthly Weather Review*, 131(5), 961–973. https://doi.org/10.1175/1520-0493(2003)131<0961:VOSACC>2.0.CO;2.

Flury T, Wu DL, Read WG (2013) Variability in the speed of the Brewer–Dobson circulation as observed by Aura/MLS, *Atmos. Chem. Phys.*, 13, 4563-4575. https://doi.org/10.5194/acp-13-4563-2013, 2013.

Forster PMF, Shine KP (1999) Stratospheric water vapour changes as a possible contributor to observed stratospheric cooling, *Geophysical Research Letters*, vol. 26, no. 21, 3309-3312.

Fueglistaler S, Dessler AE, Dunkerton TJ, Folkins I, Fu Q, Mote PW (2009) Tropical tropopause layer. *Reviews of Geophysics, 47,* RG1004. https://doi.org/10.1029/2008RG000267.

Fukuoka A (1951) A Study of 10-day Forecast (A Synthetic Report), Vol. XXII, *The Geophysical Magazine: Tokyo*; 177–218.

Garfinkel CI, Gordon A, Oman L, Li F, Davis S, Pawson S (2018) Nonlinear response of tropical lower stratospheric temperature and water vapor to ENSO. *Atmospheric Chemistry and Physics*, *18*, 4597–4615. https://doi.org10.5195/acp-2017-520.

Gelaro R, McCarty W, Suárez MJ, Todling R, Molod A, Takacs L, Randles CA, Darmenov A, Bosilovich MG, Reichle R, Wargan K, Coy L, Cullather R, Draper C, Akella S, Buchard V, Conaty A, da Silva AM, Gu W, Kim G, Koster R, Lucchesi R, Merkova D, Nielsen JE, Partyka G, Pawson S, Putman W, Rienecker M, Schubert SD, Sienkiewicz M , Zhao B (2017) The Modern-Era Retrospective Analysis for Research and Applications, Version 2 (MERRA-2). *J. Climate*, 30, 5419–5454. https://doi.org/10.1175/JCLI-D-16-0758.1.

Gettelman A, Salby ML, Sassi, F (2002) Distribution and influence of convection in the tropical tropopause region, *J. Geophys. Res.*, 107(D10), doi:10.1029/2001JD001048.

Gong D, Wang S (1999) Definition of Antarctic oscillation index. *Geophysical research letters*, 26(4), pp.459-462.

Gonzalez MH, Garbarini EM, Rolla AL, Eslamian S, (2017) Meteorological Drought Indices: Rainfall Prediction in Argentina. Handbook of Drought and Water Scarcity, Vol. 1: Principles of Drought and Water Scarcity, Francis and Taylor, USA, 541–570.

Grimm AM, Barros VR, Doyle ME (2000) Climate Variability in Southern South America Associated with El Nino and La Nina Events. *J. Climate*, 13, 35-58.

Grimm AM (2003) The El Niño impact on the summer monsoon in Brazil: Regional processes versus remote Influences. J. Climate, 16, 263-280.

Grimm AM (2004) How do La Niña events disturb the summer monsoon system in Brazil? *Climate Dynamics*, **22**(2–3): 123–138.

Grimm, AM, Tedeschi RG (2009) ENSO and Extreme Rainfall Events in South America. *J. Climate*, **22**, 1589–1609, https://doi.org/10.1175/2008JCLI2429.1.

Hardiman SC, Butchart N, Haynes PH, Hare SH (2007) A note on forced versus internal variability of the stratosphere. *Geophysical Research Letters*, *34*, L12803. https://doi.org10.1029/2007GL029726 Holton JR, Haynes PH, McIntyre ME, Douglass AR, Rood RB, Pfister L (1995) Stratosphere-troposphere exchange, Rev. Geophys., 33(4), 403–439. doi:10.1029/95RG02097.

Hoerling MP, Kumar A, Zhong M (1997) El Ni˜no, La Ni˜na, and the nonlinearity of their teleconnections, *J. Clim*. 10 1769–86.

Holton J, Tan H (1980) The influence of the equatorial quasibiennial oscillation on the global circulation at 50 mb. *J. Atmos. Sci.*, 37, 2200–2208.

Holton JR, Haynes PH, McIntyre ME, Douglass AR, Rood RB, Pfister L (1995) Stratosphere-troposphere exchange, *Rev. Geophys.*, 33(4), 403–439. doi:10.1029/95RG02097.

Holton JR (2004) An Introduction to Dynamic Meteorology, International Geophysics Series, vol.88, Elsevier Academic Press, Burlington, MA.

Hoskins BJ, Karoly DJ (1981) The Steady Linear Response of a Spherical Atmosphere to Thermal and Orographic Forcing. *J. Atmos. Sci*., 38, 1179–1196, https://doi.org/10.1175/1520-0469(1981)038<1179:TSLROA>2.0.CO;2.

Irving D, Simmonds I (2016) A new method for identifying the Pacific–South American pattern and its influence on regional climate variability. *Journal of Climate*, *29*(17), pp.6109-6125.

Kao H-Y, Yu J-Y (2009) Contrasting Eastern-Pacific and Central-Pacific types of ENSO. *J. Clim.* **22**: 615–632.

Karoly DJ (1989) Southern Hemisphere circulation features associated with El Niño Southern–Oscillation events. *J. Climate*, 2, 1239–1252.

Kayano M, Andreoli R (2007) Relations of South American summer rainfall interannual variations with the Pacific Decadal Oscillation. *International Journal of Climatology*. 27. 10.1002/joc.1417.

Kidson JW (1988) Indices of the Southern Hemisphere zonal wind. *J. Climate*, 1, 183–194.

Liebmann B, Mechoso CR (2010) The South American Monsoon System. In: The Global Monsoon System: Research and Forecast, 2nd Edition. C. P Chang et al., (eds.) World Scientific Publishing: Singapore. 550pp.

Liu C, Zipser EJ (2005) Global distribution of convection penetrating the tropical tropopause, *J. Geophys. Res.*, 110, D23104, doi:10.1029/2005JD006063.

Lorenz, E. N., 1956: Empirical Orthogonal Functions and Statistical Weather Prediction. *Tech. Rep. Stat. Forecast Proj. Rep. 1 Dep. Meteorol. MIT 49*.

Mantua NJ, Hare SR (2002) The Pacific Decadal Oscillation, Journal of Oceanography, 58: 35. https://doi.org/10.1023/A:1015820616384.

Mantua NJ, Hare SR, Zhang Y, Wallace JM, Francis RC (1997) A Pacific interdecadal climate oscillation with impacts on salmon production. Bull. Amer. Meteor. Soc., **78**, 1069–1079,doi:https://doi.org/10.1175/1520-0477(1997)078<1069:APICOW>2.0.CO;2.

Marengo JA (1992) Interannual variability of surface climate in the Amazon basin. *Int. J. Climatol*, **12,** 853–863.

Martius O, Rivière G (2016) Rossby wave breaking: Climatology, interaction with low-frequency climate variability, and links to extreme weather events. In J. Li, R. Swinbank, R. Grotjahn, & H. Volkert (eds.), Dynamics and Predictability of Large-Scale, High-Impact Weather and Climate Events (Special Publications of the International Union of Geodesy and Geophysics, pp. 69-78). Cambridge: Cambridge University Press. doi:10.1017/CBO9781107775541.006.

McCabe GJ, Dettinger MD, (1999) Decadal variations in the strength of ENSO Teleconnection with precipitation in the western United States, *Int. J. Climatol.* **19**: 1399 – 1410.

McIntosh PC, Hendon HH (2018) Understanding Rossby wave trains forced by the Indian Ocean Dipole, *Clim Dyn* 50: 2783. https://doi.org/10.1007/s00382-017-3771-1.

Mo KC, Paegle JN (2001) The Pacific–South American modes and their downstream effects. *International Journal of Climatology: A Journal of the Royal Meteorological Society*, *21*(10), pp.1211-1229.

Montini TL, Jones C, & Carvalho L MV (2019). The South American low-level jet: A new climatology, variability, and changes, Journal of Geophysical Research: Atmospheres, 124, 1200–1218. https://doi.org/10.1029/2018JD029634Dipole.

Mulholland JP, SW Nesbitt, RJ Trapp, KL Rasmussen, Salio PV, (2018) Convective Storm Life Cycle and Environments near the Sierras de Córdoba, Argentina. *Mon. Wea. Rev.*, **146**, 2541–2557, https://doi.org/10.1175/MWR-D-18-0081.1.

Newman M, Alexander MA, Ault TR, Cobb KM, Deser C, Di Lorenzo E, Mantua NJ, Miller AJ, Minobe S, Nakamura H, Schneider N (2016) The Pacific decadal oscillation, revisited. *Journal of Climate*, *29*(12), pp.4399-4427.

North GR, Bell TL, Cahalan RF, Moeng FJ (1982) Sampling Errors in the Estimation of Empirical Orthogonal Functions. Mon. Wea. Rev., 110, 699–706, https://doi.org/10.1175/1520-0493(1982)110<0699:SEITEO>2.0.CO;2.

Randel WJ, Wu F, Vo¨mel H, Nedoluha GE, Forster P (2006) Decreases in stratospheric water vapor after 2001: Links to changes in the tropical tropopause and the Brewer-Dobson circulation, *J. Geophys. Res.*, 111, D12312, doi:10.1029/2005JD006744.

Randel WJ, Garcia RR, Calvo N, Marsh D (2009) ENSO influence on zonal mean temperature and ozone in the tropical lower stratosphere. *Geophysical Research Letters*, *36*, L15822. https://doi.org10.1029/2009GL039343.

Rasmussen, KL, Zuluaga MD, Houze Jr. RA (2014) Severe convection and lightning in subtropical South America, *Geophys. Res. Lett.*, 41, 7359–7366, doi: 10.1002/2014GL061767.

Rasmussen KL, Chaplin MM, Zuluaga MD, Houze RA (2016) Contribution of Extreme Convective Storms to Rainfall in South America. *J. Hydrometeor.*, **17**, 353–367, https://doi.org/10.1175/JHM-D-15-0067.1.

Rasmussen KL, Houze RA (2016) Convective Initiation near the Andes in Subtropical South America. *Mon. Wea. Rev.*, **144**, 2351–2374, https://doi.org/10.1175/MWR-D-15-0058.1.

Revell MJ, Kidson JW, Kiladis GN (2001) Interpreting Low-Frequency Modes of Southern Hemisphere Atmospheric Variability as the Rotational Response to Divergent Forcing. *Mon. Wea. Rev.*, **129**, 2416–2425, https://doi.org/10.1175/1520-0493(2001)129<2416:ILFMOS>2.0.CO;2.

Rodrigues RR, Woollings T (2017) Impact of Atmospheric Blocking on South America in Austral Summer. J. Climate, 30, 1821–1837, https://doi.org/10.1175/JCLI-D-16-0493.1.

Ropelewski CF, Halpert MS (1987) Global and Regional Scale Precipitation Patterns Associated with the El Niño/Southern Oscillation. *Mon. Weather Rev.*, **115**, 1606–1626.
doi:10.1175/1520-0493(1987)115<1606:GARSPP>2.0.CO;2.

Salby ML, Callaghan PF (2002) Interannual Changes of the Stratospheric Circulation: Relationship to Ozone and Tropospheric Structure. *J. Climate,* **15**, 3673–3685, https://doi.org/10.1175/1520-0442(2003)015<3673:ICOTSC>2.0.CO;2.

Salio P, Nicolini M, Zipser, EJ (2007) Mesoscale convective systems over southeastern South America and their relationship with the South American low-level jet. Monthly Weather Review, 135(4), 1290–1309. https://doi.org/10.1175/MWR3305.1.

Seidel DJ, Ross RJ, Angell JK, Reid GC (2001) Climatological characteristics of the tropical tropopause as revealed by radiosondes, *J. Geophys. Res.*, 106(D8), 7857– 7878, doi:10.1029/2000JD900837.

Sherwood SC, Horinouchi T, Zeleznik HA (2003) Convective Impact on Temperatures Observed near the Tropical Tropopause. *J. Atmos. Sci.,* **60**, 1847–1856, https://doi.org/10.1175/1520-0469(2003)060<1847:CIOTON>2.0.CO;2.

Steinbrecht W, Hassler B, Claude H, Winkler P , Stolarski, RS (2003) Global distribution of total ozone and lower stratospheric temperature variations. *Atmospheric Chemistry and Physics*, *3*(5), pp.1421-1438.

Straus DM, Shukla J (2002) Does ENSO force the PNA?, *Journal of climate*, *15*(17), pp.2340-2358; Leathers, D.J., Yarnal, B. and Palecki, M.A., 1991. The Pacific/North American teleconnection pattern and United States climate. Part I: Regional temperature and precipitation associations. *Journal of Climate*, *4*(5), pp.517-528.

Tedeschi RG, Cavalcanti IFA, Grimm AM (2013) Influences of two types of ENSO on South American precipitation. *Int J Climatol,* 33: 1382−1400.

Tedeschi RG, Grimm AM, Cavalcanti IFA (2015) Influence of Central and East ENSO on extreme events of precipitation in South America during austral spring and summer. *Int J Climatol*, 35: 2045−2064.

Terray P, Dominiak S, (2005) Indian Ocean sea surface temperatures and El Niño–Southern Oscillation: A new perspective. *J. Climate,* **18,** 1351–1368.

Thompson DWJ, Wallace JM (2000) Annual modes in the extratropical circulation, Part I: month-to-month variability. J. Clim., 13, 1000–1016.

Trenberth KE, Hurrell JW (1994) Decadal atmosphere-ocean variations in the Pacific. *Climate Dynamics*, 9, 303-319, doi:10.1007/BF00204745.

Trenberth KE, Branstator GW, Karoly D, Kumar A, Lau NC, Ropelewski C. (1998) Progress during toga in understanding and modeling global teleconnections associated with

tropical sea surface temperatures. *Journal of Geophysical Research-Oceans, 103*, 14291-14324. doi:10.1029/97JC01444.

Trenberth KE, Caron JM, Stepaniak DP, Worley S (2002) Evolution of El Niño–Southern Oscillation and global atmospheric surface temperatures. *J. Geophys. Res.*, 107(D8), doi:10.1029/2000JD000298.

Wolter K, Timlin MS (1993) Monitoring ENSO in COADS with a seasonally adjusted principal component index. Proc. of the 17th Climate Diagnostics Workshop, Norman, OK, NOAA/NMC/CAC, NSSL, Oklahoma Clim. Survey, CIMMS and the School of Meteor., Univ. of Oklahoma, 52-57.

Wargan K, Labow GJ, Frith SM, Pawson S, Livesey NJ, Partyka GS, (2017) Evaluation of the Ozone Fields in NASA's MERRA-2 Reanalysis. *J. Clim*, 30, 2961–2988. DOI:10.1175/JCLI-D-16-0699.1.

Wargan K, Labow GJ, Frith SM, Pawson S, Livesey NJ, Partyka GS, (2017) Evaluation of the Ozone Fields in NASA's MERRA-2 Reanalysis. *J. Clim*, 30, 2961–2988. DOI:10.1175/JCLI-D-16-0699.1.

WMO (World Meteorological Organization) 2011 Scientific Assessment of Ozone Depletion: 2010 Global Ozone Research and Monitoring Project-Report No. 52, 516 pp., Geneva, Switzerland.

Yu B, Zwiers FW (2007) The impact of combined ENSO and PDO on the PNA climate: a 1,000-year climate modeling study. *Climate Dynamics*, 29(7-8), pp.837-851.

Yu J-Y, Zou Y, Kim ST, Lee T (2012) The changing impact of El Niño on US winter temperatures, *Geophys. Res. Lett.*, 39, L15702, doi:10.1029/2012GL052483.

Zhang Y, Wallace JM, Battisti DS (1997) ENSO-like interdecadal variability: 1900–93. J. Climate, **10**, 1004–1020, doi:https://doi.org/10.1175/1520 0442(1997)010<1004:ELIV>2.0.CO;2.

Zhang L, Delworth TL (2015) Analysis of the Characteristics and Mechanisms of the Pacific Decadal Oscillation in a Suite of Coupled Models from the Geophysical Fluid Dynamics Laboratory. *J. Climate*, **28**, 7678–7701, https://doi.org/10.1175/JCLI-D-14-00647.1.

Zipser EJ, Cecil DJ, Liu C, Nesbitt SW, Yorty DP (2006) Where are the most intense thunderstorms on Earth. Bull. *Am. Meteorol. Soc.*, 87, 1057–1071.

Chapter 3:

Configuration of the Weather Research and Forecasting Model for Simulations of Mesoscale Convective Processeses and Double Tropopause Features in South America

3.1 Abstract

Mesoscale convective systems (MCS) occur frequently in South America and are known to produce deep convection. However, the effects of deep convection on upper troposphere – lower stratosphere (UTLS) thermodynamics and stratospheric hydration are much less known, and data in this region is generally unavailable. This work utilizes the Weather Research and Forecasting (WRF) model to evaluate its ability to simulate observed MCSs and UTLS temperatures, especially double tropopause features during deep convection. Two different types of sensitivity tests were performed with WRF. First, sensitivity tests were conducted with five cumulus schemes to simulate an observed MCS. The results show that the Grell-Freitas Ensemble cumulus scheme optimally simulated the size and location of a mature MCS on November 29, 2012. Second, sensitive tests of vertical grid spacing were conducted to determine if increasing the vertical resolution in the UTLS produces observed double tropopause features. Three WRF runs were initialized with the Grell-Freitas parameterization chosen from the first sensitivity test to simulate a MCS on November 12, 2018. Results show that increasing the vertical resolution in the UTLS does improve simulated temperatures. More importantly, double tropopause events during deep convection are reasonably similar to observation in the third WRF run and the data is retained for further analysis.

3.2 Introduction

Deep convective processes drive upper troposphere – lower stratosphere (UTLS) temperature variability and the vertical transport of tropospheric water vapor and energy to the stratosphere in the tropics (Minschwaner et al., 1996; Fueglistaler et al. 2009) and the extratropics (Roach, 1967; Poulida et al., 1996; Fischer et al., 2003). Southeast South America (SESA) has been identified as an area of large mesoscale convective systems (MCS; Velasco and Fritsch 1987) and deep convection (Zipser et al. 2006). Within SESA, the southern La Plata Basin (SLPB) has become the focus of considerable research related to MCSs and Mesoscale Convective Complexes (MCC; Durkee et al. 2009; Mulholland et al. 2018). In this region, convective initiation is influenced by complex terrain, specifically the Sierra De Cordoba Mountains and portions of the Andes Mountains (cite), and the exit of the South American Low Level Jet (SALLJ; Nogues-Peagle and Mo 1997; Vera et al. 2006; Salio et al. 2007; Montini et al. 2019). The SALLJ drives the poleward transport of heat and moisture. The low-level jet exit location contributes to terrain blocked back-building and upscale growth of MCSs and MCCs in this region (Velasco and Fritsch 1987; Rasmussen and Houze 2011; Rasmussen et al. 2014; Bruick et al. 2019). These processes contribute to some of the most intense storm systems, and deepest convection on Earth (Zipser et al. 2006; Mulholland et al. 2018; Bruick et al. 2019). The heights of the storms are capable of severe weather at the surface and influence the tropopause boundary at the cloud top. In the LPB region, storms have not been examined to understand their influence on tropopause thermodynamics and the detrainment of water vapor in the stratosphere which can be photochemically altered to destroy ozone.

Deep convection in lower latitudes is also known to produce cooler tropopause temperatures (Johnson and Kriete 1982; Gettelman et al. 2002), and cloud tops can reach heights from 17-22 km (Simpson et al. 1993). Tropopause temperatures will often have a sharp change in sign, which determines the coldest point, known as the "cold point" and represents the "lowermost stratosphere" (Holton et al. 1995; Mohanakumar 2008). The vertical transport of tropospheric air across the cold point can also lead to irreversible mixing and contribute to stratospheric chemistry. Additionally, cold point temperatures have been found to modulate moisture in air parcels, dehydrating air as it crosses very cold temperatures and ascending into the lower stratosphere (Holton and Gettelman 2001; Harmann et al. 2001). The influence of convection on cold point temperature (Kuang and Bretherton 2004; Sherwood et al. 2003; Robinson and Sherwood 2005) and water vapor (Read et al. 2004; Sherwood and Dessler 2001) in the tropics has been investigated. However, these processes have been less investigated outside the tropics, where the tropopause layer is found at lower heights which may contribute to warmer cold points, less dehydrated air parcels, and the detrainment of water vapor to higher levels.

Regions of moist deep convection can alter upper troposphere – lower stratosphere (UTLS) thermodynamics and contribute to atmospheric folding (e.g. double tropopause). UTLS double tropopause events generally occur where the tropopause height decreases rapidly between the subtropics and sub-polar region (Pan et al. 2004; Homeyer et al. 2014). These events tend to be collocated with the upper level jet stream and in South America may occur over the Andes throughout the year (Peevey et al. 2012). The influence of deep convection in the SESA on the tropopause boundary during double tropopause events and STE have not been investigated. The primary goal of this work is to simulate MCSs and deep

convection in SESA to understand their influence on UTLS exchanges, especially in the presence of double tropopause events.

While radiosonde temperature data in South America is capable of demonstrating double tropopause features, these profiles are less capable of identifying stratosphere – troposphere exchanges (STE) and the maximum level of water vapor in the lower stratosphere. More importantly, radiosonde launch sites in South America are sparsely located and generally not launched during severe thunderstorms. As a result, non-hydrostatic numerical models like the Weather Research and Forecasting (WRF) model have been utilized to identify processes related to tropopause exchanges and overshooting, which satellite and in-situ data are incapable of identifying (Robinson and Sherwood 2005; Homeyer, 2014). The WRF model is an invaluable tool as a means of investigating the influence of deep convection on UTLS exchange in a data poor region.

This study conducts WRF model simulations with two primary goals. First, to simulate MCSs and deep convection in the LPB capable of overshooting tropospheric material into the lower stratosphere and second, to detect double tropopause features in model output. For this work, WRF cumulus schemes and vertical grid spacing are tested to reproduce convective processes in the LPB to answer these questions: which cumulus scheme best represents a known MCS in the LPB? how well does the model represent the size and location of the MCS? does the model simulate water vapor in the lower stratosphere related to deep convection? does the model simulate double tropopause features? Furthermore, the output from these simulations is utilized in Chapter 4 to analyze UTLS thermodynamics, and troposphere-to-stratosphere exchange resulting in stratospheric hydration. This study is explicitly divided into two separate sections: (1) sensitivity testing of WRF cumulus schemes

and (2) sensitivity testing of WRF vertical grid resolutions. This chapter is organized as follows. The data, two case studies and WRF model parameters held constant for each run are described in section 3.3. WRF cumulus sensitive testing, validation and discussion of results are in section 3.4. Sensitivity testing of WRF vertical grid resolutions, model validation and discussion of results are in 3.5. Overall conclusions are discussed in 3.6.

3.3 Data and Methodology

3.3.1 Reanalysis data

The ERA-Interim reanalysis (ERAi) dataset produced by the European Centre for Medium-Range Weather Forecasts (ECMWF) is utilized for this work (Simmons et al., 2006; Dee et al. 2011). The horizontal resolution is approximately 0.75° latitude × 0.75° longitude (~ 83 km) with 37 vertical levels from the surface to 0.1 hPa. The interpolated pressure level gridded data set is available from 1979 to present at 6-hr intervals. Model Gridded Binary (GRIB) Data ERAi data is utilized as initial and boundary conditions in the WRF model.

3.3.2 Radiosonde data

Radiosonde data was obtained from the University of Wyoming Department Of Atmospheric Sciences Weather online data archive (http://weather.uwyo.edu/upperair/sounding.html) for stations in the greater La Plata Basin region in South America. Radiosonde data is utilized to validate each model run and is described in detail in sections 3.4.2 (cumulus testing) and 3.5.2 (vertical sensitivity testing).

3.3.3 Satellite data

Geostationary Operational Environmental Satellite (GOES) data is generated for operational meteorology and is utilized here to validate WRF model output. Initially, GOES-

13 infrared satellite imagery from the longwave window band is compared to WRF simulated outgoing longwave radiation (OLR) for the November 2012 case study (described in section 3.3.4.1). On December 18, 2017, GOES-16 replaced GOES-13 as the operational GOES-East Satellite (GOES-R 2017). The GOES-16 Advanced Baseline Imager (ABI) includes 16 different spectral bands as compared to five on the GOES-13 satellite. This work uses ABI Channel 13 with a central wavelength of 10.3 (μm) to compare to WRF simulated OLR for the November 2018 case study (described in section 3.3.4.2). GOES-16 Channel 13 IR images of the La Plata Basin and central Andes have been processes for RELAMPAGO field campaign by the National Center of Atmospheric Research (NCAR) and Earth Observing Laboratory (EOL) in Boulder, Colorado.

Tropical Rainfall Mission Measurement (TRMM) data is utilized to compare precipitation totals to WRF simulated precipitation in the La Plata Basin. TRMM data is available from 1998 – 2015 and is only used to compare precipitation in the cumulus sensitivity testing for the 2012 case study. The Precipitation Radar instrument on the satellite provide 3 hour precipitation estimates with gridded 0.25˚x 0.25˚ horizontal resolution (Huffman et al. 2007).

3.3.4 MCS case studies

3.3.4.1 Algorithm to detect MCS and deep convection in the La Plata Basin

The SLPB region is subject to convective cloud processes throughout the year. However, the highest frequency and deepest convection occurs during the austral spring and summer (Rasmussen and Houze, 2011). To determine specific case studies for further analysis, I have developed an algorithm to identify MCSs associated with deep convection in the La Plata Basin between October and March. First, the Moderate Resolution Imaging

Spectroradiometer (MODIS) satellite data is used to identify deep convection. MODIS Cloud optical thickness (COT) data is used as a proxy for cloud height. Initially, the dates, and number of grid points are collected for daily COT values greater than 100 (non-dimensional). Because station radiosonde data will be utilized to validate the WRF model, only dates and locations with available radiosonde data were identified. As a result, dates and grid points where COT are greater than 100 with available radiosonde observations are retained. Next, from the list of retained dates and location, dates with a strong potential for upscale growth are identified with convective available potential energy (CAPE) greater than 2000 J/kg. Lastly, each potential case study was evaluated to estimate the height of the MCS. Only cases with equilibrium levels (based on soundings) at ~100 hPa are retained. This algorithm has identified over 35 potential dates and locations of large MCSs with deep convection from 2002 – 2016 (based on the MODIS temporal range). Figure 1 is an example of a MCS chosen from this list. The MCC in Figure 1 demonstrates organized deep convection and the extent of large MCS which have been observed in the LPB region. This event occurred on November 29, 2012 and is utilized for case study analysis, specifically, sensitivity testing of cumulus schemes with WRF.

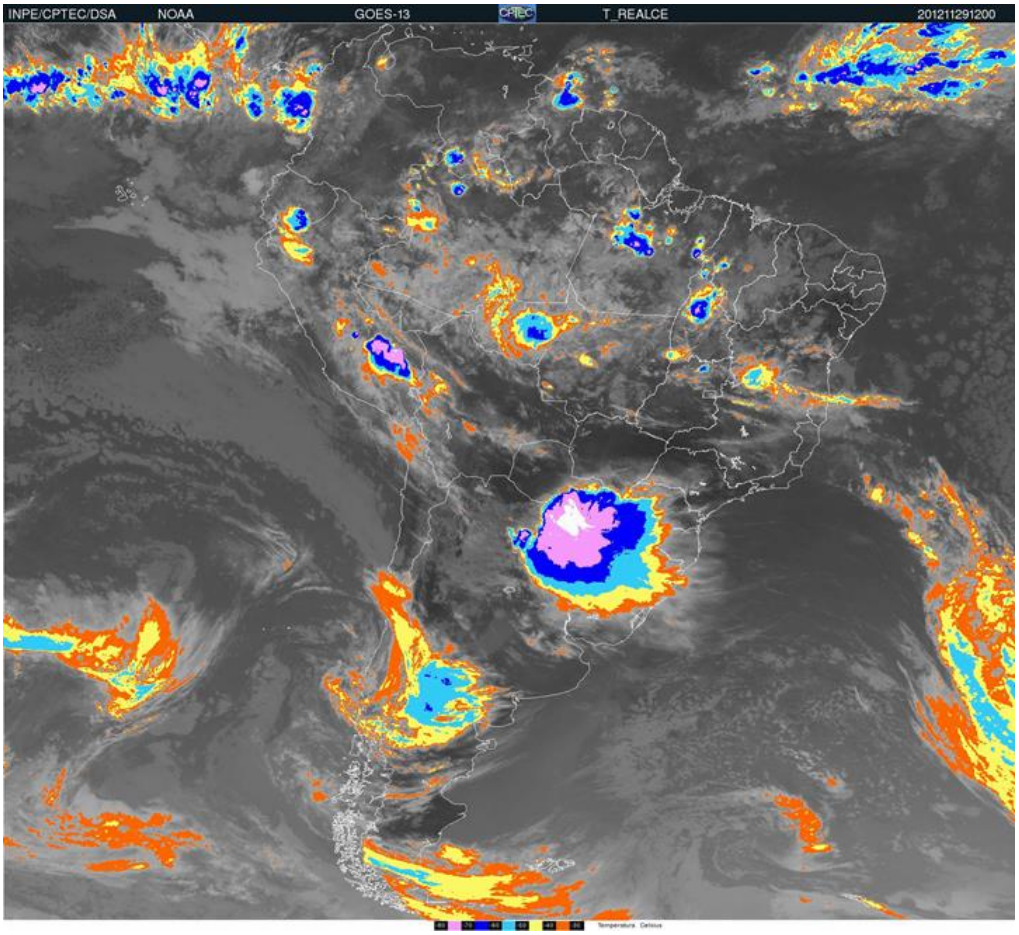

Fig. 1 GOES 13 color enhanced infrared image.

3.3.4.2 MCS case study from RLAMPAGO

A second case study is conducted from November 10 – 15, 2018 with WRF to simulate deep convention and test vertical grid spacing. The primary goal of this work is to detect double tropopause events that may contribute to lower stratospheric hydration (analysis in Chapter 4). The MCC occurred during the Remote Sensing of Electrification, Lightning, and Mesoscale/Microscale Processes with Adaptive Ground Observations (RELAMPAGO) field campaign in Cordoba, Argentina in November 2018. RELAMPAGO was designed to investigate convective processes in complex terrain with the potential for large MCSs and

severe weather. This area is within the LPB, and the field campaign investigated processes from convective initiation near the Sierra de Cordoba and Andes Mountain ranges to the production of deep convection and propagation of MCSs. This case study was chosen to investigate the prolonged influence of deep convection on the UTLS boundary. For these simulations, WRF is used to simulate stratospheric water vapor during double tropopause events. Figure 2 shows MCSs during the case study with GOES 16 IR satellite data; images are approximately 15 hours apart.

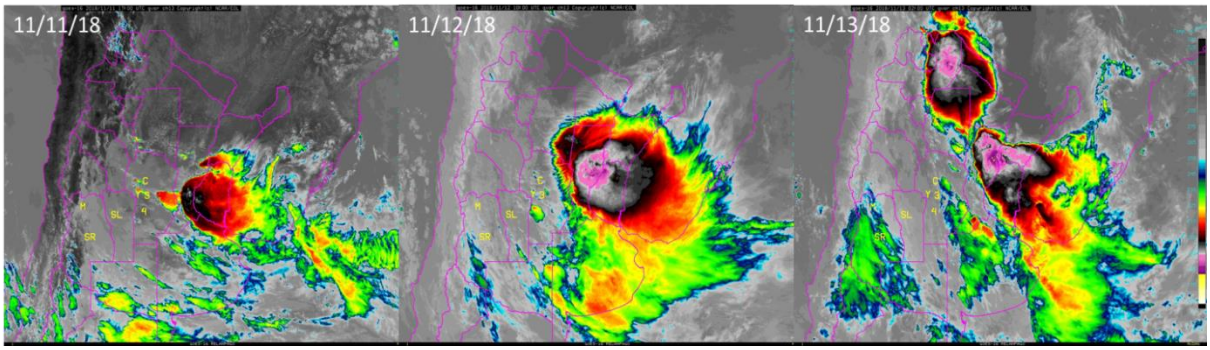

Fig. 2 NADS GOES-16 Channel 13 IR images of the La Plata Basin and central Andes were processed for the RELAMPAGO field campaign by NCAR/EOL, (left) 11/11/18 17:00 UTC, (center) 11/12/18 10:00 UTC, (right) 11/13/18 02:00 UTC.

3.3.5 WRF numerical model

The Weather Research and Forecast (WRF) numerical model version 3.9.1.1 (Skamarock et al. 2008) was utilized to simulate the MCS in the La Plata Basin. Several parameters are held constant during each model run (Table 1). Ruiz et al. (2010) performed WRF sensitivity testing of several model parameters in South America to identify optimal surface variables during the summer of 2003. They found that the best performing parameterizations included: the Yonsei University Scheme (YSU) for the Planetary

Boundary layer physics (Hong et al. 2006) and the Unified Noah Land Surface Model for the Surface layer physics (Niu et al. 2011). Other parameterizations held constant in the model include the Rapid Radiative Transfer Model for GCMs (RRTMG) scheme is used for longwave and shortwave physics (Iacono et al. 2008). The MM5 Similarity Scheme is used for the land Surface Layer physics (Paulson 1970). The model set up for sensitivity testing of the cumulus schemes are described in section 3.4, and to test the vertical resolutions in 3.5.

Parameterizations for WRF model version v3.9.1. simulations (Reference)	
Boundary layer	Yonsei University (Hong et al. 2006)
Land surface	MM5 (Paulson 1970)
Longwave radiation	RRTMG (Iacono et al. 2008)
Microphysics	Morrison 2–moment (Morrison et al. 2009)
Shortwave radiation	RRTMG (Iacono et al. 2008)
Surface layer	Noah-MP (Niu et al. 2011)

Table 1. Model parameters held constant for each simulation.

3.4 Testing Cumulus Schemes

Figure 3 shows the GOES 13 color enhanced IR imagery for the cumulus scheme testing case study. Model simulations are initiated on 28 November 2012 00 UTC and run until 01 December 2012 00 UTC. The first 12 hours of the model run is regarded as spin-up and not utilized for analysis (Maussion et al. 2014).

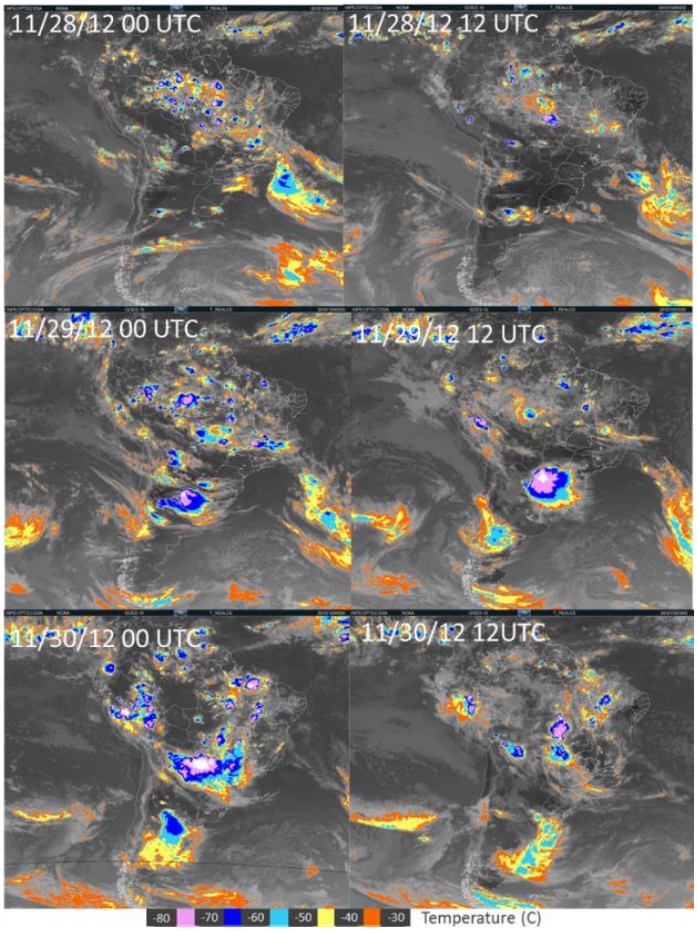

Fig. 3 GOES-13 infrared satellite imagery every from November 28 – 30, 2012 of MCS development, from pre-to-post MCS.

The model was run with two 2-way nested domains and 41 vertical levels. Because the overall interest is in the tropopause region and lower stratosphere, the model top is set at 10 hPa. Model levels are shown in Figure 4. The parent domain (D01) has 45 km grid spacing and the inner domain (D02) has 15 km grid spacing (Figure 4). The location of D01 was chosen to capture synoptic conditions surrounding the LPB, including low pressure systems propagating from the south or west, upper level westerlies across the Andes, and low-level jet activity east of the Andes transporting heat and moisture. The location of D02 was chosen based on the location of the mature MCC and deepest cloud cover on November 29, 2012 at ~12 UTC (Figure 3).

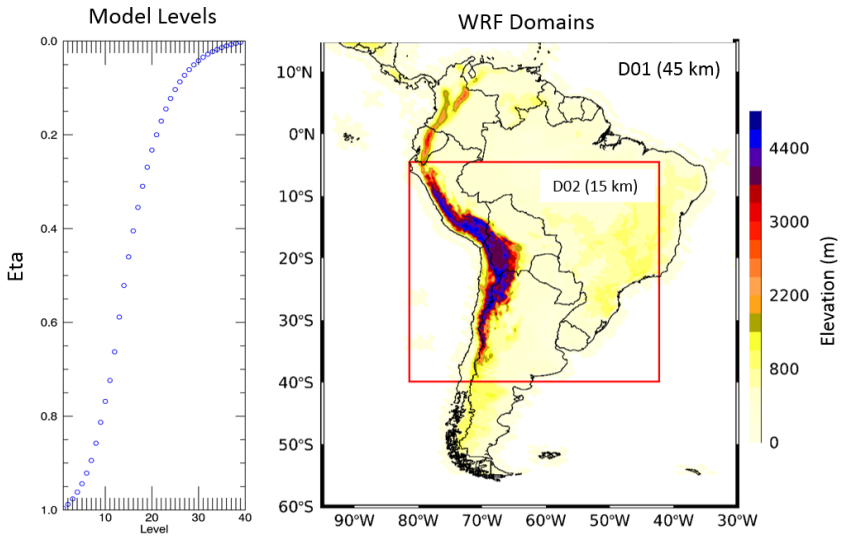

Fig. 4 WRF model domains (right) and model levels (left). Locations for radiosonde launch sites are marked with grey dots.

The physical parameters listed in Table 1 are held constant for all WRF runs. Initially, to conserve computational resources, downscaling to a 15 km horizontal resolution is performed with five cumulus schemes. The cumulus schemes tested are listed in Table 2 and a total of six runs are compared. Five WRF runs are initiated with the Morrison 2-moment microphysics scheme which accounts for five types of hydrometeors: rain, snow, cloud ice, cloud water and graupel (Morrison et al 2009).

Cumulus Schemes for WRF Simulations (Reference)
Kain–Fritsch Scheme (Kain 2004)
Grell–Freitas Ensemble (Grell and Freitas 2014)
Grell 3D Ensemble Scheme (Grell and Devenji 2002)
Betts–Miller–Janjic Scheme (Janjic 1994)
Tiedtke Scheme (Tiedtke 1989; Zhang et al. 2011)

Table 2. Cumulus schemes for sensitivity testing.

3.4.1 Model Validation and Results

Model skill is initially evaluated with GOES 13 infrared (IR) satellite imagery to estimate the size and location of the MCS. WRF simulated outgoing longwave radiation (OLR) is used as a proxy for cloud top temperature and height (Gutzler and Wood, 1990) and is compared to satellite imagery (Figure 5).

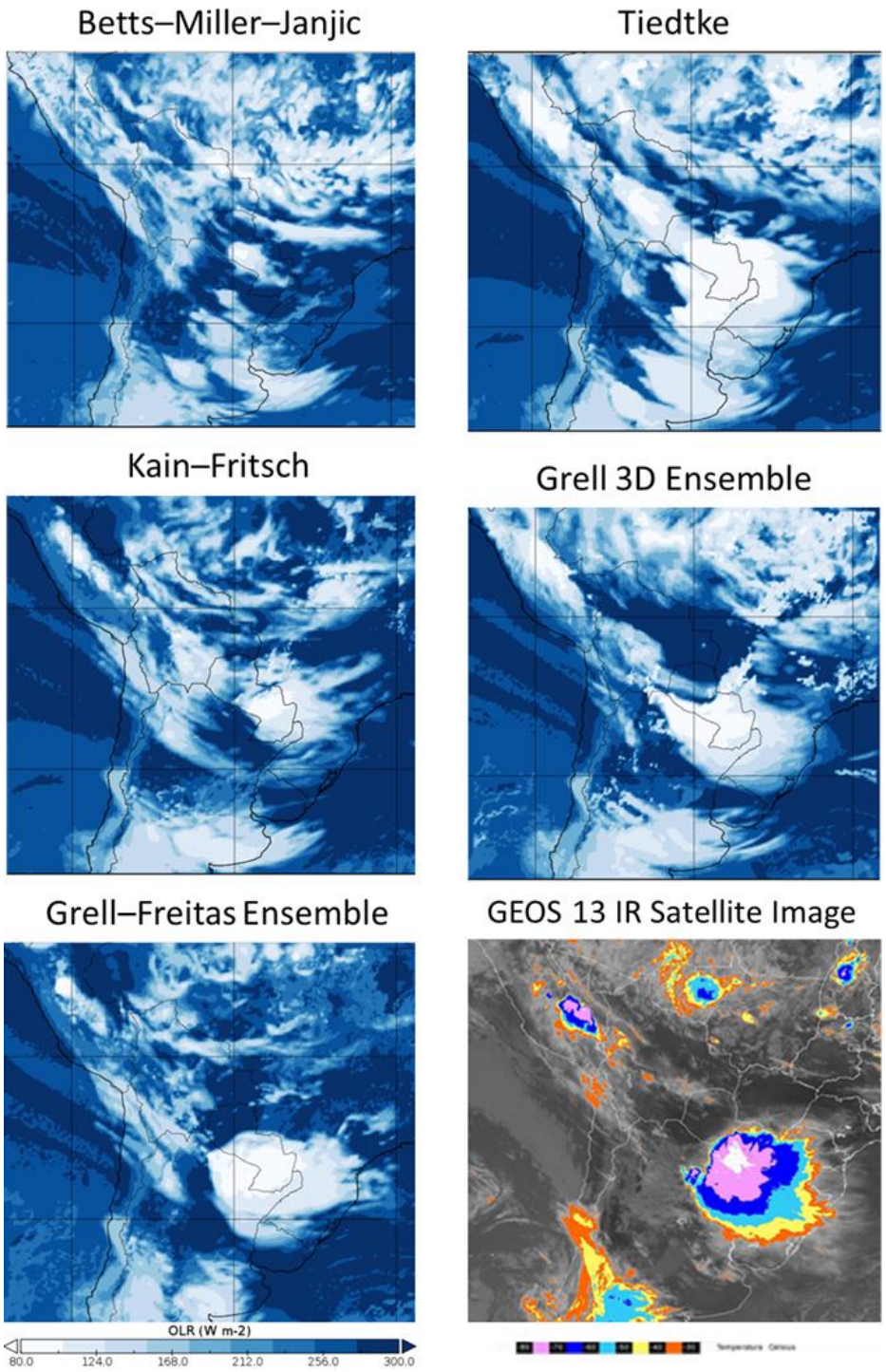

Fig. 5 WRF simulated outgoing longwave radiation (OLR) for each cumulus scheme and GOES 13 infrared (IR) image.

Overall, when visually comparing simulated OLR from the WRF runs to the GOES IR image in Figure 5, the Grell–Freitas Ensemble shows the optimal size and location of the MCC compared to other tested schemes. Additionally, the Grell-Freitas Ensemble scheme represents an evolution of the Grell 3D Ensemble scheme (Figure 5). While the Grell schemes are similar, the Grell-Freitas Ensemble scheme is able to maintain a relatively smooth transition to and from cloud-resolving scales as described by Arakawa et al. (2011). The other three runs were less successful in reproducing the observed MCC: the Tiedtke Scheme over moistens the environment and overstimulates the cloud extent, the Kain–Fritsch Scheme under simulates the cloud extent, and the Betts–Miller–Janjic Scheme does not simulate the MCC.

Next, to assess the model skill at vertical levels, radiosonde data from 12 UTC November 28, 2012 to 00 UTC December 1, 2012 at 00 and 12 UTC is used to validate the model at five standard pressure levels: 925, 850, 500, 200 and 100 hPa. Model root mean square error (RMSE) is used for all locations with all available radiosonde data (location in Figure 4). RMSE is utilized to assess the model skill of air temperature, relative humidity and wind speed as follows:

$$\text{RMSE} = \sqrt{\sum \frac{(pi-0i)^2}{N}}$$

where P is model output and O is radiosonde data. Stations with sounding data were chosen based on proximity to the MCC on 11/29/12. Model RMSE for temperature, wind speed and relative humidity is shown in Figure 6.

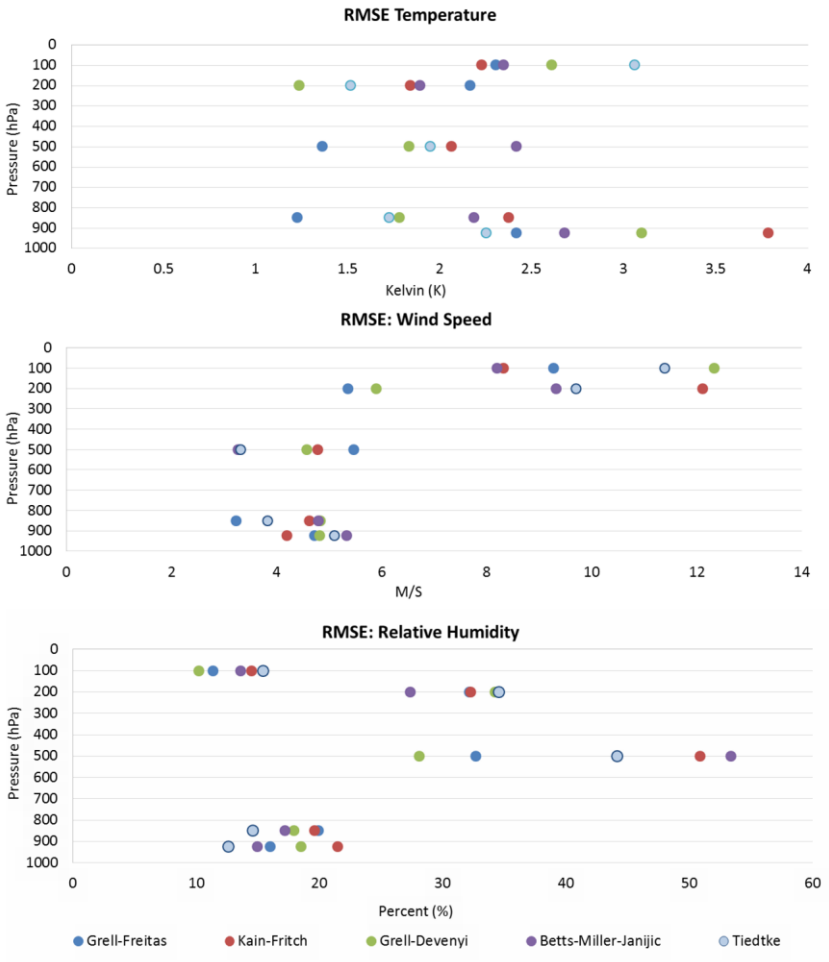

Fig. 6 Model root mean square error for temperature, wind speed and relative humidity.

Tropopause thermodynamics is of particular interest and diurnal model temperature bias is calculated with sounding output that was launched from the station nearest the mature MCS: SBFI (Fig. 4).

$$\text{Bias} = \frac{\Sigma(pi - oi)}{N}$$

Figure 7 shows the temperature bias for the Foz Do Iguacu Aero (SBFI) station data every 12 hours from 11/28 12 UTC to 12/1 00 UTC. These graphs indicate the temperature bias

before the MCS, during the mature phase, and post MCS. The MCS with deep convective processes are occurring during the 11/29 12 UTC (Figure 7 green dots/lines) and 11/30 00 UTC (Figure 7 purple dots/lines) time frames. Like the OLR comparisons to IR imagery, the WRF run with the Grell-Freitas Ensemble scheme shows has reduced temperature bias compared to other tested schemes.

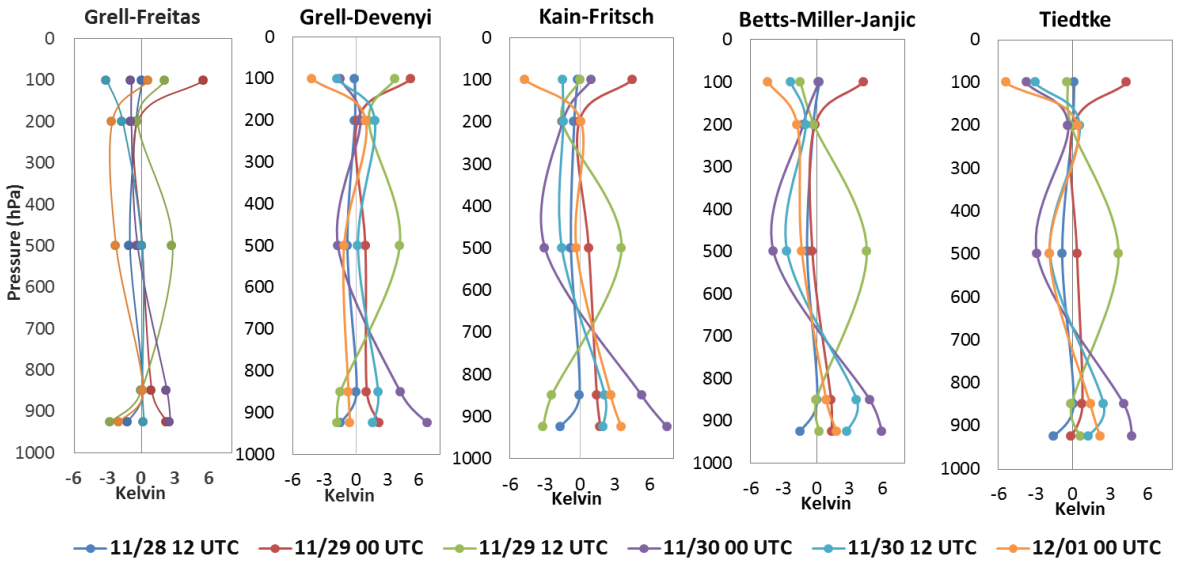

Fig. 7 Foz Do Iguacu Aero station data bias for each cumulus scheme tested. Bias is calculated every 12 hours from 11/12 12 UTC to 12/01 00 UTC.

Overall, during the mature phase of the MCS (green and purple dots), Grell-Freitas performs better than other schemes, especially at 850 and 200 hPa where very little model temperature bias is shown (Figure 7). The largest temperature bias is observed at 100 hPa, with the largest bias prior to the mature MCS phase and not during. This would require further investigation. While the Grell-Freitas Ensemble scheme has adequately simulated the size and location of the MCS, the large temperature bias in the upper tropopause – lower

stratosphere region (100 hPa) is not suitable for thermodynamic analyses and requires further WRF model testing to reduce temperature uncertainties.

3.4.2 Discussion

The case study for the sensitivity testing of cumulus schemes in South America was identified based on the algorithm described earlier, and chosen based on its horizontal extent and location of very cold cloud tops (identified with GOES 13 IR imagery). The goal is to investigate the influence of MCSs and deep convection on tropopause thermodynamics, and ultimately on the height of the detrainment of water vapor in the lower stratosphere during double tropopause events.

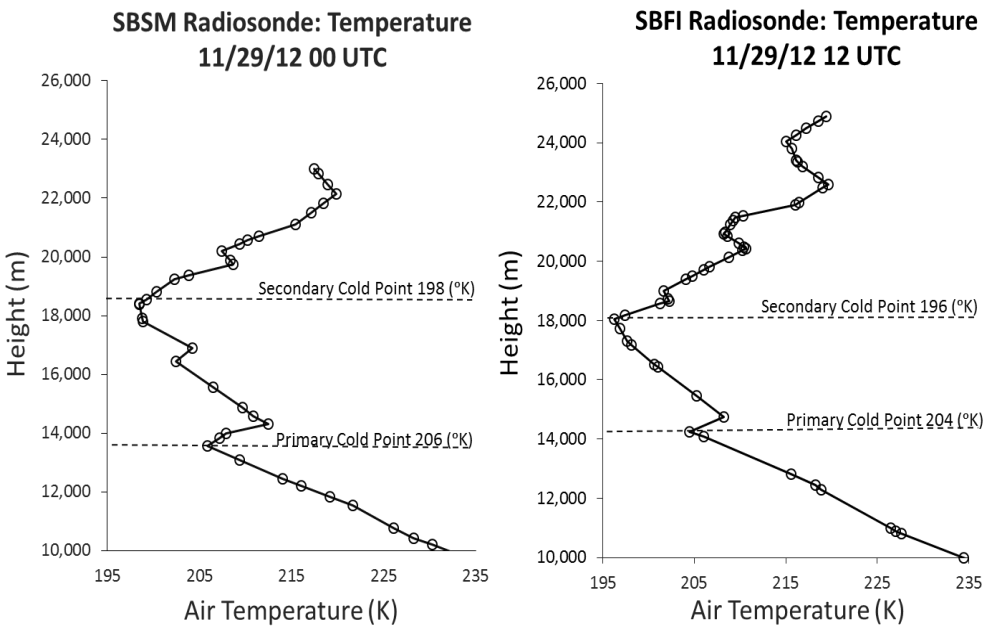

Fig. 8 Upper troposphere – Lower stratosphere station temperature data for SBSM (left) and SBFI (right).

Double tropopause events are frequent during MCSs in the La Plata Basin region of South America, and an example of a temperature profile with two cold points during this case

study is shown in Figure 8. In this region, double tropopause events can also occur due to mountain wave processes during non-convective events (not shown). The influence of these events on the lower stratosphere has not been investigated in this region. Additionally, in-situ tropopause data in South America is sparse and not adequate for determining the height of overshooting cloud tops during deep convection, as most radiosondes are not launched during severe thunderstorms. As a result, the WRF model is essential for further analysis and the first step is to identify optimal parameterizations to minimize model error.

Cumulus schemes have been tested, and the Grell-Freitas Ensemble scheme demonstrated optimal performance. However, while the WRF simulation with this Grell-Freitas Ensemble scheme adequately simulated the size and location of the mature MCS, it was not capable of adequately simulating double tropopause features. For example, when comparing radiosonde temperature data at standard pressure levels to WRF simulated temperature data at standard pressure levels, the data is smoothed and tropopause temperature features observed in the sounding data are lost. Figure 9 shows the tropopause temperature profiles for Santa Maria station data on 11/29/12, 12 UTC and WRF temperature profiles for approximately the same point. Notice the temperature profile from the sounding (Fig. 9 left panel) is showing features consistent with a double tropopause. In contrast, the WRF temperature profiles (Fig. 9 center panel) show no such features, rather these profiles (WRF D01 and D02) show a single, smoothed tropopause boundary.

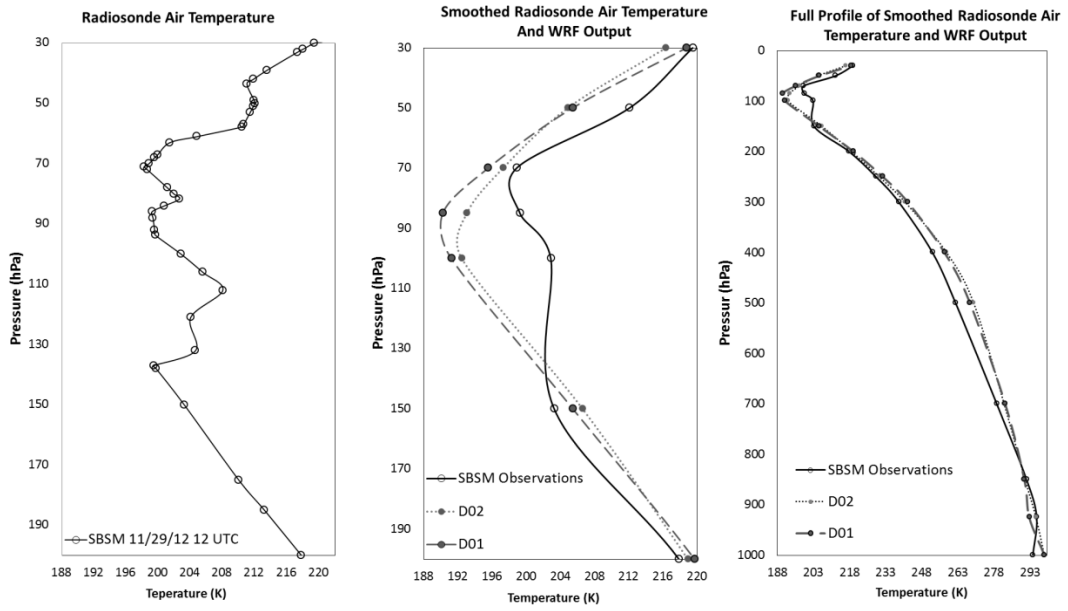

Fig. 9 The left profile shows upper troposphere – lower stratosphere SBSM sounding data on November 19, 2012, 12 UTC. The center profile shows WRF D01 (dashed line) and D02 (dotted line), and SBSM (solid line) temperature profiles on standard pressure levels above 200hPa at 12:00UTC. The right profile shows the entire profile on standard pressure levels from the surface to 10 hPa.

While the WRF model does not adequately capture double tropopause features (Figure 9), it does appear to capture expected cold point variability during the mature MCS. Figure 10 includes UTLS WRF temperature profiles for two points (red dots) during the mature MCS on November 29, from 00 to 18 UTC. For both points (a and b) the largest temperature variability is observed at 100 hPa. At his level, for location (a) the warmest cold point occurred before the MCS at 00 UTC (~199 K). At 06 UTC the temperature has decreased by 5 K, and during the mature MCS at 12 UTC, the temperature was at its coldest point (191 K). By 18 UTC cold point temperatures at 100 hPa increased and have nearly returned to pre-MCS temperatures (198 K). It should be noted that the temperatures at 150 hPa did not exhibited similar variability and temperatures above 85 hPa did not return to a

base state as quickly as at 100 hPa. At 70 hPa, for location (a) the warmest temperatures were observed just prior to the mature MCS at 09 UTC (209 K), whereas the coldest temperatures occurred post MCS (202 K).

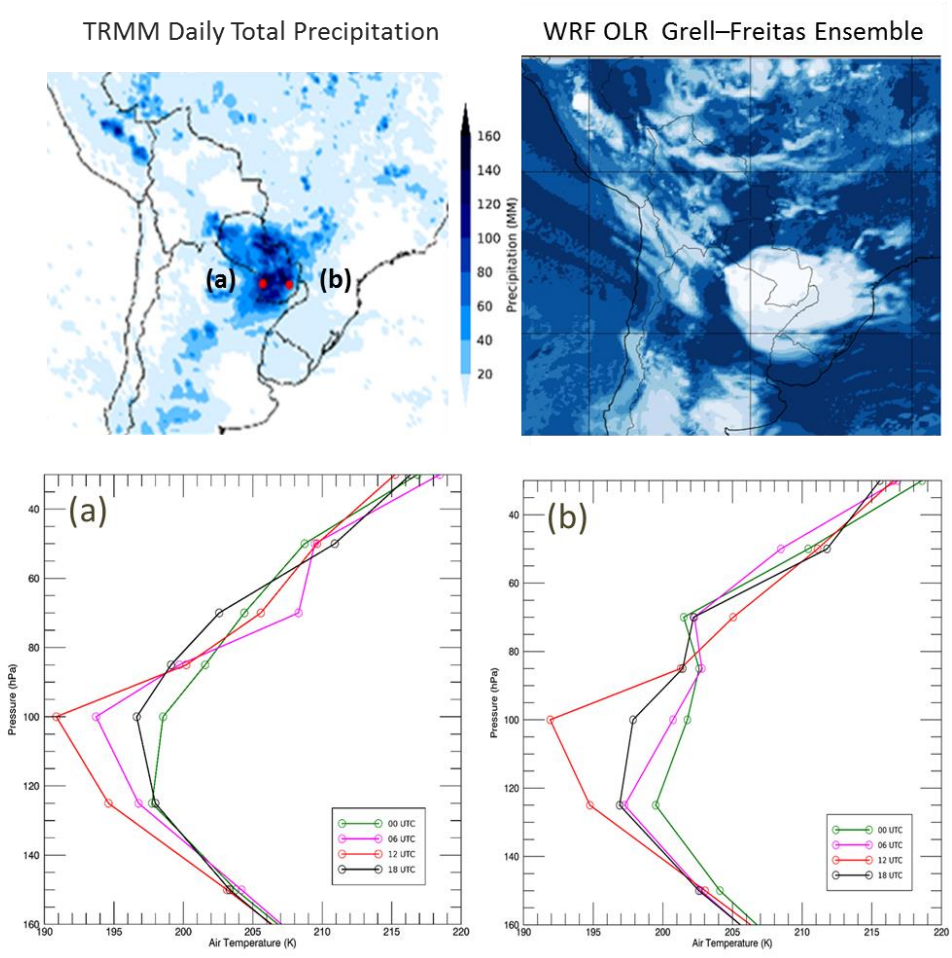

Fig. 10 UTLS temperature profiles for two points in Paraguay (a) and (b) during deep convection. Profiles are 6-hour D02 WRF simulated temperatures.

3.5 Testing Vertical Grid Resolutions to Simulate Double Tropopause Features

Sensitivity tests were performed with the WRF model at higher horizontal and vertical resolutions to simulate deep convection and double tropopause features. Model simulations were initiated on 09 November 2018 00 UTC and run until 15 November 2018 00 UTC. The parent domain (D01) has 27 km grid spacing, the second domain (D02) has 9 km grid spacing, and the inner domain (D03) has 3 km grid spacing (Figure 11). The location of D01 was chosen to capture synoptic conditions surrounding the LPB, including low pressure systems propagating from the south or west, upper level westerlies across the Andes, and low-level jet activities east of the Andes transporting heat and moisture, and the location of D03 was chosen based on the location of the mature MCC and deepest cloud cover on 12 November 2018 12 UTC (Fig. 2). The model was initiated with three 2-way nested domains and the first 18 hours were regarded as spin-up and not utilized for analysis.

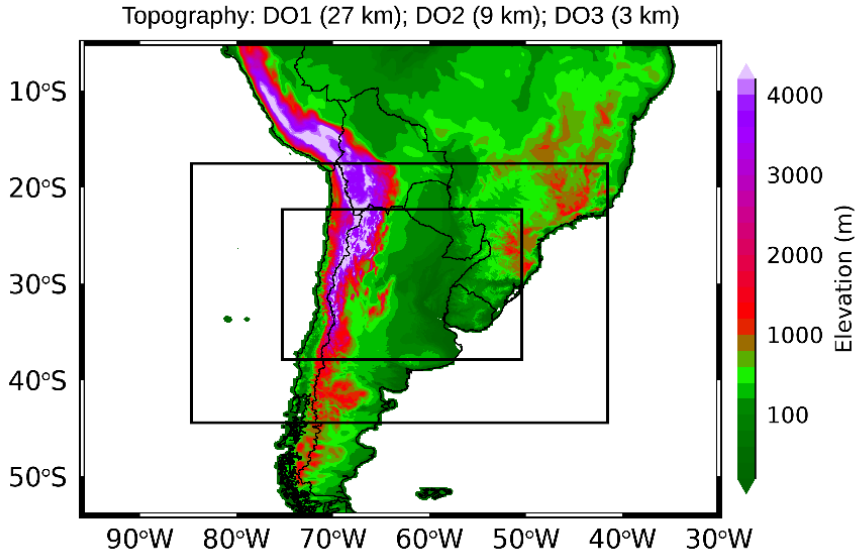

Fig. 11 WRF model domains for downscaling to 3km and vertical sensitivity testing.

WRF assigns vertical model levels based on the Eta (η) vertical coordinate system. This system is a hydrostatic-pressure vertical terrain following system based on the surface and model top boundaries with values between 1 and 0 (Skamarock et al. 2008). Because primary analyses occur in the UTLS with an emphasis on simulating observed double tropopause events, vertical sensitivity testing is performed to identify the finest vertical resolution possible in the UTLS within the D03 3 km horizontal grid spacing. First, this was accomplished by initially running WRF with 61WRF assigned η levels (R1; Fig. 12). WRF model levels for R1 are concentrated in the boundary layer to 2168 m, and equally spaced (553.7 m) until the model top of 10 hPa (~29 km). The second WRF run (R2) was also initiated with 61 levels; however, the η levels were user assigned and concentrated in the boundary layer and tropopause region (R2; Fig. 12). Next, for the third run, WRF was initialized with 81 user assigned η levels, the largest concentration of levels were located in the UTLS. This run was problematic when CFL condition errors were detected in the UTLS. It was hypothesized that transitions between η levels were not smooth enough in the UTLS. In other words, the change in height between eta levels was too abrupt in certain layers, and the grid points surrounding these abrupt changes showed the largest number of CFL condition errors. As a result, the third WRF run was re-initiated with fewer levels, 75 user assigned η levels. By reducing the number of η levels from 81 to 75, modifying the η levels to produce smoother height transitions between levels, and reducing the time step, this simulation was an improvement over the first two runs which is explained in detail in section 3.5.1. All model parameterizations were held constant during each model run (Table 1), including the Grell-Freitas cumulus scheme identified in the cumulus sensitivity testing (Section 3.4).

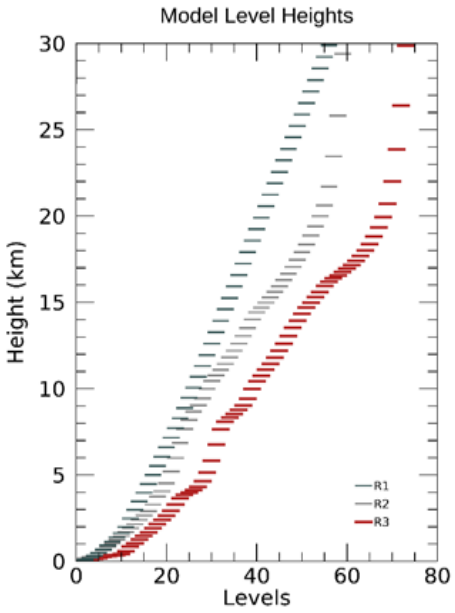

Fig. 12 WRF vertical model levels based on the Eta (η) vertical coordinate system for R1 (dark grey), R2 (light grey), and R3 (red).

3.5.1 Model Validation and Results

Like the cumulus testing, model skill is initially evaluated with infrared (IR) satellite imagery. GOES 16, channel 13 IR imagery has been provided by the RELAMPAGO field campaign. WRF simulated outgoing longwave radiation (OLR) is utilized as a proxy for cloud top temperature and height (Gutzler and Wood, 1990) and is compared to satellite imagery.

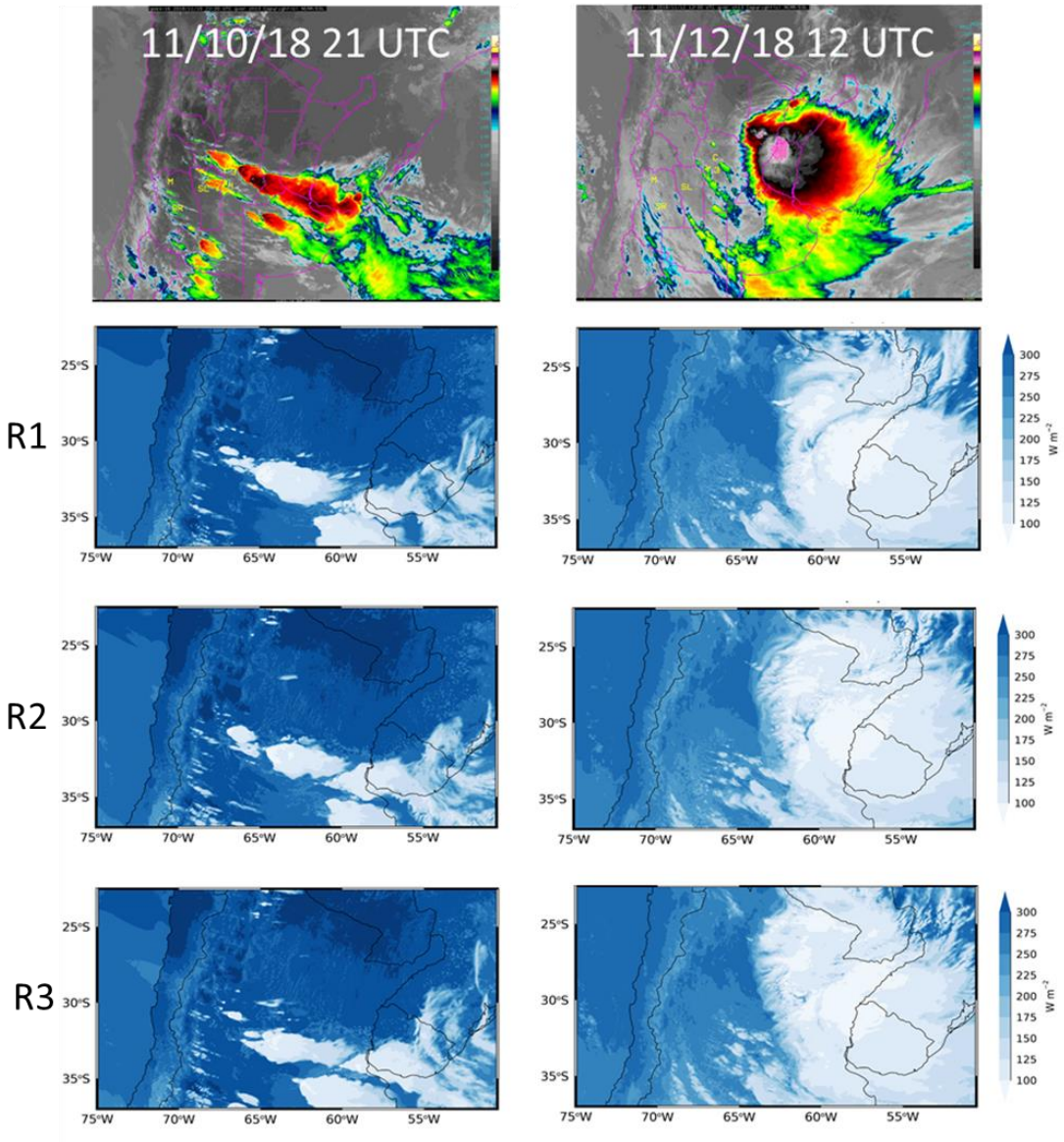

Fig. 13 WRF simulated outgoing longwave radiation (OLR) for R1, R2 and R3, and GOES 13 infrared (IR) image on 11/10 18 21 UTC (left) and 11/12/18 12 UTC (right).

Figure 13 shows GOES imagery and WRF simulated OLR for each run. Clustered discrete cells are shown on 11/10/18 21 UTC and a Mesoscale Convective Complex on 11/12/18 12 UTC. It should be noted that domain sized between the GOES 16 imagery and WRF domain 3 are not equal. Additionally, sounding data is utilized for WRF model validation at standard pressure levels from 925 – 70 hPa and double tropopause analyses.

Overall, based on visual inspection, all three runs appear to adequately simulate the size and extent of convection during both time frames. While the importance of simulating deep convection cannot be overstated, the goal for this work is to detect double tropopause features during deep convection. As a result, we continued validating these runs with sounding data, with an emphasis on upper troposphere – lower stratosphere temperatures.

Raw radiosonde data from November 10 – 15, 2018 for 00 and 12 UTC was obtained from the University of Wyoming Department Of Atmospheric Sciences weather online data archive (http://weather.uwyo.edu/upperair/sounding.html) for 8 stations in the greater La Plata Basin region in South America (Table 3). Sounding data is utilized for WRF model validation at standard pressure levels from 925 – 70 hPa and double tropopause analyses. Soundings without upper atmospheric data or soundings without standard pressure levels (e.g. SGAS) were omitted from model validation.

Id.	Number	Location	Latitude	Longitude	Launch time (UTC)
SACO	87344	Cordoba Aero	-31.3	-64.21	00 and 12
SAEZ	87576	Ezeiza Aero	-34.81	-58.53	12
SAME	87418	Mendoza Aero	-32.83	-68.78	00 and 12
SARE	87155	Resistencia Aero	-27.45	-59.05	00 and 12
SBFI	83827	Foz Do Iguacu Aero	-25.51	-54.58	00 and 12
SBSM	83937	Santa Maria	-29.72	-53.7	00 and 12
SBUG	83928	Uruguaiana	-29.78	-57.03	00 and 12
SGAS	86218	Asuncion	-25.26	-57.63	12

Table 3. List of radiosonde stations: abbreviation (id), number, location, latitude, longitude and launch time.

Model root mean square error (RMSE) is utilized to assess simulated air temperature, relative humidity, and wind speed. RMSE is calculated (section 3.4.2) for each model run and all available radiosonde data (Figure 13). Stations with sounding data were chosen based on proximity to the MCC on 11/12/18 and availability of data (Table 3). Observations were

collected for 00 and 12 UTC and RMSE is performed on standard pressure levels from 925 hPa to 70 hPa (Figure 14). Table 4 includes the vertical mean RMSE for temperature, relative humidity and wind speed. Overall, for temperature, relative humidity, and wind speed, the error is reduced in the R3 run compared to the R1 and R2 runs, especially temperature in the UTLS and lower troposphere.

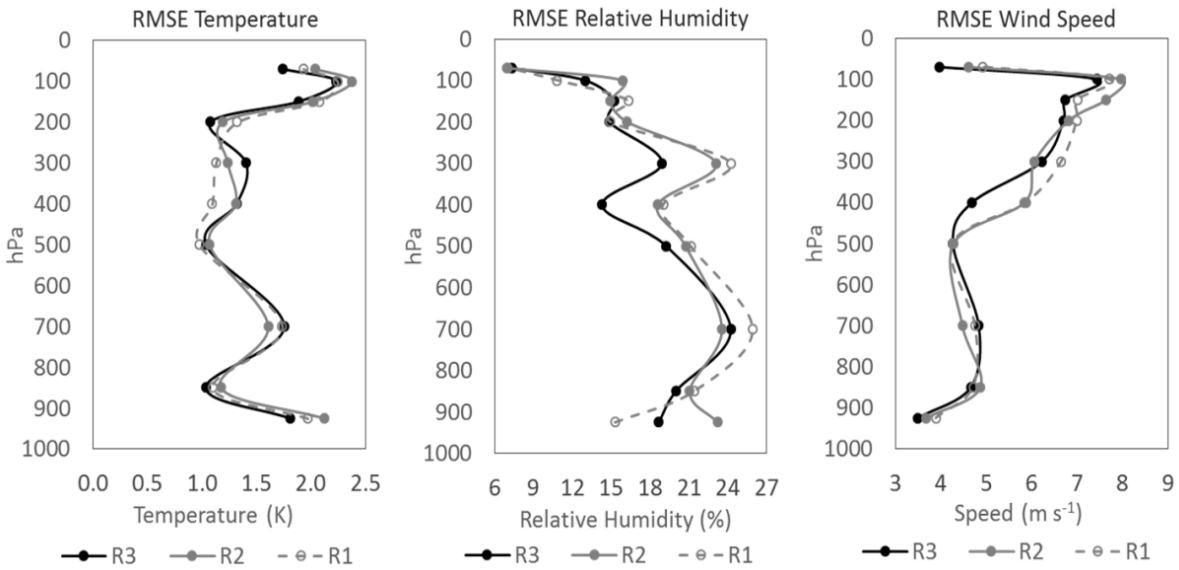

Fig. 14 Model root mean square error (RMSE) for temperature, wind speed and relative humidity.

Vertical Mean RMSE			
	R1	R2	R3
Temperature (K)	1.5587	1.6156	1.5306
Relative Humidity (%)	17.6013	18.4194	16.5775
Wind Speed (m/s)	5.6796	5.6244	5.3007

Table 4. Vertical mean RMSE for temperature, relative humidity and wind speed.

Considering the emphasis on UTLS thermodynamics, RMSE is also calculated on air temperature to evaluate each WRF run separately (Figure 15). Four locations with radiosonde

data (SARE, SAME, SBSM, and SBFI; Table 3) were chosen based on locations relative to deep convection and available data. Table 5 includes vertical mean temperature bias for each location. When averaging each run, the average temperature bias for R1 is 1.542 (K), R2 is 1.585 (K), and R3 is 1.524 (K). Overall, temperature in R3 shows an improvement compared to R1 and R2, especially in the lower troposphere and UTLS where eta model levels are concentrated.

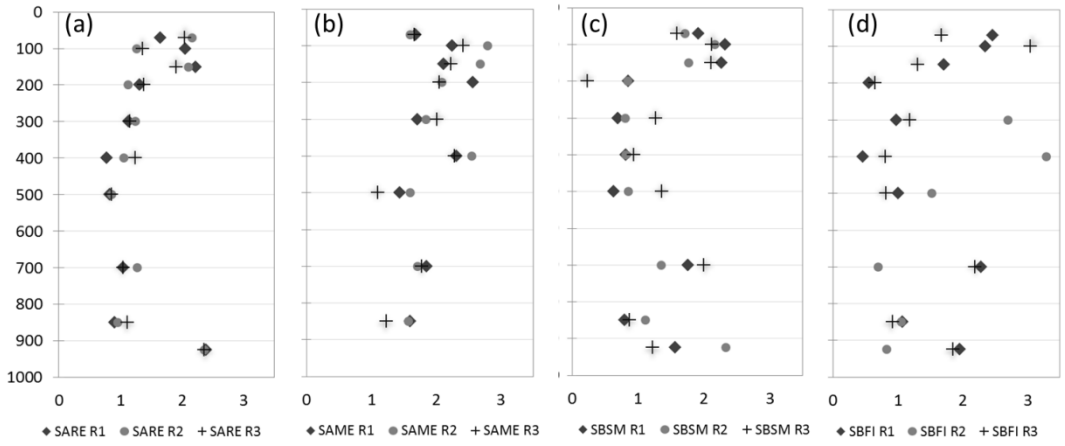

Fig. 15 Temperature (K) RMSE from SARE (a), SAME (b), SBSM (c), and SBFI (d).

Vertical Mean Temperature Bias (K)			
	R1	R2	R3
SARE	1.44240	1.44098	1.44123
SAME	1.95068	2.04901	1.86440
SBSM	1.34069	1.26932	1.38715
SBFI	1.43439	1.57987	1.40128

Table 5. Vertical mean temperature (K) bias for SARE, SAME, SBSM, and SBFI.

3.5.2 Discussion

The primary motivation for this section is to reduce WRF model error and produce UTLS temperature features for further analyses. Throughout the validation process, R3 which has user assigned WRF model levels concentrated in the UTLS, have been shown to minimize model error compared to R1 and R2. More importantly, R3 has been shown to simulate double tropopause features that are not generally exhibited in R1 or R2.

Figure 16 includes comparisons of simulated UTLS temperatures and radiosonde observations for three radiosonde sites: Santa Maria (SBSM), Foz Do Iguacu Aero (SBFI) and Mendoza Aero (SAME). Two sites, the SBSM and SBFI, were directly impacted by the MCS, whereas SAME was influenced by discrete and clustered discrete cells and mountain waves (not shown). The red lines are from radiosonde observations and show temperature features before the mature MCS 11/10/18 12 UTC (left column; Figure 16) and post MCS 11/15/18 00 UTC (right column; Figure 16). The center column in Figure 16 shows profiles during the mature MCS phase for as near as data is available. Overall, R3 (solid black line) with 75 user assigned model levels demonstrates best performance in reproducing UTLS temperature profiles compared to the observed temperatures.

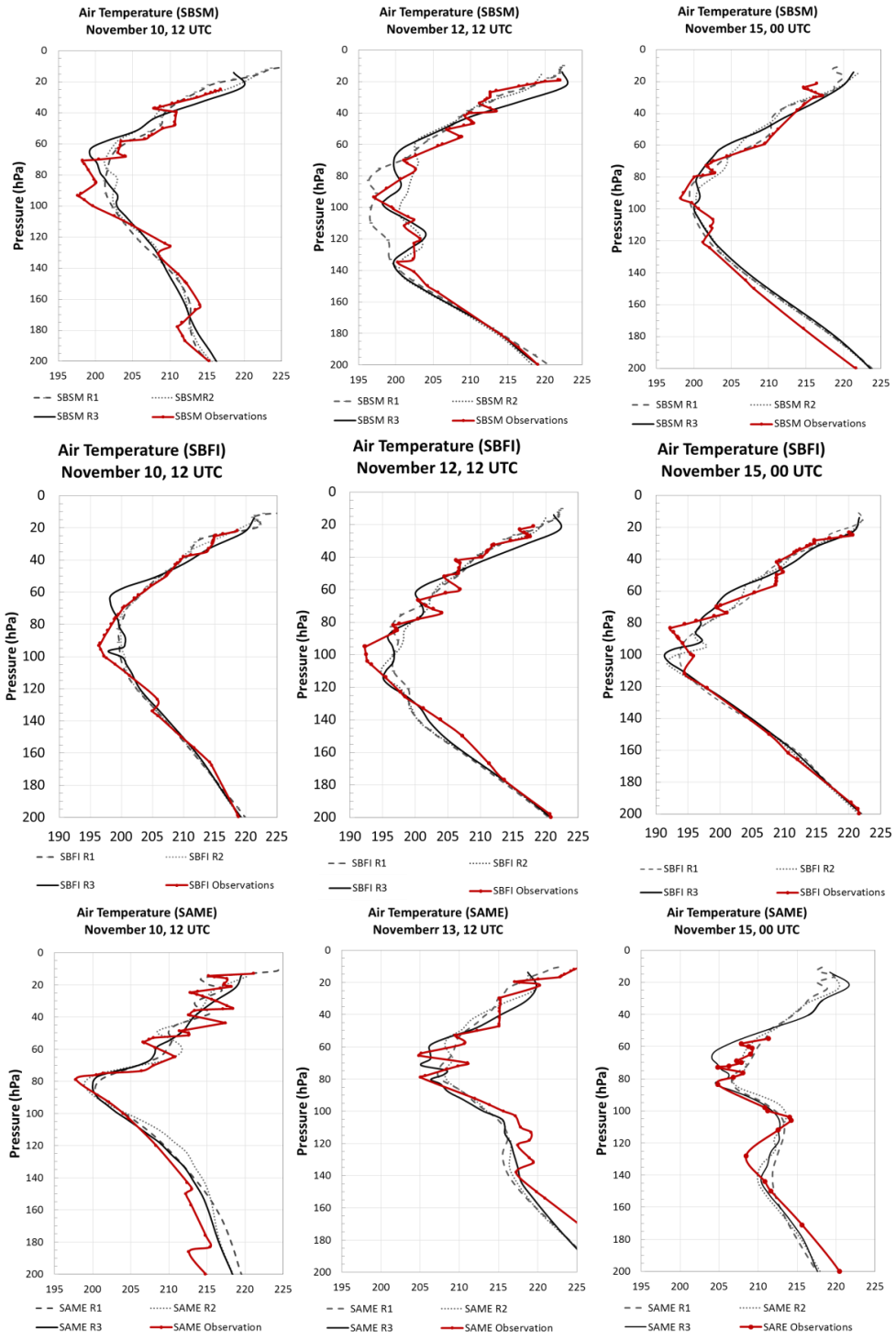

Fig. 16 Air temperature profiles for 3 stations: SBSM (top row), SBFI (middle row), and SAME (bottom row). UTLS WRF temperature for R1 (dashed line), R2 (dotted line) and R3 (solid line), and observations (red line).

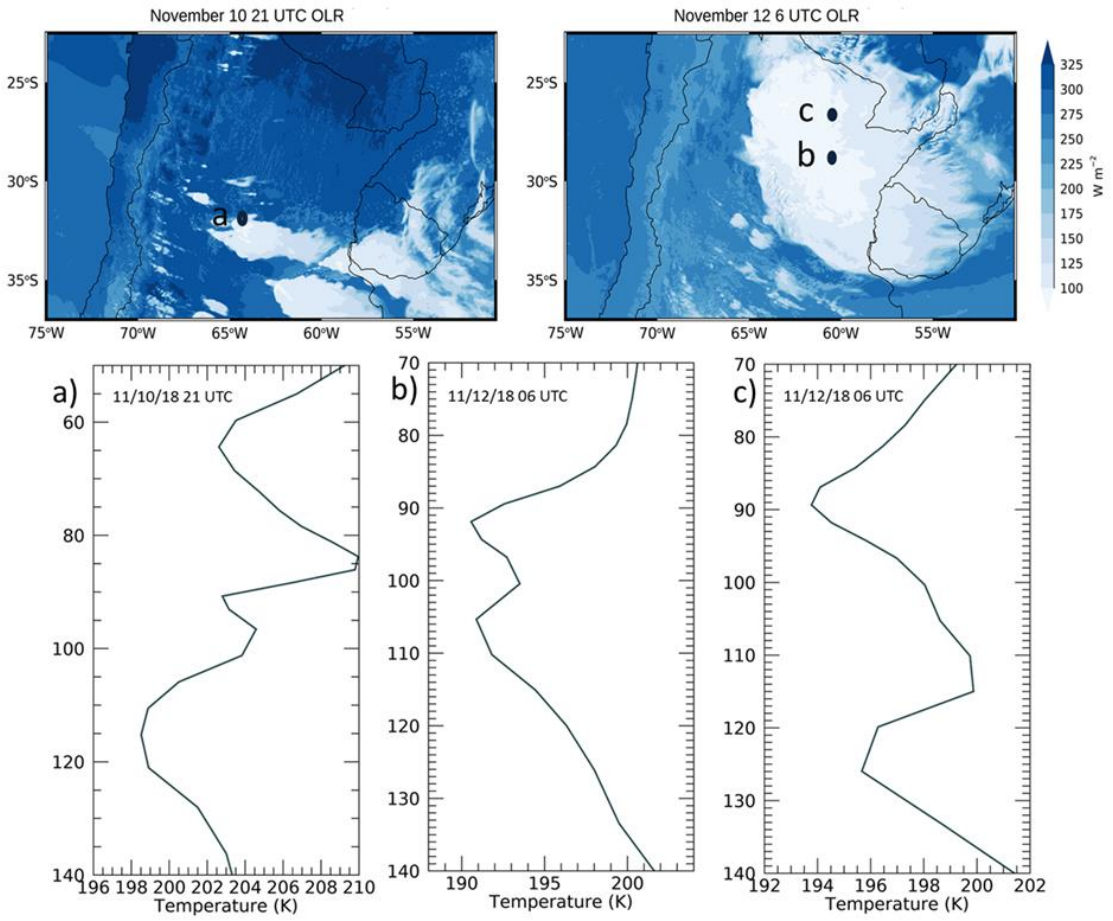

Fig. 17 WRF R3 upper troposphere – lower stratosphere air temperature collocated with deep convection. Note, x-axis temperatures are not constant for all profiles.

Figure 17 shows R3 WRF model UTLS temperature data during deep convection on 11/10/18 and 11/12/18. The model simulates double tropopause features and cold point variability. For example, an interesting feature is observed during the 11/12/18 MCS (Fig. 17 right), and grid points for two locations along the same longitude were chosen to show temperature profiles. The point at the lower latitude shows a warmer primary cold point compared to the secondary cold point, and a much larger area between cold points is observed compared to the point at the slightly higher latitude. The higher latitude grid point

indicates similar cold points and a smaller double tropopause area between cold points. This will be the bases for future work and examined in detail in Chapter 4.

3.6 Conclusions

The WRF model is initialized with ERAi reanalysis data to perform dynamical downscaling, test cumulus schemes, and test optimal vertical resolutions as a means of simulating upper troposphere – lower stratosphere (UTLS) temperature features. While the WRF model is adopted to simulate tropospheric processes like a mesoscale convective systems and deep convection, it requires sensitivity testing to minimize model error for output capable of examining their influences on UTLS exchanges. The main goal of this work is to realistically simulate double tropopause features as a means of examining UTLS exchanges.

Five cumulus schemes were tested and the Grell-Freitas Ensemble scheme demonstrated optimal performance. The case study for this work occurred on November 29, 2012, and the WRF model initiated with the Grell-Freitas Ensemble scheme adequately simulate the size and location of the mature MCS. However, this run was not capable of simulating observed UTLS thermodynamic features, and more importantly it did not adequately simulate double tropopause features. Moreover, while WRF did not adequately captured double tropopause features, it did capture expected cold point variability during the mature MCS. It was hypothesized that the lack of double tropopause features was due to the coarse vertical resolution and further sensitivity testing was required to simulate tropopause thermodynamics.

Lastly, the overarching goal for this work was to simulate observed UTLS features during deep convective events. Three WRF runs with three different vertical grid spacing were compared to determine if increasing the vertical resolution in the UTLS would produce double tropopause features, especially during the mature MCC on November 12, 2018 during the RELAMPAGO field campaign. Over the course of 4 days, the UTLS was subject to prolonged deep convection in the LPB and this was an optimal time to detect double tropopause features. Overall, R3 simulated the location and extent of the MCC reasonably well and showed an improvement in RMSE temperature and wind speed compared to R1 and R2, and more importantly, R3 temperature profiles show an improvement in double tropopause features. The WRF R3 data will be retained for further analysis of double tropopause events and lower stratospheric hydration in Chapter 4.

3.7 Acknowledgements

This research was supported by the University of California, Santa Barbara Graduate Research Mentorship Program Fellowship. The ERAi data was created by the European Centre for Medium-Range Weather Forecasts and downloaded from The National Center for Atmospheric Research. The GOES satellite data was created by the National Oceanic and Atmospheric Administration, and was downloaded from the RELAMPAGO 2018 field campaign catalog. TRMM data was acquired by an international joint project sponsored by the Japan National Space Development Agency (NASDA) and the U.S. National Aeronautics and Space Administration (NASA) Office of Earth Science.

3.8 References

Arakawa A, Jung J.-H, Wu C-M (2011) Toward unification of the multiscale modeling of the atmosphere. *Atmospheric Chemistry and Physics*, 11, 3731–3742. https://doi.org/10.5194/acp-11-3731-2011.

Bruick ZS, Rasmussen KL, Rowe AK, McMurdie LA (2019) Characteristics of Intense Convection in Subtropical South America as Influenced by El Niño-Southern Oscillation. *Mon. Wea. Rev.*. https://doi.org/10.1175/MWR-D-18-0342.1.

Dee DP, et al., (2011) The ERA-Interim reanalysis: Configuration and performance of the data assimilation system, Q. J. Roy. Meteor. Soc., 137, 553–597, doi:10.1002/qj.828.

Durkee DD, Mote TL, Shepherd (2009) The Contribution of Mesoscale Convective Complexes to Rainfall across Subtropical South America. J. Climate, 22, 4594-4605.

Fischer H, et al. (2003) Deep convective injection of boundary layer air into the lowermost stratosphere at midlatitudes, *Atmos. Chem. Phys.*, 3, 739–745.

Fueglistaler S, Dessler AE, Dunkerton TJ, Folkinsn I, Fu Q, Mote PW (2009) Tropical tropopause layer, *Rev. Geophys.,* 47, RG1004, doi:10.1029/2008RG000267.

Gettelman A, Salby ML, Sassi F (2002) Distribution and influence of convection in the tropical tropopause region. *JGR Atmospheres*, 107, ACL 6-1-ACL 6-12.

Grell GA, Devenyi D (2002) A generalized approach to parameterizing convection combining ensemble and data assimilation techniques. *Geophys. Res. Lett.*, **29**, 1693.

Grell GA, Freitas SR (2014) A scale and aerosol aware stochastic convective parameterization for weather and air quality modeling, *Atmos. Chem. Phys.*, 14, 5233-5250, doi:10.5194/acp-14-5233-2014.

GOES-R Algorithm Working Group, and GOES-R Series Program (2017): NOAA GOES-R Series Advanced Baseline Imager (ABI) Level 2 Cloud and Moisture Imagery Products (CMIP).NOAA National Centers for Environmental Information.

Gutzler DS, Wood TM, (1990) Structure of large-scale convective anomalies over Tropical Oceans. *J. Climate,* 3, 483–496.

Hartmann DL, Holton JR, Fu Q (2001) The heat balance of the tropial troppause, cirus and stratopheric dehydration. *Geophys. Res. Letters.,* 28, 1969-1972.

Holton JR, Gettelman A (2001) Horizonal transport and the dehydration of the straopshere,. *Geophys. Res. Lett.,* 28, 2799-2802.

Holton JR, Haynes PH, McIntyre ME, Douglass AR, Rood RB, Pfister L (1995) Stratosphere-troposphere exchange, *Rev. Geophys.,* 33(4), 403–439. doi:10.1029/95RG02097.

Homeyer CR, et al., (2014) Convective transport of water vapor into the lower stratosphere observed during double tropopause events, *J. Geophys. Res. Atmos.,* 119, 10 941–10 958, doi:10.1002/2014JD021485.

Hong SY, Noh Y, Dudhia J (2006) A new vertical diffusion package with an explicit treatment of entrainment processes. *Mon. Wea. Rev.*, **134**, 2318–2341. doi:10.1175/MWR3199.1.

Huffman GJ, Bolvin DT, Nelkin EJ, Wolff DB , Adler RF, Gu G, Hong Y, Bowman KP, Stocker EF (2007) The TRMM Multisatellite Precipitation Analysis (TMPA): Quasi-Global, Multiyear, Combined-Sensor Precipitation Estimates at Fine Scales. *J. Hydrometeor.*, **8**, 38–55, https://doi.org/10.1175/JHM560.1.

Iacono MJ, et al., (2008) Radiative forcing by long–lived greenhouse gases: Calculations with the AER radiative transfer models. *J. Geophys. Res.,* 113, D13103.

Janjic ZI (1994) The Step–Mountain Eta Coordinate Model: Further developments of the convection, viscous sublayer, and turbulence closure schemes. *Mon. Wea. Rev.*, **122**, 927–945.

Johnson R, Kriete D (1982) Thermodynamic circulation characteristics of winter monsoon tropical mesoscale convection. *Mon. Wea. Rev.,* **110,** 1898–1911.

Kain J.S. (2004) The Kain–Fritsch convective parameterization: An update. *J. Appl. Meteor.*, **43**, 170–181.

Kuang Z, and Bretherton C (2004) Convective influence on the heat balance of the tropical tropopause layer: A cloud-resolving model study. *J. Atmos. Sci.,* 61, 2919-2927.

Maussion F, Scherer D, Molg T, Collier E, Curio J, Finkelnburg R (2014) Precipitation seasonality and variability over the Tibetan Plateau as resolved by the High Asia Reanalysis. *J Climate* 27:1910-1927.

Minschwaner K, et al. (1996) Bulk properties of isentropic mixing into the tropics in the lower stratosphere, *J. Geophys. Res.*, **101**, 9433–9439.

Mohanakumar K. (2008) Stratosphere Troposphere Interactions: An Introduction. Springer: London, United Kingdom.

Montini TL, Jones C, & Carvalho LMV (2019) The South American low-level jet: A new climatology, variability, and changes, *Journal of Geophysical Research: Atmospheres*, 124, 1200–1218. https://doi.org/10.1029/2018JD029634.

Morrison H, Thompson G, Tatarskii V (2009) Impact of Cloud Microphysics on the Development of Trailing Stratiform Precipitation in a Simulated Squall Line:

Comparison of One– and Two–Moment Schemes. *Mon. Wea. Rev.*, 137, 991–1007. doi:10.1175/2008MWR2556.1.

Mulholland JP, Nesbitt SW, Trapp RJ, Rasmussen KL, Salio PV (2018) Convective Storm Life Cycle and Environments near the Sierras de Córdoba, Argentina. *Mon. Wea. Rev.*, **146**, 2541–2557, https://doi.org/10.1175/MWR-D-18-0081.1.

Niu GY, et al (2011) The community Noah land surface model with multiparameterization options (Noah–MP): 1. Model description and evaluation with local–scale measurements. *J. Geophys. Res.,* 116, D12109.

Nogués-Paegle J, Mo KC (1997) Alternating wet and dry conditions over South America during summer. *Mon. Wea. Rev.*, **125**, 279–291.

Pan LL, Randel WJ, Gary BL, Mahoney MJ, Hintsa EJ. (2004) Definitions and sharpness of the extratropical tropopause: a trace gas perspective. *Journal of Geophysical Research*, 109: D23103. doi:10.1029/2004JD004982.

Paulson CA (1970) The mathematical representation of wind speed and temperature profiles in the unstable atmospheric surface layer. *J. Appl. Meteor*., 9, 857–861.

Peevey TR, Gille JC, Randall CE, Kunz A (2012) Investigation of double tropopause spatial and temporal global variability utilizing High Resolution Dynamics Limb Sounder temperature observations, *J. Geophys. Res.*, 117, D01105, doi:10.1029/2011JD016443.

Poulida O, Dickerson RR, Heymsfield and A (1996) Stratosphere-troposphere exchange in a midlatitude mesoscale convective complex: 1. Observations, *J. Geophys. Res.*, **101**, 6823–6836.

Rasmussen K., Houze RA (2011) Orogenic Convection in Subtropical South America as Seen by the TRMM Satellite. *Mon. Weather Rev.*, **139**, 2399–2420, doi:10.1175/MWR-D-10-05006.1.

Rasmussen, KL, Zuluaga MD, Houze Jr. RA (2014) Severe convection and lightning in subtropical South America, *Geophys. Res. Lett.*, 41, 7359–7366, doi: 10.1002/2014GL061767.

Read WG et al. (2004) Dehydration in the tropical tropopause layer: Implication from the UARS Microwave Limb Sounder. *J. Geophys. Res*, 109.

Roach WT (1967) On nature of summit areas of severe storms in Oklahoma, *Q. J. R. Meteorol. Soc.*, 397, 318–336.

Robinson FJ, Sherwood SC (2005) Modeling the impact of entrainment on the tropical tropopause, *AMS*, 63, 1013-1027.

Ruiz JJ, Saulo C, Nogués-Paegle J. (2010) WRF Model Sensitivity to Choice of Parameterization over South America: Validation against Surface Variables. *Mon. Wea. Rev.*, **138**, 3342–3355, https://doi.org/10.1175/2010MWR3358.1.

Salio P, Nicolini M, Zipser EJ (2007) Mesoscale Convective Systems over Southeastern South America and Their Relationship with the South American Low-Level Jet, *Mon. Wea. Rev.*, 135, 1290–1309.

Sherwood SC, Horinouchi T, Zeleznik A (2003) Convective impact on temperatures observed near the tropical tropopause. *J. Atmos. Sci.*, 60, 1847-1856.

Sherwood SC, Dessler AE (2001) A model for transport across the tropical tropopause. *J. Amos. Sci*., 58, 765-779.

Simmons A, Uppala S, Dee D, Kobayashi, S (2006) ERA-Interim: New ECMWF reanalysis products from 1989 onwards, ECMWF newsletter, 110, 26–35.

Simpson J, Keenan TD, Ferrier B, Simpson RH, Holland GJ (1993) Cumulus mergers in the maritime continent region. *Meteor. Atmos. Phys.*, 51, 73-99.

Skamarock, WC, Klemp JB, Dudhia J, Gill DO, Barker DM, Duda MG, Huang X-Y, Wang W, Powers JG (2008) A Description of the Advanced Research WRF Version 3. NCAR Technical Note NCAR/TN-475+STR, doi:10.5065/D68S4MVH.

Tiedtke M (1989) A comprehensive mass flux scheme for cumulus parameterization in large–scale models. *Mon. Wea. Rev.*, **117**, 1779–1800.

Velasco I., Fritsch JM , (1987) Mesoscale convective complexes in the Americas. *J. Geophys. Res. Atmospheres*, **92**, 9591–9613, doi:10.1029/JD092iD08p09591.

Vera C, et al. (2006) The South American Low-Level Jet Experiment. *Bull. Amer. Meteor. Soc.*, **87**, 63–77.

Zhang, C, Wang Y, Hamilton K, (2011) Improved representation of boundary layer clouds over the southeast pacific in ARW–WRF using a modified Tiedtke cumulus parameterization scheme. *Mon. Wea. Rev.*, **139**, 3489–3513.

Zipser EJ, Cecil DJ, Liu C, Nesbitt SW, Yorty DP (2006) Where are the most intense thunderstorms on Earth. *Bull. Am. Meteorol. Soc.*, 87, 1057–1071.

Chapter 4:

Evaluating the Influence of Deep Convection on Tropopause Thermodynamics and Lower Stratospheric Water Vapor: A RELAMPAGO Case Study Using the WRF Model

4.1 Abstract

Lower stratospheric ozone is heavily regulated by tropospheric weather phenomena influencing tropopause thermodynamics and exchanges of mass between the troposphere and stratosphere. This exchange is driven by deep convective cloud processes capable of overshooting water and contributing to stratospheric chemistry and ultimately to ozone destruction. The La Plata Basin is a region in South America known for organized deep convective processes during the austral spring. However, lower stratospheric hydration related to deep convection has not been investigated yet. This study employs the Weather Research and Forecasting numerical model to simulate deep convection from November 10 – 15, 2018 during the Remote sensing of Electrification, Lighting and Mesoscale/microscale processes with adaptive Ground Observations (RELAMPAGO) field campaign in Argentina. The focus of this work is to investigate UTLS thermodynamics, especially double tropopause events and identify lower stratospheric hydration related to deep convection. Three deep convection systems are analyzed and compared: discrete cells, a mesoscale convective complex (MCC) and a squall line. Results show that double tropopause events occurred during each convective systems and the highest overshooting is associated with larger distances between the primary and secondary tropopause layers. This study identifies lower stratospheric hydration in both of the organized convective modes, MCC and squall line, but

not in the discrete cells. While UTLS moisture is present in all three convective types, during the discrete cell, the mixing of ice and water vapor inhibits net positive buoyancy preventing updrafts from transporting tropospheric material aloft. During the MCC and squall line events, UTLS moisture is stratified. A dry water vapor layer in the tropopause is collocated with an ice layer where net positive buoyancy is contributing to stratospheric hydration as high as 20 km.

4.2 Introduction

The tropopause region is known for troposphere-stratosphere exchanges and lower stratospheric water vapor is known to influence Earth's radiation budget (Holton et al. 1995). Because air primarily enters the stratosphere in the tropics, the air near the tropical tropopause behaves as a boundary for the global stratosphere (e.g. Brewer 1949). In this regard, most changes to the lower stratosphere are generally attributed to the vertical transport of tropospheric gases during deep convection at the tropical tropopause boundary (Khaykin et al. 2009). While deep convection is responsible for water vapor and ice particle transport to the lower stratosphere in the tropics (e.g. Brewer 1949), outside the tropics, the influence of deep convection on tropopause thermodynamics and detrainment of ice and water vapor in the lower stratosphere is less understood.

Investigating troposphere to stratosphere exchanges related to convective transport capable of modulating tropopause thermodynamics is vital to understanding stratospheric water vapor (WV). Stratospheric water vapor is a key player in stratospheric climate and chemistry and is an important greenhouse gas controlling the temperature of the stratosphere (Forster and Shine 2002). Increased stratospheric water vapor has been shown to decrease

stratospheric ozone (e.g. Stenke and Grewe 2005), which can produce warming in the troposphere and cooling in the stratosphere (Manabe and Strickle 1964; Solomon et al. 2010). The vertical transport of tropospheric air across the tropopause, especially the "cold point" (Holton et al. 1995), which generally represents the "lowermost stratosphere" (Mohanakumar 2008), can lead to irreversible mixing and contribute to stratospheric photochemistry (Hartmann et al. 2013) via water vapor oxidation and catalytic reactions (Bates and Nicolet 1950).

Tropospheric air, including water vapor and ice crystals, can be transported via deep convection to the lower stratosphere in the extratropics (Roach, 1967; Poulida et al., 1996; Fischer et al., 2003). Tropopause temperatures are generally warmer in the extratropical tropopause compared to the tropical tropopause (Dessler et al. 1995). Warmer cold point temperatures in the extratropics, compared to tropical cold point temperatures, are generally capable of larger troposphere to stratosphere exchanges, and may lead to higher water vapor mixing ratios in the lower stratosphere (Dessler et al., 2004; Dessler et al. 2013). Additionally, regions of moist deep convection can alter UTLS thermodynamics and contribute to atmospheric folding (e.g. double tropopause).

UTLS double tropopause events generally occur where the tropopause height decreases rapidly between the subtropics and sub-polar regions (Pan et al. 2004; Homeyer et al. 2014a). In South America, this is observed in the southern LPB. These events tend to be collocated to the upper level jet stream, and may occur over the central Andes Mountain range throughout the year (Peevey et al. 2012). Generally speaking, a double tropopause event has two cold points, where a stable layer of stratospheric air is found below a less stable layer of troposphere air. The introduction of warmer stratospheric air near the

lowermost cold point may contribute to instability during a deep convective event. Furthermore, this instability between cold points may influence the height of maximum water vapor levels in the stratosphere.

Stratospheric ozone chemistry is initially dependent on solar radiation - ozone chemically responds to ultra violet radiation (UV) to produce excited oxygen atoms. When excited, oxygen atoms interact with water vapor, the response is the production of a hydroxyl free radical (e.g. Seinfeld and Pandis 1998). Furthermore, when the hydroxyl free radical interacts with an ozone molecule, the ozone molecule is converted into two oxygen molecules. Ultimately, ozone in the stratosphere is naturally created and destroyed through photochemical reactions. However, stratospheric water vapor becomes a catalyst for further ozone destruction (Stenke and Grewe 2005). The impact of decreased ozone in the stratosphere is an increase in UV radiation transferred to the troposphere (Forster and Shine 1999).

Regions with deep convective processes capable of troposphere-stratosphere exchange and the vertical transport of water vapor to the stratosphere are generally understood to be localized in the tropics. However, several studies have analyzed regions with convective overshooting in the subtropics and mid-latitudes (Laing and Fritsch 1997; Brooks et al. 2003; Zipser et al. 2006; Liu and Liu 2016; Smith et al. 2017). Zipser et al. (2006) examined extreme thunderstorm events using several proxies for convective intensity and identified several regions with deep convection outside the tropics, including the central U.S. and southeast South America. They found cases in the United States, especially in the Midwestern region, where convective cloud top heights were capable of reaching up to18.25 km.

Hurst et al. (2011) investigated water vapor in the lower stratosphere due to convective overshooting in the central U.S. by examining the chemical changes with balloon-borne measurements of stratospheric WV (1980-2010) over Boulder, Colorado (40˚N). They showed an increase in stratospheric WV of ~1 ppmv (almost 30%) between 16 - 26 km (~100 - 10 hPa), and found that modeled stratospheric WV trends are predominantly driven by two processes: the warming of the cold point temperature (CPT) and the strengthening of the Brewer-Dobson circulation (Revell et al. 2016). Tropopause boundary processes connected to CPT are the strongest regulator of cross boundary transport of gasses to and from the stratosphere.

Homeyer et al. (2014a; 2015) utilized the Weather Research and Forecasting (WRF) model to conduct sensitivity testing of cloud microphysics parameterizations and analyze stratosphere – troposphere exchanges. Homeyer et al (2014a) investigated the direct injection of water vapor in the stratosphere via deep convective processes in the central U.S. Their simulations reproduced the vertical extent of each convective system modeled and showed that double tropopause events were associated with tropospheric air higher in the stratosphere, compared to single tropopause events. Additionally, Homeyer et al. (2014b) investigated a Mesoscale Convective System (MCS) and a cold front with in situ aircraft observation in the central United States in May 2012. That study was conducted to better understand lower stratospheric water vapor variability and stability during double tropopause events. Their analysis of in-situ data has shown that large-scale double tropopause events drive tropospheric air deep into the lower stratosphere influencing stratospheric chemistry.

While considerable research has been centered on the central United States, similarities exist between atmospheric dynamics, topography, and climatological features of

the mid-west region of the United States and the LPB of South America. Both regions have a long north-south mountain range (Rocky Mountains in the U.S and Andes Mountains in South America), they are influenced by low level jets transporting moisture from the tropics on the eastern side of the mountain chain (Higgins et al. 1997; Montini et al. 2019), and they have summer monsoonal processes that act to create conditions for the initiation and development of deep convective thunderstorm activity (Vera et al. 2006; Salio et al., 2007). The research conducted on the extratropical United States has been focused on frontal systems and mesoscale convective processes, their relationship to tropopause boundary dynamics, and lower stratospheric radiative processes. Similar results may be found in the LPB region of South America.

The LPB region in South America, including the Sierra De Cordoba Mountains and portions of the eastern Central Andes Mountains, is subject to deep convection and mesoscale convective systems (MCS; Rasmussen and Houze, 2016; Romatschke and Houze, 2010; Rasmussen and Houze, 2011) capable of influencing the UTLS. The RELAMPAGO (Remote sensing of Electrification, Lighting and Mesoscale/microscale processes with adaptive Ground Observations) field campaign was conducted in the austral spring from November 1 to December 16 in 2018 to investigate convective processes in the LPB between Cordoba and San Rafael in Argentina. The focus of this campaign was on the initiation and intensity of convective systems in the region, especially on the formation severe weather, mesoscale convective systems and deep convection.

Although considerable research has been conducted to identify deep convection in the LPB, the influence of deep convection on the tropopause layer, troposphere - stratosphere exchanges and relationships between convection and double tropopause events has not been

investigated yet. The primary goal of this work is to investigate mesoscale characteristics of deep convection in the LPB, identify double tropopause events and lower stratospheric hydration with the WRF model during case studies. This study examines in detail tropopause thermodynamics, especially troposphere to stratosphere exchange related to warm primary cold points and the corresponding level of maximum water vapor concentrations in the stratosphere.

For this work, a 4-day case study during the RELAMPAGO field campaign is presented. The WRF model (Skamarock et al. 2008) is utilized to simulate deep convection (described in detail in Chapter 3), and model data is analyzed to understand UTLS thermodynamics and lower stratosphere hydration. The main goal of this chapter is to answer a fundamental question: Are deep convective events hydrating the lower stratosphere in the LPB? If yes, can WRF simulate these events? Other questions addressed include: Are double tropopause events related to stratospheric hydration in the LPB? What are the primary mechanisms driving lower stratospheric hydration in the LPB? Lastly, this study compares the temperatures of primary and secondary tropopause levels to answer the question: Do warm primary tropopause events contribute to instability between tropopause layers and increase the heights of maximum level of water vapor in the lower stratosphere when compared to cold primary tropopause events? These questions will be addressed based on three types of deep convective systems: discrete convective cells, a mesoscale convective complex, and a squall line related to a cold front boundary. The study is organized as follows. The data is described in section 4.2. The WRF model configurations, sensitivity tests, and model validations are described in detail in Chapter 3. The synoptic conditions related to the large-scale formation of deep convective events are described in section 4.3. Stratospheric

water vapor is discussed in section 4.4. UTLS thermodynamics and lower stratospheric hydration is discussed in section 4.5. Conclusions are discussed in section 4.6.

4.3 Data

4.3.1 In-situ Observations

Raw radiosonde data from November 10 – 15, 2018 for 00 and 12 UTC were obtained from the University of Wyoming Department Of Atmospheric Sciences Weather online data archive (http://weather.uwyo.edu/upperair/sounding.html) for 8 stations in the greater La Plata Basin region in South America (Table 3, Chapter 3). Sounding data is utilized for WRF model validation at standard pressure levels from 925 – 70 hPa (described in Chapter 3). Soundings without upper atmospheric data or without standard pressure levels (e.g. SGAS) were omitted from model validation. See Chapter 3 for WRF model validation.

4.3.2 Satellite Data

NASA's Geostationary Operational Environmental Satellite (GOES) data is generated for operational meteorology, and for this study is utilized to validate WRF model output. The GOES-16 Advanced Baseline Imager (ABI) includes 16 different spectral bands. This work uses ABI Channel 13 with a central wavelength of 10.3μm to compare to WRF simulated Outgoing Longwave Radiation (OLR; described in Chapter 3). GOES-16 Channel 13 IR images of the La Plata Basin, the central Andes and key locations for RELAMPAGO field campaign are available by the National Center of Atmospheric Research (NCAR) and Earth Observing Laboratory (EOL) in Boulder, Colorado. Figure 1 includes GEOS 16 IR brightness temperature every 6 hours from 00UTC 11/10 – 11/15 illustrating the locations and progression of deep convection over time.

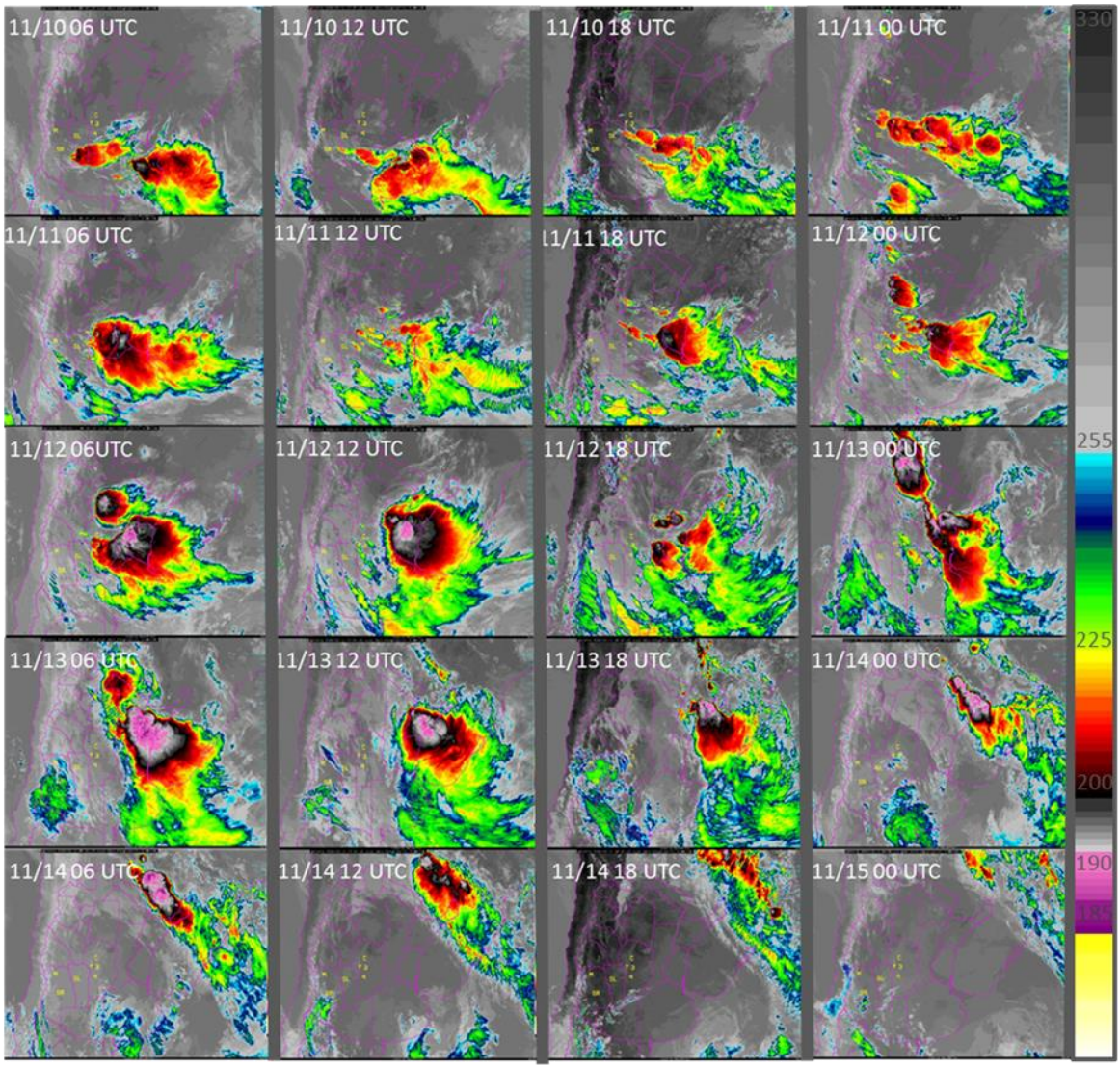

Fig. 1 GOES 16 channel 13 IR brightness temperature (K) every 6 hours, November 10 06 UTC to November 15 00 UTC.

4.3.3 Reanalysis

The ERA-Interim reanalysis (ERAi) dataset produced by the European Centre for Medium-Range Weather Forecasts (ECMWF) is utilized for synoptic-scale atmospheric conditions (Simmons et al, 2006; Dee et al. 2011). The horizontal resolution is approximately

0.75° latitude × 0.75° longitude (~ 83 km) with 37 vertical levels from the surface to 0.1 hPa. The interpolated pressure level gridded data set is available from 1979 to present at 6-hr intervals. ERAi data are utilized as initial and boundary conditions in the WRF model (described in detail in Chapter 3). ERAi data are also utilized to describe synoptic-scale atmospheric conditions in the formation of deep convection at 00 UTC November 09 - 15.

4.3.4 WRF Model

The Weather Research and Forecast (WRF) numerical model version 3.9.1.1 (Skamarock et al. 2008) was utilized to simulate deep convection from 12 UTC November 9, 2018 – 00 UTC November 15, 2018 . ERAi was used for initial and lateral boundary conditions in WRF, and grid-nudging was applied to the outermost domain (Fig. 1). Only the inner domain (Fig. 1, domain 3) is used for analysis. Details of the model set-up, spin-up time, and sensitivity tests of parameterizations and vertical resolutions, including validation are described in Chapter 3.

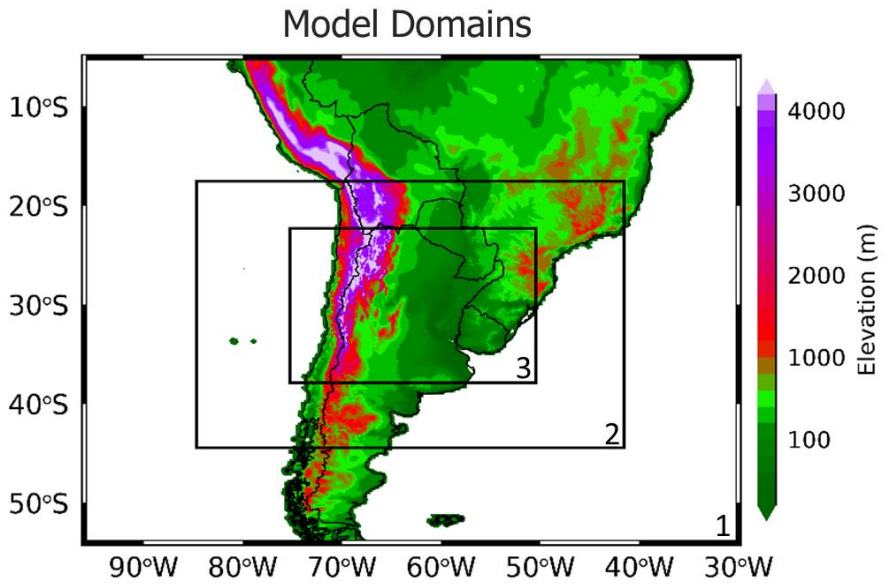

Fig. 2 Model domains for this study. The grid spacing for domain 1 is 27 km, domain 2 is 9 km and domain 1 is 3 km. Shading is model terrain elevation.

4.4 Synoptic Description of Events

The LPB region is known for deep convection and organized mesoscale convective systems (e.g. Zipser et al. 2006). Here, the large-scale atmospheric conditions are described from 11/9 – 15/2018 to show synoptic forcing from a pre-convection to post-convective environment. During November 12-13, a large organize Mesoscale Convective Complex (MCC) is located in northern Argentina. This storm is of particular interest due to its strength and duration (Fig. 1). On November 12, 2018 at 17:15 (local time), reports of a tornado near Reconquista and Goya in northeastern Argentina were nearly 24 hours prior to the systems northward propagation. While deep convective processes occur daily during this case study, the MCC is represented as Day 0 for the synoptic description of events.

As an overview of atmospheric dynamics in South America, several general characteristics contributed to the formation of deep convection and MCS/MCCs in the La Plata Basin. These characteristics include: (1) the positions of the upper-level subtropical jet stream, (2) the Bolivian High – an upper-level anticyclonic circulation typically positioned over Bolivia, (3) the Chaco Low – a surface level thermal low centered north the Sierra de Cordoba Mountains in Northern Argentina, and (4) the South American Low Level Jet (SALLJ) – a low level northerly wind with a maxima at approximately 850 hPa which is responsible for heat and moisture transport from the tropics to extra-tropics east of the Andes Mountain range (Marengo et al. 2010; Montini et al. 2019). Previous studies have characterized extreme precipitation in Argentina related to the exit of the SALLJ (Liebmann et al. 2004; Salio et al. 2007). In the SLPB, as low level moisture is transported across an active thermal low (e.g. the Chaco Low) and advected poleward, it approaches drier, cooler

air at higher latitudes, and the resulting convergence zone can contribute to convective initiation in this region.

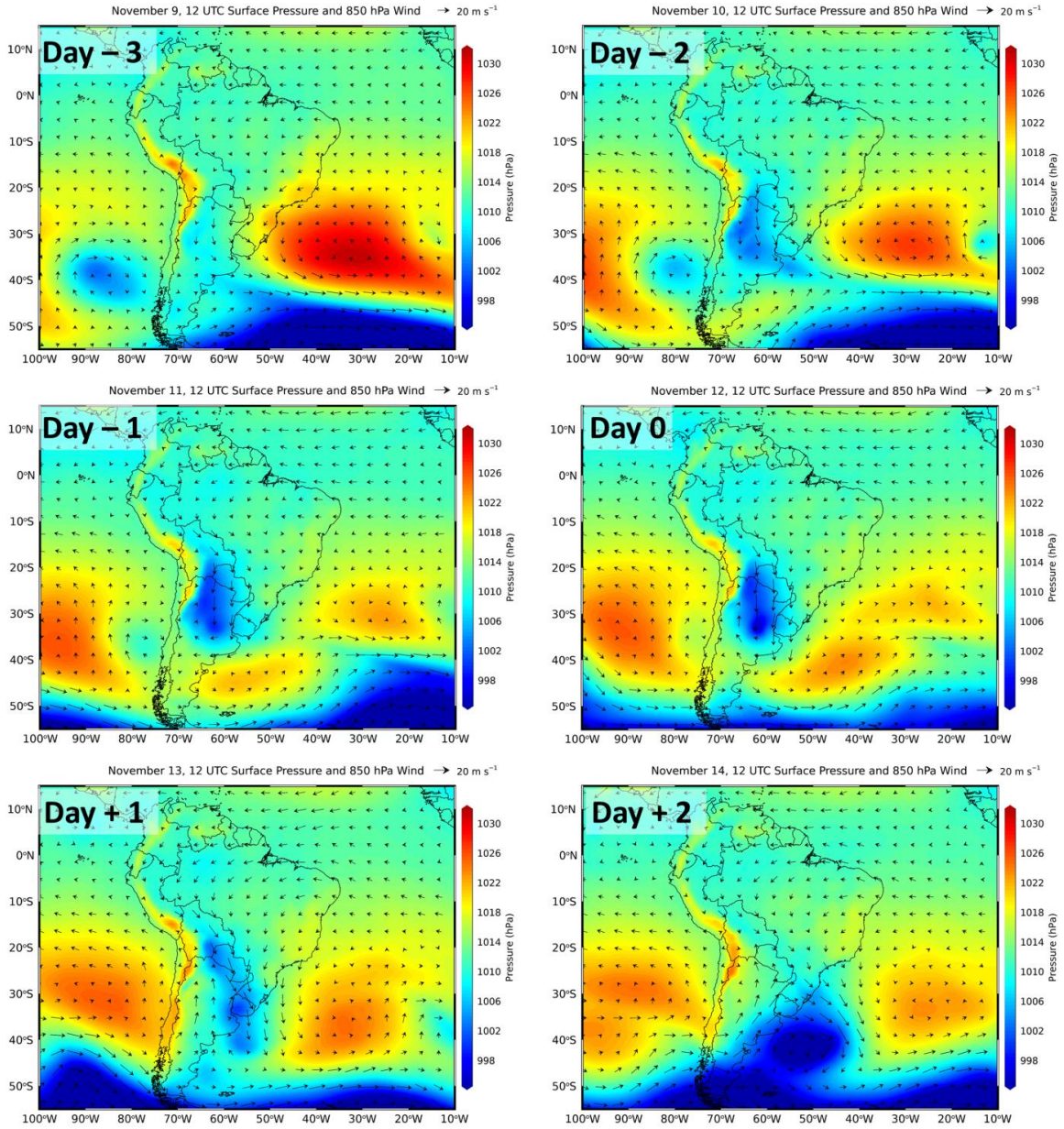

Fig. 3 ERAi mean sea level pressure (shaded) and 850 hPa wind (vectors) from 12 UTC November 9 – November 14, 2018. Each day is relative to the Mesoscale Convective Complex on 12 UTC November 12, 2018 (day 0) shown in Fig. 1.

Figure 3 illustrates mean sea level pressure and 850hPa circulation and Figure 4 shows upper level circulation (200hPa), indicating the position of the subtropical jet stream. For plots in Figure 3 and 4, each day is relative to the MCC on 12 UTC November 12, 2018 (day 0) shown in Figure 1. On November 9 (day – 3), a strong anticyclone was centered east of SESA and was supported by upper level convergence during a split upper-level jet event (Fig. 4, day -3). The position and strength of the anticyclone contributed to a low level northerly flow and moisture transport from northern to central Argentina (Fig. 3, day -3). On November 10 (day – 2), several discrete deep convective cells and clusters of cells were observed at approximately 32.5˚S (Fig. 1, 11/10). During this time, the anticyclone weakened and moved eastward and a thermal low located near Cordoba, Argentina (Chaco Low) intensified as the trough crossed the Andes.

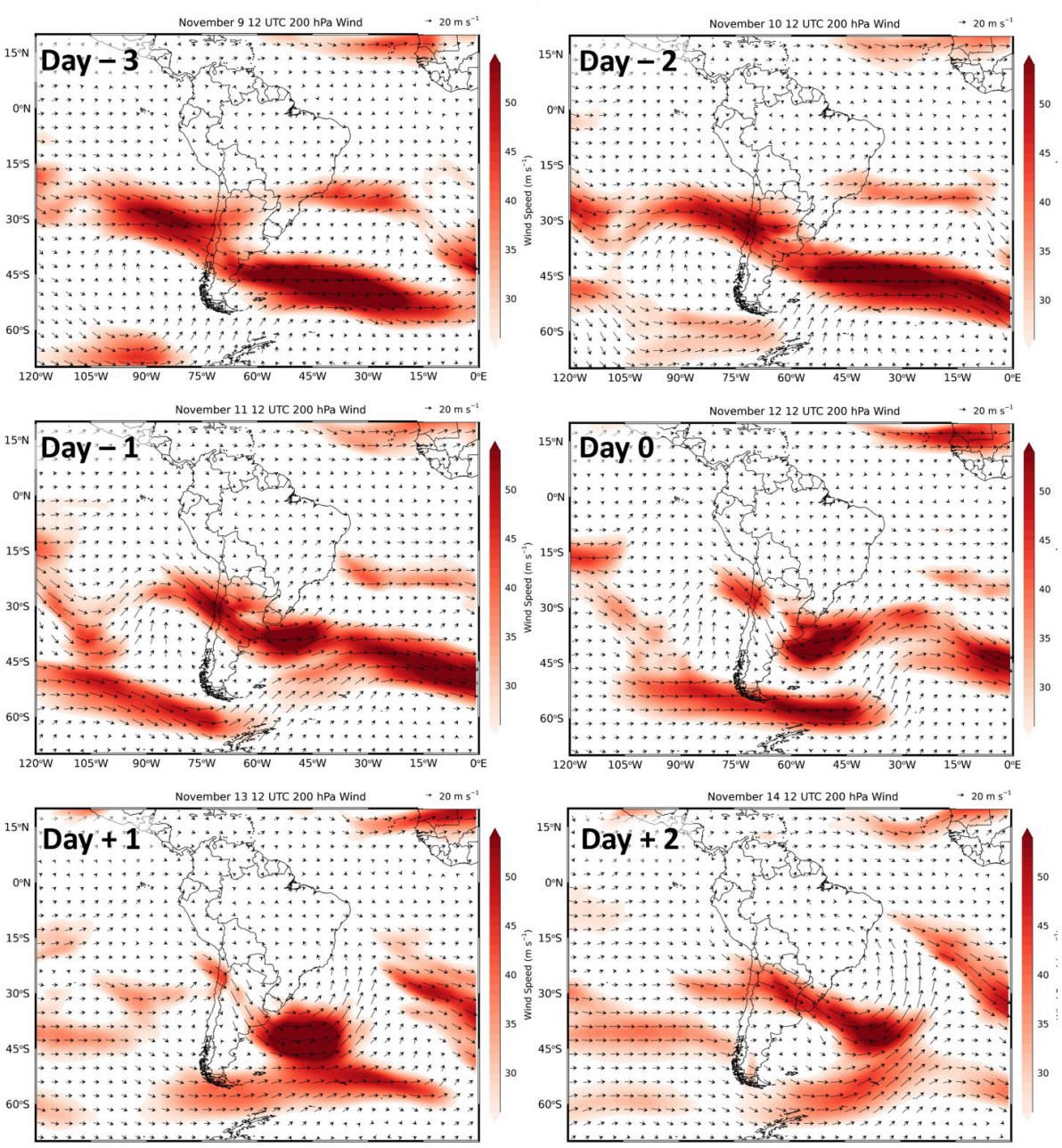

Fig. 4 ERAi 200 hPa wind (vectors) from 11/12 – 14/2018 at 12 UTC. Shading represents 200 hPa zonal winds (only zonal winds above 25 m s^{-1} are shaded).

On November 11 (Fig. 4, day – 1), the SALLJ strengthened, the Chaco Low was active and the exit of the SALLJ was located in Argentina, west of Uruguay (Fig. 1). These atmospheric conditions were consistent with Salio et al. (2007) on the formation of organized

convection in Southeast South America. On day -1 of Salio et al. (2007) experiment, the low level jet was active and transporting heat and moisture to low level convergence near the exit of the SALLJ. Additionally, the same study showed that during their experiment, upper-level divergence corresponding to the position of a jet streak contributed to the development of a "long-live" MCS on day 0. Similar conditions occurred on day -1 of this study, and appear to have contributed to the intensification of organized deep convection.

On November 12 (Fig. 3, day 0), synoptic conditions were characterized by an active SALLJ and Chaco Low in the La Plata Basin, and a trough west of the Andes. In upper levels, east of Uruguay, divergence from a left entrance jet streak likely supported surface convergence and deep convection (Fig. 4, day 0). A large MCC was centered west of Uruguay. This MCC was also associated with the tornado that was reported by news outlets and social media near Reconquista and Goya in Northeastern Argentina. The MCC slowly propagated out of the area, prolonging the influence of deep convection until 18 UTC November 13 (day + 1). On day +1, a transient surface low pressure system (polar trough) crossed the Andes Mountains in Southern South America, and was associated with a cold frontal boundary positioned in Northern Argentina from 22-35˚S. This location was similar to the position of the MCC on the previous two days, indicating sustained deep convection in the region. On November 14 (day +2), the low propagated equatorward and the frontal boundary migrated north into Brazil and Paraguay. As the system exited the Southern La Plata Basin, a strong southerly flow associated with the position of the surface low contributed to stable, cool and dry conditions in the region.

The synoptic conditions during this case study show large-scale drivers of deep convection in this region. Next, the focus turns to the influence of deep convention on

troposphere-stratosphere exchanges. WRF simulations of these convective events are now examined to investigate UTLS thermodynamics and lower stratosphere hydration. WRF output is presented for the remainder of this study.

4.5 Stratospheric Water Vapor and Deep Convection

Previous studies have shown that extratropical deep convection can hydrate the lower stratosphere via the detrainment of water vapor and ice crystals (Wang 2003; Dessler and Sherwood 2004, Le and Gallus 2012; Homeyer et al. 2017; Smith et al. 2017). This has not been investigated in South America. To begin, deep convection is classified into categories of convective systems for analysis and comparison. Previous work in this region by Mulholland et al. (2018) classified convective systems from 2015-2017 with four categories: multicell unorganized, multicell organized (MCS), discrete nonsupercell, and discrete supercell. For this four-day case study convective systems are classified into three categories: discrete (or clustered discrete) convective cells (DC), organized multicellular associated with a Mesoscale Convective Complex (MCC), and organized multicellular associated with the leading edge a cold front (squall line). Figure 5 shows each category with Outgoing Longwave Radiation (OLR; white areas represent clouds) and the associated water vapor mixing ratios at 100, 90, 80, and 70 hPa. Water vapor mixing ratios above 4.0 ppmv (Dauhut et al. 2018) are noted as mixing ratios above background levels. Background water vapor mixing rations in the lower stratosphere during this case study are between 1-4 ppmv (not shown).

Deep convection is observed on each day of this case study (Fig. 1). However, the three categories of deep convection for this analysis are examined on three different days.

The first type, DC are observed in the subtropics at approximately 32˚S, this is located in the southern La Plata Basin at 21 UTC on 11/10/18. For this category, notable water vapor concentrations above background levels are shown at 100 and 90 hPa (Fig. 5, column 1). The second category is a large, expansive MCC observed in northern Argentina at 06 UTC on 11/12/18. For the MCC, water vapor concentrations above background levels are primarily shown in subtropical locations from approximately 24-30˚S and at altitudes as high as 70 hPa (Fig. 5 column 2). The third category is a squall line crossing from Uruguay to western Paraguay at 06 UTC on 11/13/18. For this system, water vapor concentrations above background levels span from 22-35˚S. The highest levels are located at approximately 22˚S and at altitudes as high as 80 hPa (Fig. 5 column 3).

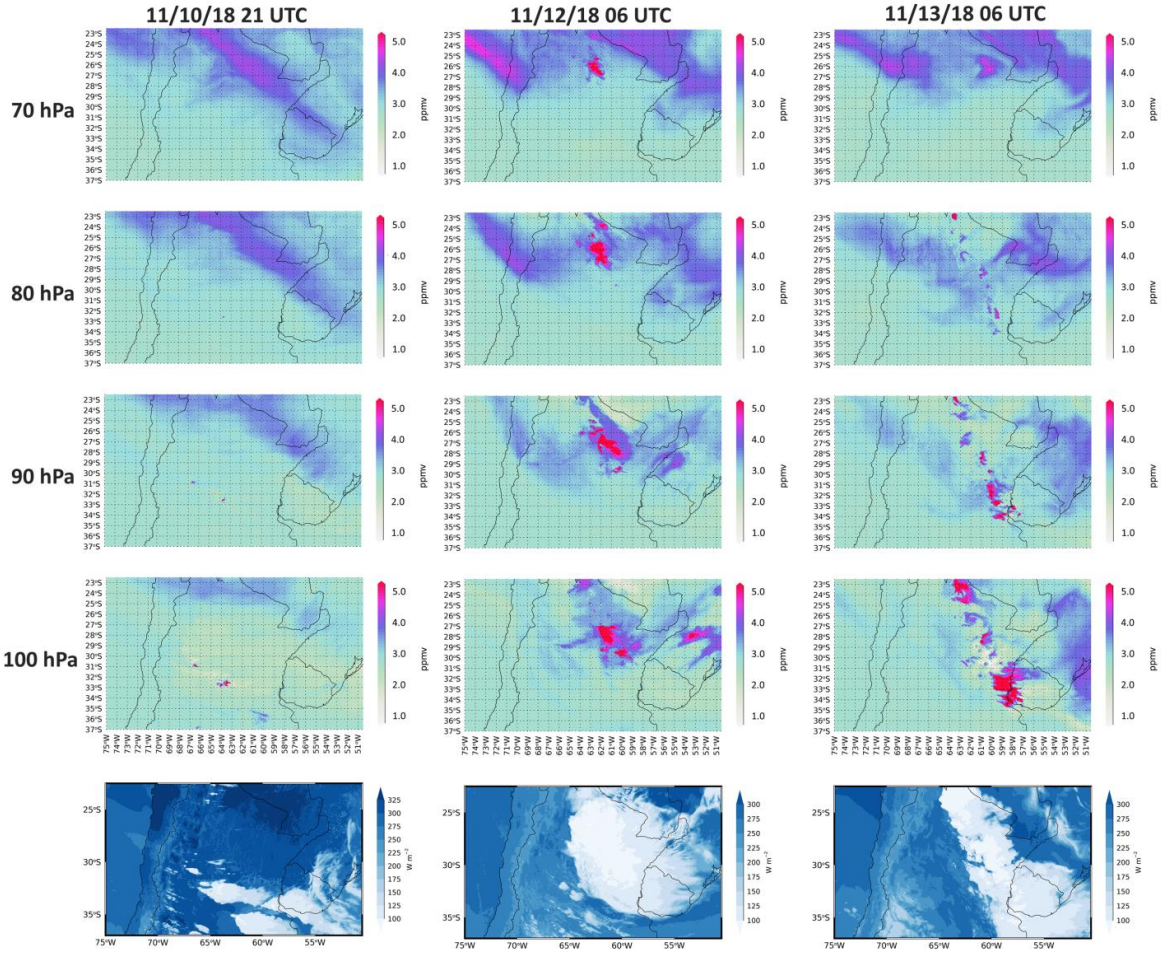

Fig. 5 WRF outgoing longwave radiation (bottom panel), and WRF water vapor mixing ratio at 100, 90, 80, and 70 hPa for three convective types: 11/10/18 21 UTC (left column), 11/12/18 06 UTC (middle column), and 11/13/18 06 UTC (right column).

It is important to note that water vapor in the stratosphere, generally above 40 hPa can be created via methane (CH_4) oxidation – CH_4 and OH becomes CH_3 and H_2O (Bates and Nicolet, 1950; Le Texier et al., 1988), and as previously described, stratospheric water vapor chemically reacts to destroy ozone. In the mid and upper stratosphere, the chemical conversion of methane is the primary source of water vapor (Brasseur and Solomon 2005). Additionally, it should be noted that the WRF model utilized for this work does not include stratospheric water vapor chemistry. Therefore, in Figure 5, water vapor concentrations in the

lower stratosphere that is not related to the detrainment of water vapor through deep convection is likely related to water vapor advected from other locations or diabatic descent related to cooling, and transport from above. These mechanisms explaining water vapor transport in the WRF simulations are not discussed in this study.

4.6 UTLS Thermodynamics and Lower Stratospheric Hydration

4.6.1 Identifying Double Tropopause Events

Double tropopauses generally occur in extratropical regions and more frequently near the subtropical jet stream (Randel et al. 2007). During this case study, the general position of the jet stream is shown in Figure 4. While the upper level jet may contribute to double tropopause events in this region, this work focuses on double tropopause events related to deep convection and the corresponding heights of maximum water vapor in the lower stratosphere (Homeyer et al. 2014; Homeyer 2015). While the tropopause can be identified in several different ways: chemical – e.g. abrupt changes in ozone concentrations, dynamical – e.g. potential vorticity, or thermal – changes in temperature lapse rates. Here we focus on temperature and the thermal tropopause. First, to identify thermal primary and secondary tropopause heights, a linear interpolation is applied to the WRF model temperature data to increase the vertical resolution to 100 m. The temperature lapse rate is then calculated ($-dT/dz$) from 5-20 km. Next, the primary (first) tropopause is identified with the WMO definition, which states that a thermal tropopause is located where the lapse rate decreases to less than or equal to 2˚ K/km (WMO 1957). Following the guidelines described in Appendix A by Peevey et al. (2012), the lapse rate is calculated above 5 km to avoid identifying low tropospheric inversions as the primary tropopause levels. Lastly, the location of the secondary

tropopause is identified. Where the lapse rate increases above 3˚ K/km within 2 km of the primary tropopause, and then decreases again to below 2˚ K/km, a secondary tropopause is identified (modified from Peevey et al. 2012).

4.6.2 Convective Overshooting and Water Vapor Detrainment in the Lower Stratosphere

Figure 6a, e and i are cross sections of lapse rates (shaded), and the points for the primary and secondary thermal lapse rate tropopause levels (filled dots), during each type of deep convection: 32.79˚S for the DC, 26.04˚S for the MCC, and 22.81˚S for the squall line. The latitudes for each cross section were chosen based on maximum water vapor concentrations in the lower stratosphere from 15-20 km during each convective event. The latent heat dynamic effect (Tao and Li 2016) appears to be occurring during each case of deep convection, where the lapse rate is decreasing in the mid and upper troposphere (Fig. 6 a, e and i). This decrease in lapse rate is likely due to diabatic processes related to latent heat release during phase changes, both condensation and freezing. Additionally, vertical velocity (shaded) and potential temperature (contour) (Figs 6b, f and j) illustrate instability and enhanced updrafts, also indicating where latent heat exchanges in the mid and upper troposphere are likely occurring (Tao and Li 2016).

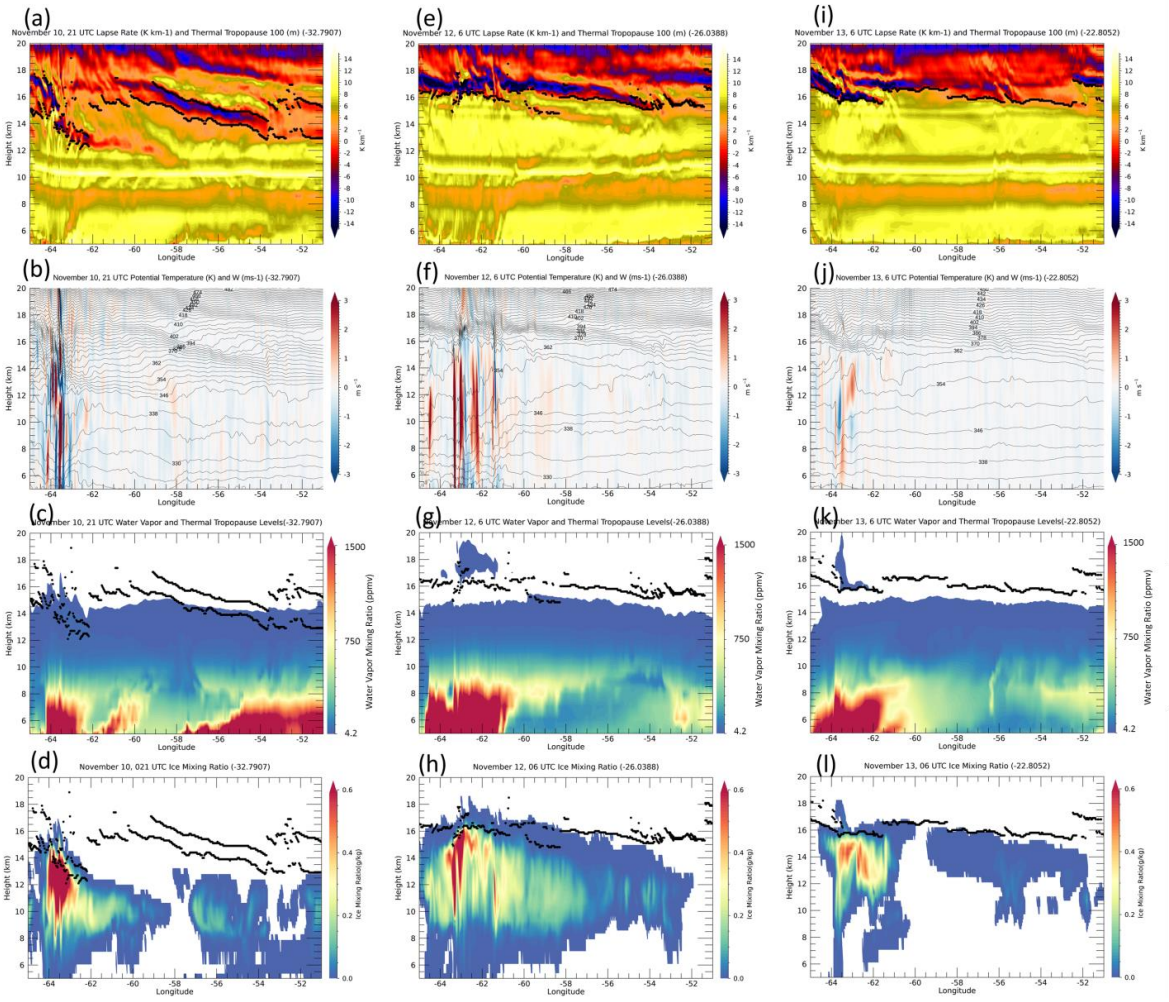

Fig. 6 The temperature lapse rate (*-dT/dz*; shaded) and thermal tropopause levels (filled dots) are on the top panel. Vertical velocity (w) and potential temperature (theta) are on the second panel. Water vapor mixing ratio greater than 4.2 ppmv (white areas are less than 4.2 ppmv) and thermal tropopause levels (filled dots) are on the third panel. Ice mixing ratios and thermal tropopause levels (filled dots) are on the fourth panel. Longitudinal cross sections (65-51˚W) for each mode: DC (a, b, c, d), MCC (e, f, g h) and Squall line (i, j, k, l).

Water vapor mixing ratio during each convective type is shown based on a minimum threshold (4.2 ppmv) in Fig 6 (c, g, and k). The threshold is used to illustrate where water vapor concentrations above the tropopause are higher than background water vapor levels (Dauhut et al. 2018). Figure 7 is a time series of points of interest during each category from

00 UTC 11/10 – 11/15 to illustrate maximum water vapor mixing ratios from 15-20 km. As previously discussed, convection is occurring each day (Fig. 1). However, maximum water vapor concentrations above the 4.2 ppmv threshold were only simulated during deep convection events. In non-convective environments water vapor mixing ratios remained below the threshold.

Areas in Figure 6c, g and k without shading (white) represent water vapor mixing ratios below the 4.2 ppmv threshold. In the MCC and Squall line categories (Fig. 6 g and k respectively), a gap exists between water vapor at or near the thermal tropopause levels with higher water vapor concentrations aloft. This dry layer may assist in identifying hydration of the lower stratosphere and indicate irreversible mixing (Dauhut et al. 2018). One explanation for this result is ice crystals formation and latent heat release near the tropopause. Diabatic heating can produce positive net buoyancy and strong updrafts forcing ice aloft. At warmer levels in the lower stratosphere, ice is sublimated, producing higher water vapor concentrations (Dessler et al.1995; Smith et al. 2017). This process appears to hydrate the lower stratosphere with the direct injection of ice particles (Khaykin et al. 2009). Figures 6d, h and i show ice mixing ratios which may support this explanation. Conversely, the DC event does not have a gap above the moist tropopause. While ice and water vapor are detected directly above the secondary tropopause, the lack of dry layer and corresponding water vapor above indicates that the lower stratosphere is not hydrated at this location by discrete cell overshooting.

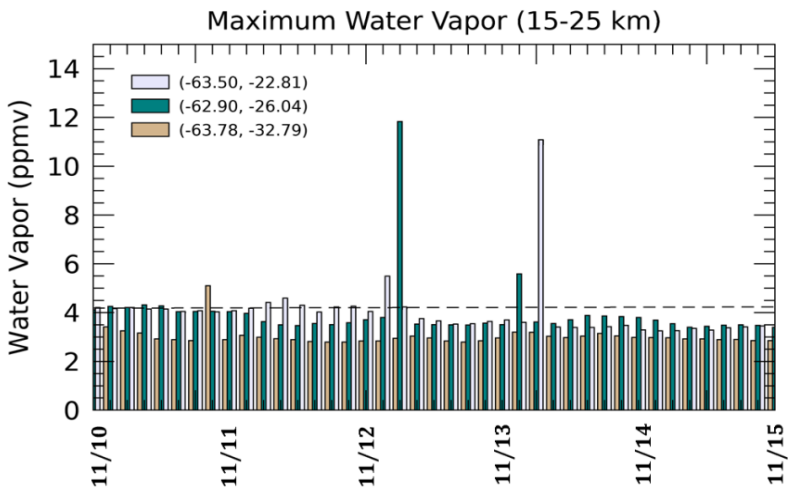

Fig. 7 November 10 – 15, 2018 maximum water vapor mixing ratio between 15 – 20 km for three grid cells related to deep convection and overshooting: DC (tan), MCC (teal), and Squall line (grey). The dashed line indicates the threshold level (4.2 ppmv) utilized to plot water vapor mixing ratio in Fig. 6.

For each convective category investigated here, water vapor detrainment in the lower stratosphere is associated with a sharp change in lapse rate. In this study, this feature is defined by a sharp change in lapse rate with height, coinciding with a sharp change in static stability. This is especially noted in the MCC and Squall line convective types (Fig. 6 e, f, I, j). For both categories, large instability below the primary tropopause level is capped by a shallow stable layer (Fig. 6f and j; potential temperature contours), where steep potential temperature gradients are observed. This is indicative of previously described double tropopause events (Homeyer et al. 2014a). Below the sharp change in lapse rate, where temperature controls the formation of ice (Jensen et al. 2007), latent heat release during ice formation is likely responsible for instability and increased water vapor levels aloft due to updrafts.

4.6.3 Primary Tropopause Temperature Variability

In this section, warmer and colder primary tropopause events are investigated. While temperature is a key regulator of cross tropopause dynamics (Holton et al. 1995), for this investigation, the temperature of the primary tropopause is only examined and categorized as warmer or colder tropopause based on its temperature relative to the secondary tropopause temperature at that grid point. In other words, is the primary tropopause warmer or colder than the secondary tropopause? The goal of this analysis is to answer a specific question: during double tropopause events, does a warmer primary tropopause contribute to higher water vapor values in the lower stratosphere? To answer this question the warmer and colder tropopause points are identified. To determine a warmer primary tropopause, the primary and secondary tropopause temperatures are compared at each grid point. Where the primary tropopause is warmer than the secondary tropopause the temperature of the grid point is retained and is classified as a warmer primary tropopause. Where the primary tropopause temperature is colder than the secondary tropopause the temperature of the grid point is retained and classified as a colder primary tropopause.

Figure 8 shows time averaged double tropopause events for warmer and colder tropopause from 11/10-15/2018. All shaded areas represent double tropopause events. Areas not shaded (white) indicate where only single tropopause events occur throughout this case study. The existence of double tropopause events is not unexpected. In general they are due to mountain wave dynamics, which produce gravity waves (de la Torre et al. 2006), and due to the position of the upper level jet stream capable of perturbing the atmosphere and producing multiple tropopause events (Peevey et al. 2012).

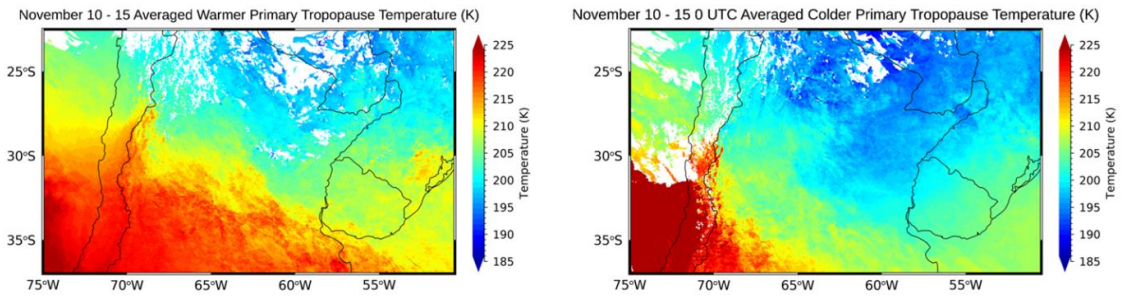

Fig. 8 Time averaged 3h WRF temperature data (11/10-15/2018 00 UTC) of warmer primary tropopause events (left) and colder primary tropopause events (right). Shaded areas are the temperature (Kelvin) at the primary tropopause level at each grid point.

Figure 9 show tropopause temperature variability related to double tropopause events during each convective event, 21 UTC 11/10 (DC), 06 UTC 11/12 (MCC) and 06 UTC 11/13 (Squall line). Spatial differences are shown in warmer primary tropopause temperature events (hereafter WPTT) compared to colder primary tropopause temperature events (hereafter CPTT) during each convective type. One feature stands out when comparing convective systems: few WPTT are observed east of the Andes Mountains range. The locations of deep convection are not collocated with WPTT events. Instead, the locations of WPPT are concentrated west of the Andes in the extratropical region. An exception to this feature is shown in the 06 UTC on 11/13 (Fig. 9). Based on the GOES 16 RELAMPAGO IR imagery and surface pressure maps (not shown), a transient low pressure system, associated with the cold front and Squall line in Northern Argentina, approached the Andes Mountains centered at approximately 35˚S. Only the center of this low coincides with CPPT on the western side of the Andes. Additionally, most double tropopause events east of the Andes are associated with CPPT events as well. For this case study, the answer to the previously posed question, WPPT events are not directly related to the height of maximum water vapor.

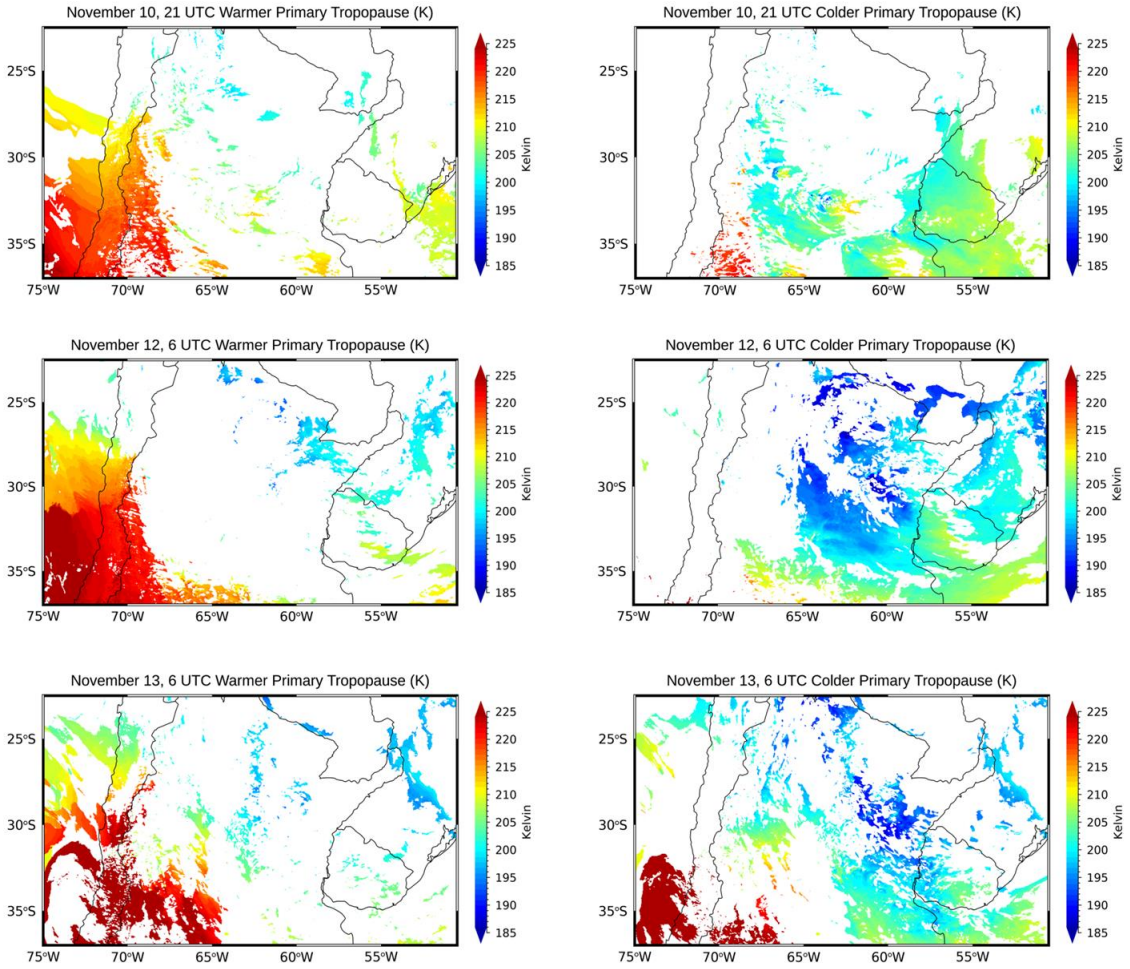

Fig. 9 Primary tropopause temperatures (K) during each convective type: 11/10/18 21 UTC (top row), 11/12/18 06 UTC (middle row), and 11/13/18 06 UTC (bottom row). The right column includes locations of warmer primary tropopause events and left column includes locations of colder primary cold tropopause events.

4.6.4 Height of Maximum Water Vapor between 15 and 20 km

Modeling studies are associated with inherent difficulties related to cloud microphysics and model parameterizations. However, several studies have explored the effects of deep convection (e.g. Feng et al. 2018) related to Mesoscale Convective Systems (MCS) on cross-tropopause overshooting and lower stratospheric hydration (e.g. Mullendore et al. 2005; Le and Gallus 2012, Homeyer et al. 14a, 14b; Homeyer 2015). For this study,

WRF simulations have shown maximum water vapor concentrations in the lower stratosphere centered on the location of deep convection and collocated with double tropopause events. For example, Figure 6c, g and k show maximum water vapor heights in grid cells with double tropopause features (dots represent primary and secondary tropopause locations). For the remainder of this study the height of water vapor in the lower stratosphere is quantified to better understand the depth of overshooting and lower stratospheric hydration.

Figure 10a, b and c show the height of maximum water vapor mixing ratios from 15-20 km related to each category of deep convection. This altitude range was chosen to detect maximum water vapor levels in the lower stratosphere that can be explained by tropopause dynamic processes, since these simulations do not have chemical reactions expected to be generally important above 20km (Noël et al. 2018). Figure 10d, e and f show the maximum water vapor mixing ratio between 15-20 km. OLR has been used as a proxy for identifying deep convection (e.g. Massie et al. 2002) and is used here to determine locations of maximum water vapor associated with each category of deep convection. Only grid points with WRF OLR data less than 100 W m^{-2} are retained to identify maximum water vapor.

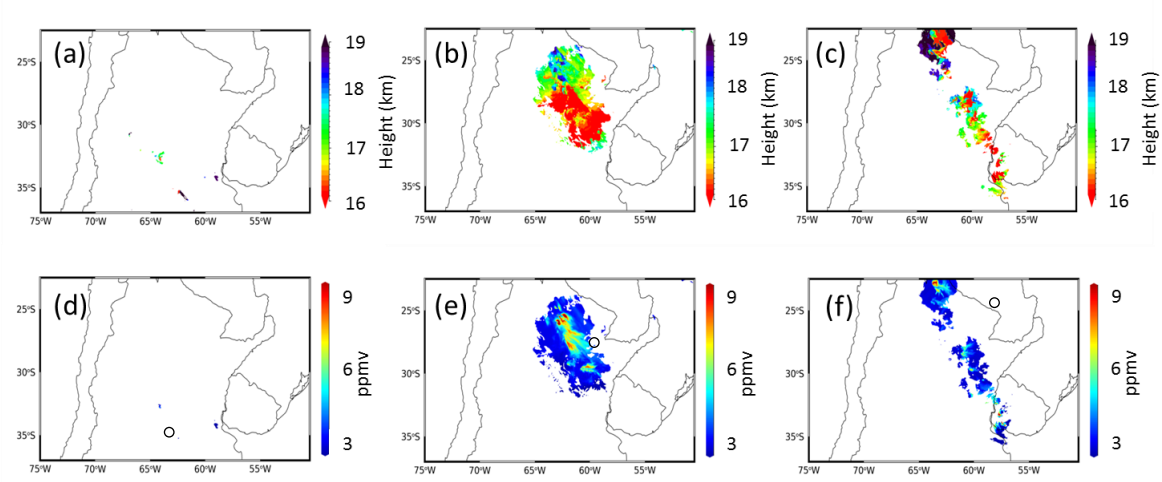

Fig. 10 Height of maximum water vapor and maximum water vapor (15-20 km).

The DC category shows moderate maximum water vapor mixing ratios (Fig. 10d) and heights (Fig. 10a) compared to the MCC and Squall line. For the MCC, maximum water vapor levels primarily occur from 25-30˚S (Fig 10e). The maximum values are centered on 26˚S at heights above 18 km (10b). The largest water vapor mixing ratios during the MCC are above 10 ppmv and maximum water vapor mixing ratios above background levels are observed up to 20 km. The Squall line shows elevated maximum water vapor concentrations in the lower stratosphere across most of the cold front boundary from 22-35˚S (Fig 10f). These elevated values are collocated with deep convection (Fig. 5). The largest water vapor concentrations occur in the tropics centered near 23˚S. This cluster of deep convection from 22-25˚S shows maximum water vapor ratios between 17-18 km, which is lower than those for the MCC. Additionally, the heights of maximum water vapor values across the Squall line do not appear to depend on latitude as typically does the tropopause height. Thermal tropopause height decreases from the tropics to mid-latitudes. Lower tropopause heights (<16.5 km) are observed across the frontal boundary in this case study (Fig. 10c).

4.6.5 Mechanisms Explaining Maximum Water Vapor Heights

To further understand the mechanisms explaining the height of maximum water vapor levels, individual grid points with large maximum water vapor concentrations identified in Figure 7 are examined during each category of deep convection with profiles of water vapor mixing ratio, ice mixing ratio, air temperature (Fig. 11), lapse rates and vertical velocity (Fig. 12). The grid point at 63.78˚W, 32.79˚S (Fig. 10d circle) is related to the DC and background water vapor mixing ratios are approximately 3.0 ppmv. The background levels are only observed above 17 km (Fig. 11, Discrete Cells left pane). At this grid point, large ice mixing ratios are observed from 13.4-15.3 km and collocated with elevated water vapor mixing

ratios. Generally speaking, the ice and water vapor mixing ratios are decreasing with height. However, just above 13 km, ice is increasing as water vapor decreases and net vertical movement is strongly positive (Fig. 12, Discrete Cells right panel). Despite this hydrated mixed layer in the UTLS and updrafts below the primary "cold point", no gap in water vapor is detected with a hydrating layer above. Additionally, vertical velocity is negative above the secondary tropopause. Warm tropopause temperatures and strong downdrafts above the secondary tropopause may also explain the lack of stratosphere hydration at this location.

The grid point at 62.91˚W, 26.03˚S (Fig. 10e circle) is related to the MCC and during this time it has background water vapor mixing ratios from 3.0-3.5 ppmv. These dry, background values are found in two layers: approximately 15-16.5 km and just below 20 km (Fig. 11, MCC left panel). During the MCC, elevated ice mixing ratio values are observed below the primary thermal tropopause level (16.3 km) and coincide with the dry water vapor layers (background levels). Additionally, a sharp change in lapse rate begins at approximately 16.5 km and a secondary tropopause is identified at 17 km. At this altitude maximum water vapor levels sharply increase, and vertical velocity shifts from negative to positive values at 17.5 km, where strong updrafts force water vapor aloft (Fig. 12, MCC right panel). This grid point has a "gap" or dry layer in tropopause water vapor with a hydrated layer above, as observed in the longitude-height profiles (Fig. 6). This point is indicating lower stratospheric hydration.

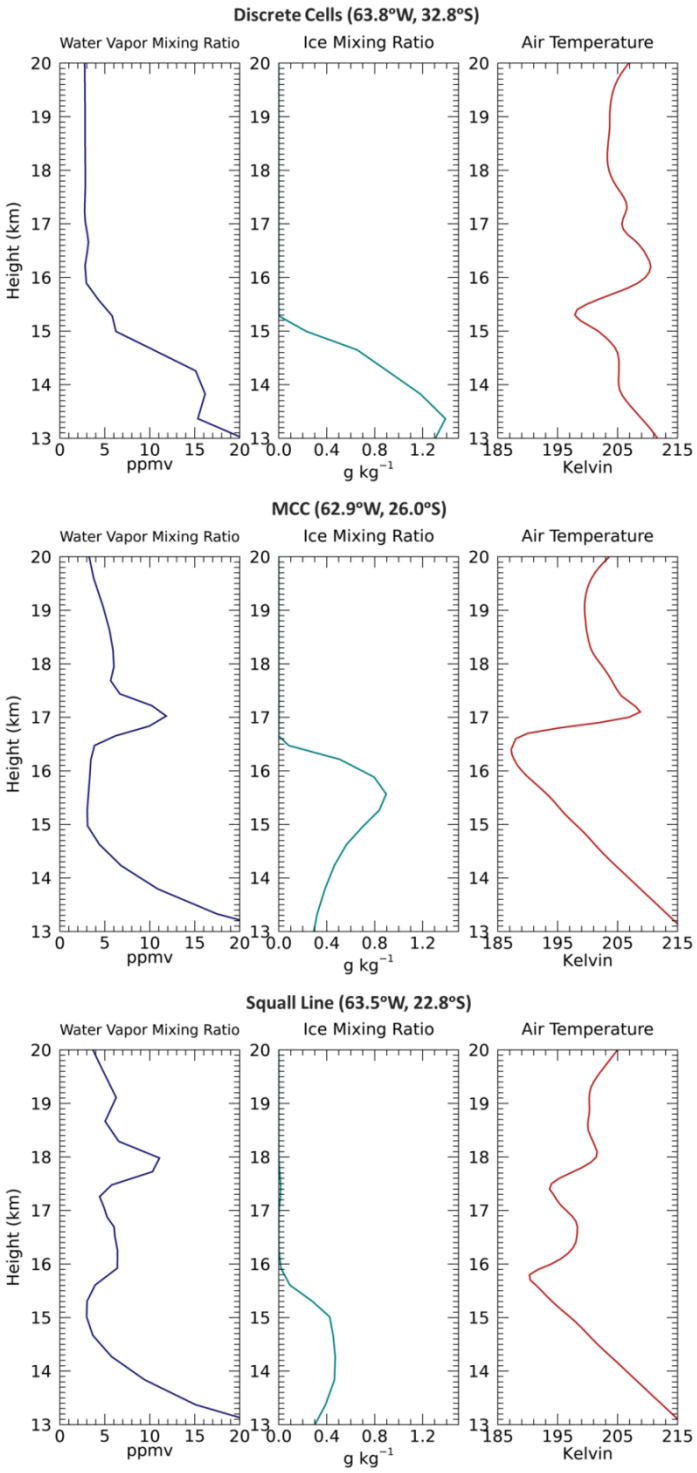

Fig. 11 Upper troposphere – lower stratosphere profiles (13 – 20 km) of WRF data: water vapor mixing ratio (left column), ice mixing ratio (center column), air temperature (right column). Grid points are selected for each convective type: discrete cells (top row), MCC (center row) and Squall line (bottom row).

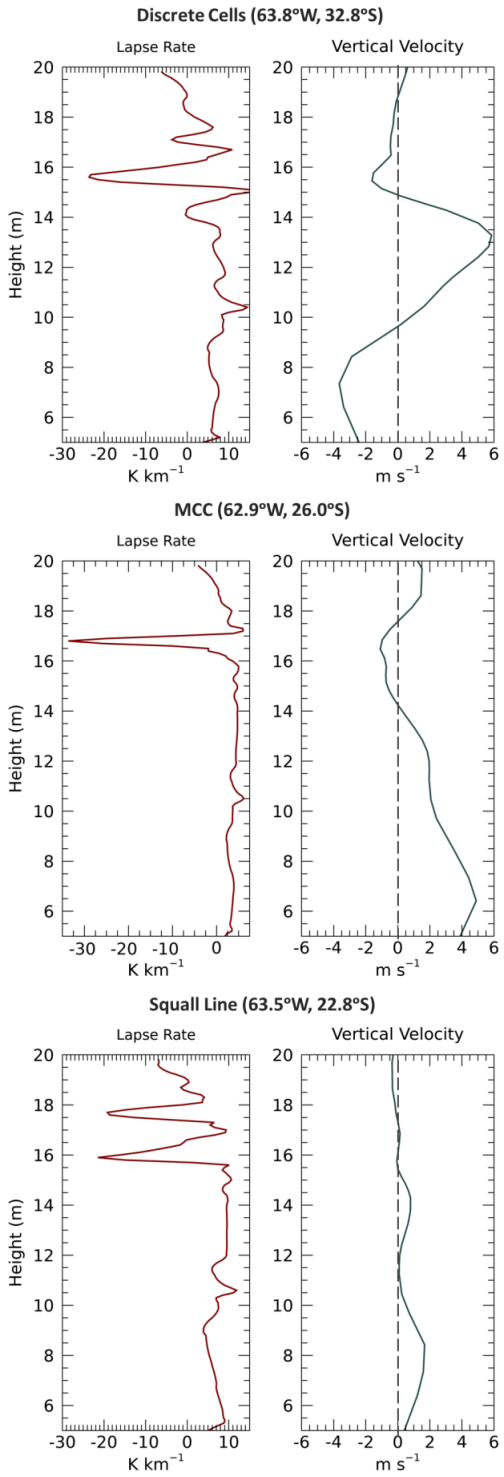

Fig. 12 Profiles (6 – 20 km) of WRF data: temperature lapse rate (left column) and vertical velocity (right column). Grid points are selected for each convective type: discrete cells (top row), MCC (center row) and Squall line (bottom row).

Lastly, the grid point at 63.50˚W, 22.81˚S (Fig. 10e circle) is related to the Squall line and has background water vapor mixing ratios from 3.0-4 ppmv. These background values are found in multiple dry layers above 13 km: approximately 15 km, 17.2 km and 20 km (Fig. 11 Squall Line left panel). At this grid point, a deep double tropopause event is occurring and while the thermal (lapse rate) tropopauses are identified at 15.7 km and 16.3 km, the secondary "cold point" is occurring at 17.4 km. Elevated ice mixing ratios occur from 13-16 km, and the maximum levels of ice are found at 15 km and coincide with a dry water vapor layer. Between the two cold points (approximately 15.8 and 17.4 km), water vapor concentrations above 5 ppmv are observed until 17 km, and small concentrations of ice are observed between 17.1 and 17.7 km. Additionally, the lapse rates at this grid point are subject to two sharp changes, and at 17 km, the increased ice mixing ratios are detected where the second lapse rate minima indicates rapid cooling. Above this level, maximum water vapor (greater than 10 ppmv) is observed at 17.9 km and a secondary maximum is observed at 19.1 km. At 20 km, water vapor concentrations begin to return to background levels. Like the MCC example, this grid point has a "gap" or dry layer in tropopause water vapor with a hydrated layer above, as observed in the earlier longitude-height profiles (Fig. 6). This point also indicates lower stratospheric hydration.

4.7 Conclusions

The Weather Research and Forecasting model (WRF) was utilized to simulate deep convection capable of perturbing the tropopause boundary and contributing to troposphere-to-stratosphere exchanges. Sensitivity testing of model parameterizations, vertical resolutions as well as model validation are presented in Chapter 3. The main goal for this work was to

simulate deep convection and investigate the importance of double tropopause for the lower stratospheric hydration. Additionally, this study evaluated mechanisms driving convective overshooting and the height of maximum water vapor with focus on the La Plata Basin. In particular, deep convection was evaluated with three types of mesoscale convective systems: discrete cells (DC), Mesoscale Convective Complex (MCC) and cold front boundary (Squall line). During these case studies, WRF detected double tropopause events and for each convective system examined double tropopauses were collocated with enhanced maximum water vapor levels in the lower stratosphere. However, only the MCC and Squall line systems hydrated the lower stratosphere.

A secondary focus of this work was to investigate primary tropopause temperatures, relative to secondary tropopause temperatures. The results show that the warmer primary tropopause events are not generally related to any category of deep convection investigated. Regardless of the primary tropopause temperature, during deep convective events the secondary tropopause temperature is warmer than the primary tropopause temperature. Additionally, during this study warmer primary tropopause events were generally located west of the Andes Mountain. These events were likely related to the interactions between the upper level jet stream and the Andes as a mountain barrier; this study requires further examination outside the scope of this work.

A key result of this study shows that the primary source of lower stratospheric hydration is ice near the thermal tropopause. Cold primary tropopause temperatures and the presence of moisture seem to contribute to ice formation in the UTLS leading to instability via latent heat exchanges and updrafts. During these events, a sharp change in lapse rate occurs where rapid cooling with height is followed by rapid warming. As ice is detrained in

the lower stratosphere, and is sublimated contributing to elevated water vapor mixing ratios and localized downdrafts. These results are sensitive to the locations chosen for analysis. However, the longitude-height cross sections for each convective system presented in section 4.5.2 clearly supports this explanation with elevated ice and water vapor mixing ratios above the secondary tropopause coinciding with instability and a sharp change in lapse rate.

Additionally, not all categories of deep convection investigated in this study hydrated the stratosphere. While all systems investigated have hydrated layers between the primary and secondary tropopause levels, only the MCC and Squall line hydrated the lower stratosphere.

Among the three categories of deep convection compared in this study, DC has the warmest primary tropopause temperatures (~200 K), and the primary tropopause is located at lower altitudes (~14 km) compared to the MCC and Squall line. During DC, the tropopause is hydrated where a mixed layer of water vapor and ice is located above the primary tropopause and extends just above the secondary tropopause. However, directly above the primary tropopause, temperatures warm quickly and updrafts are not observed. During this event, deep convection overshooting does not appear to hydrate the lower stratosphere. No pocket of air with water vapor mixing ratios above background levels are observed above the overshooting (Dauhut et al. 2018). While the mixing of ice and water vapor likely contributed to the large instability between tropopause layers, net vertical velocity is negative above the secondary tropopause which would explain why water vapor is not observed above 17 km.

For the organized systems of deep convention, the MCC and Squall line categories have colder primary tropopause temperatures (187 – 191 K), higher primary tropopause heights (~16 and ~15.75 km, respectively), pockets of low water vapor concentrations in and above the tropopause, and lower stratospheric hydration is observed in both convective types

to nearly 20 km. Additionally, above 15 km the water vapor and ice concentrations are stratified, the presence of ice and water vapor mixing ratios are in layers rather than mixed as observed with the DC system. This may have contributed to the enhanced instability below the primary tropopause level and the strong positive vertical velocity capable of overshooting tropospheric material beyond the secondary tropopause. This mechanism can explain the heights of maximum water vapor observed hydrating the lower stratosphere.

The focus of this investigation is on simulating double tropopause events related to deep convection in the LPB with the WRF model to evaluate lower stratospheric hydration. This is important because deep convection can lead to troposphere – stratosphere exchanges (Roach 1967; Poulida et al. 1996; Fischer et al. 2003) and irreversible mixing in the lower stratosphere (Hartmann et al. 2013). Additionally, the presence of enhanced water vapor mixing ratios in the stratosphere can also contribute to stratospheric chemistry (Bates and Nicolet 1950). This in turn would affect ozone chemistry, and ultimately destroy ozone (e.g. Stenke and Grewe 2005). While ozone in the UTLS region was statistically significantly decreasing from 1998 – 2016 (Chapter 1, Fig. 12i), the extent of the contribution of water vapor on stratospheric chemistry and ozone destruction has not been widely evaluated in the LPB and would require further investigation.

4.8 Acknowledgements

This research was supported by the University of California, Santa Barbara Graduate Research Mentorship Program Fellowship. The ERAi data was created by the European Centre for Medium-Range Weather Forecasts and downloaded from The National Center for Atmospheric Research. The GOES satellite data was created by the National Oceanic and

Atmospheric Administration, and was downloaded from the RELAMPAGO 2018 field campaign catalog. I would like to thank Katelyn Zigner for her assistance with a programming language during this study.

4.9 References

Bates DR, Nicolet M (1950) The photochemistry of atmospheric water vapor, *J. Geophys. Res.*, 55, 301–327.

Brasseur G, Solomon S (2005) Composition and Chemistry, in: Aeronomy of the Middle Atmosphere, 3rd edn., 265-422, *Springer*, Dordrecht, Netherlands.

Brooks HE, Lee JW, Craven JP (2003) The spatial distribution of severe thunderstorm and tornado environments from global reanalysis data, *Atmos. Res.*, 67, 73–94.

Dauhut T, Chaboureau J, Haynes PH, Lane TP (2018) The Mechanisms Leading to a Stratospheric Hydration by Overshooting Convection. *J. Atmos. Sci.*, **75**, 4383–4398, https://doi.org/10.1175/JAS-D-18-0176.1.

de laTorre A, Alexander P, Llamedo P, Menéndez C , Schmidt T, Wickert J (2006) Gravity waves above the Andes detected from GPS radio occultation temperature profiles: Jet mechanism?, *Geophys. Res. Lett.*, **33**, L24810, doi:10.1029/2006GL027343.

Dee DP, Uppala SM, Simmons AJ, Berrisford P, Poli P, Kobayashi S, Andrae U, Balmaseda M A, Balsamo G, Bauer P, Bechtold P, Beljaars ACM, van de Berg L, Bidlot J, Bormann N, Delsol C, Dragani R, Fuentes M, Geer AJ, Haimberger L, Healy SB, Hersbach H, Holm EV, Isaksen L, Kallberg P, Köhler M, Matricardi M, McNally AP, Monge-Sanz BM, Morcette J-J, Park B-K, Peubey C, de Rosnay P, Tavolato C, Thepaut J-N, Vitart F., (2011) The ERA-Interim reanalysis: Configuration and

performance of the data assimilation system, *Q. J. Roy. Meteor. Soc.*, 137, 553–597, doi:10.1002/qj.828.

Dessler AE, Hintsa EJ, Weinstock EM , Anderson JG, Chan KR (1995) Mechanisms controlling water vapor in the lower stratosphere: "A tale of two stratospheres", *J. Geophys. Res.*, 100(D11), 23,167–23,172.

Dessler AE, Sherwood SC (2004) Effect of convection on the summertime extratropical lower stratosphere, *J. Geophys. Res., 109*, D23301, doi:10.1029/2004JD005209.

Dessler AE, Schoeberl MR, Wang T, Davis SM, Rosenlof KH (2013) Stratospheric water vapor feedback. *Proceedings of the National Academy of Sciences of the United States of America*, *110*(45), 18087–18091. doi:10.1073/pnas.1310344110.

Durkee DD, Mote TL, Shepherd (2009) The Contribution of Mesoscale Convective Complexes to Rainfall across Subtropical South America. *J. Climate*, 22, 4594-4605.

Fischer H et al. (2003), Deep convective injection of boundary layer air into the lowermost stratosphere at midlatitudes, *Atmos. Chem. Phys.*, **3**, 739–745.

Fueglistaler S, Haynes PH (2005) Control of interannual and longer-term variability of stratospheric water vapor, *Journal of Geophysical Research*, 110, D24108, doi:10.1029/2005JD006019.

Fueglistaler S, and coauthors (2013) The relation between atmospheric humidity and temperature trends for stratospheric water, *Journal of Geophysical Research*, 118, 1052–1074, doi:10.1002/jgrd.50157.

Grell GA Freitas SR (2014) A scale and aerosol aware stochastic convective parameterization for weather and air quality modeling, *Atmos. Chem. Phys.*, **14**, 5233-5250, doi:10.5194/acp-14-5233-2014.

Gutzler DS, Wood TM (1990) Structure of large-scale convective anomalies over Tropical Oceans. *J. Climate*, 3, 483–496.

Hartmann DL, Klein Tank AMG, Rusticucci M (Coordinating Lead Authors) (2013) Observations: Atmosphere and Surface, Chapter 2 in Climate Change 2013: The Physical Science Basis. Contribution of Working Group I to the Fifth Assessment Report of the Intergovernmental Panel on Climate Change, *Cambridge University Press*, Cambridge, U. K. and New York, NY, U. S. A., 2013.

Higgins RW, Yao Y, Yarosh ES, Janowiak JE, Mo KC (1997) Influence of the Great Plains low-level jet on summertime precipitation and moisture transport over the central United States. *Journal of Climate*, *10*(3), pp.481-507.

Homeyer CR, Pan LL, Barth MC (2014a) Transport from convective overshooting of the extratropical tropopause and the role of large-scale lower stratosphere stability, *J. Geophys. Res. Atmos.*, *119*, 2220–2240, doi:10.1002/2013JD020931.

Homeyer CR, et al. (2014b) Convective transport of water vapor into the lower stratosphere observed during double tropopause events, *J. Geophys. Res. Atmos.*, *119*, 10 941–10 958,doi:10.1002/2014JD021485.

Homeyer CR (2015) Numerical simulations of extratropical tropopause-penetrating convection: Sensitivities to grid resolution, *J. Geophys. Res. Atmos.*, 120, 7174–7188,doi:10.1002/2015JD023356.

Homeyer C, McAuliffe JD, Bedka KM (2017) On the development of above-anvil cirrus plumes in extratropical convection, *J. Atmos. Sci.*, 74, 1617–1633.

Holton JR, Haynes PH, McIntyre ME, Douglass AR, Rood RB, Pfister L (1995) Stratosphere-troposphere exchange, *Rev. Geophys.*, 33, 403–440.

Hong S–Y, Noh Y, Dudhia J (2006) A new vertical diffusion package with an explicit treatment of entrainment processes. *Mon. Wea. Rev.*, **134**, 2318–2341. doi:10.1175/MWR3199.1

Iacono MJ, Delamere JS, Mlawer EJ, Shephard MW, Clough SA, Collins WD (2008) Radiative forcing by long–lived greenhouse gases: Calculations with the AER radiative transfer models. *J. Geophys. Res.*, **113**, D13103.

IPCC: Climate Change (2013) The Physical Science Basis. Contribution of Working Group I to the Fifth Assessment Report of the Intergovernmental Panel on Climate Change, edited by: Stocker T F, Qin D, Plattner G-K, Tignor M, Allen SK, Boschung J, Nauels A, Xia Y, Bex V, and Midgley PM, *Cambridge University Press*, Cambridge, UK and New York, NY, USA, 1535 pp, 2013.

Jensen E, Ackerman AS, Smith JA (2007) Can overshooting convection dehydrate the tropical tropopause layer?, *J. Geophys. Res.*, 112, D11209, doi:10.1029/2006JD007943.

Khaykin S, Pommereau J-P, Korshunov L, Yushkov V, Nielsen J, Larsen N, Christensen T, Garnier A, Lukyanov A, Williams E (2009). Hydration of the lower stratosphere by ice crystal geysers over land convective systems. *Atmospheric Chemistry and Physics.* 8. 10.5194/acpd-8-15463-2008.

Laing AG, Fritsch JM (1997) The global population of mesoscale convective complexes, *Q. J. R. Meteorol. Soc.*, 123(538), 389–405.

Le Texier H, Solomon, S, Garcia RR (1988) The role of molecular hydrogen and methane oxidation in the water vapour budget of the stratosphere, *Q. J. R. Meteorol. Soc.*, 114, 281-295, doi:10.1002/qj.49711448002.

Le TV, Gallus Jr. WA(2012) Effect of an extratropical mesoscale convective system on water vapor transport in the upper troposphere/lower stratosphere: A modeling study, *J. Geophys. Res.*, 117, D03111, doi:10.1029/2011JD016685.

Liu N, Liu C (2016) Global distribution of deep convection reaching tropopause in 1 year GPM observations, *J. Geophys. Res. Atmos.*, 121, 3824–3842, doi:10.1002/2015JD024430.

Manabe S, Strickler RF (1964) Thermal equilibrium of the atmosphere with a convective adjustment. *Journal of the Atmospheric Sciences*, 21, 361–385.

Massie S, Gettelman A, Randel W, Baumgardner D (2002) Distribution of tropical cirrus in relation to convection, *J. Geophys. Res*., 107(D21), 4591, doi:10.1029/2001JD001293.

McIntosh PC, Hendon HH (2018) Understanding Rossby wave trains forced by the Indian Ocean Dipole. *Clim Dyn*, 50: 2783. https://doi.org/10.1007/s00382-017-3771-1.

Minschwaner K, Dessler AE, Elkins JW, Volk CM , Fahey DW, Loewenstein M, Podolske J R, Roche AE, Chan KR (1996), Bulk properties of isentropic mixing into the tropics in the lower stratosphere, *J. Geophys. Res.*, **101**, 9433–9439.

Mohanakumar K. (2008) Stratosphere Troposphere Interactions: An Introduction. *Springer*: London, United Kingdom.

Montini TL, Jones C, & Carvalho LMV (2019) The South American low-level jet: A new climatology, variability, and changes, *Journal of Geophysical Research: Atmospheres*, 124, 1200–1218. https://doi.org/10.1029/2018JD029634.

Morrison H, Thompson G, Tatarskii V (2009) Impact of Cloud Microphysics on the Development of Trailing Stratiform Precipitation in a Simulated Squall Line:

Comparison of One– and Two–Moment Schemes. *Mon. Wea. Rev.*, **137**, 991–1007. doi:10.1175/2008MWR2556.1.

Mulholland JP, Nesbitt SW, Trapp RJ, Rasmussen KL, Salio PV (2018) Convective Storm Life Cycle and Environments near the Sierras de Córdoba, Argentina. *Mon. Wea. Rev.*, **146**, 2541–2557, https://doi.org/10.1175/MWR-D-18-0081.1.

Mullendore GL, Durran DR, Holton JR (2005) Cross-tropopause tracer transport in midlatitude convection, *J. Geophys. Res.*, 110, D06113, doi:10.1029/2004JD005059.

Niu G–Y, Yang Z–L, Mitchell KE, Chen F, Ek MB, Barlage M, Kumar A, Manning, Niyogi D, Rosero E, Tewari M, Xia Y (2011) The community Noah land surface model with multiparameterization options (Noah–MP): 1. Model description and evaluation with local–scale measurements. *J. Geophys. Res.*, 116, D12109.

Noël S, Weigel K, Bramstedt K, Rozanov A, Weber M, Bovensmann H, and Burrows JP (2018) Water vapour and methane coupling in the stratosphere observed using SCIAMACHY solar occultation measurements, *Atmos. Chem. Phys.*, 18, 4463–4476, https://doi.org/10.5194/acp-18-4463-2018.

Pan LL, Randel WJ, Gary BL, Mahoney MJ, Hintsa EJ. (2004) Definitions and sharpness of the extratropical tropopause: a trace gas perspective. *Journal of Geophysical Research* 109: D23103. doi:10.1029/2004JD004982.

Paulson CA (1970) The mathematical representation of wind speed and temperature profiles in the unstable atmospheric surface layer. *J. Appl. Meteor.*, 9, 857–861.

Peevey TR, Gille JC, Randall CE, Kunz A (2012) Investigation of double tropopause spatial and temporal global variability utilizing High Resolution Dynamics Limb Sounder

temperature observations, J. Geophys. Res., 117, D01105, doi:10.1029/2011JD016443.

Poulida O, Dickerson RR, Heymsfield A (1996) Stratosphere-troposphere exchange in a midlatitude mesoscale convective complex: 1. Observations, *J. Geophys. Res.*, **101**, 6823–6836.

Qu Z, Huang Y, Vaillancourt P, Cole J, Milbrandt J, Yau M, Walker K. & Grandpré J (2020) Simulation of convective moistening of extratropical lower stratosphere using a numerical weather prediction model. Atmosperic Chemistry and Physics. 20. 10.5194/acp-20-2143-2020.

Randel WJ, Seidel DJ, Pan LL (2007), Observational characteristics of double tropopauses, J. Geophys. Res., 112, D07309, doi:10.1029/2006JD007904.

Rasmussen KL, Houze RA (2016) Convective Initiation near the Andes in Subtropical South America. *Mon. Wea. Rev.*, **144**, 2351–2374, https://doi.org/10.1175/MWR-D-15-0058.1.

Rasmussen KL, Zuluaga MD, Houze Jr. RA (2014) Severe convection and lightning in subtropical South America, *Geophys. Res. Lett.*, 41, 7359–7366, doi:10.1002/2014GL061767.

Rasmussen KL, Houze Jr. RA (2011) Orogenic convection in subtropical South America as seen by the TRMM satellite, *Mon. Weather Rev.*, 139, 2399– 2420.

Roach WT (1967), On nature of summit areas of severe storms in Oklahoma, *Q. J. R. Meteorol. Soc.*, **397**, 318–336.

Romatschke U, Houze Jr. RA(2010) Extreme summer convection in South America, *J. Clim.*, **23**, 3761– 3791.

Salio P, Nicolini M, Zipser EJ (2007) Mesoscale Convective Systems over Southeastern South America and Their Relationship with the South American Low-Level Jet. *Mon. Wea. Rev.*, 135, 1290–1309, https://doi.org/10.1175/MWR3305.1.

Seinfeld JH, Pandis SN (1998) Atmospheric chemistry and physics: From air pollution to climate change, 1360 pp., John Wiley & Sons, Inc., New York, NY.

Simmons A, Uppala S, Dee D, Kobayashi S (2006) ERA-Interim: New ECMWF reanalysis products from 1989 onwards, *ECMWF newsletter*, 110, 26–35.

Skamarock, WC, Klemp JB, Dudhia J, Gill DO, Barker DM, Duda MG, Huang X-Y, Wang W, Powers JG (2008) A Description of the Advanced Research WRF Version 3. NCAR Technical Note NCAR/TN-475+STR, doi:10.5065/D68S4MVH.

Smith JB et al. (2017), A case study of convectively sourced water vapor observed in the overworld stratosphere over the United States, *J. Geophys. Res. Atmos.*, 122, 9529–9554, doi:10.1002/2017JD026831.

Solomon S, Rosenlof K, Portmann R, Daniel J, Davis S, Sanford T, Plattner G (2010) Contributions of stratospheric water vapor to decadal changes in the rate of global warming. *Science*, 327, 1219-1223.

Stenke A, Grewe V (2005) Simulation of stratospheric water vapor trends: impact on stratospheric ozone chemistry, *Atmos. Chem. Phys.*, 5, 1257-1272, https://doi.org/10.5194/acp-5-1257-2005.

Tao W-K, Li X(2016), The relationship between latent heating, vertical velocity, and precipitation processes: The impact of aerosols on precipitation in organized deep convective systems, *J. Geophys. Res. Atmos.*, 121, 6299–6320, doi:10.1002/2015JD024267.

Thompson G, Field PR, Rasmussen RM, Hall WD (2008) Explicit Forecasts of Winter Precipitation Using an Improved Bulk Microphysics Scheme. Part II: Implementation of a New Snow Parameterization. *Mon. Wea. Rev.*, **136**, 5095–5115. doi:10.1175/2008MWR2387.1.

Wang PK (2003) Moisture plumes above thunderstorm anvils and their contributions to cross-tropopause transport of water vapor in midlatitudes, *J. Geophys. Res.,* 108, D002581, doi:10.1029/2002JD002581.

Vera C, Baez J, Douglas M, Emmanuel CB, Marengo J, Meitin J, Nicolini M, Nogues-Paegle J, Paegle J, Penalba O, Salio P, Saulo C, Silva Dias MA, Dias PS, Zipser E (2006) The South American Low-Level Jet Experiment. *Bull. Amer. Meteor. Soc.*, **87**, 63–77, doi:https://doi.org/10.1175/BAMS-87-1-63.

WMO, Scientific Assessment of Ozone Depletion (1995) WMO 37, Geneva, Switzerland.

WMO, World Meteorological Organization (1957) Meteorology — A three dimensional science: Second session of the Commission for Aerology, *WMO Bulletin,* vol. IV(no. 4), 134–138.

Zipser EJ, Cecil DJ, Liu C, Nesbitt SW, Yorty DP (2006) Where are the most intense thunderstorms on earth?. *Bull. Amer. Meteor. Soc.*, **87**, 1057–1072, https://doi.org/10.1175/BAMS-87-8-1057.

Conclusions

Stratospheric ozone protects Earth's surface from harmful ultraviolet radiation and understanding stratospheric ozone depletion is vital to protect human health and the Environment. Despite low ozone concentration at 100 hPa in the upper troposphere-lower stratosphere (UTLS), ozone variability at this level plays an important role in regulating air temperatures, which in turn regulates troposphere to stratosphere exchanges and stratospheric chemistry. In South America, these exchanges are driven by tropospheric weather and climate variability, especially deep convective processes perturbing the UTLS. This work investigates the spatial and temporal ozone variability in the UTLS over South America, with an emphasis on the La Plata Basin (LPB). This variability is investigated at multiple time-scales to understand the influence of teleconnections originating in the Pacific Ocean, specifically, the El Niño-Southern Oscillation (ENSO) on interannual time scales, and the Pacific Decadal Oscillation (PDO) on interdecadal time scales. Furthermore, on shorter time scales, deep convective clouds capable of detraining water vapor in the lower stratosphere may contribute to stratospheric chemistry and ultimately to ozone destruction (Forster and Shine 1999). This work fills a knowledge gap 1) by identifying primary modes of ozone variably related to large-scale processes (e.g. ENSO and PDO), and 2) by simulating deep convection with the Weather Research and Forecasting (WRF) model and quantifying lower stratospheric hydration.

Dissertation Objectives

5) Compare satellite and reanalysis ozone data, and provide an overview of stratospheric ozone variability in South America, including trends and interactions between ENSO and PDO during the wet season (Chapter 1).

6) Establish relationships between UTLS ozone patterns to ENSO and PDO in South America during the austral spring, with an emphasis on local mechanisms driving UTLS ozone patterns, circulation and temperature variability during El Niño events (Chapter 2).
7) Utilize the Weather Research and Forecasting (WRF) model to simulate MCSs and improve vertical model resolutions, and to reproduce observed double tropopause features in the UTLS for thermodynamic analysis during deep convective events (Chapter 3).
8) Investigate the influence of deep convection on UTLS double tropopause features and instability contributing to maximum water vapor height in the lower stratosphere (Chapter 4).

Key Results

Throughout this dissertation, a strong emphasis is placed on the UTLS region and tropopause boundary layer. This is a complex region influenced by tropospheric and stratospheric dynamics and chemistry. The focus of this work is to understand large-scale variably influencing ozone in the UTLS, and troposphere to stratosphere exchanges related transport via deep convection resulting in lower stratospheric hydration.

The first chapter focuses on spatial and temporal variability of wet season stratospheric ozone patterns in South America at 100, 50 and 10 hPa. This work was conducted with AIRS satellite data and MERRA2 reanalysis data to investigate ozone patterns from 2002-2016. Because AIRS data has a limited time frame, MERRA2 data is used for ozone trend analysis from 1980 – 2016, and to investigate interannual to interdecadal UTLS ozone variability related to ENSO and PDO for the same time frame. Results show that at 10 hPa and 50 hPa, ozone is strongly correlated to QBO. At these levels, patterns in the primary mode of variability may be explained by the Brewer Dobson Circulation and

modulated by QBO. When the QBO winds (stratospheric winds) are westerlies (positive QBO) the vertical velocity related to BDC is suppressed and ozone concentrations increase, the opposite is observed for easterly stratospheric winds. Additionally, at these levels no mode of variability is explained by ENSO or PDO. Conversely, at 100 hPa, no relationship to ozone variability is established with QBO. However, at 100 hPa relationships between the primary mode of ozone variability and PDO are observed and modulated by El Niño induced Rossby wave trains interacting with South America. While no strong connection between ozone anomalies at 100 hPa and ENSO are established during the last warm PDO phase (1980 – 1997), during the last cool PDO phase (1998 – 2016) strong relationships between ENSO and ozone anomalies are observed.

Trend analysis is applied to 100, 50 and 10 hPa. At 10hPa, negative trends occur across central South America and are collocated to the trends detected in the third mode of the PCA (PC3) principal components. The data used for this analysis has not been detrended and the positive trend in PC3 principal components may account for long term trends observed at 10 hPa. Furthermore, because the wet season spans the spring and summer, we investigated the impact of seasonal trends on the wet season patterns. At 10 hPa, the patterns of negative ozone related to positive PC3 are also observed in both of the spring and summer trend patterns. At 50 hPa, positive trends are observed in spring and summer and centered over the Amazon River in northern South America. The second mode of variability in the PCA (PC2) is also showing an increasing trend in the principal components at 50 hPa. Weak patterns in PC2 are detected in both the spring and summer trend patterns, and at this level neither season is showing a dominate impact in the PC2 patterns. Unlike 10 and 50 hPa, the 100 hPa spring and summer trends show the influences of tropospheric seasonal variably in

the trend patterns. At 100 hPa, the spring trend pattern closely resembles the third mode of variability (PC3) which has trends detected in the principal components. While few trends are detected in the summer analysis, during the spring, negative ozone trends span the eastern and southeastern South America and eastward across the Andes Mountain range.

The influence of low frequency UTLS ozone variability is shown with this work. These results may have additional implications for a potential feedback in Southeast South America. A study by Wu and Polvani (2017) using the Community Earth System Model Large Ensemble experiments from 1955 - 2005 showed that decreasing stratospheric ozone influenced extreme precipitation in Southeast South America – where decreased ozone increased extreme precipitation. Here, we show that lower stratospheric ozone variability is modulated by PDO, and during the cool PDO, El Niño events show relationships to decreasing ozone in Southeast South America, collocated to increasing extreme precipitation (Wu and Polvani 2017). This has implications for a possible positive feedback. Suggesting that while ozone patterns in the Southeast South America are related to large scale tropospheric circulation, as extreme precipitation and convective transport of cloud material in the lower stratosphere increases, ozone may decrease, and in turn enhance extreme precipitation in this region, repeating the cycle. While this theory may explain the ozone patterns in is region, it would require further investigation.

Chapter two investigates ozone patterns in South America based on results from chapter one. The focus of this chapter is on mechanism driving austral spring UTLS ozone variability related to El Niño's influence on South American circulation, geopotential height, and temperatures. Results in this chapter show that each mechanism is modulated by PDO phase. El Niño forced Rossby wave trains were found to influence UTLS temperature and

ozone variability in the La Plata Basin region of South America during the cool PDO, which are not observed during the warm PDO phase. We evaluated the linear and non-linear 200 hPa geopotential height response to ENSO in the two PDO phases, and showed that both responses (linear and non-linear) exhibit distinct spatial characteristics that depend on PDO. Furthermore, the non-linear response may indicate a shift in Rossby wave pattern during the warm PDO. In this case, Rossby wave breaking is diminished in the La Plata Basin when wave trains continue across the Southern Atlantic and Indian Oceans, rather than crossing the Andes Mountains, propagating equatorward, and breaking. This may explain the lack of ozone response during the warm PDO to El Niño. Additionally, during the warm PDO, the position of warm sea surface temperature anomalies related to El Niño: traditional (canonical) El Niños and central (Modoki) El Niños, is highly variable; whereas during the cool PDO, the majority of El Niños are Modoki El Niños. The large interannual variability during the warm PDO precludes identifying the primary mechanism driving UTLS ozone variability in South America and requires further analysis.

Unlike the warm PDO, the cool PDO phase demonstrates a strong connection to Rossby wave breaking in the La Plata Basin. Results show that during El Niño events, the upper level jet stream is shifted poleward over South America, and in the La Plata Basin region, 200 hPa geopotential heights are higher, 100 hPa temperatures are cooler, and 100 hPa ozone is decreasing. The roll of vertical circulation was also investigated over the Amazon and the southern La Plata basin. A shift in the steady state between the warm and cool PDO is observed over the tropics in UTLS vertical pressure velocity and 200 hPa zonal winds. In the tropics, upwelling is generally associated with the deep branch of the BDC. However, over the Amazon during the cool PDO, downwelling occurred at 100 hPa and was

likely transporting ozone from higher altitudes to 100 hPa, which accounts for increasing ozone concentrations. Conversely, circulation in the La Plata Basin during the cool PDO is showing weak average vertical circulation and decreasing ozone. This may be explained by Rossby wave breaking in this region, destabilizing the atmosphere and becoming more susceptible to deep convection capable of detraining water vapor in the lower stratosphere and influencing ozone chemistry. Identifying the primary mechanism driving lower stratospheric hydration in the LPB is explored in Chapters 3 and 4.

Chapter three focuses on mesoscale modeling of the UTLS with the Weather Research and Forecasting (WRF) numerical model (Skamarock 2008). For this chapter, sensitivity testing is conducted with two case studies during the austral spring to configure the model to 1) simulate deep convection associated with mesoscale convective systems in the LPB and to 2) determine the optimal model vertical resolution to simulate double tropopause features. Five cumulus schemes were tested and the Grell-Freitas Ensemble scheme demonstrated optimal performance. The case study for this work occurred on November 29, 2012. The WRF model, initiated with the Grell-Freitas Ensemble scheme, adequately simulate the size and location of the mature MCS. To maximize computational resources, this case study was conducted with a 15 km inner domain and 41 vertical model levels. While the simulation does adequately simulate the MCS, the vertical resolution is coarse and does not simulate double tropopause events observed in sounding data. As a result, the simulations are further downscaled to 3 km horizontal resolution for vertical sensitivity testing allowing for fine scale vertical resolutions.

For the second case study in Chapter 3, a mesoscale convective complex (MCC) was identified on November 12, 2018 during the RELAMPAGO field campaign. The goal for this

work was to improve the model resolution in the UTLS and simulate observed double tropopause features. WRF was run three times and initiated with 1) 61 WRF assigned model levels, 2) 61 user assigned model levels and 3) 75 user assigned model levels. The results show that the third run, with user assigned model levels clustered in the boundary layer and UTLS does improve model simulations. Overall, the third run simulated the location and extent of the MCC reasonably well and showed an improvement in RMSE temperature and wind speed compared to runs 1 and 2, and more importantly, temperature profiles in the third run show an improvement in simulating double tropopause features. The data from the third run is retained for further analysis of double tropopause events and lower stratospheric hydration in Chapter 4.

Chapter four utilizes the optimally configured WRF model output from chapter three to conduct case study analysis. This work seeks to understand UTLS instability and temperature variability and quantify lower stratospheric hydration capable of influencing stratospheric chemistry during deep convection. The influence of deep convection on UTLS double tropopause events is investigated with three types of deep convection: discrete convective cells, a MCC and a frontal boundary (Squall line). During this case study, WRF detected double tropopause events for each convective system examined, and double tropopauses were collocated to enhanced maximum water vapor levels in the lower stratosphere. However, only the MCC and Squall line systems were hydrating the lower stratosphere.

A key result of this study shows that the primary source of lower stratospheric hydration is ice near the thermal tropopause. Cold primary tropopause temperatures and the presence of moisture seem to contribute to ice formation in the UTLS leading to instability

via latent heat exchanges and updrafts. Among the three categories of deep convection compared in this study, discrete cells have the warmest primary tropopause temperatures and located at lower altitudes compared to the MCC and Squall line. During discrete convective cells, the tropopause is hydrated where a mixed layer of water vapor and ice is located above the primary tropopause and extends just above the secondary tropopause. However, directly above the primary tropopause temperatures warm quickly and updrafts are not observed. During this type of event, deep convection overshooting does not appear to be hydrating the lower stratosphere and net vertical velocity is negative above the secondary tropopause which would explain why water vapor is not observed above 17 km.

For the organized systems of deep convention, the MCC and Squall line types have colder primary tropopause temperatures and higher primary tropopause heights compared to the discrete cells. For these events, pockets of low water vapor concentrations occur in and above the tropopause. However, above the secondary tropopause, lower stratospheric hydration is observed in both modes to nearly 20 km. Additionally, above 15 km the water vapor and ice concentrations are stratified, the presence of ice and water vapor mixing ratios are in layers rather than mixed as observed with the discrete cells. This may have contributed to the enhanced instability below the primary tropopause level and the strong positive vertical velocity capable of overshooting tropospheric material beyond the secondary tropopause. This mechanism can explain the heights of maximum water vapor hydrating the lower stratosphere.

The focus of this investigation is on simulating double tropopause events related to deep convection in the LPB with the WRF model to evaluate lower stratospheric hydration. This is valuable information as deep convection can lead to troposphere – stratosphere

exchanges and irreversible mixing in the lower stratosphere. Additionally, the presence of enhanced water vapor mixing ratios in the stratosphere can also contribute to stratospheric chemistry. This in turn would affect ozone chemistry, and ultimately destroy ozone. While ozone in the UTLS region statistically significantly decreased from 1998 – 2016 (Chapter 1, Fig. 12i), the extent of the contribution of water vapor on stratospheric chemistry and ozone destruction has not been widely evaluated in the LPB and would require further investigation.

Suggestions for Future Work

The focus of this research is on UTLS variability on multiple spatial and temporal scales, and yet results lead to further questions for investigation and analysis.

1. On a climatological scale, more work emphasizing mechanisms driving warm PDO variability is necessary. Specifically, investigate the mechanisms related to the linear and non-linear 200 hPa geopotential height response to ENSO. Furthrmore, a better understanding of the influences of El Niño based on the location of warm anomalies in the Pacific Ocean.
2. On a regional scale, investigating the redistribution of heat and moisture to the La Plata Basin. Especially the influence of the South American Low Level Jet (SALLJ) to identify the source of moisture for lower stratosphere hydration.
3. On a local scale, investigating the influence stratosphere to troposphere exchanges. Specifically, stratospheric intrusions and their influence on tropospheric processes

References

Forster PMF, Shine KP (1999) Stratospheric water vapour changes as a possible contributor to observed stratospheric cooling, *Geophysical Research Letters*, vol. 26, no. 21, 3309-3312.

Wu Y, Polvani LM (2017) Recent Trends in Extreme Precipitation and Temperature over Southeastern South America: The Dominant Role of Stratospheric Ozone Depletion, *J. Climate*, 30, 6433-6441.